

Université de Lille

THÈSE

pour obtenir le grade de

DOCTEUR DE L'UNIVERSITÉ DE LILLE

Ecole doctorale Sciences de la Matière, du Rayonnement et de l'Environnement

Discipline : Chimie des matériaux

---

Insights into structure-stability-property relationships in hybrid perovskites using solid-state NMR spectroscopy

(Etude des relations structure-stabilitépropriété dans les pérovskites hybrides par spectroscopie RMN à l'état solide)

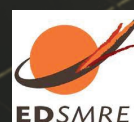
---

par

Parth Raval

Présentée et soutenue publiquement le 13 Décembre 2022 devant la commission d'examen:

M. Philip Schulz (DR)	CNRS-IPVF, France	Président du jury
M. Nicolas Mercier (PR)	Université Angers, France	Rapporteur de thèse
M. Jens Dittmer (PR)	Le Mans Université, France	Rapporteur de thèse
Mme Elodie Salager (CR)	CNRS-CEMHTI, France	Examineur de thèse
Mme Claire Roiland (IR)	Université de Rennes 1, France	Examineur de thèse
M. Olivier Lafon (PR)	Université de Lille, France	Directeur de thèse
M. Laurent Delevoye (DR)	CNRS-UCCS, France	Co-directeur de thèse
M. G N Manjunatha Reddy (MCF)	Université de Lille, France	Encadrant de thèse







# Abstract

---

In the last decade, there has been a progressive increase in the performance of solution-processed hybrid lead halide perovskite solar cells (PSCs), which has been enabled by means of compositional tailoring and interfacial engineering of the perovskite absorber layer and the charge transport layers. However, the long-term operational stability of these materials, including state-of-the-art perovskite formulations, is a major bottleneck in commercializing these materials. In this context, the main objective of this thesis is to understand the different degradation reactions and kinetics aspects of these reactions in hybrid perovskite layers and charge transport layers, especially in the presence of moisture. The degradation reactions in methylammonium (MA) and formamidinium (FA)-based perovskite formulation, in particular, MAPbI<sub>3</sub>, FAPbI<sub>3</sub>, and CsMAFAPbI<sub>x</sub>Br<sub>3-x</sub>, which are among the high-performing perovskite formulations in PSCs, are studied, analyzed, and compared. In doing so, these materials in crystalline and thin film forms are exposed to low (40% relative humidity, RH) and high (85% RH) water-vapor concentrations. However, the coexistence of the different organic/inorganic and hybrid byproducts and dilute concentrations of different phases formed during the degradation reactions raise challenges in terms of structural characterization. A multi-technique approach involving XRD, microscopy, and solid-state (ss)NMR spectroscopy has been employed to characterize the different degradation products. As a quantitative local characterization technique, ssNMR spectroscopy has notably the ability to probe dilute concentrations of organic byproducts formed upon degradation, which are challenging to detect using other structure-determining techniques. In particular, insights into the moisture-induced phase transformation reactions of FAPbI<sub>3</sub> as a function of water vapor concentration, particle size, and light illumination have been obtained by this multi-technique approach. This concept has been later extended to investigate the cascading degradation reactions in MAPbI<sub>3</sub>-based perovskites with and without surface passivating agents. Our studies indicate that the stability of the perovskite can be adjusted from a few days to several months, depending on the moisture-exposure conditions. Finally, a combination of ssNMR, ssEPR, and computational modelling (NMR crystallography) has been employed to gain insight into the structure-stability-property relationship in a hole-transporting layer spiro-OMeTAD. A detailed study of degradation reactions using multiscale characterization techniques described in this thesis has wider implications for the molecular-level understanding of structure-processing-stability-property relationships in hybrid perovskites and charge transport layers.





# Résumé

---

Les performances des cellules solaires à base de pérovskites hybrides contenant des halogénures de plomb (PSC) ont été fortement améliorées depuis dix ans. Ces améliorations ont été rendues possibles en ajustant les compositions et en jouant sur la nature des interfaces des couches de pérovskite et de transport de charge. Cependant, la stabilité opérationnelle à long terme de ces matériaux reste un problème majeur dans l'optique d'une commercialisation de ces matériaux. Dans ce contexte, l'objectif principal de cette thèse est de comprendre les différentes réactions de dégradation et les aspects cinétiques de ces réactions dans les couches de pérovskites hybrides et les couches de transport de charge, notamment en atmosphère humide. Nous avons notamment analysé les réactions de dégradation des pérovskites à base de méthylammonium (MA) et de formamidinium (FA), en particulier  $\text{MAPbI}_3$ ,  $\text{FAPbI}_3$  et  $\text{CsMAFAPbI}_x\text{Br}_{3-x}$ . Ces matériaux sous forme de cristaux et de couches minces ont été exposés à des concentrations faibles (40%) et élevées (85%) de vapeur d'eau. Cependant, la coexistence des différents sous-produits organiques/inorganiques et hybrides ainsi que les concentrations diluées des différentes phases formées lors des réactions de dégradation posent des difficultés en terme de caractérisation structurale. Une approche multi-technique combinant la diffraction des rayons, la microscopie et la spectroscopie RMN à l'état solide a été utilisée pour caractériser les différents produits de dégradation. En particulier, la spectroscopie RMN des solides, en tant que méthode de caractérisation locale quantitative, permet de mesurer des concentrations diluées de sous-produits organiques formés lors de la dégradation, qui sont difficiles à détecter à l'aide d'autres techniques de caractérisation. En particulier, cette approche multi-technique a permis d'obtenir des informations uniques sur les transformations de phase du  $\text{FAPbI}_3$  en fonction du taux d'humidité, de la taille des particules et de l'irradiation lumineuse. Cette approche a ensuite été étendue pour étudier les réactions de dégradation en cascade des pérovskites à base de  $\text{MAPbI}_3$  avec et sans agent passivant de surface. Enfin, des mesures RMN et RPE sur les solides ont été combinées avec des calculs de chimie théorique, selon une approche de cristallographie RMN, afin de mieux comprendre la relation structure-stabilité-propriété dans un matériau de transport de trous, spiro-OMeTAD. Une étude détaillée des réactions de dégradation à l'aide de techniques de caractérisation multi-échelles décrites dans cette étude a des implications plus larges pour la compréhension au niveau moléculaire des relations structure-traitement-stabilité-propriété dans les pérovskites hybrides et les semi-conducteurs organiques.



# Acknowledgment

---

I am fortunate to have pursued my doctoral research at Université de Lille while enjoying exciting French culture. The past three years have significantly developed my scientific vision, skill sets, and professionalism. All this would not have been possible without the people in my personal and professional life who helped me along the way.

First, I would like to thank the members of the jury, Dr. Philip Schulz, Prof. Nicolas Mercier, Prof. Jens Dittmer, Dr. Elodie Salager, and Dr. Claire Roiland, who kindly agreed to evaluate my doctoral work. I thank Dr. Dominik Kubicki for the insightful discussions.

I would like to express my gratitude to my thesis advisors, Prof. Olivier Lafon, Dr. Laurent Delevoye, and Dr. G N Manjunatha Reddy for their constant support throughout my PhD. Besides my scientific development, they showed me how to always be ready for a new challenge (opportunity), while maintaining composure and a smile, and efficiently resolving the challenges. I would like to thank Manju for his constructive remarks throughout my time in Lille. All in all, it was a wonderful experience to have multiple sources of guidance and encouragement, for which I am grateful.

I would like to acknowledge the financial support from Université de Lille and Région Hauts-de-France for my subsistence in France so far. I thank EU H2020 for its financial support in covering the experimental expenses.

Apart from my thesis advisors, if there is another person responsible for my progress in Lille, it is Dr. Julien Trébosc. Julien has a knack of solving practical NMR-related hurdles, and I appreciate his insights into NMR experiments and analyses. I am also grateful to Bertrand Doumert, Bertrand Revel, and Dr. Andrew Rankin, for well-maintaining a fantastic NMR facility in Lille.

I am thankful to the research groups of Prof. Mercouri Kanatzidis (Northwestern University, USA), Prof. Michael Chabynec and Prof. Thuc-Quyen Nguyen (University of California, Santa Barbara, USA), Dr. Frédéric Sauvage (Université de Picardie Jules Verne, France), Dr. Herve Vezin and Dr. Pascal Roussel (CNRS/Université de Lille), Dr. Debangshu



Chaudhuri (IISER Kolkata, India) and Dr. Tomasz Pawlak (Polish Academy of Sciences, Poland). They have been excellent collaborators, and it was a privilege to work alongside them.

A big thanks to Philippe Devaux, Myriam Wastiaux, Maxence Vandewalle, and Edouard Capoen for their support in the laboratory. I would like to thank Batoul and Maxime for their help related to the glovebox. I cannot forget the conversations with Dr. Giuseppe Sicoli and Dr. Hania Ahouari and their support while sharing the NMR sample preparation room.

It was a privilege to share my office with Jennifer, Guillaume, Florian, Racha, Lama, Diane, Jess, Batoul, Neethu, Athulya, Pierre, and Raphael. Thanks for maintaining a wonderful work environment and countless wonderful experiences. A special mention to Jennifer (Regi) and Racha (Princess) for guiding me through the tedious bureaucracy. I genuinely realized your efforts when I was helping Neethu and Athulya with the same. Lunch-time conversations and games with Diane (Oh la la!) and her help in proofing emails in French are some things I won't forget. Assisting Lama, Margot, Mouhamed, Claire, and Itzel during their Masters' internship was exciting and fun.

My time in Lille introduced me to some delightful people – Liesel, Sreekala, Doha, Gayathri, Zack, Karishma, and Sindhu. I thank them for their friendship, for all the food and drinks, and trips together. I would like to extend my gratitude to my roommates in the past 3 years, Marie-Astrid, Lara, Romain, Sabrina, Alice, Louis, and Swann, for the French food, the maintaining the vibe of the place, and for organizing surprise late-night parties on occasion. Thanks to Parvathy, who was a blessing in the latter half of my PhD for her unconditional support and hilarious dinner conversations.

My IISER Mohali family has always supported and encouraged me in their ways. I appreciate late-night conversations with Akanksha, Nilotpal, Shivangi, Nishant, Samita, Pinku, and Nitish. It was/is fun to hear their stories and rants and I wish them all for a well-deserved promising future.

Finally, I would like to thank my family – Dhyansh, Hariom, and Ami for all the cheerful and fun conversations, and endless support. I am forever indebted to my parents for all their love, and for living as an example that molded me throughout my life.

# Table of content

---

<b>Abstract</b>	<b>I</b>
<b>Résumé</b>	<b>III</b>
<b>Acknowledgment</b>	<b>V</b>
<b>Table of content</b>	<b>VII</b>
<b>List of figures</b>	<b>IX</b>
<b>List of tables</b>	<b>XV</b>
<b>Preface</b>	<b>XVII</b>
<b>Chapter 1 - Introduction</b>	<b>1</b>
1.1. Emerging photovoltaic materials based on metal halide perovskites	1
1.1.1. Potential of solar energy	1
1.1.2. Perovskites	2
1.1.3. Lead halide perovskite	3
1.2. Perovskite solar cells	6
1.3. Instability associated with lead halide perovskites	7
1.3.1. Moisture-induced degradation	7
1.3.2. Temperature-induced degradation	8
1.3.3. Light-induced degradation	9
1.4. Approaches for stability enhancements	10
1.4.1. Compositional engineering of lead halide perovskites	10
1.4.2. Low-dimensional perovskites	12
1.4.3. Defect passivation	15
1.5. Characterization of metal halide perovskites	17
1.6. Solid-state NMR spectroscopy	19
1.6.1. Interactions in NMR spectroscopy	19
1.6.2. Resolution and sensitivity enhancement in solid-state NMR	24
1.6.3. 1D NMR experiments	26
1.6.4. Two-dimensional NMR experiments	29
1.7. Outline of the thesis	32
1.8. References	33
<b>Chapter 2 - Instability in formamidinium-based lead halide perovskites</b>	<b>47</b>
2.1. Formamidinium-based perovskites for high-performance photovoltaics	47
2.2. Understanding the kinetics of phase-transformation	53
2.2.1. Influence of the particle size on moisture-induced phase transformation	54
2.2.2. The role of water vapor concentration on FAPbI <sub>3</sub> instability	57
	<b>VII</b>

2.2.3.	Influence of light on $\alpha \rightarrow \delta$ FAPbI <sub>3</sub> phase transformation	58
2.3.	Insight into local interfacial structures of $\alpha$ -  $\delta$ -FAPbI <sub>3</sub>	59
2.4.	The role of halide ions in the stability of FAPbX <sub>3</sub>	68
2.5.	Instability in FA-rich formulations	72
2.6.	Instability in formamidinium-based lead halide perovskite: Key learnings from ssNMR	77
2.7.	References	78
<b>Chapter 3 - Probing moisture-induced degradation reactions in methylammonium-based perovskites</b>		<b>85</b>
3.1.	Methylammonium lead iodide (MAPbI <sub>3</sub> ) for photovoltaic applications	85
3.2.	Probing moisture-induced degradation reactions in methylammonium lead iodide	88
3.3.	Defect-passivated methylammonium lead iodide and its moisture stability	97
3.4.	Moisture-catalyzed transformative reactions and degradation products: Summary	103
3.5.	Conclusion	107
3.6.	References	108
<b>Chapter 4 - Structural insights into the p-doped hole transporting materials</b>		<b>115</b>
4.1	Organic semiconductors as hole-transporting materials in perovskite solar cells	115
4.2	NMR crystallography of spiro-OMeTAD	119
4.3	Chemically doped spiro-OMeTAD by BCF	124
4.4	Moisture stability of chemically doped spiro-OMeTAD:BCF blends	136
4.5	Conclusion	139
4.6	References	140
<b>Chapter 5 - Conclusions and perspectives</b>		<b>147</b>
5.1	Conclusions	147
5.2	Perspectives	152
5.3	References	153
<b>Experimental Section</b>		<b>155</b>
	Chapter 2	155
	Chapter 3	161
	Chapter 4	165
	References	168
<b>Curriculum Vitae</b>		<b>171</b>

# List of Figures

---

**Figure 1.1.** Perovskite structural scheme. A (black) is a monovalent, and B (blue) is a divalent cation. X, shown in red, is a monovalent anion.

**Figure 1.2.** Electronic band structure diagram of MAPbI<sub>3</sub> without considering spin-orbit coupling interaction. The origin of the energy scale is taken at the top of the valence band. (Figure adapted from Ref )

**Figure 1.3.** The emission wavelength of CH<sub>3</sub>NH<sub>3</sub>PbX<sub>n</sub>Y<sub>3-n</sub> can be tuned from 390 to 790 nm wavelength. (Figure adapted from reference)

**Figure 1.4.** Optical absorption coefficient of crystalline silicon and MAPbI<sub>3</sub> perovskite as a function of wavelength of the incident light. (Figure adapted from reference)

**Figure 1.5.** Power Conversion Efficiency (PCE) evolution of perovskite solar cells (PSCs) along with the composition of perovskite photo-absorbing layer.

**Figure 1.6.** Crystal structure of (a) BA<sub>2</sub>PbI<sub>4</sub> (RP-phase) and (b) (4AMP)PbI<sub>4</sub> (DJ-phase)

**Figure 1.7.** "Larger A-site" cations used to form deficient/ hollow perovskite

**Figure 1.8.** Chemical structures of (a) nitrogen-based, (b) oxygen-based, and (c) sulphur-based defect passivating agents (Lewis base).

**Figure 1.9.** Comparison of length and timescales: the range of timescales of physical processes in MHPs is presented alongside the fundamental time and length scales that several characterization techniques can probe in MHPs. Figure reproduced from reference.

**Figure 1.10.** Schematic representation of the magnitude of the spin interactions in solid-state NMR spectroscopy for a quadrupolar nucleus with  $I \geq 1$ .

**Figure 1.11.** Schematic diagram of the energy levels of (a) spin  $I = 1/2$  and (b) spin  $I = 3/2$  nucleus in an external magnetic field  $B_0$  due to Zeeman interaction in the absence of quadrupolar coupling.

**Figure 1.12.** Magic angle spinning. The sample is spun in a cylindrical rotor about a spinning axis ( $\beta_{RL} = 54.736^\circ$ ) with respect to the applied magnetic field  $B_0$ .

**Figure 1.13.** Continuous-wave decoupling on I nuclei during S nuclei detection

**Figure 1.14.** Pulse sequence of the single-pulse experiment

**Figure 1.15.** Pulse sequence of the spin-echo experiment

**Figure 1.16.** Saturation recovery pulse sequence along with a schematic of the build-up of signal intensity as the time  $\tau$  is varied.

**Figure 1.17.** Basic 2D pulse scheme. The evolution period,  $t_1$ , between the preparation and mixing time elements incremented, followed by another period that allows for mixing before detection in the  $t_2$  period.



**Figure 1.18.** Pulse sequence and coherence transfer pathway diagram for a  $^1\text{H}$  DQ-SQ MAS experiment using the BaBa recoupling sequence for the excitation and reconversion of DQ coherence.

**Figure 1.19.** The pulse sequence and coherence transfer pathway diagram for a NOESY-type spin diffusion experiment

**Figure 2.1.** Photoluminescence spectra of  $\text{FAPbI}_3$  as a function of moisture (85% RH) exposure time.

**Figure 2.2.** Powder XRD patterns of  $\text{FAPbI}_3$  particles acquired before and after exposure to moisture at 85% RH for different durations as indicated, along with the simulated powder XRD patterns of  $\alpha$ - and  $\delta$ - $\text{FAPbI}_3$  of published crystal structures using Mercury software.

**Figure 2.3.** 1D (a)  $^{207}\text{Pb}$  and (b)  $^1\text{H}$  MAS NMR spectra of fresh ( $\alpha$ - $\text{FAPbI}_3$ ) and aged ( $\alpha|\delta$ - $\text{FAPbI}_3$ ,  $\delta$ - $\text{FAPbI}_3$ ) materials upon exposure to moisture (85% RH). Signals associated with  $\alpha$  and  $\delta$  polymorphs are indicated and color-coded as depicted in the schematic structure in (b). All  $^1\text{H}$  (900.2 MHz) and  $^{207}\text{Pb}$  (167.6 MHz) spectra were acquired with 50 kHz MAS.

**Figure 2.4.** Normalized  $^1\text{H}$  (-CH) signal intensity of FA cations in  $\alpha$ - $\text{FAPbI}_3$  plotted as a function of moisture (85% RH in the air) exposure time.

**Figure 2.5.** SEM images and particle-size distribution analyses of (a,b) large particles and (c,d) small particles, respectively.

**Figure 2.6.** Comparison of (a)  $\alpha$ - and (b)  $\delta$ - $\text{FAPbI}_3$  phase transformation kinetics by means of  $^1\text{H}$  signal intensity decay and build-up of -CH sites for small (20-40  $\mu\text{m}$ , squares) and large (40-100  $\mu\text{m}$ , dots) particles.

**Figure 2.7.** Kinetics plots of  $^1\text{H}$  signal intensity build-up of -CH sites of  $\text{FA}^+$  cations in  $\delta$ - $\text{FAPbI}_3$  and the simultaneous  $^1\text{H}$  signal intensity decay for the same sites in  $\alpha$ - $\text{FAPbI}_3$  as a function of exposure time to moisture in the dark at relative humidity levels of (a) 85% and (b) 40%.

**Figure 2.8.** Kinetics plots of  $^1\text{H}$  signal intensity build-up of -CH sites associated with  $\delta$ - $\text{FAPbI}_3$  and the simultaneous  $^1\text{H}$  signal intensity loss of the same sites in  $\alpha$ - $\text{FAPbI}_3$  as a function of exposure time at 85% RH (a) in the absence and (b) presence of laboratory illumination. The phase transformation kinetics can be modeled to first-order rate kinetics, leading to the estimation of rate constants. For kinetic studies, smaller particles  $\alpha$ - $\text{FAPbI}_3$   $\approx 32$  nm were used.

**Figure 2.9.** Schematic of  $\alpha \rightarrow \delta$   $\text{FAPbI}_3$  transformation upon exposure to moisture.

**Figure 2.10.** 2D  $^1\text{H}$ - $^{207}\text{Pb}$  CP-HETCOR spectra of  $\alpha|\delta$ - $\text{FAPbI}_3$  phase obtained after exposure to moisture (24 h, 85% RH), acquired with 6 ms of cross-polarization contact time, at room temperature, 18.8 T, 50 kHz MAS frequency.

**Figure 2.11.** Solid-state 2D  $^1\text{H}$ - $^1\text{H}$  DQ-SQ correlation NMR spectra of (a) cubic  $\alpha$ - $\text{FAPbI}_3$ , (b) partially transformed  $\alpha|\delta$ - $\text{FAPbI}_3$ , and (c)  $\delta$ - $\text{FAPbI}_3$  materials acquired at 21 T ( $^1\text{H}$ , 900.2 MHz) and at 50 kHz MAS frequency. Signals corresponding to -CH and - $\text{NH}_2$  are color-coded as depicted in the figure inset of (a).

**Figure 2.12.** Solid-state 2D  $^1\text{H}$ - $^1\text{H}$  spin-diffusion NMR spectra of (a,d) fresh and aged (b,c,e,f) FAPbI<sub>3</sub> materials acquired at 21 T ( $^1\text{H}$  900.2 MHz) with 50 kHz MAS. Signals corresponding to  $-\text{CH}$  and  $-\text{NH}_2$  sites are color-coded as depicted in the figure inset of (a). (a-c) are acquired with 1 ms of mixing time, and (d-f) are acquired with 200 ms of spin diffusion time.

**Figure 2.13.** Solid-state static 1D  $^2\text{H}$  NMR spectra of FAPbI<sub>3</sub> acquired at room temperature as a function of exposure time to D<sub>2</sub>O vapor (85% RH) together with the 1D  $^2\text{H}$  NMR spectrum of liquid D<sub>2</sub>O acquired under the same conditions. A static  $^2\text{H}$  NMR spectrum of control  $\delta$ -FAPbI<sub>3</sub> material obtained after exposure to D<sub>2</sub>O for 48h is acquired and compared. All spectra were acquired at 18.8 T ( $^2\text{H}$  = 122.8 MHz) and at room temperature.

**Figure 2.14.** 1D  $^1\text{H}$  MAS NMR spectra indicate the  $\alpha$ - $\delta$  FAPbI<sub>3</sub> transformation upon exposure to D<sub>2</sub>O at 85% RH. Signal intensity loss associated with NH<sub>2</sub> sites (7-8 ppm) indicates the on-the-fly deuteration of NH<sub>2</sub> sites of FA<sup>+</sup> cations.

**Figure 2.15.** Powder X-ray diffraction patterns of experimental and simulated FAPbBr<sub>3</sub>.

**Figure 2.16.** 1D (a)  $^{207}\text{Pb}$  and (b)  $^1\text{H}$  NMR spectra of fresh and aged (7 days, 85% RH) FAPbBr<sub>3</sub> acquired at 21.1 T, 50 kHz MAS

**Figure 2.17.** (a) Solid-state 2D  $^1\text{H}$ - $^1\text{H}$  DQ-SQ NMR correlation spectrum of fresh and aged (85  $\pm$  5% RH, 7 days) FAPbBr<sub>3</sub> acquired at 21 T ( $^1\text{H}$  900 MHz) and at 50 kHz MAS frequency. The corresponding skyline projections are shown along the top  $^1\text{H}$  SQ horizontal and  $^1\text{H}$  DQ vertical axes, respectively. Correlated signal intensities originating from dipolar-coupled  $^1\text{H}$ - $^1\text{H}$  pairs are depicted by colored circles.

**Figure 2.18.** Solid-state 1D (a)  $^2\text{H}$  NMR spectra recorded under static (bottom) and MAS (top) conditions, and (b)  $^1\text{H}$  MAS NMR spectra of FAPbBr<sub>3</sub> acquired after exposure to D<sub>2</sub>O for 48 h (top) and its line shape deconvolution analysis (bottom), suggesting 33% of deuteration of NH<sub>2</sub> sites.

**Figure 2.19.** Solid-state 1D MAS NMR spectra of CsMAFA acquired at 18.8 T, room temperature: (a)  $^{133}\text{Cs}$  (b)  $^1\text{H}$  MAS NMR spectra before and after exposure to moisture at 85% RH. The black and magenta vertical bands indicate the Cs ions associated with perovskite and non-perovskite phases.

**Figure 2.20.**  $^{133}\text{Cs}$  NMR spectrum of CsPb<sub>2</sub>Br<sub>x</sub>I<sub>5-x</sub> acquired at 18.8 T and room temperature.

**Figure 2.21.** Solid-state 1D MAS NMR spectra of CsMAFA acquired at 18.8 T, room temperature: (a)  $^{133}\text{Cs}$  (b)  $^1\text{H}$  MAS NMR spectra before and after exposure to moisture at 40% RH. The black and magenta vertical bands indicate the Cs ions associated with perovskite and non-perovskite phases.

**Figure 2.22.** Solid-state 2D  $^1\text{H}$ - $^1\text{H}$  SD NMR spectrum of CsMAFA acquired with 500 ms mixing time for (a) pristine and after exposure to moisture for (b) 167 h at 85% RH and (c) 1 year at 40% RH. Peaks correspond to MA<sup>+</sup>, and FA<sup>+</sup> cations are color-coded as depicted in the boxes.

**Figure 3.1.** Orthorhombic, tetragonal, and cubic crystal structures of methylammonium lead iodide.

**Figure 3.2.** XRD patterns of MAPbI<sub>3</sub> before and after exposure to moisture (85% RH) for different durations as indicated. The peaks are labeled corresponding to Bragg planes of MAPbI<sub>3</sub> (black), MAPbI<sub>3</sub>.H<sub>2</sub>O (green), and PbI<sub>2</sub> (red), along with the schematic structure of MAPbI<sub>3</sub> in the inset.

**Figure 3.3.** Experimental and simulated 1D <sup>1</sup>H MAS NMR spectra of MAPbI<sub>3</sub> before and after exposure to moisture (85% RH). The spectra were simulated as the sum of the signals of four species: MAPbI<sub>3</sub> (black), MAPbI<sub>3</sub>.H<sub>2</sub>O (green), MAI (magenta) exhibiting signals of NH<sub>3</sub><sup>+</sup> and CH<sub>3</sub> groups, and H<sub>2</sub>O (turquoise). The integrated intensities of the simulated spectra are indicated in Table 3.1. All spectra were acquired at 18.8 T and room temperature.

**Figure 3.4.** (a) 2D <sup>1</sup>H-<sup>1</sup>H DQ-SQ and (b) 2D <sup>1</sup>H-<sup>1</sup>H spin diffusion spectra of fresh MAPbI<sub>3</sub> (blue) and exposed to moisture (red) during 17 h at 85% RH acquired at 18.8 T.

**Figure 3.5.** 1D <sup>1</sup>H MAS NMR spectrum of MAI acquired at 18.8 T, with peaks depicting CH<sub>3</sub> and NH<sub>3</sub> moieties.

**Figure 3.6.** Solid-state 1D <sup>1</sup>H NMR spectra of MAPbI<sub>3</sub> after exposure to moisture at 40% RH during duration indicated on the right side of the spectra. All spectra were acquired at 18.8 T and room temperature.

**Figure 3.7.** 2D <sup>1</sup>H-<sup>1</sup>H spin-diffusion spectra of MAPbI<sub>3</sub>: (a) fresh and (b-d) exposed to moisture (85% RH) during (b) 17 h, (c) 34 h and (d) 45 h, acquired at 18.8 T. The signals corresponding to different phases (i, ii, and iii) are color-coded, as depicted in Figure 3.2.

**Figure 3.8.** 2D <sup>1</sup>H-<sup>1</sup>H DQ-SQ correlation NMR spectra of MAPbI<sub>3</sub> thin film acquired (a) before and (b) after exposure to 45 h moisture (85% RH). Gray arrow indicating distortions in the CH<sub>3</sub> peak corresponding to the formation of the solid solution of MAPbI<sub>3</sub> hydrate.

**Figure 3.9.** Solid-state 2D <sup>1</sup>H-<sup>1</sup>H (a) spin-diffusion and (b) DQ-SQ MAS NMR spectra of aged (1 year, 40% RH) MAPbI<sub>3</sub> acquired at 18.8 T, room temperature. The signals corresponding to different phases (i and ii) are color-coded, as depicted in Figure 3.2.

**Figure 3.10.** 1D <sup>1</sup>H NMR spectrum of TPAI acquired at 18.8 T, with MAS frequency of 58 kHz along with its structure.

**Figure 3.11.** XRD patterns of MAPbI<sub>3</sub>.TPA (4 mol%) before and after exposure to moisture (85% RH) with Bragg reflections labeled for MAPbI<sub>3</sub> (black), MAPbI<sub>3</sub>.H<sub>2</sub>O (green), and PbI<sub>2</sub> (red) along with the schematic of MAPbI<sub>3</sub>.TPA(4 mol.%) in the inset.

**Figure 3.12.** Solid-state 1D <sup>1</sup>H MAS NMR spectra of MAPbI<sub>3</sub>.TPA (4 mol%) before and after exposure to moisture at 85% RH acquired at 18.8 T. Grey band indicates the region (7-9 ppm, inset) corresponding to the NH<sub>3</sub> signal of MAI.

**Figure 3.13.** Solid-state 1D <sup>1</sup>H MAS NMR spectra of MAPbI<sub>3</sub>.TPA (4 mol%) before and after exposure to moisture at 40% RH during duration indicated on the right side of the spectra acquired at 18.8 T. The inset on the left shows the expanded region (7-9 ppm) of the NH<sub>3</sub> signal of MAI.

**Figure 3.14.** Solid-state 2D (a) <sup>1</sup>H-<sup>1</sup>H SD and (b) <sup>1</sup>H-<sup>1</sup>H DQ-SQ correlation NMR spectra of pristine MAPbI<sub>3</sub>.TPA (4mol.%).

**Figure 3.15.** Solid-state 2D  $^1\text{H}$ - $^1\text{H}$  (a) spin-diffusion and (b) DQ-SQ MAS NMR spectra of aged (72 h, 85% RH) MAPbI<sub>3</sub>.TPA (4mol.%).

**Figure 3.16.** Solid-state 2D  $^1\text{H}$ - $^1\text{H}$  (a) spin-diffusion and (b) DQ-SQ MAS NMR spectra of aged (1 year, 40% RH) MAPbI<sub>3</sub>.TPA (4mol.%).

**Figure 3.17.** Proposed reaction degradation pathways of (a) MAPbI<sub>3</sub>, (b) MAPbI<sub>3</sub>.TPA (4 mol.%), (c) FAPbI<sub>3</sub>, and (d) CsMAFA materials after exposure to different water vapor concentration (85%/ 40% RH).

**Figure 4.1.** (a) Schematic of n-i-p perovskite solar cell device with different layers stacked on top of each other as indicated. (b) Energy level diagram adapted from reference.

**Figure 4.2.** Chemical structures of (a) common organic hole transporting material and (b) their dopants.

**Figure 4.3.** Solid-state 1D (a)  $^1\text{H}$  MAS and (b)  $^1\text{H} \rightarrow ^{13}\text{C}$  CP-MAS NMR spectra of neat spiro-OMeTAD (CP contact time of 2 ms – top and 60  $\mu\text{s}$  – bottom). The peaks are color-coded, as depicted in the schematic structure in (b). All the spectra were acquired at 18.8 T, room temperature, and 50 kHz MAS frequency.

**Figure 4.4.** (a) GIPAW DFT-D geometry optimized crystal structure of spiro-OMeTAD with specific inter- and intramolecular packing interactions that contribute to 2D peaks in the  $^1\text{H}$ - $^{13}\text{C}$  HETCOR NMR spectra. Solid-state 2D  $^1\text{H}$ - $^{13}\text{C}$  HETCOR NMR spectra of spiro-OMeTAD with CP contact time of (b) 100  $\mu\text{s}$  (c) 3 ms along with the skyline projections of  $^1\text{H}$  and  $^{13}\text{C}$  spectra in the top and left, respectively. DFT calculated NMR chemical shifts of spiro-OMeTAD are overlaid on their spectra. All 2D spectra were acquired at 18.8 T, room temperature, and 50 kHz MAS frequency. For the crystal structures of spiro-OMeTAD, the DFT calculated  $^1\text{H}$  and  $^{13}\text{C}$  chemical shifts for all  $^1\text{H}$ - $^{13}\text{C}$  pairs within (a) 1.3 Å and (b) 2.6 Å is depicted by the overlaid crosses.

**Figure 4.5.** UV-Vis spectra of undoped and BCF-doped spiro-OMeTAD as a function of dopant concentration in chlorobenzene.

**Figure 4.6.** Powder XRD patterns of pristine undoped and doped spiro-OMeTAD thin films drop cast on ITO-coated glass substrates.

**Figure 4.7.** Solid-state attenuated total reflection FT-IR spectra of undoped and doped spiro-OMeTAD thin films acquired at room temperature.

**Figure 4.8.** Solid-state (a)  $^{11}\text{B}$  and (b)  $^{19}\text{F}$  MAS NMR spectra of neat BCF and spiro-OMeTAD:BCF blends of the relative molar concentration of 1:1 and 1:4.

**Figure 4.9.** Solid-state 1D (a)  $^1\text{H}$  and (b)  $^1\text{H} \rightarrow ^{13}\text{C}$  CPMAS NMR spectra of spiro-OMeTAD:BCF blends of relative molar concentration indicated in the inset. 1D  $^1\text{H}$  and  $^{13}\text{C}$  MAS NMR spectra of pristine spiro-OMeTAD are presented as well for comparison.

**Figure 4.10.** Solid-state  $^1\text{H}$ - $^1\text{H}$  DQ-SQ correlation MAS NMR spectra of (a) undoped and (b) spiro-OMeTAD:BCF (1:4) blend acquired at 18.8 T ( $^1\text{H}$  800 MHz), 50 kHz MAS and at room temperature. For the undoped spiro-OMeTAD shown in (a), the GIPAW DFT-D calculated chemical shifts for all  $^1\text{H}$ - $^1\text{H}$  pairs within 2.5 Å are overlaid on top of the experimental spectrum



(blue crosses). The horizontal line-cut spectra of (c) undoped spiro-OMeTAD and (d) spiro-OMeTAD:BCF blend are extracted and compared for specific  $^1\text{H}$  DQ peaks ( $\sim 7.0$ ,  $9.7$ , and  $12.9$  ppm) as indicated by the horizontal dashed lines in (a) and (b).

**Figure 4.11.** Solid-state CW EPR spectrum for the neat spiro-OMeTAD and spiro-OMeTAD:BCF blends at 1:1 and 1:4 molar ratios.

**Figure 4.12.** Solid-state 2D HYSORE spectrum of spiro-OMeTAD:BCF (1:1 molar ratio) acquired at 10 K.

**Figure 4.13.** 1D (a)  $^{11}\text{B}$  and (b)  $^1\text{H}$  MAS NMR spectra of spiro-OMeTAD:BCF (1:1 molar ratio) blend as a function of moisture exposure at 40% RH (top) and 85% RH (bottom) for the time indicated on the right side of the spectra. All the spectra were acquired at 18.8 T, room temperature, and 50 kHz MAS frequency.

**Figure 4.14.** Solid-state 2D  $^1\text{H}$ - $^{11}\text{B}$  CP-HETCOR NMR spectrum of aged (160h, 85% RH) spiro-OMeTAD:BCF (1:1 molar ratio) blend with CP contact time of 2 ms along with the skyline projections of  $^{11}\text{B}$  and  $^1\text{H}$  spectra in the top and left, respectively. The spectrum was acquired at 18.8 T, room temperature, and 50 kHz MAS frequency.

**Figure 5.1.** Stability issues in perovskite material and perovskite solar cells that cause variation in PCEs during the damp-heat test (85% RH and 85 °C) of encapsulated 3D perovskite devices. These figures have been adapted from Ref.

**Figure 5.2.** (a) *In situ* X-ray diffraction patterns of  $\text{MAPbI}_3$  as a function of aging time until 1000 min under 85% RH. (b) corresponding evolution of the peak intensity as a function of time for the (110) plane of  $\text{MAPbI}_3$  (black), ( $-101$ ) plane of  $\text{MAPbI}_3\cdot\text{H}_2\text{O}$  (red), and (001) plane of  $\text{PbI}_2$  (blue). (c) *In situ* Transmission Electron Microscopy (TEM) showing the morphology of  $\text{MAPbI}_3$ ,  $\text{MAPbI}_3\cdot\text{H}_2\text{O}$ , and  $\text{PbI}_2$ . (d)  $^1\text{H}$  MAS NMR spectra of fresh ( $\alpha$ -FAPbI<sub>3</sub>) and aged ( $\alpha$ - $\delta$ -FAPbI<sub>3</sub>,  $\delta$ -FAPbI<sub>3</sub>) materials upon exposure to moisture (85% RH) (Same as Figure 2.3b). (e) Line shape deconvolution analyses for  $^1\text{H}$  MAS NMR spectrum of 20 h aged (85% RH) FAPbI<sub>3</sub> to estimate the quantity of  $\alpha$ - and  $\delta$ -FAPbI<sub>3</sub>. (f) Kinetics plots of  $^1\text{H}$  signal intensity buildup of  $-\text{CH}$  sites ( $\text{FA}^+$  cations) in  $\delta$ -FAPbI<sub>3</sub> and the simultaneous  $^1\text{H}$  signal intensity decay for the same sites in  $\alpha$ -FAPbI<sub>3</sub> as a function of exposure time to moisture (85% RH). (g) Photoluminescence spectra of FAPbI<sub>3</sub> as a function of moisture (85% RH) exposure time (Same as Figure 2.1). These figures have been adapted from Ref.

# List of Tables

---

**Table 2.1.** Half-life decay times of black FAPbI<sub>3</sub> crystals upon exposure to moisture at 85% RH.

**Table 2.2.** Half-life decay time associated with  $\alpha \rightarrow \delta$  phase FAPbI<sub>3</sub> transformation in the dark with varying relative humidity. The particle size distribution is 20-40  $\mu\text{m}$ .

**Table 3.1.** The integrated intensities associated with different phases obtained from the line shape deconvolution of the 1D <sup>1</sup>H NMR spectrum in Figure 3.3.

**Table 3.2.** Moisture-induced degradation products in hybrid perovskites as analyzed by different characterization techniques.

**Table 4.1.** Hole mobility ( $\text{cm}^2 \cdot \text{V}^{-1} \cdot \text{s}^{-1}$ ) of a few common organic hole transporting materials.

**Table ES.1.** Experimental parameters used for the acquisition of NMR spectra of MAPbI<sub>3</sub> exposed to 85% RH.

**Table ES.2.** Experimental parameters used for the acquisition of NMR spectra of MAPbI<sub>3</sub> exposed to 40% RH.

**Table ES.3.** Experimental parameters used for the acquisition of NMR spectra of MAPbI<sub>3</sub>.TPA(4%) exposed to 85% RH.

**Table ES.4.** Experimental parameters used for the acquisition of NMR spectra of MAPbI<sub>3</sub>.TPA(4%) exposed to 40% RH.



# Preface

---

The progressive increase in the performance of solution-processed hybrid lead halide perovskite solar cells (PSCs) has been enabled by means of compositional tailoring and interfacial modification of/between the perovskite absorber layer and the charge transport layers. However, the long-term operational stability of the state-of-the-art compositional tailored perovskites is a major hurdle in commercializing these materials. In this context, the main objective of this thesis is to understand the ambient stability and degradation reactions in hybrid perovskite layers and contact layers, especially in the presence of moisture. To begin with, chapter 1 describes the basic aspects of hybrid perovskites and the recent developments in compositional engineering and the dimensional tailoring of perovskites in photovoltaic applications. In addition, the instability associated with these materials and the synthetic approaches to enhance perovskite stability are explained, and the characterization challenges of these materials are outlined. In particular, the degradation reactions in MAPbI<sub>3</sub>, FAPbI<sub>3</sub>, and CsMAFAPbI<sub>x</sub>Br<sub>3-x</sub> and grain boundary passivated MAPbI<sub>3</sub> (using Lewis acid) are discussed. The existence of the different organic/inorganic and hybrid byproducts and dilute concentrations of different phases formed during the degradation reactions raise challenges in terms of structural characterization. In this regard, the multi-technique approach is best suited to characterize the different degradation products. In particular, solid-state NMR spectroscopy is a powerful technique to probe atomic-scale structures and structural dynamics associated with these materials. In the later parts of the chapter, an overview of theoretical aspects of ssNMR relevant to this thesis is presented.

Chapter 2 presents a detailed analysis of the transformative and reconstructive reactions in FAPbI<sub>3</sub>. Understanding such reaction pathways is crucial in developing environmentally more stable perovskite-based devices. The ambient stability of the  $\alpha$ -FAPbI<sub>3</sub> depends on external stimuli, such as light and moisture. Specifically, the kinetics of  $\alpha \rightarrow \delta$  FAPbI<sub>3</sub> reaction as functions of water vapor concentration, particle size, and light illumination are investigated, along with the chemical nature of the kinetically trapped  $\alpha|\delta$ -FAPbI<sub>3</sub> phase. The  $\alpha \rightarrow \delta$  FAPbI<sub>3</sub> phase transformation kinetics is different at the grain and sub-grain boundaries. This enables a



variation of the transformation time from days to several months depending upon the external environmental conditions. The transformation involves surface-initiated local dissolution and precipitation process, as revealed by the on-the-fly deuteration technique. Robustness towards moisture elucidated by the bromide counterpart indicates a thermodynamically stable  $\text{FAPbBr}_3$  phase in comparison to the kinetically stable  $\alpha\text{-FAPbI}_3$  phase. Building upon the understanding of the stability of FA-based perovskites, the moisture stability of FA-rich compositional engineered  $\text{Cs}_{0.05}(\text{MA}_{0.17}\text{FA}_{0.83})_{0.95}\text{Pb}(\text{Br}_{0.17}\text{I}_{0.83})_3$  ( $\text{CsMAFA}$ ) was investigated.  $\text{CsMAFA}$  was systematically exposed to different concentrations of water vapor to realize partial elimination of  $\text{Cs}^+$  cation but retention of organic cations in the perovskite framework even after aging the material for up to one year. Results of this chapter are presented in Raval et al., *ACS Energy Lett.* 2022, 7, 1534–1543. The results presented here are the outcome of collaborations with Prof. Mercuri Kanatzidis at Northwestern University and Prof. Michael Chabynyc at the University of California, Santa Barbara. The results described in Section 2.5 are the outcome of collaboration with Dr. Frederic Sauvage at Université de Picardie Jules Verne. I performed the ssNMR spectroscopic characterizations of pristine samples and subjected the materials to moisture to analyze the moisture stability of these materials using ssNMR spectroscopy.

Chapter 3 extends the concept of understanding the cascading degradation reactions in methyl ammonium-based hybrid perovskites. Here a systematic long-term moisture-stability of methylammonium lead iodide perovskites ( $\text{MAPbI}_3$ ) is presented.  $\text{MAPbI}_3$  is subjected to low (40%) and high (85%) relative humidity to identify the formation of different degraded products. The advantage of employing ssNMR spectroscopy lies in determining dilute concentrations of organic byproducts formed that are challenging to detect using other structure-determining techniques. X-ray diffraction is employed to determine the inorganic byproducts formed, complimenting the results and analysis from ssNMR spectroscopy. Interestingly, the degradation reaction depends on the concentration of water molecules as at high relative humidity, the material irreversibly transforms into byproducts, but at low relative humidity,  $\text{MAPbI}_3$  is observed to be in equilibrium with its hydrate for up to one year. In addition, the role of surface defect passivation in enhancing moisture stability is presented in this chapter. A dilute concentration (4 wt.%) of tetra propyl ammonium cation ( $\text{TPA}^+$ ) is utilized to passivate the grain boundaries in  $\text{MAPbI}_3$  thin film. At low relative humidity, the  $\text{TPA}^+$  cations inhibit the water molecules from entering the perovskite lattice, enabling the one-year-long stability of this

material. On the other hand, upon exposure to high relative humidity, the  $\text{TPA}^+$  cation partially segregates from the grain boundary, allowing the water molecules to irreversibly transform the  $\text{MAPbI}_3$  material. However, the extent of byproduct formation in the case of passivated  $\text{MAPbI}_3$  is much lower in comparison with control  $\text{MAPbI}_3$  material. These results indicate the direct correlation of grain boundary passivation with sluggish irreversible transformation. Results of this chapter are submitted to, Raval et al., *Chem. Mater.*, in revision. The results presented here are the outcome of collaborations with Dr. Frederic Sauvage at Université de Picardie Jules Verne. I performed the ssNMR spectroscopic characterizations of pristine samples and subjected the materials to moisture to analyze the moisture stability of these materials using ssNMR spectroscopy.

In a conventional perovskite solar cell, the perovskite active layer is sandwiched between the charge-extracting layers. Chapter 4 presents an approach to performing structural-characterization of the hole-transporting material (HTM), which usually lacks long-range order. Specifically, NMR crystallography, a concept of combining experimental solid-state NMR results and computational calculations, has been implemented on spiro-OMeTAD. Tris(pentafluoro phenyl) borane (BCF), a Lewis acid, is utilized to p-dope spiro-OMeTAD. The local structures and interactions between the dopant (BCF) and host organic semiconductor (spiro-OMeTAD) are elucidated using magnetic resonance spectroscopy and crystallography modeling techniques. These techniques reveal the miscibility of the dopant and the host and indicate the formation of different paramagnetic species. NMR crystallography analysis presented here rationalizes the structural changes in the spiro-OMeTAD films before and after doping with BCF molecules. The results of this chapter are presented in *Electrochim. Acta* 2022, 424, 140602. The results presented here are the outcome of collaborations with Prof. Thuc-Quyen Nguyen at the University of California Santa Barbara, U. S. A., Dr. Tomasz Pawlak, Polish Academy of Sciences, and Hervé Vezin and Pascal Roussel at the University of Lille, CNRS, France. I synthesized the material and carried out UV-Vis, FT-IR, and ssNMR spectroscopic characterizations of pristine and doped spiro-OMeTAD samples.



# Chapter 1- Introduction

---

## 1.1. Emerging photovoltaic materials based on metal halide perovskites

### 1.1.1. Potential of solar energy

As the global energy demand is rising,<sup>1</sup> there is a great interest in searching the renewable energy sources to cope with energy needs. In addition, the growing climate change due to the emission of greenhouse gases further necessitates the search for low-carbon emissions and renewable energy sources. Among renewable sources such as wind, geothermal, and biomass, solar energy has garnered much attention in recent years. If adequately harvested, the collectible solar energy that strikes the Earth's surface is more than adequate to meet the global energy demand.<sup>2</sup> In 1954, Bell Labs created the first photovoltaic (PV) cell, which used silicon as a light-absorbing layer and achieved solar-to-electrical power conversion efficiency (PCE) of up to 6%. While this initial design has been improved over several years, today, silicon-based solar cells achieve PCEs of over 26%.<sup>3</sup> However, it is difficult to achieve this using the current silicon-based solar cell technology due to many factors that will influence the production/installation costs and the number of years it can take to pay off your panels by means of energy savings. The most common estimate of the average payback period for solar panels is six to ten years. Meanwhile, the second-generation solar cells, such as cadmium telluride (CdTe), gallium arsenide (GaAs), and copper indium gallium selenide (CIGS) - based solar cells emerged during the 1970s, which showed great promise in being widely adopted by the energy market. However, while they have made great strides in real-world applications, there still remain issues, such as the scarcity and toxicity of the metals used. To sufficiently harvest solar energy, low-cost and efficient photovoltaic materials need to be developed.

Metal halide perovskites (MHPs) have shown great promise as emerging low-cost photovoltaic technologies, with solar cell efficiencies of over 25%. In contrast to the traditional Si solar cells that require high-temperature synthesis, the MHP-based solar cells use solution processing with conventional organic solvents, reducing the production costs associated with the high-quality thin films. In addition, tunable bandgap by compositional and dimensional tailoring are among the attractive features of MHPs for photovoltaic applications.

### 1.1.2. Perovskites

The term perovskite refers to any material exhibiting an  $ABX_3$ -type empirical formula (where A is a monovalent cation, B is a divalent cation, and X is a monovalent anion). 'A' site cation is surrounded by corner-sharing  $BX_6$  octahedra, as shown in Figure 1.1. Perovskites were first discovered in the 1830s when the naturally occurring mineral  $CaTiO_3$  was found. In the 1950s, the crystal structure of  $CaTiO_3$  was elucidated, and the term "perovskite" was then used to refer to any material with the same  $ABX_3$  crystal structure.<sup>4</sup>

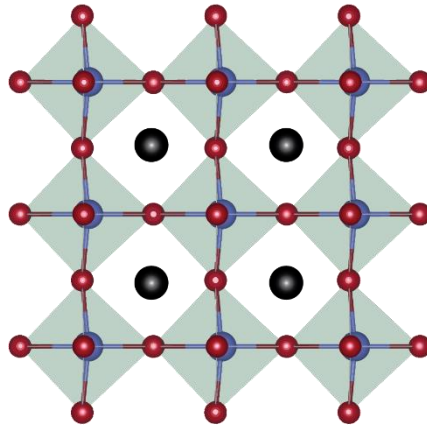


**Figure 1.1.** Perovskite structural scheme. A (black) is a monovalent, and B (blue) is a divalent cation. X, shown in red, is a monovalent anion.

A wider variety of elements can be used in A, B, and X sites to synthesize perovskites. However, the perovskite formation and stability are governed by the Goldschmidt tolerance factor and the octahedral factors, as derived from the oxide perovskite research.<sup>5</sup> The Goldschmidt tolerance factor for a particular set of ions can be calculated using Eq 1.1.

$$t = \frac{(r_A + r_X)}{\sqrt{2}(r_B + r_X)} \quad \text{Eq 1-1}$$

where  $r_i$  refers to the ionic radius of each element. The unitless  $t$  value can be used to describe the tolerance factor of the structure, which is in the range between 0.81 and 1.0 for orthorhombic, tetragonal, and cubic perovskites. Octahedral distortions occur due to the size mismatch of the ionic species, leading to the formation of these distinct stable and metastable perovskite phases and interconversions between them. Significant deviations of the tolerance factor from the abovementioned range lead to the non-perovskite phase formation. In order for the tolerance

factor to fall in this region, only certain combinations of ions can be used together, severely limiting the possible elements that can be used to obtain perovskites.

Additionally, the octahedral factor describes the stability of the  $BX_6$  octahedra in the perovskite and is described by the ratio of ionic radii of the B and X ions, as seen in Eq 1-2. The octahedral factor lies between 0.44 and 0.9 for most stable perovskites. Again, this tolerance factor greatly influences the number of ions that can be used to create a stable perovskite.

$$\mu = \frac{r_B}{r_X} \quad \text{Eq 1-2}$$

The overall number of stable perovskite compositions and structures is significantly reduced with these two parameters taken together. However, new stable compositions can be achieved by fine-tuning these factors. For instance, stable perovskites do not necessarily have the desired optical or electronic properties in order to be employed for light-harvesting or emitting applications. However, one family of perovskites has emerged as the ideal candidate with both useful optical and electronic properties and can be synthesized stably.

### 1.1.3. Lead halide perovskite

Lead halide perovskites are a family of perovskites where lead occupies the B site and a halide, such as iodide, bromide, or chloride, occupies the X site. These perovskites are known to be one of the ideal candidates for photovoltaics. The Pb 6s and X 5p orbitals hybridize to form a pair of bonding and antibonding states in the upper valence band, while the Pb 6p orbital hybridizes with the X 5p orbital to form a bonding state in the upper valence band and an antibonding state in the conduction band minimum, as described by Even *et al.* and shown in Figure 1.2.<sup>6-9</sup> As a result, the original atomic orbitals are close to the band edges rather than inside the bandgap. As an approximation, one can consider that the defect states form close to the original atomic orbitals, and the electronic structure of lead halide perovskite makes it more likely that these defect states are resonant with the bands or shallow within the bandgap. On the other hand, in conventional semiconductors such as silicon, the bonding-antibonding states form across the bandgap as the original atomic orbitals are within the bandgap. The formation of trap states (localized states within the energy gap of the semiconductor) is more likely in such scenarios. The presence of heavy elements in lead halide perovskite (especially in  $APbI_3$ ) facilitates strong spin-orbit coupling, and the high polarizability of  $Pb^{2+}$  ion in combination with

shallowness in the trap energy levels checks the trap-assisted recombination despite high defect densities. Due to these phenomena, lead halide perovskites are often considered "defect tolerant". One important thing to note is that defect tolerance cannot be generalized across the entire lead-halide perovskite family. Also, the hybridized valence and the conduction band arise solely from the X and Pb atoms and have a minor contribution from the A-site cation.

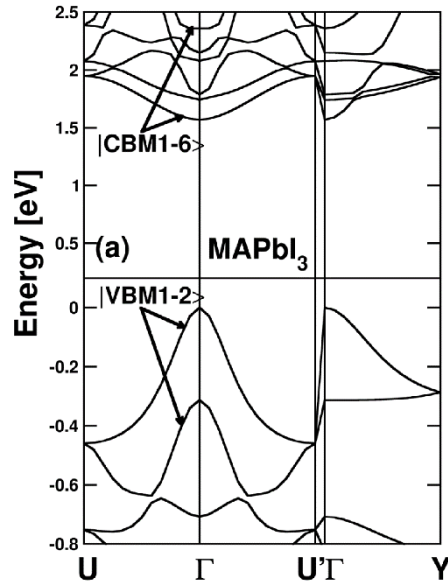


**Figure 1.2.** Electronic band structure diagram of  $\text{MAPbI}_3$  without considering spin-orbit coupling interaction. The origin of the energy scale is taken at the top of the valence band. (Figure adapted from Ref <sup>8</sup>)

With this configuration, many A site cations can be used to achieve allowable Goldschmidt tolerance factors. The A-site cation can be occupied by inorganic species, such as cesium, as well as organic species, such as methylammonium or formamidinium. Regardless of the A site species, lead halide perovskites ( $\text{APbX}_3$ ) have shown the promises of all perovskite species for utilization in photovoltaic devices.

Lead halide perovskites have been known to have optical tunability and photoconductive properties. As explained earlier, the valence band maximum and the conduction band minimum are mainly composed of the Pb and X orbitals; the bandgap tunability mainly arises by halide substitution. The trend of the bandgap is as the following:

$$\text{APbCl}_3 > \text{APbBr}_3 > \text{APbI}_3$$

Precise stoichiometric composition of the distinct halide can lead to narrow linewidth excitonic emission ranging from 390 nm to 790 nm, as shown in Figure 1.4. As a result, lead halide perovskite is often utilized in highly efficient energy-saving LEDs and lasers. Very recently, an impressive external quantum efficiency (EQE) of 28.1% was achieved for perovskite-based LED, where the quasi-2D hybrid organic-inorganic perovskite material is employed.<sup>10</sup>

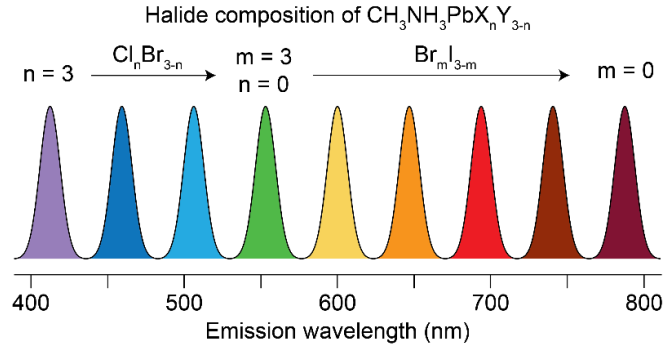


**Figure 1.3.** The emission wavelength of  $\text{CH}_3\text{NH}_3\text{PbX}_n\text{Y}_{3-n}$  can be tuned from 390 to 790 nm wavelength. (Figure adapted from reference <sup>11</sup>)

Moreover, perovskite materials tend to have a higher absorption coefficient in the visible light region than other semiconductor materials like silicon, as shown in Figure 1.5. The optical absorption coefficient determines how deep into the material light of a particular wavelength penetrates before it is absorbed. A higher absorption coefficient in perovskites ensures more-readily absorption of the photons, which facilitates the excitation of the electron into the conduction band.

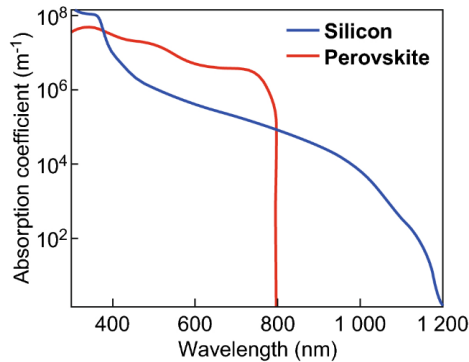


**Figure 1.4.** Optical absorption coefficient of crystalline silicon and  $\text{MAPbI}_3$  perovskite as a function of wavelength of the incident light. (Figure adapted from reference <sup>12</sup>)



These properties suggest that very little (thin) material is needed to harvest an appreciable amount of light suitable for photovoltaic applications.

## 1.2. Perovskite solar cells

In 2009, Miyasaka *et al.* reported the first perovskite solar cell with an efficiency of 3.8%.<sup>13</sup> This device employed a dye-sensitized solar cell architecture but used MAPbBr<sub>3</sub> and MAPbI<sub>3</sub> as sensitizers, whereby MAPbBr<sub>3</sub> and MAPbI<sub>3</sub> devices achieved meager efficiencies of 3.13% and 3.81%, respectively.<sup>13</sup> These devices were photodegraded under ambient conditions. While the meager efficiencies and stabilities were concerning for the material, this finding was still enough to intrigue the interest of researchers throughout the solar energy research community.

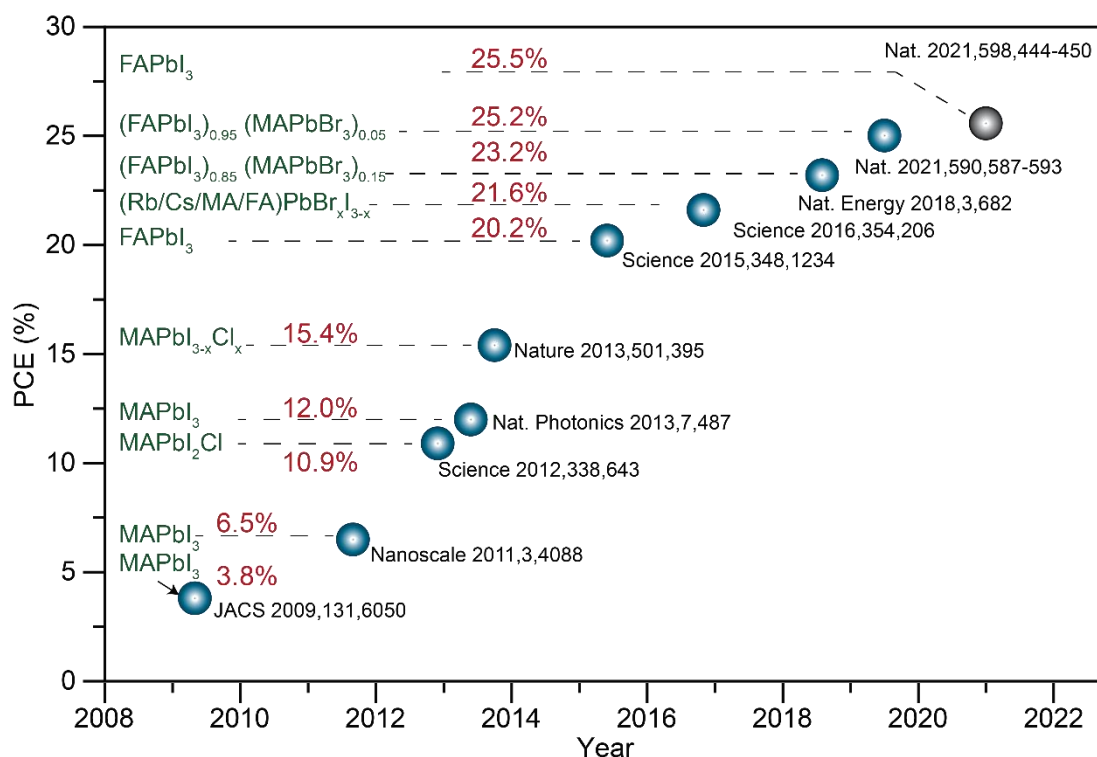


**Figure 1.5.** Power Conversion Efficiency (PCE) evolution of perovskite solar cells (PSCs) along with the composition of perovskite photo-absorbing layer.<sup>13–22</sup>

One reason that perovskite research has sustained such remarkable growth is due to the unique properties lead halide perovskites possess, which differentiates them from other semiconductor light absorbers. Perovskites are reported to have long charge carrier diffusion

lengths ( $\sim 2.2 \mu\text{m}$ ),<sup>23</sup> the ability to be used in thin-film, flexible architectures, wide tunable bandgaps across the entire visible region, and ease of deposition methods. Despite such attractive properties, stability remains a major concern for up-scaling and commercializing these materials.

### **1.3. Instability associated with lead halide perovskites**

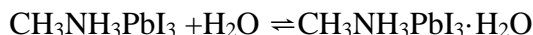
In order for perovskite photovoltaics to gain traction in the commercial market, they must not only have high power conversion efficiencies, but they must also be as stable under operating conditions as other commercialized cells. This means that perovskite solar cells must maintain their output for a period of years in order to compete with commercialized silicon solar cells. Great strides have been made in order to enhance the stability of these materials. The first perovskite solar cell was only stable for a matter of minutes before degrading. More recently, however, perovskite solar cell was reported to maintain adequate efficiency for one year.<sup>24</sup> This has been achieved through careful studies that identified the various types of instability that can occur in a perovskite solar cell. There are several extrinsic parameters that are known to cause degradation, among which moisture, temperature, light, oxygen, and electrical bias are particularly important. Some of these aspects are discussed in this thesis.

#### **1.3.1. Moisture-induced degradation**

Relative humidity (RH in %) in the air is one of the most prevalent factors impacting perovskite materials and, subsequently, PSC performance due to its ability to form solvated phases.<sup>25–27</sup> However, during the formation of the perovskite film, the water molecule can form hydrogen bonds with uncoordinated ions on the surface of the perovskite film,<sup>28</sup> leading to improved film quality and larger grain sizes.<sup>29–37</sup> Furthermore, the water molecules can penetrate into the perovskite crystal and further form an intermediate hydrated phase.<sup>38,39</sup> In comparison, the hydration process is reversible at low relative humidity, and the decomposition of halide perovskite happens upon prolonged exposure to highly humid conditions.<sup>27,40,41</sup> All inorganic phases, such as  $\text{Cs}_4\text{PbX}_6$ , which is non-luminescent when exposed to water, usually induces the formation of  $\text{CsPbX}_3$ .<sup>42</sup> However, prolonged exposure to moisture transforms these phase to  $\text{CsPb}_2\text{X}_5$  and further into  $\text{CsX}$  and  $\text{PbX}$  salt.<sup>43,44</sup>

In the case of organic-inorganic hybrid perovskite, the moisture-induced structural changes are quite different. The photoactive  $\alpha\text{-FAPbI}_3$  undergoes phase transformation (more details in

Chapter 2) to  $\delta$ -FAPbI<sub>3</sub>, even under the protection of nitrogen. These transitions can be accelerated by moisture.<sup>45-47</sup> This affects the photophysical properties significantly as the bandgap of the material increase to about 2.5 eV.<sup>46,48,49</sup> On the other hand, in the case of MAPbI<sub>3</sub>, the moisture-induced degradation pathway involves the formation of an intermediate hydrate phase. Based on a few reports,<sup>27,38,50-52</sup> water molecules can hydrate the perovskite and form a mono/dihydrate phase as:



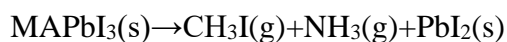
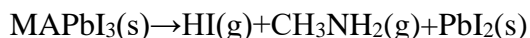
Both of these reactions are reversible. So, if the hydrated perovskites are stored in an inert environment, they can be dehydrated to form a black-colored MAPbI<sub>3</sub> perovskite phase. The hydration of the perovskite causes structural deformation of (PbI<sub>6</sub>)<sup>4-</sup> octahedra which converts the 3D network of the (PbI<sub>6</sub>)<sup>4-</sup> octahedra into a 1D chain of octahedra for the monohydrate. These weaken the chemical bonds between the A-site moiety and the (PbI<sub>6</sub>)<sup>4-</sup>, thus making the perovskite more vulnerable to other extrinsic factors. Once the perovskite material is saturated by the moisture, the hydration will become irreversible, and it irreversibly will decompose to produce CH<sub>3</sub>NH<sub>3</sub>I and PbI<sub>2</sub>. These aspects will be discussed in detail in Chapter 3.

### 1.3.2. Temperature-induced degradation

Solar modules need to be operated in direct sunlight, and the nominal operating solar module temperature can go beyond 50 °C.<sup>53</sup> Depending on the geographical/environmental conditions, the module experiences a wide range of extreme temperatures. Thermal stability is an important aspect of perovskite-based solar cells. MAPbI<sub>3</sub> undergoes a phase transformation from tetragonal phase to cubic phase at about 56 °C,<sup>54-56</sup> which lies within the operational range of the solar cell module. Hence, it is tremendously important for a photoactive perovskite phase to be thermally stable within the range of operational temperature conditions.

Misra *et al.* compared the MAPbX<sub>3</sub> (X= I, Br) based device stability and observed that just after 60 min of concentrated sunlight (100 sun equivalent) exposure and within the temperature range of 44-55 °C, MAPbI<sub>3</sub> based device experienced degradation.<sup>57</sup> On the other hand, the MAPbBr<sub>3</sub>-based device did not degrade in the abovementioned conditions.<sup>57</sup> This was reasoned to be the shorter and stronger Pb-Br bond compared to the Pb-I bond.<sup>58</sup> Thermogravimetric

analysis (TGA) shows that MAPbI<sub>3</sub> undergoes mass loss above 200 °C due to loss of HI and methylamine gas.<sup>59</sup> Further investigations by Nenon *et al.* and Bækbo *et al.* supported the evidence based on the results from complementary structural determining techniques.<sup>60,61</sup> Temperature-induced decomposition of MAPbI<sub>3</sub> can be summarized as follows:



where the first reaction is kinetically favored as the reaction is proceeded by breaking of N-H and Pb-I bonds. On the other hand, the second reaction is thermodynamically favored but is much slower, as it requires the breaking of a less labile C-N bond.<sup>50,62-64</sup>

Comparing the influence of the A-site cation, a few studies reported that the FA-based devices show superior thermal stability compared to the MA-based devices.<sup>65,66</sup> However, by using thermogravimetric differential thermal analysis (TG-DTA) coupled with mass spectrometry (MS), FAPbX<sub>3</sub> is identified to decompose into sym-triazine, HCN, formamidine, and NH<sub>3</sub>.<sup>67</sup>

Replacing the organic cations like MA and FA with inorganic cations such as Cs was therefore implemented to improve the thermal stability of the perovskite. Zhang *et al.* showed that CsPbBr<sub>3</sub> nanocrystals were stable up to 417 °C under vacuum, beyond which the nanocrystals sublimed.<sup>68</sup> In another study, a combination of *in situ* pXRD and *in situ* Raman spectroscopy revealed that the thermal stability of Cs-based lead halide perovskite depends on the choice of the anion.<sup>69</sup> It followed the following order: CsPbI<sub>3</sub> (stable up to 250 °C) < CsPbBr<sub>3</sub> (stable up to 450°C) < CsPbCl<sub>3</sub> (stable above 500 °C).

### 1.3.3. Light-induced degradation

One of the key environmental stressors of importance to PSCs is light. Although there are numerous reports demonstrating the stability of PSCs over hundreds of hours of illumination, there are substantial studies describing photoinduced changes to the perovskite structure and hence the PSC performance.<sup>15,70-80</sup>

The photoinduced changes are mainly caused by light-activated trap states,<sup>81,82</sup> photoinduced ion migration/segregation<sup>82-85</sup>, and photodecomposition.<sup>72,80</sup> In addition,

photodecomposition occurs more rapidly in the air than in a vacuum or in an inert atmosphere.<sup>86,87</sup>

Specifically, MAPbI<sub>3</sub> has been extensively studied for the photoinduced decomposition process. *In situ* X-ray diffraction, X-ray photoelectron spectroscopy (XPS) have been mainly utilized to find that MAPbI<sub>3</sub> decomposes into PbI<sub>2</sub>, which further decomposes into metallic Pb.<sup>85,88–91</sup> The formation of PbI<sub>2</sub> and metallic Pb was also observed while photodegradation of MAPb(I<sub>0.83</sub>Br<sub>0.17</sub>)<sub>3</sub>, FA<sub>0.83</sub>MA<sub>0.17</sub>Pb(I<sub>0.83</sub>Br<sub>0.17</sub>)<sub>3</sub>, and Cs<sub>0.1</sub>(FA<sub>0.83</sub>MA<sub>0.17</sub>)<sub>0.9</sub>Pb(I<sub>0.83</sub>Br<sub>0.17</sub>)<sub>3</sub>.<sup>79</sup> PbO, PbCO<sub>3</sub>, and Pb(OH)<sub>2</sub> have also been observed as photodegraded byproducts of MAPbI<sub>3</sub>.<sup>88,91,92</sup> Methylamine, and HI gas were observed as primary products during the photoinduced decomposition of MAPbI<sub>3</sub>, when analyzed using mass spectrometry, along with traces of hydrogen, ammonia, and iodine gas.<sup>93</sup>

## 1.4. Approaches for stability enhancements

### 1.4.1. Compositional engineering of lead halide perovskites

The chemical composition of perovskite materials is often modified through the partial substitution of A, B, and X ions by organic or inorganic elements. This technique can be used to enhance device efficiency and long-term stability.<sup>94</sup> It has been found that perovskite stability problems can be associated with intrinsic structural properties, which affect the Goldschmidt tolerance factor. As described above, an ideal perovskite material has a tolerance factor that approaches the range of 0.8-1.0, with deviations from this value indicating possible structural instability.<sup>95</sup> The tolerance factor can be modulated by changing or mixing ions of different sizes, providing a promising pathway to stability enhancement.

#### *A-site engineering*

Since MAPbI<sub>3</sub> was the first developed absorber in perovskite PV technology, the primary goal of A-site engineering was to find a suitable cation that enhances performance as well as stability. The more suitable bandgap of FAPbI<sub>3</sub> led to the tailoring of the A-site using a combination of FA and MA cations.<sup>65,96–99</sup> Pellet *et al.* explored the combination of FA (larger size cation) and MA (smaller size cation) to create the perovskite (MA)<sub>x</sub>(FA)<sub>1-x</sub>PbI<sub>3</sub> (x = 0-1) (MAFA). This composition was shown to drive a significant improvement in the optical, structural and electrical properties of the resultant, leading to a PCE value of 14.9%.<sup>97</sup> MAFA

system exhibited mediocre operational stability as it lost over 50% of PCE within 100 h of 1 sun illumination under a nitrogen atmosphere at room temperature.<sup>100</sup>

Stoichiometric addition of cesium cation to the MAFA system was first reported by Saliba *et al.*<sup>100</sup> Cesium cation being smaller in size (ionic radii = 1.81 Å) than MA (2.70 Å) and FA (2.79 Å), serves as phase-stabilizer to the black phase of FA-based perovskites.<sup>97,101,102</sup> A small concentration of Cs (5%) cation was sufficient to inhibit yellow non-perovskite phase formation, along with the increase in grain size. Due to grain size enhancement and phase stabilization, unencapsulated CsMAFA PSC exhibited notable operational stability by retaining 90% of the original PCE after 250 h in a nitrogen atmosphere and at room temperature.<sup>100</sup>

The stoichiometric addition of Cs cation is not limited to the MAFA system, but it is also implemented for FAPbI<sub>3</sub> perovskites<sup>101–104</sup>. In addition, a small concentration of Rb(5%) incorporation in the perovskite framework induced larger grain sizes compared to CsMAFA.<sup>105</sup> RbCsMAFA-based PSCs (unencapsulated) using poly(triaryl amine) (PTAA) as the hole transporting material retained 95% of initial PCE after 500 h of 1-sun illumination at 85 °C under a nitrogen atmosphere.<sup>19</sup> Since the HTM and stability-test conditions are not identical, it is not conclusive that Rb incorporation enhances the stability in the CsMAFA system.

### ***B-site engineering***

The Pb<sup>2+</sup> ions tend to convert into Pb atoms during device fabrication or operational conditions, causing abundant deep defect states and, thus, severe degradation.<sup>106,107</sup> Tin (Sn) is a good alternative to Pb due to its identical electronic configuration. Complete/partial substitution of Pb with Sn can narrow the bandgap of the perovskite (1.3 eV MASnI<sub>3</sub>, 1.41 eV FASnI<sub>3</sub>), which is better for absorption of the solar spectrum.<sup>108–110</sup> Although Sn-based PSCs lose their PCE within a few minutes due to the tendency of oxidation of Sn<sup>2+</sup> to Sn<sup>4+</sup> in the air, Sn-Pb alloy partially inhibits the oxidation of Sn<sup>2+</sup>.<sup>101,107,111,112</sup> For example, a MAPb<sub>0.9</sub>Sn<sub>0.1</sub>I<sub>3</sub> PSC device was produced by partially replacing Pb with Sn, which retained 90% of the original PCE of 18.3% after 500 h under light illumination.<sup>113</sup> Although the operational stability of Pb-Sn-based PSCs is still lower than that of the Pb-based PSCs, mainly due to the tendency of Sn<sup>2+</sup> oxidation, the small bandgap of Pb-Sn alloy is valuable in developing perovskite-perovskite tandem photovoltaic device.

### *X-site engineering*

Introducing Br in iodide-based perovskite could not only tune the bandgap of the perovskite but also enhances the materials' robustness towards moisture. Noh *et al.* reasoned the enhanced moisture-stability of  $\text{MAPbI}_x\text{Br}_{3-x}$  to compact and stable structure.<sup>114</sup> The substitution of a large  $\text{I}^-$  anion with a smaller  $\text{Br}^-$  anion led to the reduction of the lattice-constant, which meant stronger non-covalent interactions between the cation and inorganic framework. However, some studies have reported that the phase segregation in mixed halide systems occurs depending upon the operating conditions<sup>83,115,116</sup> and calls for a more systematic and robust design of the structure and composition of the material.

Besides  $\text{Br}^-$ ,  $\text{Cl}^-$  is also utilized for tuning the photophysical and structural properties. Since the Cl-based perovskites have a large bandgap ( $\sim 3.0$  eV),<sup>117</sup> they are not an ideal material for light-harvesting as a single junction solar cell. However, small  $\text{Cl}^-$  containing molecules, such as  $\text{MACl}$ , and  $\text{MDACl}_2$  (methylene diammonium chloride), serve as additives to enhance the grain size and/or stabilize (in terms of structural constraints) the phase.<sup>118–124</sup> In addition, Cl incorporation is responsible for the suppression of vacancy defect by lattice strain (due to size mismatch between A-site cation and lead halide cage, leading to  $\text{BX}_6$  octahedral tilting) relaxation.<sup>125</sup>

#### **1.4.2. Low-dimensional perovskites**

The size constraints imposed by the tolerance factor for the 3D dimensional perovskite can be relaxed by tailoring the dimensionality of the material. A 2D perovskite can be thought of as layers obtained by slicing the 3D perovskite structure.<sup>126–129</sup> As a result, the layered perovskite structure can accommodate larger/complex cations (spacer cation, R). This provides a large scope for material exploration through the choice of spacer cation. However, there are two factors that one needs to account for while designing the cation; (i) molecule must have a one/two-terminal polar functional group such that it can interact with an inorganic framework (generally by means of hydrogen bonding), and (ii) width of the molecule is regulated by space defined by adjacent corner-sharing  $\text{BX}_6$  octahedra.<sup>130–133</sup> These low dimensional perovskite show remarkable moisture resistance due to the hydrophobic nature of R cation.<sup>128,134</sup>

### ***Ruddlesden-Popper (RP) phase perovskites***

The Ruddlesden–Popper (RP) homologous series is a two-dimensional (2D) perovskite with a chemical structure of  $R_2A_{n-1}B_nX_{3n+1}$ , where R is the spacer cation.<sup>135</sup> The  $n$  value defines the number of layers of  $BX_6$  octahedra sandwiched between the spacer cation along the pseudo-perovskite  $\langle 100 \rangle$  direction.<sup>129,136</sup> Linear alkyl monoamine spacers-based 2D perovskites were first reported by Mitzi *et al.*, who synthesized and analyzed a series of butylammonium cation-based 2D (Sn) perovskite with different  $n$ -values.<sup>137</sup> When butylammonium (BA)-based 2D perovskite was first employed as a light-absorber in PSCs, 4.02% PCE was observed.<sup>126</sup> The efficiency of PSCs has then been greatly improved as the PCE of BA-based PSCs crossed over 15%.<sup>138</sup> Alkyl monoamine with different chain lengths has been explored by the scientific community.<sup>131–133,139</sup> The variation in chain length induces distortion of the  $PbI_6$  octahedra (generally explained in terms of Pb-I-Pb bond angle) due to their interactions with the inorganic layer, further influencing the band gap of the material.<sup>129,140</sup> Aromatic spacer cation, such as phenylethylammonium (PEA) cation, is one of the widely used bulky R cations in 2D perovskites.<sup>141,142</sup> Exploiting the high performance of 3D perovskites and superior stability of 2D perovskites, quasi-2D perovskite can be designed.<sup>143,144</sup>  $PEA^+$  and  $MA^+$  cations are one such pair of cations to form a quasi-2D perovskite structure ( $PEA_2MA_{n-1}Pb_nI_{3n+1}$ ). The thickness of the inorganic sheet can be increased by the increasing  $MA^+$  stoichiometric ratio, which eventually decreases the bandgap and exciton-binding energy.<sup>141,142</sup> The original power conversion efficiency of 15.3% was reduced to 11.3% when the device was operated for 60 days at a 55% RH atmosphere. Butylammonium/methylammonium-based quasi-2D ( $n=3$ ) perovskite  $(BA)_2(MA)_2Pb_3I_{10}$  perovskite are reported to have 12% PCE, however, their performances drop by 30% after running for 2,250h in ambient conditions.<sup>145</sup> Grancini *et al.* reported one-year stable perovskite devices by utilizing aminovaleric acid iodide ( $(HOOC(CH_2)_4NH_3)_2PbI_4$ ) based 2D and  $MAPbI_3$ -based 3D perovskite. This 2D/3D multidimensional perovskite yielded 14.6% PCE and showed extraordinary long-term stability of  $>10000$  h ( $> 1$  year).<sup>24</sup>

### ***Dion-Jacobson (DJ) phase perovskites***

The major difference between the RP phase and DJ phase is that in an RP phase, the interdigitating monovalent cation is employed as a spacer, which enforces the inorganic layer to be staggered by half a unit cell. On the other hand, in a DJ phase, compact divalent cations are employed to form an eclipsed stacking of the inorganic layer (inorganic layer exactly on top of



each other).<sup>130</sup> Kanatzidis and co-workers reported the first examples of hybrid DJ lead iodide perovskites ( $n = 1 - 4$ ) with aminomethyl piperidinium (AMP) derivatives as spacer cation along with methylammonium cation (for  $n = 2 - 4$ ).<sup>140</sup> Propyl- and butyl-diammonium spacer cation along with methylammonium cation is reported to have 14.16% and 16.38% PCE.<sup>146</sup> Ahmad *et al.* reported that the van der Waals gaps (present in RP phase) can be eliminated by incorporating diammonium cations into 3D perovskites, such as MAPbI<sub>3</sub>.<sup>147</sup> The unencapsulated devices from propyl diammonium/methyl ammonium-based DJ phase retained over 95% PCE upon exposure to ambient humidity (40-70% RH) for 4000 h.<sup>147</sup> This electrically insulating aliphatic diammonium could hamper effective charge transport due to its low dielectric constant.<sup>148</sup> On the other hand, delocalized  $\pi$ - electrons enable better conductivity and a larger dielectric constant in the case of the aromatic spacer. Extensive  $\pi$ -electron delocalization along the conjugated backbone could augment the charge transport and reduce the dielectric mismatch between the inorganic layer and the organic spacer layer.<sup>148-150</sup> In this regard, Xu *et al.* developed a fused thiophene-based organic spacer, which demonstrated 18.82% PCE for  $n = 4$  2D DJ perovskite phase.<sup>151</sup> More interestingly, the unencapsulated device retained 99% of initial PCE under the nitrogen atmosphere for 4400 h (> 6 months).<sup>151</sup>

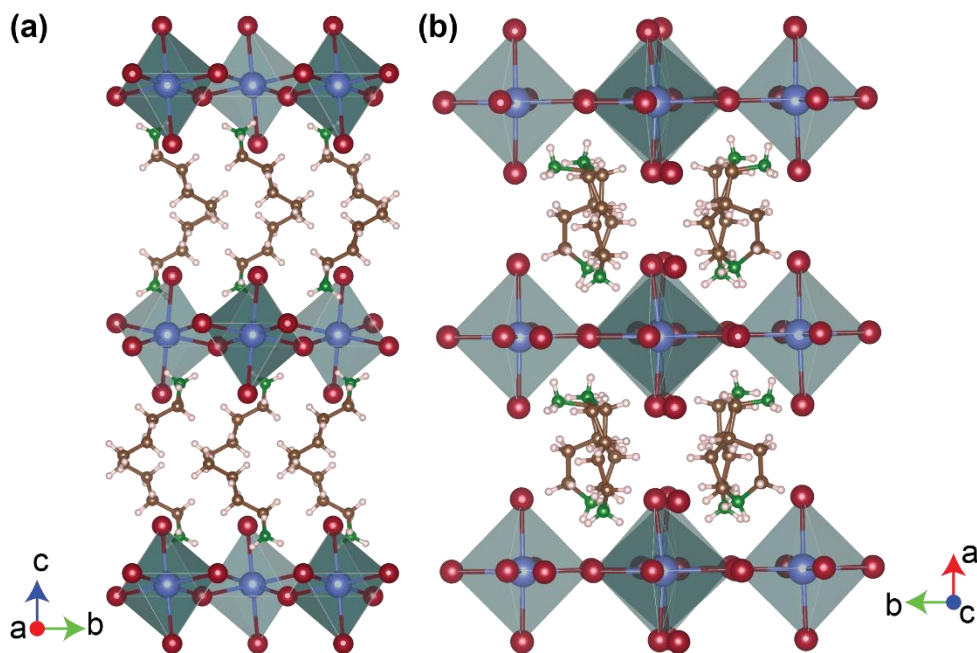


**Figure 1.6.** Crystal structure of (a) BA<sub>2</sub>PbI<sub>4</sub> (RP-phase) and (b) (4AMP)PbI<sub>4</sub> (DJ-phase)

### *B-site deficient perovskites*

Perovskite structure with sub-stoichiometric B-site (lead/tin deficient) can be synthesized by incorporating the organic cations that are much larger in size, deviating significantly from the Goldschmidt tolerance factor rules. These larger "A-site" cations are accommodated in the cuboctahedral cage by replacing the regular A-site cation such as  $\text{MA}^+$ , and  $\text{FA}^+$ , along with partial removal of B and X atoms from the  $\text{ABX}_3$  crystal structure of perovskite.<sup>152,153</sup> Hydroxyethylammonium (HEA), ethylenediammonium (en), and 1,2,4-triazolium (TzH) are some of the "larger A-site" cations utilized to host in the perovskite lattice by randomly generating B and X-site vacancy, yet conserving its isotropic 3D structure.<sup>152–160</sup> Stoichiometric addition of en to FAI and  $\text{SnI}_2$  forms "hollow" (en)  $\text{FASnI}_3$  with significantly improved stability. The PSC devices fabricated using this material retained 96% of their initial PCE after aging over 1000 h with encapsulation.<sup>153</sup>

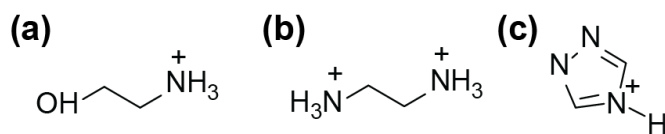


**Figure 1.7.** "Larger A-site" cations used to form deficient/ hollow perovskite

#### **1.4.3. Defect passivation**

Defect passivation, as the name suggests, involves passivating the defects with additives. The additives often introduce a chemical interaction. For instance, manipulating the redox reactions to eliminate  $\text{I}^0/\text{Pb}^0$  defects by redox pairs. There are a variety of passivators utilized. This section mainly focuses on some of the Lewis acid/base-based defect passivating agents.

##### *Passivation by Lewis acids.*

Introducing a Lewis acid that has the capability of accepting a pair of electrons is generally utilized to passivate the electron-rich defects. The undercoordinated  $\text{I}^-$  and antisite  $\text{PbI}_3^-$  may generally contribute to deep traps at the surface and grain boundaries of the perovskite thin films, causing non-radiative recombination. The Lewis acid passivator forms a Lewis adduct, eliminating the corresponding trap and reducing the undesired recombination, and enhancing the solar cell performance.

PbI<sub>2</sub> is a typical Lewis acid-based passivator, forming the PbI<sub>2</sub>.DMSO or MAI.PbI<sub>2</sub>.DMSO complexes when reacting with the solvent (DMSO) in MAPbI<sub>3</sub> precursor solution. These complexes retard crystallization, which subsequently leads to the formation of a highly uniform perovskite film.<sup>161–163</sup> Moreover, a small amount of PbI<sub>2</sub> could improve the electronic property of the electron transport layer (ETL)/perovskite interface as self-induced passivation boosts the PSC device performance.<sup>164–166</sup>

Alkali metal ion incorporation has also garnered much attention for defect passivation in high-performing PSCs. Li<sup>+</sup>, Na<sup>+</sup>, and K<sup>+</sup> have been utilized to effectively passivate the trap states and defects at the grain boundaries, along with improved film morphology.<sup>167–172</sup> Doping perovskite layer or at the interface between ETL and perovskite, Na<sup>+</sup> cation has been utilized to obtain prolonged stability.<sup>172–174</sup>

Fluorine-containing aromatic molecules are also used as Lewis acid passivator. Iodopentafluorobenzene (IPFB) consists of strong electronegative fluorine atoms that can inductively withdraw electron density out of the aromatic ring, leaving a local positive charge.<sup>175–177</sup> Defect passivation using such agents is mediated by non-covalent interactions.<sup>178</sup> Tris(pentafluorophenyl) phosphine (TPFP) with a strong positive charge centered at the phosphorus atom has been used for surface halide defect passivation to achieve a maximum PCE of about 22%.<sup>176</sup>

Fullerene (C<sub>60</sub>) and its derivative, such as [6,6]-phenyl-C<sub>61</sub>-butyric acid methyl ester (PCBM), can be employed as Lewis acid for its unique ability to accept electrons that is not due to chemical reactivity but is attributed to the strain resulting from its spherical shape.<sup>143,179–182</sup> The perovskite-PCBM hybrid film has been reported to have suppressed hysteresis and enhanced photovoltage for planar PSCs.<sup>183–185</sup>

### ***Passivation by Lewis bases***

Organic molecules containing electron lone pair donors such as nitrogen,<sup>186–188</sup> sulphur,<sup>186,189</sup> or oxygen<sup>190–192</sup> have been shown to effectively passivate the defect induced due to cation and undercoordinated cation sites in perovskites.<sup>193</sup> Nitrogen-based Lewis-base generally bears –NH<sub>2</sub> tails or –CN chain molecules such that lone pair of electrons on the N atom can passivate the undercoordinated Pb<sup>2+</sup> ion defects in perovskites.<sup>194–196</sup> The hydrophobic carbon chains consisting of –NH<sub>2</sub> tails can resist moisture-induced degradations, hence maintaining

operational stability for more extended periods.<sup>195</sup> Pyridine and its derivatives, such as bipyridine (BPy), Poly-vinylpyridine (PVP), and terpyridine (Tpy), have been applied to passivate the cation defects hampering the trap-assisted recombination and efficient electron-hole separation.<sup>196–199</sup> In chapter 3, the influence of quaternary ammonium salt on impeding moisture-induced degradation of perovskite material has been widely discussed.

Oxygen-containing Lewis-base has been employed to passivate the Pb antisite, mediated through the adduct formation with the carbonyl functional group.<sup>200</sup> Intermolecular interactions due to the conjugated structure of small molecules such as theophylline, caffeine, and theobromine have been reported to fabricate high-performing PSC devices (PCE > 20%).<sup>191</sup> Snaith *et al.* reported that thiophene (S-donor) passivation effectively suppresses non-radiative carrier recombination.<sup>186</sup> Thiourea, as a Lewis base defect passivating agent, has been utilized to have large perovskite grain size and performance of the PSC devices.<sup>201,202</sup>

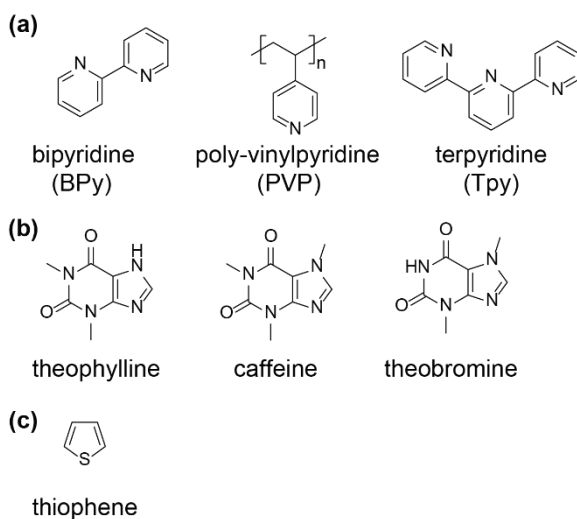


**Figure 1.8.** Chemical structures of (a) nitrogen-based, (b) oxygen-based, and (c) sulphur-based defect passivating agents (Lewis base).

### 1.5. Characterization of metal halide perovskites

Highly crystalline 3D perovskite materials can be investigated using a variety of techniques. Structure-determining techniques such as X-ray, electron, or neutron scattering techniques have been widely used to elucidate the atomic structure of such crystalline materials with high precision. However, these techniques require long-range order (over 0.1  $\mu\text{m}$ ). Although long-range techniques can study the change in phase and crystal lattice parameters

upon composition engineering, information about small organic cations utilized as A-site cations, additives, or spacer cations is difficult to obtain. In this regard, solid-state NMR (ssNMR) spectroscopy can probe short-range interactions and structures at the sub-nanometer length scale. ssNMR spectroscopy provides structural insights such as the doping, nanoscale mixing of the passivator with perovskite, phase segregation, decomposition/transformation pathways, and cation dynamics.<sup>38,203–214</sup> ssNMR can access the timescales of the picosecond to seconds which covers a broad range of physical processes from cation tumbling to phase transformations.<sup>203</sup> NMR active nuclei that are relevant to PSCs are:  $^1\text{H}$ ,  $^7\text{Li}$ ,  $^{11}\text{B}$ ,  $^{13}\text{C}$ ,  $^{14}\text{N}$ ,  $^{15}\text{N}$ ,  $^{19}\text{F}$ ,  $^{33}\text{S}$ ,  $^{35}\text{Cl}$ ,  $^{37}\text{Cl}$ ,  $^{39}\text{K}$ ,  $^{41}\text{K}$ ,  $^{49}\text{Ti}$ ,  $^{55}\text{Mn}$ ,  $^{63}\text{Cu}$ ,  $^{65}\text{Cu}$ ,  $^{67}\text{Zn}$ ,  $^{73}\text{Ge}$ ,  $^{79}\text{Br}$ ,  $^{81}\text{Br}$ ,  $^{85}\text{Rb}$ ,  $^{87}\text{Rb}$ ,  $^{107}\text{Ag}$ ,  $^{109}\text{Ag}$ ,  $^{113}\text{Cd}$ ,  $^{119}\text{Sn}$ ,  $^{121}\text{Sb}$ ,  $^{123}\text{Sb}$ ,  $^{123}\text{Te}$ ,  $^{125}\text{Te}$ ,  $^{127}\text{I}$ ,  $^{133}\text{Cs}$ ,  $^{207}\text{Pb}$ , and  $^{209}\text{Bi}$ . In the following section, some basic concepts and techniques relevant to perovskite characterization using ssNMR spectroscopy are highlighted.

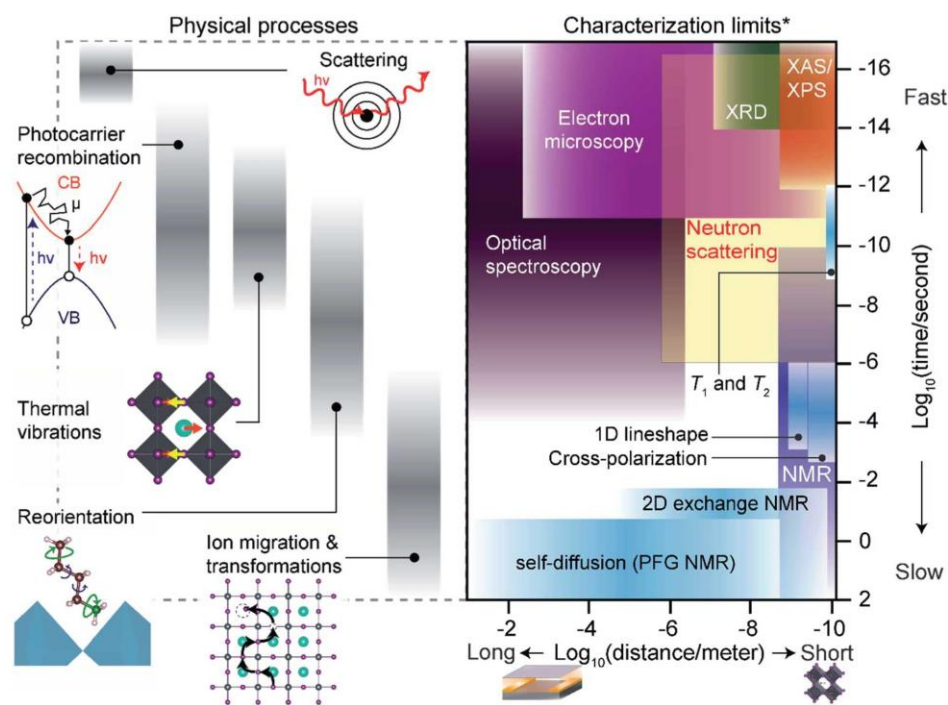


**Figure 1.9.** Comparison of length and timescales: the range of timescales of physical processes in MHPs is presented alongside the fundamental time and length scales that several characterization techniques can probe in MHPs. Figure reproduced from reference <sup>203</sup>.

## 1.6. Solid-state NMR spectroscopy

### 1.6.1. Interactions in NMR spectroscopy

Atomic nuclei with an odd number of protons and/or neutrons often possess nuclear spin quantum number,  $I$ . NMR spectroscopy is a powerful technique that can probe the chemical environment of specific nuclei that have spin greater than or equal to half. Most of the elements in the periodic table have at least one NMR active isotope. A nucleus with nonzero nuclear spin ( $I$ ) is associated with nuclear spin magnetic moment ( $\mu$ ), which can be written as  $\mu = \gamma \times I$ , where  $\gamma$  is a gyromagnetic ratio, an intrinsic property. In the presence of a constant external magnetic field ( $B_0$ ), the nuclear spin ensemble begins to precess about the applied field. There are numerous interactions/perturbations, a nuclear spin experience, which can be written in terms of external interactions (i.e., large static magnetic field) and internal interactions (i.e., interactions among spins).<sup>215</sup> The cumulative effect of these perturbations can be described in terms of total Hamiltonian as,

$$\hat{H}_{\text{total}} = \hat{H}_z + \hat{H}_{CS} + \hat{H}_{DD} + \hat{H}_J + \hat{H}_Q \quad \text{Eq 1-3}$$

where  $\hat{H}_z$ ,  $\hat{H}_{CS}$ ,  $\hat{H}_{DD}$ ,  $\hat{H}_J$  and  $\hat{H}_Q$  describe the Zeeman, chemical shielding, dipolar coupling, scalar ( $J$ ) spin-spin coupling, and quadrupolar coupling, respectively. The quadrupolar coupling is nonzero only for a spin  $I \geq 1$ . Figure 1.11 compares the typical magnitudes of all the nuclear spin interactions in solids.

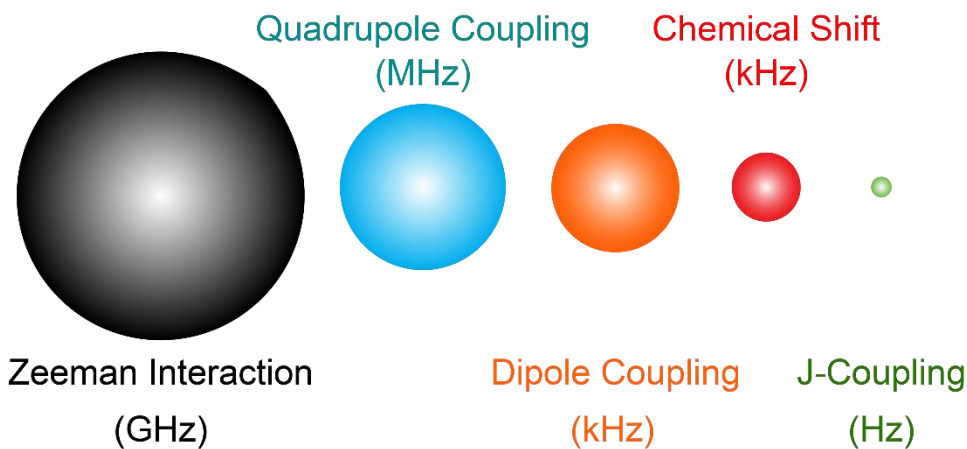


**Figure 1.10.** Schematic representation of the magnitude of the spin interactions in solid-state NMR spectroscopy for a quadrupolar nucleus with  $I \geq 1$ .

### ***Zeeman Interaction***

For a nucleus with a spin  $I$ , there are  $2I+1$  possible energy levels. Each energy level is labeled in terms of magnetic nuclear spin quantum number,  $m_I$ , where  $m_I = +I, +I - 1, +I - 2, \dots, -I$ . Upon the application of an external magnetic field, the spin-states,  $m_I$  and  $-m_I$ , become non-degenerate as different nuclear spin-state precess about the applied magnetic field. The frequency of the precession (Larmor frequency,  $\omega_0$ ) for a given nucleus is given by the negative product of gyromagnetic ratio ( $\gamma$ ) and applied external magnetic field strength ( $B_0$ ),  $\omega_0 = -\gamma \times B_0$ . The splitting between the different nuclear spin levels is called Zeeman splitting. Therefore, the energy difference between subsequent spin states is given by:

$$\Delta E = h\nu_0 = \hbar\omega_0 = \hbar\gamma B_0 \quad \text{Eq 1-4}$$

where  $\hbar = h/(2\pi) = 1.054 \times 10^{-34}$  J.s is the reduced Planck's constant. Figure 1.12 shows the Zeeman interaction for a spin-1/2 and spin-3/2 nucleus.

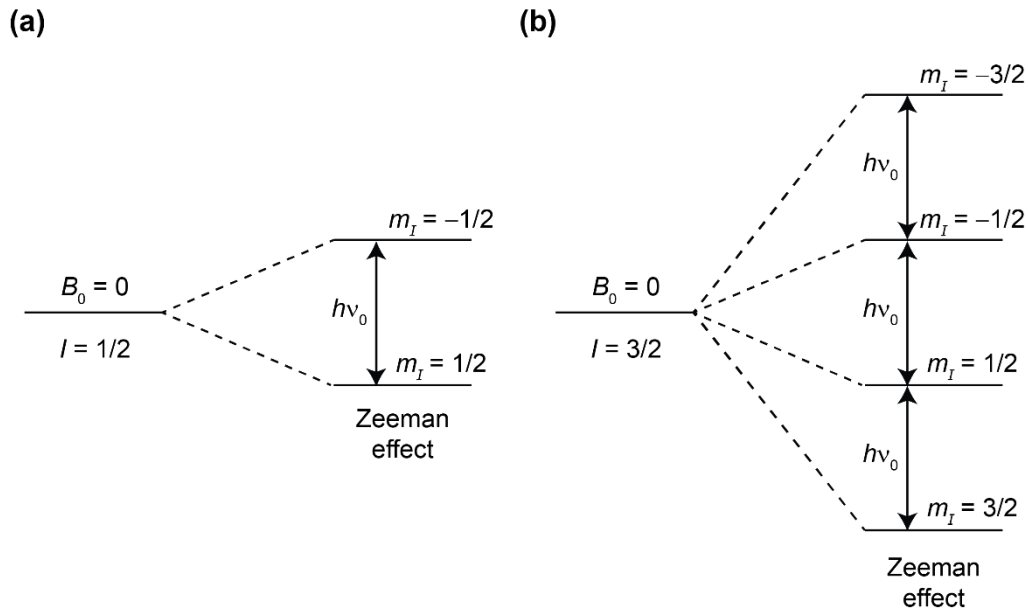


**Figure 1.11.** Schematic diagram of the energy levels of (a) spin  $I = 1/2$  and (b) spin  $I = 3/2$  nucleus in an external magnetic field  $B_0$  due to Zeeman interaction in the absence of quadrupolar coupling.

As the energy difference between the nuclear spin states increases, the population difference between energy levels also increases. The Boltzmann distribution determines the ratio of population difference between energy states by:

$$\frac{N_2}{N_1} = e^{-\left(\frac{E_2 - E_1}{k_B T}\right)} \quad \text{Eq 1-5}$$

where  $N_i$  and  $E_i$  are the population and energy of the  $i^{\text{th}}$  spin-state,  $k_B = 1.38 \times 10^{-23} \text{ J.K}^{-1}$  is the Boltzmann constant, and  $T$  is the temperature in K. Hence, temperature and magnetic field strength influence the population distribution significantly. The magnitude of the population difference dictates the detection sensitivity of an NMR experiment.

### ***Chemical shielding interaction***

The electrons near the nucleus interact with the external magnetic field to produce a secondary field.<sup>216</sup> This secondary field influences the total magnetic field experienced by the nucleus and hence has the potential to change the resonating frequency of the nucleus. This interaction of the secondary field generated by the electrons is called the chemical shielding interaction. The frequency shift caused by this interaction is called the chemical shift. The chemical shielding Hamiltonian acting on a spin,  $I$ , is magnetic field-dependent and is given by:

$$\hat{H}_{CS} = \gamma I \cdot \delta \cdot B_0 \quad \text{Eq 1-6}$$

where  $\delta$  is a second-rank tensor, called chemical shielding tensor. This chemical shielding tensor can be diagonalized in a different axis frame  $\{X, Y, Z\}$ , referred to as the principal axis system (PAS).

$$\delta = \begin{pmatrix} \delta_{xx} & \delta_{xy} & \delta_{xz} \\ \delta_{yx} & \delta_{yy} & \delta_{yz} \\ \delta_{zx} & \delta_{zy} & \delta_{zz} \end{pmatrix} \xrightarrow{\text{diagonalized}} \delta^{\text{PAS}} = \begin{pmatrix} \delta_{xx}^{\text{PAS}} & 0 & 0 \\ 0 & \delta_{yy}^{\text{PAS}} & 0 \\ 0 & 0 & \delta_{zz}^{\text{PAS}} \end{pmatrix}$$

The distribution of the electrons in the molecule determines the orientation of the principal axis system. The isotropic chemical shift  $\delta_{\text{iso}}$  is defined as:

$$\delta_{\text{iso}} = \frac{1}{3} (\delta_{xx}^{\text{PAS}} + \delta_{yy}^{\text{PAS}} + \delta_{zz}^{\text{PAS}}) \quad \text{Eq 1-7}$$

and by the Haerberlen convention

$$|\delta_{zz}^{\text{PAS}} - \delta_{\text{iso}}| \geq |\delta_{xx}^{\text{PAS}} - \delta_{\text{iso}}| \geq |\delta_{yy}^{\text{PAS}} - \delta_{\text{iso}}|$$

The chemical shift anisotropy,  $\delta_{\text{aniso}}$ , is defined as:

$$\delta_{\text{aniso}} = \delta_{zz}^{\text{PAS}} - \delta_{\text{iso}} \quad \text{Eq 1-8}$$



whereas the asymmetry parameters of the chemical shift tensor,  $\eta_{CS}$ , is defined as:

$$\eta_{CS} = \frac{\delta_{YY}^{PAS} - \delta_{XX}^{PAS}}{\delta_{aniso}} \quad \text{Eq 1-9}$$

In solution, molecules are rapidly re-orienting, which averages out the anisotropic effects of the CS tensor, leading to the observation of sharp peaks. However, in the microcrystalline powder (solid-state), the molecules are oriented randomly in numerous possible orientations with respect to the magnetic field. This generates a "powder pattern" as each crystallite gives rise to a distinct frequency.

### ***Dipole-dipole interactions***

The direct dipolar interaction is the interaction between the nuclear spin through space. The Hamiltonian of dipolar coupling between spin J and K has the form:

$$\hat{H}_{JK}^D = b_{JK} (3(\hat{\mathbf{I}}_J \cdot \mathbf{e}_{JK})(\hat{\mathbf{I}}_K \cdot \mathbf{e}_{JK}) - \hat{\mathbf{I}}_J \cdot \hat{\mathbf{I}}_K) \quad \text{Eq 1-10}$$

where  $\mathbf{e}_{JK}$  is a unit vector parallel to the line joining the nuclei J and K, and the dipolar coupling constant  $b_{JK}$  in  $\text{rad}\cdot\text{s}^{-1}$  is given by:

$$b_{JK} = \frac{\mu_0}{4\pi} \frac{h}{2\pi} \frac{\gamma_J \gamma_K}{r_{JK}^3} \quad \text{Eq 1-11}$$

where  $\mu_0$  is the permeability constant,  $\gamma_J$ ,  $\gamma_K$  are the gyromagnetic ratios of nuclei J and K, and  $r_{JK}$  is the distance between nuclei J and K. Expanding the dipolar Hamiltonian in spherical polar coordinates and expanding the scalar products, one obtains:

$$\hat{H}_{JK}^D = R_{DD} [A + B + C + D + E + F] \quad \text{Eq 1-12}$$

from which terms  $A$  and  $B$  have  $(3\cos^2\beta_{PL} - 1)$  dependence, where  $\beta_{PL}$  is the angle between the internuclear vector and  $B_0$ . The terms  $A$  and  $B$  are secular parts of the dipolar Hamiltonian, whereas the terms  $C$  to  $F$  are the non-secular part, meaning they do not commute with the Zeeman Hamiltonian, and hence, their contribution to the energy level is negligible. In solution-state NMR spectroscopy, the spatial dependence of the dipolar Hamiltonian  $(3\cos^2\beta_{PL} - 1)$  is canceled due to rapid molecular motions, which averages out this term to zero. On the other hand, in solid-state, molecular motions are rather constrained, and therefore the dipolar

interactions are not usually averaged to zero. Strong dipolar couplings give rise to line broadening, which can severely limit the spectral resolution. Later in this chapter, we will see how one can improve the resolution in solid-state NMR spectroscopy using a technique called magic angle spinning (MAS).

### ***J-coupling***

Indirect spin-spin interaction (or *J*-coupling) is the interaction mediated by the electrons in the molecular orbitals that are involved in the chemical bonding.<sup>217</sup> For two directly bonded spins, *I* and *S*, the splitting in the peaks of *I* and *S* NMR spectra are observed as  $2S + 1$  and  $2I + 1$ , respectively. Thus, *J*-coupling provides information about the connectivity between different nuclei, and its magnitude is field-independent. Although being a very sensitive probe to molecular structure changes, since the magnitude of interaction is very small, it is often not considered significant in solid-state NMR spectroscopy. The *J*-coupling is an anisotropic interaction. Nevertheless, when *I* and *S* nuclei are both isotopes of the first rows of the periodic table, the *J* anisotropy is usually much smaller than the dipolar coupling and can usually be neglected.

### ***Quadrupolar interaction***

More than 74% of NMR active nuclei have a spin  $I \geq 1$  and are termed quadrupolar nuclei.<sup>218,219</sup> The quadrupolar interaction is the interaction between the electric nuclear quadrupole moment (*Q*) and the local electric field gradient (EFG) at the nucleus. Unlike spin-1/2 nuclei, where the charge distribution is symmetric, the quadrupolar nucleus ( $I \geq 1$ ) exhibits asymmetric charge distribution in the nucleus. The strength of the interaction depends upon the magnitude of the nuclear quadrupole moment and the EFG. The interaction between the EFG and quadrupolar nucleus gives rise to a quadrupolar coupling constant,  $C_Q$ ; this term and the nuclear quadrupolar frequency,  $\nu_Q$ , are given by:

$$C_Q = \frac{e^2 q Q}{h} \quad \text{Eq 1-12}$$

$$\nu_Q = \frac{3C_Q}{2I(2I - 1)} \quad \text{Eq 1-13}$$

where  $e = 1.602 \times 10^{-19}$  C is the elementary charge,  $eq = V_{ZZ}$  is the largest of the three components  $\{V_{XX}, V_{YY}, V_{ZZ}\}$  of the EFG in PAS since, by convention

$$|V_{ZZ}| \geq |V_{YY}| \geq |V_{XX}|$$

$h = 6.626 \times 10^{-34}$  J.s is Planck's constant, and  $I$  is the nuclear spin quantum number. The traceless EFG tensor can be described by  $V_{ZZ}$ , and the asymmetry parameter of the EFG tensor,

$$\eta_Q = \frac{V_{XX} - V_{YY}}{V_{ZZ}} \quad \text{Eq 1-14}$$

When  $C_Q = 0$ , it means that the environment of the nucleus is in an environment with spherical symmetry (for instance, tetrahedral, octahedral, and cubic). The asymmetry parameter,  $\eta_Q$  (ranges from  $0 \leq \eta_Q \leq 1$ ), describes the axial symmetry of the EFG tensor.  $\eta_Q = 0$  means that the EFG tensor is axially symmetric.

It should be noted that quadrupolar interactions, like chemical shielding, are field-dependent. Broadening due to the chemical shift anisotropy generally scales proportionally with the magnetic field, whereas the quadrupolar interaction is inversely proportional to the magnetic field strength.

### 1.6.2. Resolution and sensitivity enhancement in solid-state NMR

In solutions, rapid molecular tumbling leads to averaging of chemical shielding anisotropy, dipolar and first-order quadrupolar interactions, leading to narrow resonances. On the other hand, in solids, molecules lack isotropic reorientation. The solid-state NMR spectrum has broader resonances due to chemical shielding anisotropy, dipolar, and first-order quadrupolar interactions. There are several ways to increase the resolution in solid-state NMR spectra. These techniques are particularly beneficial when the difference between the resonating frequency of the two chemically inequivalent nuclei is not significant.

#### *Magic-Angle Spinning (MAS)*

In order to narrow these broad resonances, Magic-Angle Spinning (MAS) is one of the techniques used to narrow the broad resonances caused due to abovementioned reasons. As mentioned earlier, a number of NMR interactions have essentially the same spatial orientations dependence of the factor  $(3\cos^2\beta_{RL} - 1)$ , where  $\beta_{RL}$  is the angle between the rotor axis and the magnetic field,  $B_0$ . When this spatial orientation dependence factor of  $(3\cos^2\beta_{RL} - 1)$  is equated to zero, the spatial dependences are averaged out to zero, resulting in a significant narrowing. This factor is equal to zero when the angle mentioned above is equal to  $54.736^\circ$ . Therefore, MAS

involves spinning the sample, with a frequency of the order of several kHz, along the rotation axis aligned at an angle of  $54.736^\circ$  with respect to the external magnetic field, as shown in Figure 1.13. The spinning frequency must be greater than the magnitude of anisotropic interactions to average the anisotropic interactions completely. Upon spinning (at a frequency less than the magnitude of anisotropic interactions), sample rotation modulates these interactions, creating rotational spin echoes and giving rise to spinning sidebands in the frequency domain spectrum. Spectral acquisition at variable spinning speeds can easily distinguish between the spinning sidebands and the signals.

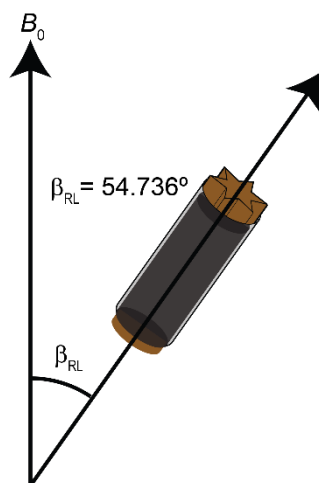


**Figure 1.12.** Magic angle spinning. The sample is spun in a cylindrical rotor about a spinning axis ( $\beta_{RL} = 54.736^\circ$ ) with respect to the applied magnetic field  $B_0$ .

Although MAS enables averaging out (partly or wholly) CSA, dipolar interactions, and first-order quadrupolar interactions, second-order quadrupolar interactions involve a different angular dependence term along with  $(3\cos^2\beta_{RL} - 1)$ . Therefore, spinning the sample at a single angle cannot completely average the 2<sup>nd</sup>-order quadrupolar interactions.

### ***Decoupling by radio frequency pulses***

Radiofrequency (RF) decoupling aims at the removal of unwanted interactions by applying RF irradiation. One can utilize multi-pulse decoupling or continuous irradiation decoupling. RF decoupling can be further classified into the hetero- and homonuclear dipolar coupling. As the name suggests, homonuclear decoupling occurs when the nuclei observed and irradiated with rf are the same. On the other hand, during heteronuclear decoupling, nuclei observed and rf irradiated are different. Figure 1.14 sketches the  $^1\text{H}$  decoupling during the  $^{13}\text{C}$  detection in a

cross-polarization experiment, discussed later. There are various decoupling techniques have been proposed, such as TPPM, SPINAL-64, XiX, etc.<sup>220</sup>

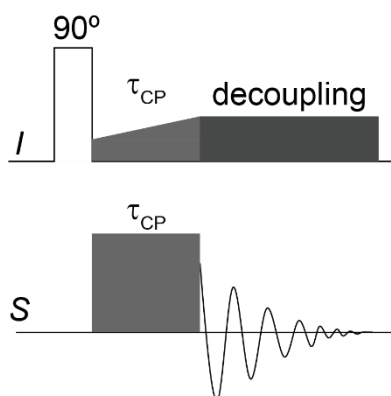


**Figure 1.13.** Continuous-wave decoupling on I nuclei during S nuclei detection

Besides increasing the resolution, one can obtain a better NMR spectrum by increasing its detection sensitivity. One of the ways through which sensitivity enhancement can be achieved is by increasing the magnetic field strength.

### ***High magnetic field***

For spin-1/2 isotopes for which their linewidth is governed by relaxation and hence, is barely independent of  $B_0$ , the resolution only depends on the difference in resonance frequencies due to distinct isotropic chemical shifts and hence, is proportional to  $B_0$ . The equilibrium magnetization is proportional to  $B_0$ , the induced electromotive force is proportional to the Larmor frequency and hence  $B_0$ , whereas the electronic noise is inversely proportional to  $B_0^{1/4}$ , when taking into account the skin effect. As a result, the sensitivity for the detection of spin-1/2 nuclei is proportional to  $B_0^{7/4}$ .<sup>221</sup> Furthermore, for quadrupolar nuclei, the second-order quadrupolar broadening is inversely proportional to  $B_0$ , and hence, the resolution and the sensitivity are proportional to  $B_0$  and  $B_0^{11/4}$ , respectively.<sup>222</sup>

### **1.6.3. 1D NMR experiments**

Several 1D and multidimensional experiments are designed to gain structural information and enhance the nuclei's resolution or sensitivity. Here are a few experiments described that were utilized in this thesis.

### ***Detecting NMR signal***

To observe a signal in an NMR spectrum, the net magnetization (bulk magnetization vector) needs to be arranged parallel with the magnetic field; this is a process known as longitudinal relaxation. In the most straightforward NMR experiment, a "single pulse," a radio frequency (RF) pulse, is applied to tilt this magnetization vector from the z-axis into the transverse plane, as shown in Figure 1.15 below. A  $\pi/2$  pulse rotates the magnetization vector by  $90^\circ$  to the transverse plane.

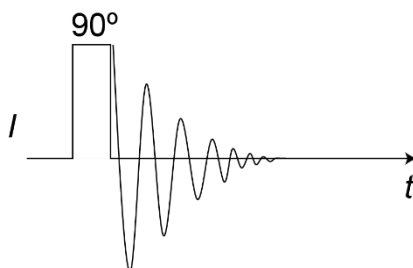


**Figure 1.14.** Pulse sequence of the single-pulse experiment

When in the transverse plane, the precession of the nuclei induces a current at the resonating frequency of the nucleus. As the magnetization vector relaxes, less signal is detected on the x-axis. This current is recorded over time and forms the free induction decay (FID). The FID can be Fourier transformed to a frequency domain NMR spectrum.

### ***Spin-echo experiment***

Like the single pulse experiment, the transverse magnetization is first generated by a  $90^\circ$  pulse in the spin-echo experiment. Followed by this, the spin system is allowed to evolve over time  $\tau$ . Due to local field inhomogeneities, the spin starts dephasing. After the evolution period  $\tau$ , a  $180^\circ$  pulse is applied, inverting the effect and refocusing all the spins after time,  $\tau$ . This pulse sequence (Figure 1.16) can be utilized to measure spin-spin relaxation by varying the  $\tau$  intervals.

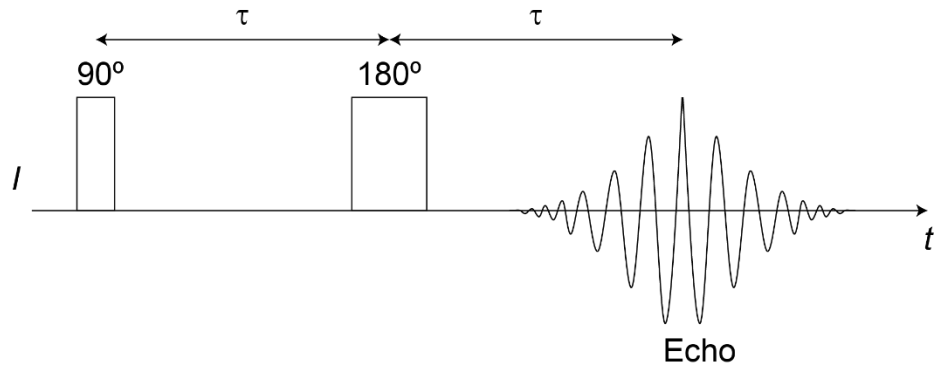


**Figure 1.15.** Pulse sequence of the spin-echo experiment

***Saturation recovery experiment***

The idea of the saturation recovery experiment is to saturate the bulk magnetization to zero and then allow the relaxation for time,  $\tau$ , on the z-axis, followed by the  $90^\circ$  pulse to tilt the magnetization to the transverse plane and to acquire the signal, as shown in Figure 1.17. This method results in a build-up curve of magnetization, eventually recovering all magnetization resulting in a plateau. From this,  $T_1$  (spin-lattice relaxation) can be determined, and it is this experiment that has been used throughout the thesis to estimate the  $T_1$  values.

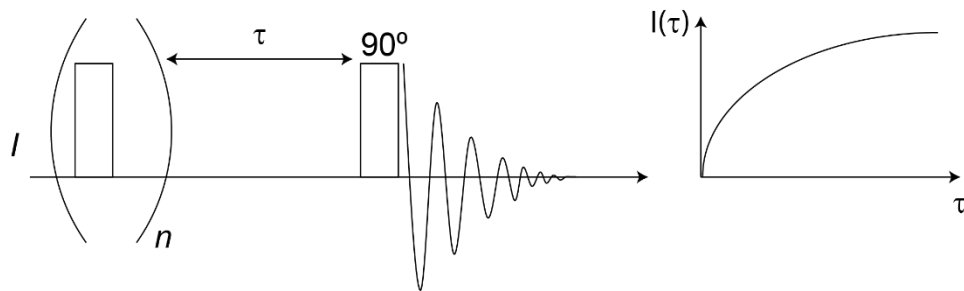


**Figure 1.16.** Saturation recovery pulse sequence along with a schematic of the build-up of signal intensity as the time  $\tau$  is varied.

***Cross-polarization experiment***

The Cross-polarization (CP) experiment is one possibility to overcome the issue of low sensitivity for nuclei with low abundance. In the CP experiment, the reintroduction of dipolar interaction enables the magnetization transfer from abundant nuclei,  $I$ , such as  $^1\text{H}$  and  $^{19}\text{F}$ , to

other nuclei,  $S$ , typically of low natural abundances, such as  $^{13}\text{C}$  and  $^{15}\text{N}$ .<sup>223</sup> For CP to be effective, the Hartman-Hahn match condition must be met when CP is performed with MAS:

$$\nu_1(^1\text{H}) = \nu_1(^{13}\text{C}) + n\nu_{\text{R}}$$

where  $n = 0, \pm 1$  or  $\pm 2$ ,  $\nu_1(^1\text{H})$  and  $\nu_1(^{13}\text{C})$  denote the nutation frequencies around the RF fields on  $^1\text{H}$  and  $^{13}\text{C}$  channels during the CP transfer, and  $\nu_{\text{R}}$  is the MAS frequency. The nuclei with longitudinal relaxation, such as  $^{13}\text{C}$  at natural abundance, for example, require long recycle intervals between each transient, resulting in long experimental times. Through CP, they can receive magnetization from an  $I$  nucleus with faster relaxation, i.e.,  $^1\text{H}$  in the present case. This leads to faster spectral acquisition as the recycle delay depends on the longitudinal relaxation of the excited isotope,  $I$ . The combined effect of magnetization transfer and shorter recycle delay leads to signal enhancement compared to the direct excitation of nuclei  $S$ .

The pulse sequence for the CP experiment is shown in Figure 1.13. It begins with a  $90^\circ$  pulse on the  $I$  nucleus. The resulting magnetization is then transferred to the  $S$  nucleus during the contact time ( $\tau_{\text{CP}}$ ), during which both nuclei are irradiated. The contact time can be varied in order to allow for magnetization transfer to nuclei that are more distant in space. Then the FID of nuclei,  $S$ , is recorded along with an irradiated decoupling pulse on nuclei,  $I$ , to improve the spectral resolution.

#### 1.6.4. Two-dimensional NMR experiments

Two-dimensional (2D) NMR techniques can probe selective NMR interactions and are often insightful in structural determination. In a 2D NMR experiment, signals are recorded as a function of two time variables, and then Fourier transformed with respect to these two variables yielding two frequency axes. A typical 2D NMR experiment is performed with the scheme shown in Figure 1.18, which consists of preparation, evolution, mixing, and detection. The indirect evolution period  $\Delta t_1$  is incremented to build up a time-domain dataset which can be Fourier transformed to yield a 2D frequency-domain spectrum.



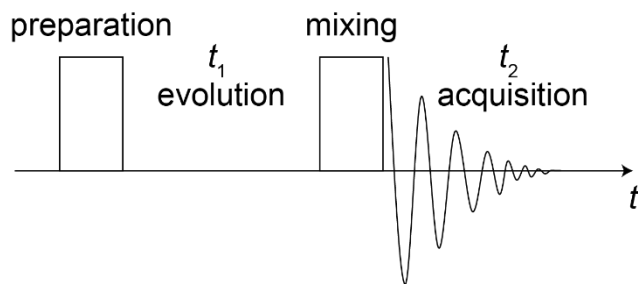


**Figure 1.17.** Basic 2D pulse scheme. The evolution period,  $t_1$ , between the preparation and mixing time elements incremented, followed by another period that allows for mixing before detection in the  $t_2$  period.

### *Double-Quantum- Single-Quantum experiment*

For dipolar-coupled nuclei, fast MAS with 2D Double Quantum (DQ) - Single Quantum (SQ) NMR spectroscopy achieves high resolution while allowing access to the dipolar coupling inherent to the structure. Specifically, the homonuclear  $^1\text{H}$ - $^1\text{H}$  double-quantum (DQ) MAS experiment can be applied to proton-proton proximities.<sup>224</sup> 2D DQ-SQ NMR spectrum is acquired by using a rotor-synchronized Back to Back (BaBa) recoupling sequence for excitation (4 steps) and reconversion (4 steps) of DQ coherence.<sup>225</sup> Double quantum coherence is excited, which evolves during the incremented time  $t_1$ , which eventually is converted back to SQ coherence, and detected during the acquisition time,  $t_2$ , as shown in Figure 1.19.

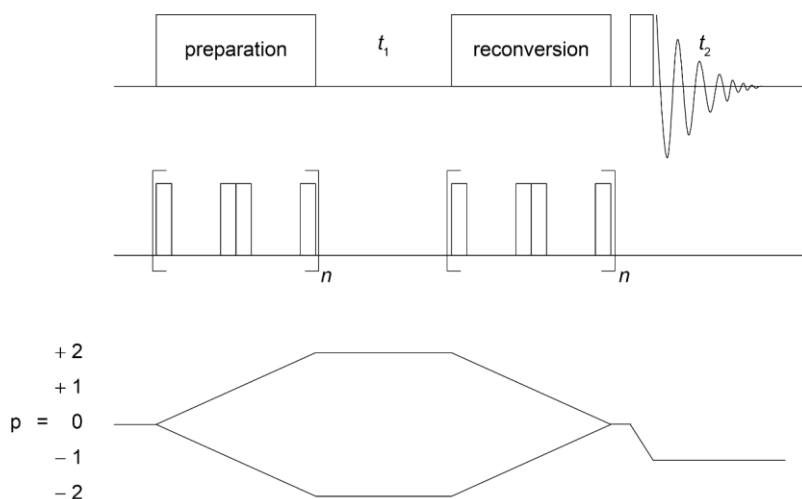


**Figure 1.18.** Pulse sequence and coherence transfer pathway diagram for a  $^1\text{H}$  DQ-SQ MAS experiment using the BaBa recoupling sequence for the excitation and reconversion of DQ coherence.

In a DQ-SQ NMR spectrum, the DQ signal is observed at a cumulative sum of SQ frequencies of the dipolar coupled nuclei. If the nuclei are chemically equivalent, their correlation appears on the diagonal (auto-correlation peak), whereas if the nuclei are chemically inequivalent, their correlation appears as an off-diagonal (cross-correlation) peak.<sup>224</sup> The DQ-SQ homonuclear correlation allows the detection of proximities between the nearest neighbors since the large homonuclear recoupled dipolar interactions between nearby nuclei in the first-order Hamiltonian attenuates the coherence transfer between distant nuclei. This phenomenon is called dipolar truncation.<sup>226</sup>

### *Spin-diffusion experiment*

Spin-diffusion experiment is less susceptible to dipolar truncation than DQ-SQ homonuclear recoupling since they rely on cross-terms between distinct homonuclear dipolar interactions or homo- and hetero-nuclear dipolar interactions in the second-order Hamiltonian. As a result, they allow probing longer-range distances.<sup>224</sup> The spin-diffusion experiment follows a typical NOESY (Nuclear Overhauser Effect Spectroscopy) type experiment,<sup>227</sup> in which two periods of single-quantum coherence evolution are separated by a mixing time, as shown in Figure 1.20.

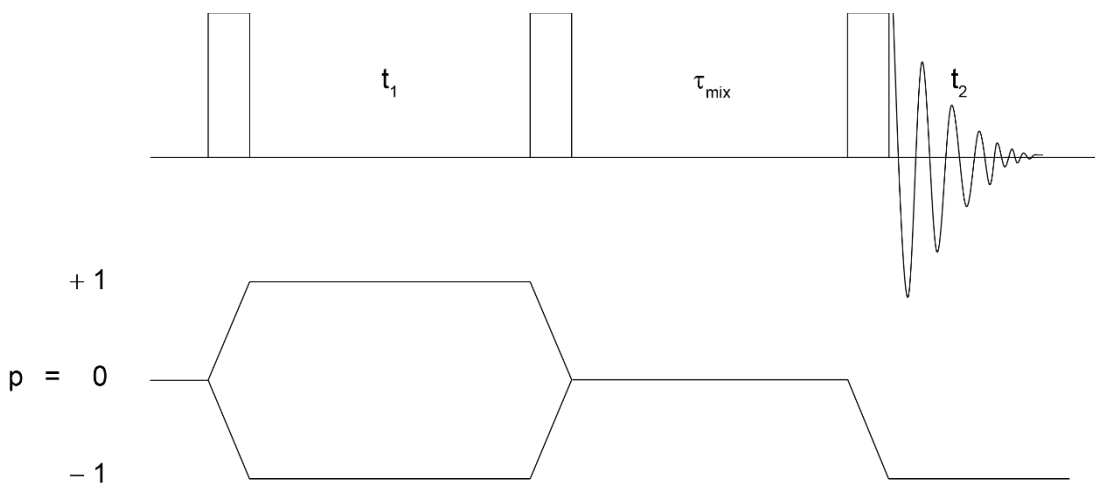


**Figure 1.19.** The pulse sequence and coherence transfer pathway diagram for a NOESY-type spin diffusion experiment

The dipolar network among the proton is most substantial in organic molecules due to the large gyromagnetic ratio and high density of protons.  $^1\text{H}$  spin diffusion has been widely

exploited in solid-state NMR to probe internuclear proximities over a range of distances from about 0.1 nm up to distances of 200.0 nm in the polymeric material.

### ***Cross Polarization HETeronuclear CORrelation (CP HETCOR) experiment***

The pulse sequence of a CP HETCOR experiment can be considered a derivative of a conventional CP experiment, which was discussed earlier. The experiment begins with the creation of  $I$  spin SQ coherences which evolve during  $t_1$ . The magnetization is then transferred from  $I$  to  $S$  using a CP step, and subsequent signal acquisition occurs during  $t_2$ . In this thesis, the  $^1\text{H}$ - $^{13}\text{C}$  CP HETCOR experiment is mainly utilized. The primary motivation for recording a  $^1\text{H}$ - $^{13}\text{C}$  HETCOR experiment is to determine and identify the  $^1\text{H}$  chemical shifts of the protons bound to particular carbons. It mainly facilitates assigning proton signals through fairly resolved  $^{13}\text{C}$  signals.

## **1.7. Outline of the thesis**

This thesis describes the application of solid-state NMR spectroscopy along with a combination of other analytical techniques at complimentary lengths and timescales in the characterization of hybrid lead halide perovskites and organic hole-transporting material.

Chapter 2 presents a detailed analysis of the transformative and reconstructive reactions in  $\text{FAPbI}_3$ . The ambient stability of the  $\alpha$ - $\text{FAPbI}_3$  depends on external stimuli such as light and moisture. Specifically, the kinetics of  $\alpha \rightarrow \delta$   $\text{FAPbI}_3$  reaction as functions of water vapor concentration, particle size, and light illumination are investigated, along with the chemical nature of the kinetically trapped  $\alpha|\delta$ - $\text{FAPbI}_3$  phase.

Chapter 3 extends the concept of understanding the cascading degradation reactions in methyl ammonium-based hybrid perovskites. Here a systematic long-term moisture-stability of methylammonium lead iodide perovskites ( $\text{MAPbI}_3$ ) is presented.  $\text{MAPbI}_3$  is subjected to low (40%) and high (85%) relative humidity to identify the formation of different degraded products. The advantage of employing ssNMR spectroscopy is highlighted in determining dilute concentrations of organic byproducts formed that are challenging to detect using other structure-determining techniques. In addition, the role of surface defect passivation in enhancing moisture stability is presented in this chapter.

Chapter 4 present an approach to performing structural- characterization of the hole-transporting material (HTM), which usually lacks long-range order. Specifically, NMR crystallography, a concept of combining experimental solid-state NMR results and computational calculations, has been implemented on spiro-OMeTAD material. Tris(pentafluoro phenyl) borane (BCF), a Lewis acid, is utilized to p-dope spiro-OMeTAD. The local structures and interactions between the dopant (BCF) and host organic semiconductor (spiro-OMeTAD) are elucidated using magnetic resonance spectroscopy and crystallography modeling techniques.

## 1.8. References

- 1 World Energy Outlook 2021, [www.iea.org/weo](http://www.iea.org/weo), (accessed 1 December 2021).
- 2 World Energy Assessment: Energy and the Challenge of Sustainability | United Nations Development Programme, <https://www.undp.org/publications/world-energy-assessment-energy-and-challenge-sustainability>, (accessed 1 December 2021).
- 3 Best Research-Cell Efficiency Chart | Photovoltaic Research | NREL, [www.nrel.gov/pv/cell-efficiency.html](http://www.nrel.gov/pv/cell-efficiency.html), (accessed 12 September 2022).
- 4 H. F. Kay and P. C. Bailey, *Acta Crystallogr.*, 1957, **10**, 219–226.
- 5 V. M. Goldschmidt, *Naturwissenschaften*, 1926, **14**, 477–485.
- 6 W. J. Yin, T. Shi and Y. Yan, *J. Phys. Chem. C*, 2015, **119**, 5253–5264.
- 7 A. K. Jena, A. Kulkarni and T. Miyasaka, *Chem. Rev.*, 2019, **119**, 3036–3103.
- 8 J. Even, L. Pedesseau, J. M. Jancu and C. Katan, *J. Phys. Chem. Lett.*, 2013, **4**, 2999–3005.
- 9 J. Ye, M. M. Byranvand, C. O. Martínez, R. L. Z. Hoye, M. Saliba and L. Polavarapu, *Angew. Chemie Int. Ed.*, 2021, **60**, 21636–21660.
- 10 Z. Liu, W. Qiu, X. Peng, G. Sun, X. Liu, D. Liu, Z. Li, F. He, C. Shen, Q. Gu, F. Ma, H.-L. Yip, L. Hou, Z. Qi and S.-J. Su, *Adv. Mater.*, 2021, **33**, 2103268.
- 11 B. R. Sutherland and E. H. Sargent, *Nat. Photonics*, 2016, **10**, 295–302.
- 12 M. I. Hossain, W. Qarony, S. Ma, L. Zeng, D. Knipp and Y. H. Tsang, *Nano-Micro Lett.*, 2019, **11**, 58.
- 13 A. Kojima, K. Teshima, Y. Shirai and T. Miyasaka, *J. Am. Chem. Soc.*, 2009, **131**, 6050–6051.
- 14 J. H. Im, C. R. Lee, J. W. Lee, S. W. Park and N. G. Park, *Nanoscale*, 2011, **3**, 4088–4093.
- 15 M. M. Lee, J. Teuscher, T. Miyasaka, T. N. Murakami and H. J. Snaith, *Science*, 2012, **338**, 643–647.
- 16 J. H. Heo, S. H. Im, J. H. Noh, T. N. Mandal, C. S. Lim, J. A. Chang, Y. H. Lee, H. J. Kim, A. Sarkar, M. K. Nazeeruddin, M. Grätzel and S. Il Seok, *Nat. Photonics*, 2013, **7**,

- 486–491.
- 17 M. Liu, M. B. Johnston and H. J. Snaith, *Nature*, 2013, **501**, 395–398.
  - 18 W. S. Yang, J. H. Noh, N. J. Jeon, Y. C. Kim, S. Ryu, J. Seo and S. Il Seok, *Science*, 2015, **348**, 1234–1237.
  - 19 M. Saliba, T. Matsui, K. Domanski, J. Y. Seo, A. Ummadisingu, S. M. Zakeeruddin, J. P. Correa-Baena, W. R. Tress, A. Abate, A. Hagfeldt and M. Grätzel, *Science*, 2016, **354**, 206–209.
  - 20 N. J. Jeon, H. Na, E. H. Jung, T.-Y. Yang, Y. G. Lee, G. Kim, H.-W. Shin, S. Il Seok, J. Lee and J. Seo, *Nat. Energy*, 2018, **3**, 682–689.
  - 21 J. J. Yoo, G. Seo, M. R. Chua, T. G. Park, Y. Lu, F. Rotermund, Y. K. Kim, C. S. Moon, N. J. Jeon, J. P. Correa-Baena, V. Bulović, S. S. Shin, M. G. Bawendi and J. Seo, *Nature*, 2021, **590**, 587–593.
  - 22 H. Min, D. Y. Lee, J. Kim, G. Kim, K. S. Lee, J. Kim, M. J. Paik, Y. K. Kim, K. S. Kim, M. G. Kim, T. J. Shin and S. Il Seok, *Nature*, 2021, **598**, 444–450.
  - 23 A. Bou, H. Ā Bolinš, A. Ashoka, H. Cruanyes, A. Guerrero, F. Deschler and J. Bisquert, *ACS Energy Lett.*, 2021, **6**, 2248–2255.
  - 24 G. Grancini, C. Roldán-Carmona, I. Zimmermann, E. Mosconi, X. Lee, D. Martineau, S. Narbey, F. Oswald, F. De Angelis, M. Graetzel and M. K. Nazeeruddin, *Nat. Commun.*, 2017, **8**, 15684.
  - 25 J. Yang, B. D. Siempelkamp, D. Liu and T. L. Kelly, *ACS Nano*, 2015, **9**, 1955–1963.
  - 26 J. A. Christians, P. A. Miranda Herrera and P. V. Kamat, *J. Am. Chem. Soc.*, 2015, **137**, 1530–1538.
  - 27 A. M. A. Leguy, Y. Hu, M. Campoy-Quiles, M. I. Alonso, O. J. Weber, P. Azarhoosh, M. Van Schilfgaarde, M. T. Weller, T. Bein, J. Nelson, P. Docampo and P. R. F. Barnes, *Chem. Mater.*, 2015, **27**, 3397–3407.
  - 28 W. Zhou, Y. Zhao, C. Shi, H. Huang, J. Wei, R. Fu, K. Liu, D. Yu and Q. Zhao, *J. Phys. Chem. C*, 2016, **120**, 4759–4765.
  - 29 M. K. Gangishetty, R. W. J. Scott and T. L. Kelly, *Nanoscale*, 2016, **8**, 6300–6307.
  - 30 L. Ling, S. Yuan, P. Wang, H. Zhang, L. Tu, J. Wang, Y. Zhan, L. Zheng, L. Ling, S. Yuan, P. Wang, H. Zhang, L. Tu, J. Wang, Y. Zhan and L. Zheng, *Adv. Funct. Mater.*, 2016, **26**, 5028–5034.
  - 31 M. Lv, X. Dong, X. Fang, B. Lin, S. Zhang, X. Xu, J. Ding and N. Yuan, *RSC Adv.*, 2015, **5**, 93957–93963.
  - 32 X. Gong, M. Li, X. B. Shi, H. Ma, Z. K. Wang and L. S. Liao, *Adv. Funct. Mater.*, 2015, **25**, 6671–6678.
  - 33 N. Adhikari, A. Dubey, E. A. Gaml, B. Vaagensmith, K. M. Reza, S. A. A. Mabrouk, S. Gu, J. Zai, X. Qian and Q. Qiao, *Nanoscale*, 2016, **8**, 2693–2703.
  - 34 H. Gao, C. Bao, F. Li, T. Yu, J. Yang, W. Zhu, X. Zhou, G. Fu and Z. Zou, *ACS Appl. Mater. Interfaces*, 2015, **7**, 9110–9117.

- 35 H. Zhou, Q. Chen, G. Li, S. Luo, T. B. Song, H. S. Duan, Z. Hong, J. You, Y. Liu and Y. Yang, *Science*, 2014, **345**, 542–546.
- 36 C. G. Wu, C. H. Chiang, Z. L. Tseng, M. K. Nazeeruddin, A. Hagfeldt and M. Grätzel, *Energy Environ. Sci.*, 2015, **8**, 2725–2733.
- 37 A. Solanki, S. S. Lim, S. Mhaisalkar and T. C. Sum, *ACS Appl. Mater. Interfaces*, 2019, **11**, 25474–25482.
- 38 A. M. Askar, G. M. Bernard, B. Wiltshire, K. Shankar and V. K. Michaelis, *J. Phys. Chem. C*, 2017, **121**, 1013–1024.
- 39 M. A. A. Kazemi, P. Raval, K. Cherednichekno, J.-N. Chotard, A. Krishna, A. Demortiere, G. N. M. Reddy and F. Sauvage, *Small Methods*, 2021, **5**, 2000834.
- 40 B. Akbali, G. Topcu, T. Guner, M. Ozcan, M. M. Demir and H. Sahin, *Phys. Rev. Mater.*, 2018, **2**, 034601.
- 41 G. Niu, W. Li, F. Meng, L. Wang, H. Dong and Y. Qiu, *J. Mater. Chem. A*, 2014, **2**, 705–710.
- 42 L. Wu, H. Hu, Y. Xu, S. Jiang, M. Chen, Q. Zhong, D. Yang, Q. Liu, Y. Zhao, B. Sun, Q. Zhang and Y. Yin, *Nano Lett.*, 2017, **17**, 5799–5804.
- 43 B. Turedi, K. J. Lee, I. Dursun, B. Alamer, Z. Wu, E. Alarousu, O. F. Mohammed, N. Cho and O. M. Bakr, *J. Phys. Chem. C*, 2018, **122**, 14128–14134.
- 44 M. Liu, J. Zhao, Z. Luo, Z. Sun, N. Pan, H. Ding and X. Wang, *Chem. Mater.*, 2018, **30**, 5846–5852.
- 45 M. T. Weller, O. J. Weber, J. M. Frost and A. Walsh, *J. Phys. Chem. Lett.*, 2015, **6**, 3209–3212.
- 46 X. Zheng, C. Wu, S. K. Jha, Z. Li, K. Zhu and S. Priya, *ACS Energy Lett.*, 2016, **1**, 1014–1020.
- 47 W. S. Yang, B. W. Park, E. H. Jung, N. J. Jeon, Y. C. Kim, D. U. Lee, S. S. Shin, J. Seo, E. K. Kim, J. H. Noh and S. Il Seok, *Science*, 2017, **356**, 1376–1379.
- 48 T. Chen, B. J. Foley, C. Park, C. M. Brown, L. W. Harriger, J. Lee, J. Ruff, M. Yoon, J. J. Choi and S. H. Lee, *Sci. Adv.*, 2016, **2**, e1601650.
- 49 L. Gu, D. Zhang, M. Kam, Q. Zhang, S. Poddar, Y. Fu, X. Mo and Z. Fan, *Nanoscale*, 2018, **10**, 15164–15172.
- 50 I. Deretzis, A. Alberti, G. Pellegrino, E. Smecca, F. Giannazzo, N. Sakai, T. Miyasaka and A. La Magna, *Appl. Phys. Lett.*, 2015, **106**, 131904.
- 51 J. Zhao, B. Cai, Z. Luo, Y. Dong, Y. Zhang, H. Xu, B. Hong, Y. Yang, L. Li, W. Zhang and C. Gao, *Sci. Rep.*, 2016, **6**, 21976.
- 52 J. Huang, S. Tan, P. D. Lund and H. Zhou, *Energy Environ. Sci.*, 2017, **10**, 2284–2311.
- 53 M. Koehl, M. Heck, S. Wiesmeier and J. Wirth, *Sol. Energy Mater. Sol. Cells*, 2011, **95**, 1638–1646.
- 54 T. Baikie, Y. Fang, J. M. Kadro, M. Schreyer, F. Wei, S. G. Mhaisalkar, M. Graetzel and

- T. J. White, *J. Mater. Chem. A*, 2013, **1**, 5628–5641.
- 55 T. Baikie, N. S. Barrow, Y. Fang, P. J. Keenan, P. R. Slater, R. O. Piltz, M. Gutmann, S. G. Mhaisalkar and T. J. White, *J. Mater. Chem. A*, 2015, **3**, 9298–9307.
- 56 C. C. Stoumpos, C. D. Malliakas and M. G. Kanatzidis, *Inorg. Chem.*, 2013, **52**, 9019–9038.
- 57 R. K. Misra, S. Aharon, B. Li, D. Mogilyansky, I. Visoly-Fisher, L. Etgar and E. A. Katz, *J. Phys. Chem. Lett.*, 2015, **6**, 326–330.
- 58 M. Benavides-Garcia and K. Balasubramanian, *J. Chem. Phys.*, 1998, **100**, 2821.
- 59 A. Dualeh, P. Gao, S. Il Seok, M. K. Nazeeruddin and M. Grätzel, *Chem. Mater.*, 2014, **26**, 6160–6164.
- 60 D. P. Nenon, J. A. Christians, L. M. Wheeler, J. L. Blackburn, E. M. Sanehira, B. Dou, M. L. Olsen, K. Zhu, J. J. Berry and J. M. Luther, *Energy Environ. Sci.*, 2016, **9**, 2072–2082.
- 61 M. J. Bækbo, O. Hansen, I. Chorkendorff and P. C. K. Vesborg, *RSC Adv.*, 2018, **8**, 29899–29908.
- 62 A. Ciccioli and A. Latini, *J. Phys. Chem. Lett.*, 2018, **9**, 3756–3765.
- 63 I. L. Ivanov, A. S. Steparuk, M. S. Bolyachkina, D. S. Tsvetkov, A. P. Safronov and A. Y. Zuev, *J. Chem. Thermodyn.*, 2018, **116**, 253–258.
- 64 A. Latini, G. Gigli and A. Ciccioli, *Sustain. Energy Fuels*, 2017, **1**, 1351–1357.
- 65 G. E. Eperon, S. D. Stranks, C. Menelaou, M. B. Johnston, L. M. Herz and H. J. Snaith, *Energy Environ. Sci.*, 2014, **7**, 982–988.
- 66 S. Aharon, A. Dymshits, A. Rotem and L. Etgar, *J. Mater. Chem. A*, 2015, **3**, 9171–9178.
- 67 E. J. Juarez-Perez, L. K. Ono and Y. Qi, *J. Mater. Chem. A*, 2019, **7**, 16912–16919.
- 68 C. Zhang, J. F. S. Fernando, K. L. Firestein, J. E. Von Treifeldt, D. Siriwardena, X. Fang and D. Golberg, *APL Mater.*, 2019, **7**, 071110.
- 69 M. Liao, B. Shan and M. Li, *J. Phys. Chem. Lett.*, 2019, **10**, 1217–1225.
- 70 Y. Wu, F. Xie, H. Chen, X. Yang, H. Su, M. Cai, Z. Zhou, T. Noda, L. Han, Y. Wu, F. Xie, M. Cai, Z. Zhou, T. Noda, L. Han, H. Chen, X. Yang and H. Su, *Adv. Mater.*, 2017, **29**, 1701073.
- 71 T. Sekimoto, T. Matsui, T. Nishihara, R. Uchida, T. Sekiguchi and T. Negami, *ACS Appl. Energy Mater.*, 2019, **2**, 5039–5049.
- 72 A. F. Akbulatov, L. A. Frolova, M. P. Griffin, I. R. Gearba, A. Dolocan, D. A. Vanden Bout, S. Tsarev, E. A. Katz, A. F. Shestakov, K. J. Stevenson, P. A. Troshin, A. F. Akbulatov, L. A. Frolova, A. F. Shestakov, P. A. Troshin, M. P. Griffin, D. A. Vanden Bout, S. Tsarev, K. J. Stevenson and E. A. Katz, *Adv. Energy Mater.*, 2017, **7**, 1700476.
- 73 W. Chen, Y. Wu, Y. Yue, J. Liu, W. Zhang, X. Yang, H. Chen, E. Bi, I. Ashraful, M. Grätzel and L. Han, *Science*, 2015, **350**, 944–948.
- 74 H. Tsai, W. Nie, J. C. Blancon, C. C. Stoumpos, R. Asadpour, B. Harutyunyan, A. J. Neukirch, R. Verduzco, J. J. Crochet, S. Tretiak, L. Pedesseau, J. Even, M. A. Alam, G.

- Gupta, J. Lou, P. M. Ajayan, M. J. Bedzyk, M. G. Kanatzidis and A. D. Mohite, *Nature*, 2016, **536**, 312–316.
- 75 K. Wojciechowski, T. Leijtens, S. Siprova, C. Schlueter, M. T. Hörantner, J. T. W. Wang, C. Z. Li, A. K. Y. Jen, T. L. Lee and H. J. Snaith, *J. Phys. Chem. Lett.*, 2015, **6**, 2399–2405.
- 76 S. Seo, S. Jeong, C. Bae, N.-G. Park, H. Shin, S. Seo, S. Jeong, C. Bae, H. Shin and N. Park, *Adv. Mater.*, 2018, **30**, 1801010.
- 77 Z. Wang, Q. Lin, B. Wenger, M. G. Christoforo, Y. H. Lin, M. T. Klug, M. B. Johnston, L. M. Herz and H. J. Snaith, *Nat. Energy*, 2018, **3**, 855–861.
- 78 K. A. Bush, A. F. Palmstrom, Z. J. Yu, M. Boccard, R. Cheacharoen, J. P. Mailoa, D. P. McMeekin, R. L. Z. Hoyer, C. D. Bailie, T. Leijtens, I. M. Peters, M. C. Minichetti, N. Rolston, R. Prasanna, S. Sofia, D. Harwood, W. Ma, F. Moghadam, H. J. Snaith, T. Buonassisi, Z. C. Holman, S. F. Bent and M. D. McGehee, *Nat. Energy*, 2017, **2**, 17009.
- 79 J. Yang, Q. Hong, Z. Yuan, R. Xu, X. Guo, S. Xiong, X. Liu, S. Braun, Y. Li, J. Tang, C. Duan, M. Fahlman and Q. Bao, *Adv. Opt. Mater.*, 2018, **6**, 1800262.
- 80 B. Chen, J. Song, X. Dai, Y. Liu, P. N. Rudd, X. Hong, J. Huang, B. Chen, X. Dai, P. N. Rudd, J. Huang, J. Song, X. Hong and Y. Liu, *Adv. Mater.*, 2019, **31**, 1902413.
- 81 W. Nie, J. C. Blancon, A. J. Neukirch, K. Appavoo, H. Tsai, M. Chhowalla, M. A. Alam, M. Y. Sfeir, C. Katan, J. Even, S. Tretiak, J. J. Crochet, G. Gupta and A. D. Mohite, *Nat. Commun.*, 2016, **7**, 11574.
- 82 E. T. Hoke, D. J. Slotcavage, E. R. Dohner, A. R. Bowring, H. I. Karunadasa and M. D. McGehee, *Chem. Sci.*, 2014, **6**, 613–617.
- 83 S. J. Yoon, S. Draguta, J. S. Manser, O. Sharia, W. F. Schneider, M. Kuno and P. V. Kamat, *ACS Energy Lett.*, 2016, **1**, 290–296.
- 84 D. W. DeQuilettes, W. Zhang, V. M. Burlakov, D. J. Graham, T. Leijtens, A. Osherov, V. Bulović, H. J. Snaith, D. S. Ginger and S. D. Stranks, *Nat. Commun.*, 2016, **7**, 11683.
- 85 G. Abdelmageed, C. Mackeen, K. Hellier, L. Jewell, L. Seymour, M. Tingwald, F. Bridges, J. Z. Zhang and S. Carter, *Sol. Energy Mater. Sol. Cells*, 2018, **174**, 566–571.
- 86 M. Long, T. Zhang, M. Liu, Z. Chen, C. Wang, W. Xie, F. Xie, J. Chen, G. Li, J. Xu, M. Z. Long, T. K. Zhang, Z. F. Chen, J. B. Xu, M. Z. Liu, C. Wang, W. G. Xie, F. Y. Xie, J. Chen and G. Li, *Adv. Mater.*, 2018, **30**, 1801562.
- 87 D. Bryant, N. Aristidou, S. Pont, I. Sanchez-Molina, T. Chotchunangatchaval, S. Wheeler, J. R. Durrant and S. A. Haque, *Energy Environ. Sci.*, 2016, **9**, 1655–1660.
- 88 X. Tang, M. Brandl, B. May, I. Levchuk, Y. Hou, M. Richter, H. Chen, S. Chen, S. Kahmann, A. Osvet, F. Maier, H. P. Steinrück, R. Hock, G. J. Matt and C. J. Brabec, *J. Mater. Chem. A*, 2016, **4**, 15896–15903.
- 89 Q. M. Hong, R. P. Xu, T. Y. Jin, J. X. Tang and Y. Q. Li, *Org. Electron.*, 2019, **67**, 19–25.
- 90 R. P. Xu, Y. Q. Li, T. Y. Jin, Y. Q. Liu, Q. Y. Bao, C. O’Carroll and J. X. Tang, *ACS Appl. Mater. Interfaces*, 2018, **10**, 6737–6746.



- 91 C. Das, M. Wussler, T. Hellmann, T. Mayer and W. Jaegermann, *Phys. Chem. Chem. Phys.*, 2018, **20**, 17180–17187.
- 92 W. Huang, J. S. Manser, P. V. Kamat and S. Ptasinska, *Chem. Mater.*, 2016, **28**, 303–311.
- 93 Z. Song, C. Wang, A. B. Phillips, C. R. Grice, D. Zhao, Y. Yu, C. Chen, C. Li, X. Yin, R. J. Ellingson, M. J. Heben and Y. Yan, *Sustain. Energy Fuels*, 2018, **2**, 2460–2467.
- 94 Q. Chen, H. Zhou, Y. Fang, A. Z. Stieg, T. Bin Song, H. H. Wang, X. Xu, Y. Liu, S. Lu, J. You, P. Sun, J. McKay, M. S. Goorsky and Y. Yang, *Nat. Commun.*, 2015, **6**, 7269.
- 95 M. Kim, T. K. Lee, I. W. Choi, H. W. Choi, Y. Jo, J. Lee, G. H. Kim, S. K. Kwak and D. S. Kim, *Sustain. Energy Fuels*, 2020, **4**, 3753–3763.
- 96 A. Binek, F. C. Hanusch, P. Docampo and T. Bein, *J. Phys. Chem. Lett.*, 2015, **6**, 1249–1253.
- 97 N. Pellet, P. Gao, G. Gregori, T. Y. Yang, M. K. Nazeeruddin, J. Maier and M. Grätzel, *Angew. Chemie Int. Ed.*, 2014, **53**, 3151–3157.
- 98 T. M. Koh, K. Fu, Y. Fang, S. Chen, T. C. Sum, N. Mathews, S. G. Mhaisalkar, P. P. Boix and T. Baikie, *J. Phys. Chem. C*, 2014, **118**, 16458–16462.
- 99 O. J. Weber, B. Charles and M. T. Weller, *J. Mater. Chem. A*, 2016, **4**, 15375–15382.
- 100 M. Saliba, T. Matsui, J. Y. Seo, K. Domanski, J. P. Correa-Baena, M. K. Nazeeruddin, S. M. Zakeeruddin, W. Tress, A. Abate, A. Hagfeldt and M. Grätzel, *Energy Environ. Sci.*, 2016, **9**, 1989–1997.
- 101 Z. Li, M. Yang, J. S. Park, S. H. Wei, J. J. Berry and K. Zhu, *Chem. Mater.*, 2016, **28**, 284–292.
- 102 C. Yi, J. Luo, S. Meloni, A. Boziki, N. Ashari-Astani, C. Grätzel, S. M. Zakeeruddin, U. Röthlisberger and M. Grätzel, *Energy Environ. Sci.*, 2016, **9**, 656–662.
- 103 J.-W. Lee, D.-H. Kim, H.-S. Kim, S.-W. Seo, S. M. Cho and N.-G. Park, *Adv. Energy Mater.*, 2015, **5**, 1501310.
- 104 Y. Jiang, M. R. Leyden, L. Qiu, S. Wang, L. K. Ono, Z. Wu, E. J. Juarez-Perez, Y. Qi, Y. Jiang, M. R. Leyden, L. Qiu, S. Wang, L. K. Ono, Z. Wu, E. J. Juarez-Perez and Y. B. Qi, *Adv. Funct. Mater.*, 2018, **28**, 1703835.
- 105 N. Li, X. Niu, Q. Chen and H. Zhou, *Chem. Soc. Rev.*, 2020, **49**, 8235–8286.
- 106 L. Wang, H. Zhou, J. Hu, B. Huang, M. Sun, B. Dong, G. Zheng, Y. Huang, Y. Chen, L. Li, Z. Xu, N. Li, Z. Liu, Q. Chen, L. D. Sun and C. H. Yan, *Science*, 2019, **363**, 265–270.
- 107 Q. Tai, X. Guo, G. Tang, P. You, T. W. Ng, D. Shen, J. Cao, C. K. Liu, N. Wang, Y. Zhu, C. S. Lee and F. Yan, *Angew. Chemie Int. Ed.*, 2019, **58**, 806–810.
- 108 I. Chung, B. Lee, J. He, R. P. H. Chang and M. G. Kanatzidis, *Nature*, 2012, **485**, 486–489.
- 109 N. K. Noel, S. D. Stranks, A. Abate, C. Wehrenfennig, S. Guarnera, A. A. Haghighirad, A. Sadhanala, G. E. Eperon, S. K. Pathak, M. B. Johnston, A. Petrozza, L. M. Herz and H. J. Snaith, *Energy Environ. Sci.*, 2014, **7**, 3061–3068.

- 110 T. M. Koh, T. Krishnamoorthy, N. Yantara, C. Shi, W. L. Leong, P. P. Boix, A. C. Grimsdale, S. G. Mhaisalkar and N. Mathews, *J. Mater. Chem. A*, 2015, **3**, 14996–15000.
- 111 G. E. Eperon, T. Leijtens, K. A. Bush, R. Prasanna, T. Green, J. T. W. Wang, D. P. McMeekin, G. Volonakis, R. L. Milot, R. May, A. Palmstrom, D. J. Slotcavage, R. A. Belisle, J. B. Patel, E. S. Parrott, R. J. Sutton, W. Ma, F. Moghadam, B. Conings, A. Babayigit, H. G. Boyen, S. Bent, F. Giustino, L. M. Herz, M. B. Johnston, M. D. McGehee and H. J. Snaith, *Science*, 2016, **354**, 861–865.
- 112 R. Lin, K. Xiao, Z. Qin, Q. Han, C. Zhang, M. Wei, M. I. Saidaminov, Y. Gao, J. Xu, M. Xiao, A. Li, J. Zhu, E. H. Sargent and H. Tan, *Nat. Energy*, 2019, **4**, 864–873.
- 113 Y. Yin, S. Fu, S. Zhou, Y. Song, L. Li, M. Zhang, J. Wang, P. Mariyappan, S. M. Alshehri, T. Ahamad and Y. Yamauchi, *Electron. Mater. Lett.*, 2020, **16**, 224–230.
- 114 J. H. Noh, S. H. Im, J. H. Heo, T. N. Mandal and S. Il Seok, *Nano Lett.*, 2013, **13**, 1764–1769.
- 115 F. Brivio, C. Caetano and A. Walsh, *J. Phys. Chem. Lett.*, 2016, **7**, 1083–1087.
- 116 D. J. Slotcavage, H. I. Karunadasa and M. D. McGehee, *ACS Energy Lett.*, 2016, **1**, 1199–1205.
- 117 S. Tao, I. Schmidt, G. Brocks, J. Jiang, I. Tranca, K. Meerholz and S. Olthof, *Nat. Commun.*, 2019, **10**, 2560.
- 118 M. Kim, G. H. Kim, T. K. Lee, I. W. Choi, H. W. Choi, Y. Jo, Y. J. Yoon, J. W. Kim, J. Lee, D. Huh, H. Lee, S. K. Kwak, J. Y. Kim and D. S. Kim, *Joule*, 2019, **3**, 2179–2192.
- 119 H. Yu, F. Wang, F. Xie, W. Li, J. Chen and N. Zhao, *Adv. Funct. Mater.*, 2014, **24**, 7102–7108.
- 120 F. Xie, C. C. Chen, Y. Wu, X. Li, M. Cai, X. Liu, X. Yang and L. Han, *Energy Environ. Sci.*, 2017, **10**, 1942–1949.
- 121 C. Fei, L. Guo, B. Li, R. Zhang, H. Fu, J. Tian and G. Cao, *Nano Energy*, 2016, **27**, 17–26.
- 122 G. Kim, H. Min, K. S. Lee, D. Y. Lee, S. M. Yoon and S. Il Seok, *Science*, 2020, **370**, 108–112.
- 123 Z. Wang, Y. Zhou, S. Pang, Z. Xiao, J. Zhang, W. Chai, H. Xu, Z. Liu, N. P. Padture and G. Cui, *Chem. Mater.*, 2015, **27**, 7149–7155.
- 124 C. Mu, J. Pan, S. Feng, Q. Li, D. Xu, C. Mu, J. Pan, S. Feng, Q. Li and D. Xu, *Adv. Energy Mater.*, 2017, **7**, 1601297.
- 125 M. I. Saidaminov, J. Kim, A. Jain, R. Quintero-Bermudez, H. Tan, G. Long, F. Tan, A. Johnston, Y. Zhao, O. Voznyy and E. H. Sargent, *Nat. Energy*, 2018, **3**, 648–654.
- 126 D. H. Cao, C. C. Stoumpos, O. K. Farha, J. T. Hupp and M. G. Kanatzidis, *J. Am. Chem. Soc.*, 2015, **137**, 7843–7850.
- 127 C. M. Mauck and W. A. Tisdale, *Trends Chem.*, 2019, **1**, 380–393.
- 128 C. C. Stoumpos, D. H. Cao, D. J. Clark, J. Young, J. M. Rondinelli, J. I. Jang, J. T. Hupp and M. G. Kanatzidis, *Chem. Mater.*, 2016, **28**, 2852–2867.

- 129 B. Saparov and D. B. Mitzi, *Chem. Rev.*, 2016, **116**, 4558–4596.
- 130 X. Li, J. M. Hoffman and M. G. Kanatzidis, *Chem. Rev.*, 2021, **121**, 2230–2291.
- 131 D. G. Billing and A. Lemmerer, *Acta Crystallogr. Sect. B Struct. Sci.*, 2007, **63**, 735–747.
- 132 A. Lemmerer and D. G. Billing, *Dalt. Trans.*, 2012, **41**, 1146–1157.
- 133 D. G. Billing and A. Lemmerer, *New J. Chem.*, 2008, **32**, 1736–1746.
- 134 Y. Chen, Y. Sun, J. Peng, J. Tang, K. Zheng, Z. Liang, P. Y. Chen, Y. Sun, J. Peng, J. Tang, Z. Liang and K. Zheng, *Adv. Mater.*, 2018, **30**, 1703487.
- 135 G. Grancini and M. K. Nazeeruddin, *Nat. Rev. Mater.*, 2018, **4**, 4–22.
- 136 L. Mao, C. C. Stoumpos and M. G. Kanatzidis, *J. Am. Chem. Soc.*, 2019, **141**, 1171–1190.
- 137 D. B. Mitzi, C. A. Feild, W. T. A. Harrison and A. M. Guloy, *Nature*, 1994, **369**, 467–469.
- 138 X. Li, G. Wu, M. Wang, B. Yu, J. Zhou, B. Wang, X. Zhang, H. Xia, S. Yue, K. Wang, C. Zhang, J. Zhang, H. Zhou, Y. Zhang, X. Li, G. Wu, J. Zhou, X. Zhang, H. Xia, K. Wang, Y. Zhang, M. Wang, B. Yu, C. Zhang, B. Wang, S. Yue, J. Zhang and H. Zhou, *Adv. Energy Mater.*, 2020, **10**, 2001832.
- 139 I. Spanopoulos, I. Hadar, W. Ke, Q. Tu, M. Chen, H. Tsai, Y. He, G. Shekhawat, V. P. Dravid, M. R. Wasielewski, A. D. Mohite, C. C. Stoumpos and M. G. Kanatzidis, *J. Am. Chem. Soc.*, 2019, **141**, 5518–5534.
- 140 L. Mao, W. Ke, L. Pedesseau, Y. Wu, C. Katan, J. Even, M. R. Wasielewski, C. C. Stoumpos and M. G. Kanatzidis, *J. Am. Chem. Soc.*, 2018, **140**, 3775–3783.
- 141 L. N. Quan, M. Yuan, R. Comin, O. Voznyy, E. M. Beauregard, S. Hoogland, A. Buin, A. R. Kirmani, K. Zhao, A. Amassian, D. H. Kim and E. H. Sargent, *J. Am. Chem. Soc.*, 2016, **138**, 2649–2655.
- 142 X. Gan, O. Wang, K. Liu, X. Du, L. Guo and H. Liu, *Sol. Energy Mater. Sol. Cells*, 2017, **162**, 93–102.
- 143 D. Thrithamarassery Gangadharan and D. Ma, *Energy Environ. Sci.*, 2019, **12**, 2860–2889.
- 144 F. Zhang, D. H. Kim and K. Zhu, *Curr. Opin. Electrochem.*, 2018, **11**, 105–113.
- 145 H. Tsai, W. Nie, J. C. Blancon, C. C. Stoumpos, R. Asadpour, B. Harutyunyan, A. J. Neukirch, R. Verduzco, J. J. Crochet, S. Tretiak, L. Pedesseau, J. Even, M. A. Alam, G. Gupta, J. Lou, P. M. Ajayan, M. J. Bedzyk, M. G. Kanatzidis and A. D. Mohite, *Nature*, 2016, **536**, 312–317.
- 146 Y. Zheng, T. Niu, J. Qiu, L. Chao, B. Li, Y. Yang, Q. Li, C. Lin, X. Gao, C. Zhang, Y. Xia, Y. Chen and W. Huang, *Sol. RRL*, 2019, **3**, 1900090.
- 147 S. Ahmad, P. Fu, S. Yu, Q. Yang, X. Liu, X. Wang, X. Wang, X. Guo and C. Li, *Joule*, 2019, **3**, 794–806.
- 148 X. Li, W. Ke, B. Traoré, P. Guo, I. Hadar, M. Kepenekian, J. Even, C. Katan, C. C. Stoumpos, R. D. Schaller and M. G. Kanatzidis, *J. Am. Chem. Soc.*, 2019, **141**, 12880–

- 12890.
- 149 W. Ke, L. Mao, C. C. Stoumpos, J. Hoffman, I. Spanopoulos, A. D. Mohite and M. G. Kanatzidis, *Adv. Energy Mater.*, 2019, **9**, 1803384.
- 150 E. A. Muljarov, S. G. Tikhodeev and N. A. Gippius, *Phys. Rev. B*, 1995, **51**, 14370.
- 151 Z. Xu, D. Lu, X. Dong, M. Chen, Q. Fu, Y. Liu, Z. Xu, D. Lu, X. Dong, M. Chen, Q. Fu and Y. Liu, *Adv. Mater.*, 2021, **33**, 2105083.
- 152 A. Leblanc, N. Mercier, M. Allain, J. Dittmer, V. Fernandez and T. Pauporté, *Angew. Chemie Int. Ed.*, 2017, **56**, 16067–16072.
- 153 W. Ke, C. C. Stoumpos, M. Zhu, L. Mao, I. Spanopoulos, J. Liu, O. Y. Kontsevoi, M. Chen, D. Sarma, Y. Zhang, M. R. Wasielewski and M. G. Kanatzidis, *Sci. Adv.*, 2017, **3**, e1701293.
- 154 A. Leblanc, N. Mercier, M. Allain, J. Dittmer, T. Pauporté, V. Fernandez, F. Boucher, M. Kepenekian and C. Katan, *ACS Appl. Mater. Interfaces*, 2019, **11**, 20743–20751.
- 155 I. Spanopoulos, W. Ke, C. C. Stoumpos, E. C. Schueller, O. Y. Kontsevoi, R. Seshadri and M. G. Kanatzidis, *J. Am. Chem. Soc.*, 2018, **140**, 5728–5742.
- 156 W. Ke, I. Spanopoulos, Q. Tu, I. Hadar, X. Li, G. S. Shekhawat, V. P. Dravid and M. G. Kanatzidis, *J. Am. Chem. Soc.*, 2019, **141**, 8627–8637.
- 157 M. Worku, Y. Tian, C. Zhou, H. Lin, M. Chaaban, L. J. Xu, Q. He, D. Beery, Y. Zhou, X. Lin, Y. F. Su, Y. Xin and B. Ma, *Sci. Adv.*, 2020, **6**, eaaz5961.
- 158 A. Senocrate, I. Spanopoulos, N. Zibouche, J. Maier, M. S. Islam and M. G. Kanatzidis, *Chem. Mater.*, 2021, **33**, 719–726.
- 159 W. Ke, C. C. Stoumpos, I. Spanopoulos, M. Chen, M. R. Wasielewski and M. G. Kanatzidis, *ACS Energy Lett.*, 2018, **3**, 1470–1476.
- 160 J. A. McNulty, A. M. Z. Slawin and P. Lightfoot, *Dalt. Trans.*, 2020, **49**, 15171–15174.
- 161 D. Y. Son, J. W. Lee, Y. J. Choi, I. H. Jang, S. Lee, P. J. Yoo, H. Shin, N. Ahn, M. Choi, D. Kim and N. G. Park, *Nat. Energy*, DOI:10.1038/nenergy.2016.81.
- 162 M. Wang, F. Cao, K. Deng and L. Li, *Nano Energy*, 2019, **63**, 103867.
- 163 J. Cao, X. Jing, J. Yan, C. Hu, R. Chen, J. Yin, J. Li and N. Zheng, *J. Am. Chem. Soc.*, 2016, **138**, 9919–9926.
- 164 D. Bi, W. Tress, M. I. Dar, P. Gao, J. Luo, C. Renevier, K. Schenk, A. Abate, F. Giordano, J. P. Correa Baena, J. D. Decoppet, S. M. Zakeeruddin, M. K. Nazeeruddin, M. Grätzel and A. Hagfeldt, *Sci. Adv.*, 2016, **2**, e1501170.
- 165 C. Roldán-Carmona, P. Gratia, I. Zimmermann, G. Grancini, P. Gao, M. Graetzel and M. K. Nazeeruddin, *Energy Environ. Sci.*, 2015, **8**, 3550–3556.
- 166 J. an Yang, A. Xiao, L. Xie, K. Liao, X. Deng, C. Li, A. Wang, Y. Xiang, T. Li and F. Hao, *Electrochim. Acta*, 2020, **338**, 135697.
- 167 C. Li, A. Wang, L. Xie, X. Deng, K. Liao, J. A. Yang, T. Li and F. Hao, *J. Mater. Chem. A*, 2019, **7**, 24150–24163.

- 168 W. Zhao, Z. Yao, F. Yu, D. Yang, S. Liu, W. Zhao, Z. Yao, F. Yu, D. Yang and S. Liu, *Adv. Sci.*, 2018, **5**, 1700131.
- 169 J. Zhang, R. Chen, Y. Wu, M. Shang, Z. Zeng, Y. Zhang, Y. Zhu, L. Han, J. Zhang, R. Chen, Z. Zeng, Y. Zhang, Y. Zhu, Y. Wu, L. Han and M. Shang, *Adv. Energy Mater.*, 2018, **8**, 1701981.
- 170 M. Abdi-Jalebi, Z. Andaji-Garmaroudi, S. Cacovich, C. Stavrakas, B. Philippe, J. M. Richter, M. Alsari, E. P. Booker, E. M. Hutter, A. J. Pearson, S. Lilliu, T. J. Savenije, H. Rensmo, G. Divitini, C. Ducati, R. H. Friend and S. D. Stranks, *Nature*, 2018, **555**, 497–501.
- 171 J. Li, F. Cai, L. Yang, F. Ye, J. Zhang, R. S. Gurney, D. Liu and T. Wang, *Appl. Phys. Lett.*, 2017, **111**, 053301.
- 172 S. Li, Z. Shi, F. Zhang, L. Wang, Z. Ma, D. Yang, Z. Yao, D. Wu, T. T. Xu, Y. Tian, Y. Zhang, C. Shan and X. J. Li, *Chem. Mater.*, 2019, **31**, 3917–3928.
- 173 H. Li, D. Li, W. Zhao, S. Yuan, Z. Liu, D. Wang and S. Liu, *J. Power Sources*, 2020, **448**, 227586.
- 174 N. Li, S. Tao, Y. Chen, X. Niu, C. K. Onwudinanti, C. Hu, Z. Qiu, Z. Xu, G. Zheng, L. Wang, Y. Zhang, L. Li, H. Liu, Y. Lun, J. Hong, X. Wang, Y. Liu, H. Xie, Y. Gao, Y. Bai, S. Yang, G. Brocks, Q. Chen and H. Zhou, *Nat. Energy*, 2019, **4**, 408–415.
- 175 A. Abate, M. Saliba, D. J. Hollman, S. D. Stranks, K. Wojciechowski, R. Avolio, G. Grancini, A. Petrozza and H. J. Snaith, *Nano Lett.*, 2014, **14**, 3247–3254.
- 176 Z. Yang, J. Dou, S. Kou, J. Dang, Y. Ji, G. Yang, W. Q. Wu, D. Bin Kuang and M. Wang, *Adv. Funct. Mater.*, 2020, **30**, 1910710.
- 177 J. Luo, J. Xia, H. Yang, H. A. Malik, F. Han, H. Shu, X. Yao, Z. Wan and C. Jia, *Nano Energy*, 2020, **70**, 104509.
- 178 L. Meazza, J. A. Foster, K. Fucke, P. Metrangolo, G. Resnati and J. W. Steed, *Nat. Chem.*, 2013, **5**, 42–47.
- 179 F. Zhang, S. Wang, X. Li and Y. Xiao, *Curr. Nanosci.*, 2015, **12**, 137–156.
- 180 R. C. Haddon, *Philos. Trans. R. Soc. London. Ser. A Phys. Eng. Sci.*, 1993, **343**, 53–62.
- 181 B. Chen, P. N. Rudd, S. Yang, Y. Yuan and J. Huang, *Chem. Soc. Rev.*, 2019, **48**, 3842–3867.
- 182 K. Liu, S. Chen, J. Wu, H. Zhang, M. Qin, X. Lu, Y. Tu, Q. Meng and X. Zhan, *Energy Environ. Sci.*, 2018, **11**, 3463–3471.
- 183 J. Xu, A. Buin, A. H. Ip, W. Li, O. Voznyy, R. Comin, M. Yuan, S. Jeon, Z. Ning, J. J. McDowell, P. Kanjanaboos, J. P. Sun, X. Lan, L. N. Quan, D. H. Kim, I. G. Hill, P. Maksymovych and E. H. Sargent, *Nat. Commun.*, 2015, **6**, 7081.
- 184 Y. Shao, Z. Xiao, C. Bi, Y. Yuan and J. Huang, *Nat. Commun.*, 2014, **5**, 5784.
- 185 Y. Wu, X. Yang, W. Chen, Y. Yue, M. Cai, F. Xie, E. Bi, A. Islam and L. Han, *Nat. Energy*, 2016, **1**, 16148.
- 186 N. K. Noel, A. Abate, S. D. Stranks, E. S. Parrott, V. M. Burlakov, A. Goriely and H. J.

- Snaith, *ACS Nano*, 2014, **8**, 9815–9821.
- 187 F. Zhang, D. Bi, N. Pellet, C. Xiao, Z. Li, J. J. Berry, S. M. Zakeeruddin, K. Zhu and M. Grätzel, *Energy Environ. Sci.*, 2018, **11**, 3480–3490.
- 188 A. Krishna, M. A. Akhavan Kazemi, M. Sliwa, G. N. M. Reddy, L. Delevoye, O. Lafon, A. Felten, M. T. Do, S. Gottis and F. Sauvage, *Adv. Funct. Mater.*, 2020, **30**, 1909737.
- 189 D. Bi, X. Li, J. V. Milić, D. J. Kubicki, N. Pellet, J. Luo, T. LaGrange, P. Mettraux, L. Emsley, S. M. Zakeeruddin and M. Grätzel, *Nat. Commun.*, 2018, **9**, 4482.
- 190 C. Qin, T. Matsushima, T. Fujihara, C. Adachi, C. Qin, T. Matsushima, C. Adachi and T. Fujihara, *Adv. Mater.*, 2017, **29**, 1603808.
- 191 R. Wang, J. Xue, K. L. Wang, Z. K. Wang, Y. Luo, D. Fenning, G. Xu, S. Nuryyeva, T. Huang, Y. Zhao, J. L. Yang, J. Zhu, M. Wang, S. Tan, I. Yavuz, K. N. Houk and Y. Yang, *Science*, 2019, **366**, 1509–1513.
- 192 A. Krishna, H. Zhang, Z. Zhou, T. Gallet, M. Dankl, O. Ouellette, F. T. Eickemeyer, F. Fu, S. Sanchez, M. Mensi, S. M. Zakeeruddin, U. Rothlisberger, G. N. M. Reddy, A. Redinger, M. Grätzel and A. Hagfeldt, *Energy Environ. Sci.*, 2021, **14**, 5552–5562.
- 193 S. Wang, A. Wang, X. Deng, L. Xie, A. Xiao, C. Li, Y. Xiang, T. Li, L. Ding and F. Hao, *J. Mater. Chem. A*, 2020, **8**, 12201–12225.
- 194 M. A. Kamarudin, D. Hirotani, Z. Wang, K. Hamada, K. Nishimura, Q. Shen, T. Toyoda, S. Iikubo, T. Minemoto, K. Yoshino and S. Hayase, *J. Phys. Chem. Lett.*, 2019, **10**, 5277–5283.
- 195 W. Q. Wu, Z. Yang, P. N. Rudd, Y. Shao, X. Dai, H. Wei, J. Zhao, Y. Fang, Q. Wang, Y. Liu, Y. Deng, X. Xiao, Y. Feng and J. Huang, *Sci. Adv.*, 2019, **5**, eaav8925.
- 196 L. Zuo, H. Guo, D. W. DeQuilettes, S. Jariwala, N. De Marco, S. Dong, R. DeBlock, D. S. Ginger, B. Dunn, M. Wang and Y. Yang, *Sci. Adv.*, 2017, **3**, e1700106.
- 197 S. M. Jain, Z. Qiu, L. Häggman, M. Mirmohades, M. B. Johansson, T. Edvinsson and G. Boschloo, *Energy Environ. Sci.*, 2016, **9**, 3770–3782.
- 198 B. Chaudhary, A. Kulkarni, A. K. Jena, M. Ikegami, Y. Udagawa, H. Kunugita, K. Ema and T. Miyasaka, *ChemSusChem*, 2017, **10**, 2473–2479.
- 199 J. Chen, S. G. Kim, X. Ren, H. S. Jung and N. G. Park, *J. Mater. Chem. A*, 2019, **7**, 4977–4987.
- 200 Z. Wu, S. R. Raga, E. J. Juarez-Perez, X. Yao, Y. Jiang, L. K. Ono, Z. Ning, H. Tian, Y. Qi, Z. Wu, S. R. Raga, E. J. Juarez-Perez, Y. Jiang, L. K. Ono, Y. B. Qi, X. Yao, H. Tian and Z. Ning, *Adv. Mater.*, 2018, **30**, 1703670.
- 201 J. W. Lee, H. S. Kim and N. G. Park, *Acc. Chem. Res.*, 2016, **49**, 311–319.
- 202 S.-G. Ko, G.-I. Ryu, B. Kim, G.-J. Cha, J.-H. Ri, G.-S. Sonu and U.-C. Kim, *Sol. Energy Mater. Sol. Cells*, 2019, **196**, 105–110.
- 203 C. J. Dahlman, D. J. Kubicki and G. N. M. Reddy, *J. Mater. Chem. A*, 2021, **9**, 19206–19244.
- 204 H. Grüninger, M. Bokdam, N. Leupold, P. Tinnemans, R. Moos, G. A. De Wijs, F. Panzer

- and A. P. M. Kentgens, *J. Phys. Chem. C*, 2021, **125**, 1742–1753.
- 205 W. M. J. Fransen and A. P. M. Kentgens, *Solid State Nucl. Magn. Reson.*, 2019, **100**, 36–44.
- 206 A. Mishra, M. A. Hope, M. Almalki, L. Pfeifer, S. M. Zakeeruddin, M. Grätzel and L. Emsley, *J. Am. Chem. Soc.*, 2022, **144**, 15175–15184.
- 207 D. J. Kubicki, S. D. Stranks, C. P. Grey and L. Emsley, *Nat. Rev. Chem.*, 2021, **5**, 624–645.
- 208 J. V. Milić, J. Im, D. J. Kubicki, A. Ummadisingu, J. Seo, Y. Li, M. A. Ruiz-Preciado, M. I. Dar, S. M. Zakeeruddin, L. Emsley and M. Grätzel, *Adv. Energy Mater.*, 2019, **9**, 1900284.
- 209 T. A. S. Doherty, S. Nagane, D. J. Kubicki, Y.-K. Jung, D. N. Johnstone, A. N. Iqbal, D. Guo, K. Frohna, M. Danaie, E. M. Tennyson, S. Macpherson, A. Abfalterer, M. Anaya, Y.-H. Chiang, P. Crout, F. S. Ruggeri, S. M. Collins, C. P. Grey, A. Walsh, P. A. Midgley and S. D. Stranks, *Science*, 2021, **374**, 1598–1605.
- 210 D. J. Kubicki, D. Prochowicz, A. Pinon, G. Stevanato, A. Hofstetter, S. M. Zakeeruddin, M. Grätzel and L. Emsley, *J. Mater. Chem. A*, 2019, **7**, 2326–2333.
- 211 A. Q. Alanazi, D. J. Kubicki, D. Prochowicz, E. A. Alharbi, M. E. F. Bouduban, F. Jahanbakhshi, M. Mladenović, J. V. Milić, F. Giordano, D. Ren, A. Y. Alyamani, H. Albrithen, A. Albadri, M. H. Alotaibi, J. E. Moser, S. M. Zakeeruddin, U. Rothlisberger, L. Emsley and M. Grätzel, *J. Am. Chem. Soc.*, 2019, **141**, 17659–17669.
- 212 D. J. Kubicki, D. Prochowicz, E. Salager, A. Rakhmatullin, C. P. Grey, L. Emsley and S. D. Stranks, *J. Am. Chem. Soc.*, 2020, **142**, 7813–7826.
- 213 D. J. Kubicki, D. Prochowicz, A. Hofstetter, P. Péchy, S. M. Zakeeruddin, M. Grätzel and L. Emsley, *J. Am. Chem. Soc.*, 2017, **139**, 10055–10061.
- 214 E. A. Alharbi, A. Y. Alyamani, D. J. Kubicki, A. R. Uhl, B. J. Walder, A. Q. Alanazi, J. Luo, A. Burgos-Caminal, A. Albadri, H. Albrithen, M. H. Alotaibi, J. E. Moser, S. M. Zakeeruddin, F. Giordano, L. Emsley and M. Grätzel, *Nat. Commun.*, 2019, **10**, 3008.
- 215 M. H. Levitt, *Spin Dynamics: Basics of Nuclear Magnetic Resonance, Second Edition*, John Wiley & Sons Ltd, Chichester, England, 2008.
- 216 D. M. Grant, *eMagRes*, , DOI:10.1002/9780470034590.emrstm0074.
- 217 R. E. Wasylshen, *eMagRes*, , DOI:10.1002/9780470034590.emrstm0125.
- 218 S. E. Ashbrook and S. Wimperis, *eMagRes*, , DOI:10.1002/9780470034590.emrstm1073.
- 219 D. L. Bryce, *Solid-state NMR of quadrupolar nuclei: Selected new methods and applications*, Elsevier Ltd., 2022, vol. 107.
- 220 P. K. Madhu, *Isr. J. Chem.*, 2014, **54**, 25–38.
- 221 D. I. Hoult and R. E. Richards, *J. Magn. Reson.*, 1969, **24**, 71–85.
- 222 M. E. Smith, *eMagRes*, 2007, 1–14.
- 223 S. R. Hartmann and E. L. Hahn, *Phys. Rev.*, 1962, **128**, 2042–2053.

- 224 S. P. Brown, *Prog. Nucl. Magn. Reson. Spectrosc.*, 2007, **50**, 199–251.
- 225 I. Schnell, A. Lupulescu, S. Hafner, D. E. Demco and H. W. Spiess, *J. Magn. Reson.*, 1998, **133**, 61–69.
- 226 M. J. Bayro, M. Huber, R. Ramachandran, T. C. Davenport, B. H. Meier, M. Ernst and R. G. Griffin, *J. Chem. Phys.*, 2009, **130**, 114506.
- 227 J. Jeener, B. H. Meier, P. Bachmann and R. R. Ernst, *J. Chem. Phys.*, 2008, **71**, 4546.





# Chapter 2- Instability in formamidinium-based lead halide perovskites

---

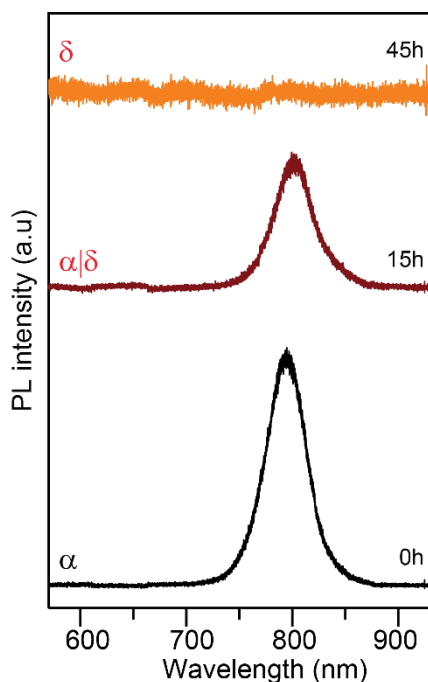
## 2.1. Formamidinium-based perovskites for high-performance photovoltaics

FAPbI<sub>3</sub> crystal structure was first reported by Kanatzidis *et al.* in 2013.<sup>1</sup> Perovskite formulations containing formamidinium (FA) cation exhibit enhanced thermal stability, paving the way towards stable and efficient formulations that are also among the highest performing perovskite solar cells today.<sup>2-7</sup> FAPbI<sub>3</sub> benefits from the most appropriate bandgap in terms of the theoretical Shockley-Queisser limit, leading to the highest PCE (calculated).<sup>8</sup> In this interest, research on hybrid perovskites is focused on addressing the long-term stability with regard to the stringent standards of damp heat test (International Electrotechnical Commission IEC-61215 stability assessment at 85 °C and 85% relative humidity in the air for over 1000 h).<sup>9,10</sup> These experiments have so far been conducted on the FA-based alloy compositions ((Cs, FA)Pb(Br, I)<sub>3</sub> and (Cs, MA, FA)PbI<sub>3</sub>) that are utilized in solar cells.<sup>11-13</sup> Recent years have seen a lot of effort spent on stabilizing the black( $\alpha$ )-FAPbI<sub>3</sub> phase using additive and interfacial engineering techniques that result in stable and efficient solar cells.<sup>2,14-21</sup> The transformational reactions and degradation of the reference compound with single-cation/single-anion compositions such as FAPbI<sub>3</sub> and FAPbBr<sub>3</sub> must first be understood in order to comprehend how to further enhance the stability of multi-cation/anion compositions. Therefore, much attention was given to these two compositions, with a particular interest in FAPbI<sub>3</sub>, as this composition is known to be less stable at near ambient temperatures.<sup>22,23</sup>

The instability in perovskites is thought to be influenced by the dynamic interface between organic cations and corner-sharing lead halide octahedra. This is further dependent on compositions and other external stimuli that cause structural degradation and point defects. At room temperature, the metastable black-colored cubic FAPbI<sub>3</sub> phase ( $\alpha$ ) transforms into the yellow-colored hexagonal phase ( $\delta$ ).<sup>24,25</sup> A free energy barrier of the order of hundreds of meV separates the various intermediate stages of  $\alpha \rightarrow \delta$  FAPbI<sub>3</sub> transition. This barrier causes a significant thermal hysteresis between the  $\delta \rightarrow \alpha$  transition at 350 K and the  $\alpha \rightarrow \delta$  transition at 290 K, which suggest, at least in part, how the  $\alpha$ -FAPbI<sub>3</sub> can be kinetically trapped at ambient

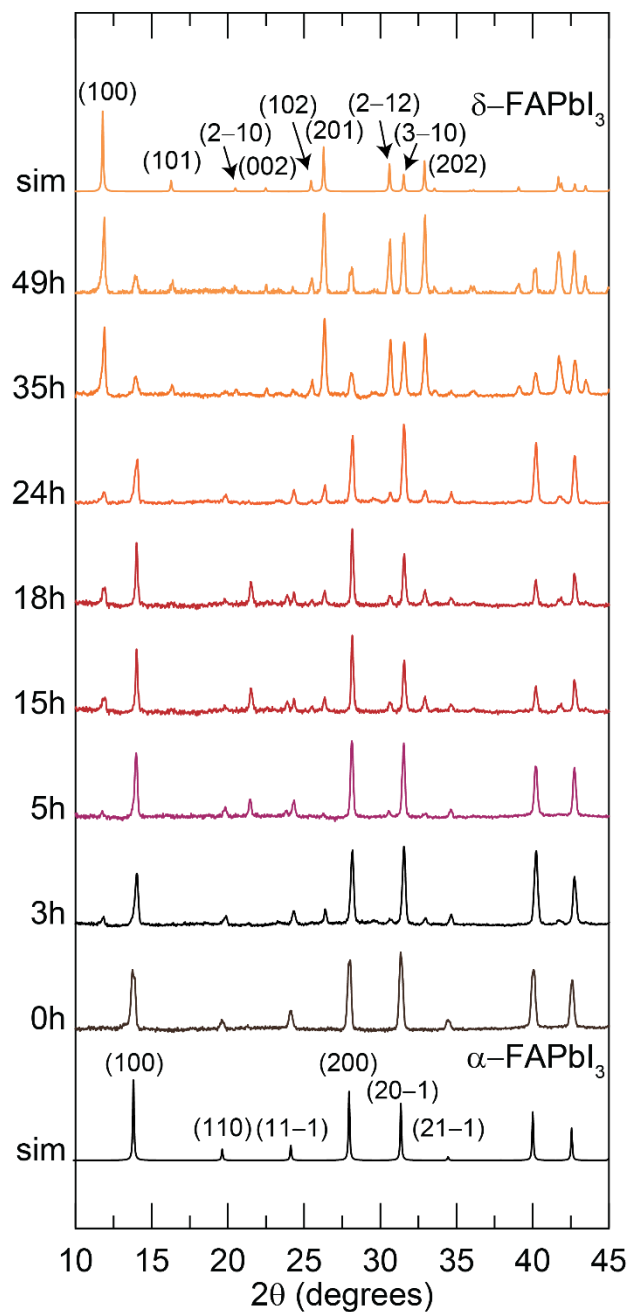
temperature.<sup>25</sup> It has been suggested that water intrusion at the susceptible grain boundaries can cause phase transformation.<sup>26</sup> However, a precise understanding of how water molecules induce a “catalysis-like” transformative reaction, i.e., how water reacts without directly integrating into the initial perovskite ( $\alpha$ ) or the final non-perovskite ( $\delta$ ) FAPbI<sub>3</sub> structures, and insight into the nature of the intermediate phase(s) is lacking, which necessitates further investigation. In addition, this reaction is reported to endure between hours to months to complete, as different studies report different synthetic, fabrication, and aging conditions.<sup>27–29</sup> Because this reaction contributes to the FAPbI<sub>3</sub> instability that rigorously affects the performance of solar cells, it is crucially important to understand the molecular origins of the phase transition, and kinetic and thermodynamic factors, which influence the degradation of hybrid perovskites.<sup>30</sup> Phase stability in FA-based and FA-rich perovskites has been investigated using a variety of *in-situ* and *ex-situ* characterization approaches.<sup>20,31,32</sup> Notably, photo thermal-induced resonance (PTIR with a spatial resolution of ~100 nm) and time-of-flight secondary ion mass spectrometry (TOF-SIMS) techniques have been employed to characterize the humidity-induced phase transformations and to probe surface and sub-surface compositions in FA-rich perovskites.<sup>33</sup>

As explained in Chapter 1, solid-state NMR (ssNMR) spectroscopy is a local probe that provides information on the structures and dynamics in hybrid perovskites with site-specificity: for example, ssNMR techniques have been used to gain insight into chemical doping, cation-ordering and dynamics, interfacial engineering, phase stability, and degradation products.<sup>34–40</sup> In this Chapter, the  $\alpha \rightarrow \delta$  FAPbI<sub>3</sub> transformative reaction triggered by water vapor is examined. The role of particle size, water vapor, and light in  $\alpha \rightarrow \delta$  FAPbI<sub>3</sub> phase transformation is investigated. The transformative reactions are characterized at different length scales ranging from  $\mu\text{m}$  to sub-nm using multiple analytical techniques. Specifically,  $\alpha \rightarrow \delta$  FAPbI<sub>3</sub> phase transformation reaction is characterized using photoluminescence (PL), X-ray diffraction (XRD), and 1D <sup>1</sup>H and <sup>207</sup>Pb MAS NMR spectroscopy techniques.



**Figure 2.1.** Photoluminescence spectra of FAPbI<sub>3</sub> as a function of moisture (85% RH) exposure time.

Figure 2.1 presents the PL spectra of FAPbI<sub>3</sub>. The PL studies of fresh FAPbI<sub>3</sub> material show a strong PL intensity peak at 790 nm, which is reduced after 15 h, suggesting the formation of an intermediate ( $\alpha|\delta$ - FAPbI<sub>3</sub>) phase (85% RH, 15 h of exposure). The lack of PL intensity after 45 h of exposure to moisture indicates the formation of a non-perovskite phase. To obtain structural insights into variation in the bulk emission response, XRD was implemented. XRD is a powerful technique to identify different phases present in a crystalline material. XRD patterns of the FAPbI<sub>3</sub> crystals were acquired at regular intervals of time to observe structural changes upon exposure to moisture (85% RH).



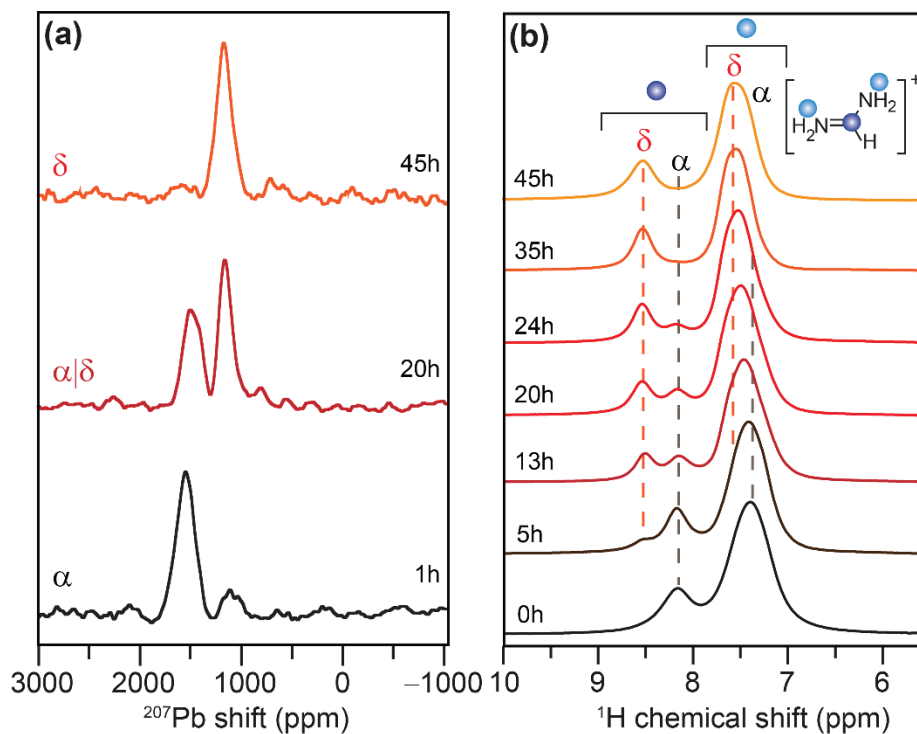
**Figure 2.2.** Powder XRD patterns of FAPbI<sub>3</sub> particles acquired before and after exposure to moisture at 85% RH for different durations as indicated, along with the simulated powder XRD patterns of  $\alpha$ - and  $\delta$ -FAPbI<sub>3</sub> of published crystal structures<sup>1,41</sup> using Mercury software.<sup>42</sup>

Figure 2.2 shows the cubic ( $\alpha$ ) to hexagonal ( $\delta$ ) phase transition in bulk crystals as observed by powder X-Ray Diffraction (XRD). For XRD, the close match in peak locations and intensities between the simulated (using Mercury software)<sup>42</sup> and experimental XRD patterns

indicates that the powders of the  $\alpha$  and  $\delta$  phases are phase-pure in bulk.<sup>1,41</sup> Interestingly, even after exposure to water vapor (85% RH) for more than 2 days,  $\alpha$ -FAPbI<sub>3</sub> is not fully transformed to  $\delta$ -FAPbI<sub>3</sub>, as suggested by (100) reflection.

To examine the cubic ( $\alpha$ ) to hexagonal ( $\delta$ ) phase transition more closely, high-field <sup>207</sup>Pb and <sup>1</sup>H ssNMR spectroscopy were employed. <sup>207</sup>Pb is a spin,  $I = \frac{1}{2}$  nuclei with a natural abundance of 22%, which allows facile detection in bulk perovskite samples. Faster longitudinal relaxation times,  $T_1$  associated with <sup>207</sup>Pb enables shorter experimental times. Specifically, the <sup>207</sup>Pb chemical shift is sensitive to Pb-I distances, apical Pb-I-Pb bond angles, and distortions in lead iodide octahedra.<sup>40,43-45</sup> 1D <sup>207</sup>Pb magic-angle spinning (MAS) spectra of black, intermediate, and yellow FAPbI<sub>3</sub> crystals exhibit different signals, whereby the signal centered at ~1556 ppm in the fresh FAPbI<sub>3</sub> corresponds to Pb atoms in cubic phase ( $\alpha$ -FAPbI<sub>3</sub>), as shown in Figure 2.3. The same material, upon exposure to moisture (85±5% RH, 20h), exhibited two well-resolved <sup>207</sup>Pb signals at ~1556 and ~1164 ppm, which are attributable to two distinct <sup>207</sup>Pb local environments in the cubic and hexagonal phases. After exposure to 85±5% humidity for 45 h, only the peak near ~1164 ppm is present, which confirms that this peak corresponds to the hexagonal phase. The low-frequency shift of <sup>207</sup>Pb peak near 1164 ppm indicates octahedral tilting, consistently with previous <sup>207</sup>Pb signal assignments.<sup>43-45</sup>

<sup>1</sup>H is spin,  $I = \frac{1}{2}$  nuclei with >99.9% of natural abundance and inherently high sensitivity. Limited resolution due to the small span of chemical shift (~20 ppm) and longer relaxation delays yielding prolonged experimental times are a few of the challenges associated with <sup>1</sup>H NMR. Yet, <sup>1</sup>H NMR is an ideal probe to analyze organic cations in perovskite. While the <sup>1</sup>H MAS NMR spectrum (Figure 2.3 (b)) of the black phase displays signals associated with -CH (8.1 ppm) and -(NH<sub>2</sub>)<sub>2</sub> groups (7.4 ppm) of FA<sup>+</sup> cations, additional signals corresponding to -CH (8.5 ppm) and -(NH<sub>2</sub>)<sub>2</sub> groups (7.6 ppm) of FA<sup>+</sup> cations in the yellow phase have emerged after 5 h of exposure to moisture and complete conversion into the yellow phase occurs after 45 h (~2 days). Trace amounts of surface-preabsorbed chemical species, such as trapped water, dioxygen, or precursors used in the synthesis process, may also contribute to the degradation process.<sup>46</sup> However, the species were not detected either in NMR or XRD experiments, suggesting that any such chemical residues are at minuscule concentrations if present.



**Figure 2.3.** 1D (a)  $^{207}\text{Pb}$  and (b)  $^1\text{H}$  MAS NMR spectra of fresh ( $\alpha$ -FAPbI<sub>3</sub>) and aged ( $\alpha|\delta$ -FAPbI<sub>3</sub>,  $\delta$ -FAPbI<sub>3</sub>) materials upon exposure to moisture (85% RH). Signals associated with  $\alpha$  and  $\delta$  polymorphs are indicated and color-coded as depicted in the schematic structure in (b). All  $^1\text{H}$  (900.2 MHz) and  $^{207}\text{Pb}$  (167.6 MHz) spectra were acquired with 50 kHz MAS.

Amongst the techniques mentioned so far, ssNMR spectroscopy enables one to provide quantitative insights into the distribution of organic cations in distinct phases. Notably, high-field  $^1\text{H}$  MAS NMR (21 T, 900 MHz) improves the resolution abilities to examine reaction kinetics of the  $\alpha \rightarrow \delta$  phase transformation, as discussed in the later section.

## 2.2. Understanding the kinetics of phase-transformation

To examine reaction kinetics, various models are reported in the literature: for solids, Johnson-Mehl-Avrami-Kolmogorov (JMAK) model is often used to analyze phase transformation kinetics, which is described by the equation as:  $y = 1 - \exp(-Bt^n)$ , where  $y$  is the fraction of the transformed phase, pre-factor  $B$  depends on the nucleation rate of the homogeneously distributed particles, and  $n$  is the Avrami exponent that depends on the dimensionality of the growth.<sup>47-52</sup> More sophisticated solid-state kinetic models have been reported.<sup>53,54</sup> It has also been shown that the Jander equation can model the kinetics of reactions in a powder form, which can be described as  $k_t/R^2 = [1-(1-\alpha)^{1/3}]^2$  where  $k$  is a rate constant,  $t$  is time,  $R$  is the initial radius of a solid particle, and  $\alpha$  is the fractional degree of reaction.<sup>55,56</sup> Some of these models postulate that the particles are spheres of the same size, which does not represent the FAPbI<sub>3</sub> particles used in this study. Although the defect concentration plays a crucial role in the  $\alpha \rightarrow \delta$  FAPbI<sub>3</sub> transformation, disentangling surface and bulk defects (sizes and shapes, stacking faults) and expressing defect concentrations in terms of Kroger-Vink notation is also relatively less straightforward. To this end, the kinetic behavior of the  $\alpha \rightarrow \delta$  FAPbI<sub>3</sub> phase transformations was analyzed by plotting normalized <sup>1</sup>H signal intensity of -CH (FA<sup>+</sup>) as a function of moisture exposure time. Different orders of reaction kinetics were compared: (i) Normalized <sup>1</sup>H signal intensities (for zeroth order), (ii) the natural logarithm of normalized <sup>1</sup>H signal intensity (for first/ pseudo-first-order), and (iii) the inverse of normalized <sup>1</sup>H signal intensity (for second-order) were plotted against time as shown in Figure 2.4. A better agreement of experimental integral values (dots) with the fitted data (red line) was observed for the first-order kinetics with the coefficient of determination  $R^2=0.995$ . Significant deviations are observed for both zeroth and second-order kinetics equations, as indicated by  $R^2$  in the range of 0.851-0.901. Although the surface area limited solid-state reactions are expected to follow the zeroth-order rate law, this analysis suggests that the  $\alpha \rightarrow \delta$  FAPbI<sub>3</sub> transformation reaction can be faithfully modelled to the (pseudo)first-order reaction kinetics. The (pseudo)first-order reaction kinetics suggests that the phase transformation is mediated by “liquid-like” transient species (described in later section). It can be hypothesized that the reaction rate depends on the surface wettability (water vapor concentration) and/or the particle exposure area, indicating the surface-induced dissolution of the black phase followed by precipitation of the yellow phase.



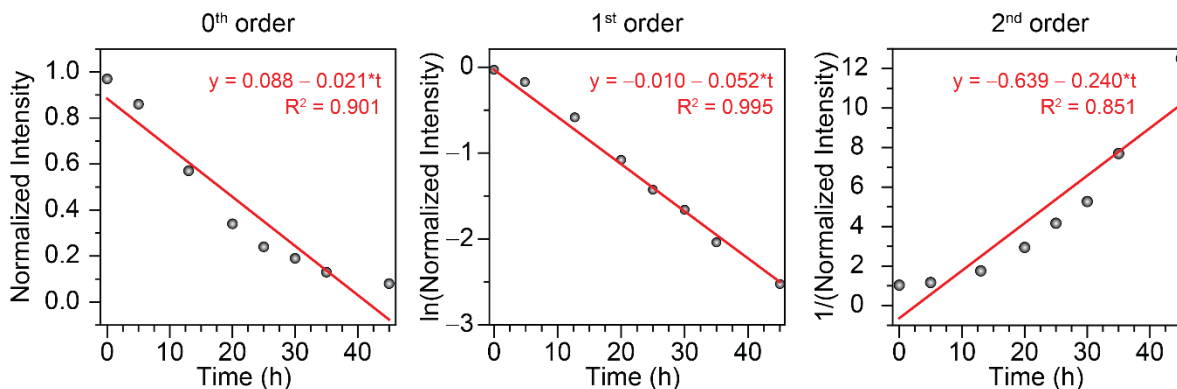


**Figure 2.4.** Normalized  $^1\text{H}$  (-CH) signal intensity of FA cations in  $\alpha\text{-FAPbI}_3$  plotted as a function of moisture (85% RH in the air) exposure time.

It is important to disentangle the distinct external stimuli to comprehensively understand the impact of each of them. In this section, the role of different external stimuli that influence the  $\alpha \rightarrow \delta$  FAPbI<sub>3</sub> phase transformation is discussed, namely, the influence of particle size, the extent of relative humidity, and light.

### 2.2.1. Influence of the particle size on moisture-induced phase transformation

To examine how different particle sizes react with water vapor,  $\alpha\text{-FAPbI}_3$  with different particle sizes was synthesized following the synthetic protocol of the previous report.<sup>57</sup> The SEM images acquired for larger and smaller particle sizes are shown in Figure 2.5, respectively. The acquired SEM images were then utilized to analyze particle size distribution for these particles. ImageJ software was used to estimate the particle sizes observed in the SEM images. Based on this analysis, a histogram (particle size vs. count) was generated and fitted with a Gaussian distribution function to extract the mean particle size and the standard deviation related to the particle size. The particle size distributions for small and large grains were found to be  $\approx 32 \pm 11$   $\mu\text{m}$  and  $\approx 74 \pm 41$   $\mu\text{m}$ , respectively.

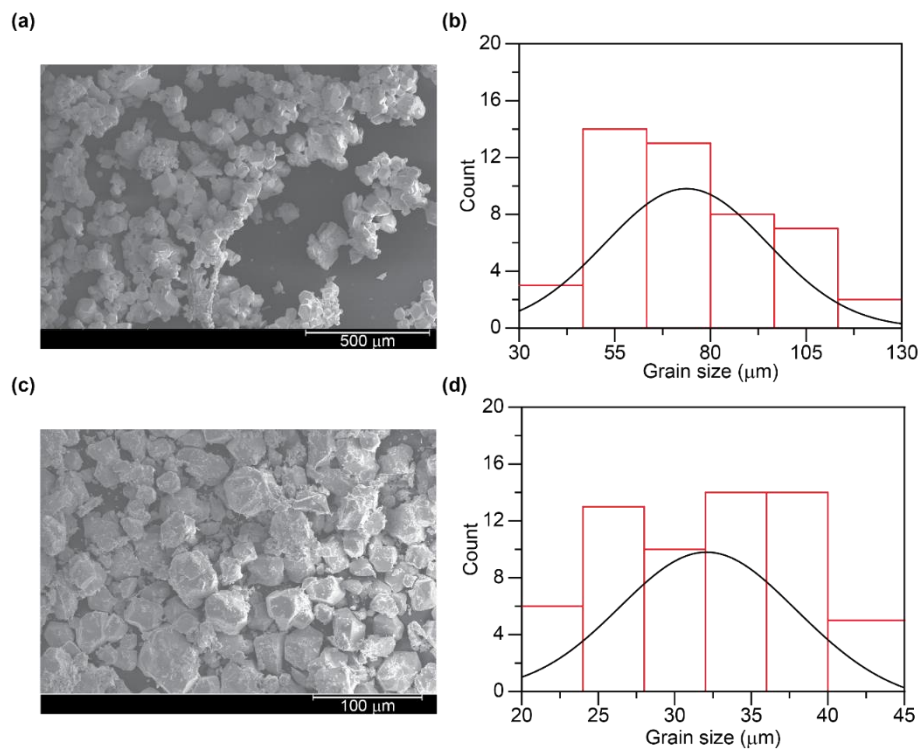


**Figure 2.5.** SEM images and particle-size distribution analyses of (a,b) large particles and (c,d) small particles, respectively.

For different distributions of particle sizes, the kinetics of  $\alpha \rightarrow \delta$  FAPbI<sub>3</sub> in the presence of water vapor (85% RH and laboratory illumination) are presented in Figure 2.6. As mentioned earlier, increased resolution of <sup>1</sup>H NMR enabled by high field and fast MAS allows one to measure and distinguish -CH sites in  $\alpha$ - and  $\delta$ - FAPbI<sub>3</sub> phases. By plotting the -CH peak integrals for these phases as a function of moisture exposure time, kinetic plots can be constructed. The kinetics plots enabled by <sup>1</sup>H MAS analysis are particularly useful for estimating the half-life times for different particle sizes. For large particles (40-100 μm), water vapor accelerates  $\alpha \rightarrow \delta$  FAPbI<sub>3</sub> transformation during the early state of hydration, having one-half of the material converted to  $\delta$ -FAPbI<sub>3</sub> phase within 14 h, which increases to over 90% in less than two days; however, the rest of the transformation takes much longer exposure time. Therefore, a complete  $\alpha \rightarrow \delta$  FAPbI<sub>3</sub> transformation is expected to take up to a week or longer. The sluggish transformation after prolonged exposure to moisture can be reasoned to sparse contact of water molecules with  $\alpha$ -phase as they are encapsulated by  $\delta$ -FAPbI<sub>3</sub> phase.

**Table 2.1.** Half-life decay times of black FAPbI<sub>3</sub> crystals upon exposure to moisture at 85% RH.

Particle size	Half-life time ( $t_{1/2}$ , h)
Large ( $\approx 74 \mu\text{m}$ )	13.3
Small ( $\approx 32 \mu\text{m}$ )	11.4

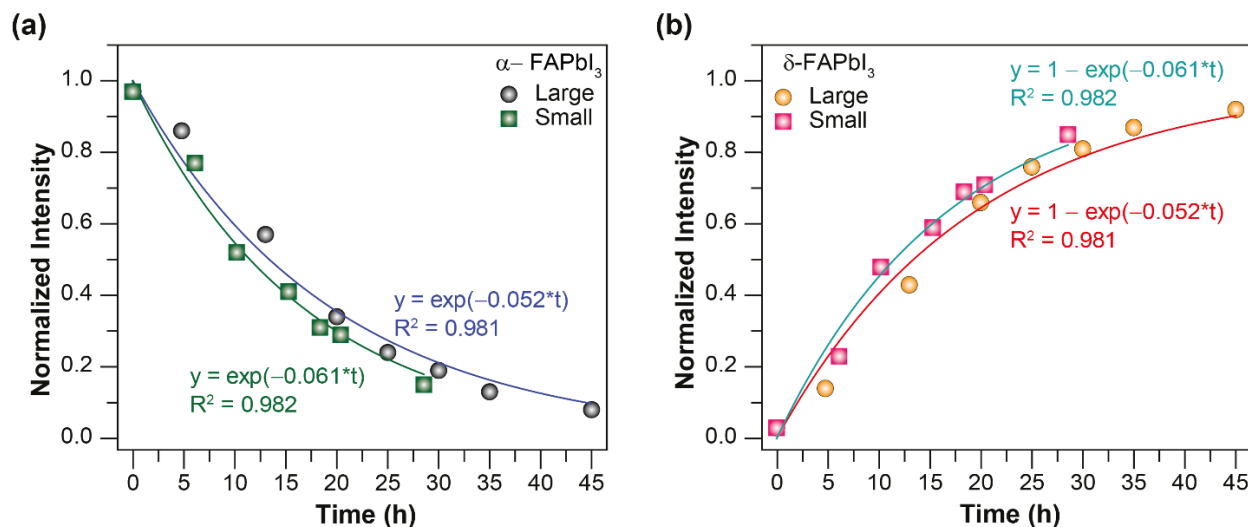


**Figure 2.6.** Comparison of (a)  $\alpha$ - and (b)  $\delta$ -FAPbI<sub>3</sub> phase transformation kinetics by means of <sup>1</sup>H signal intensity decay and build-up of -CH sites for small (20-40  $\mu\text{m}$ , squares) and large (40-100  $\mu\text{m}$ , dots) particles.

In contrast to the large particles, the small particles (20-40  $\mu\text{m}$ ) exposed to moisture (85% RH) shows an identical trend, but the rate and half-life decay are different. These results suggest that the phase transformation follows the same pathway, but the kinetic rate depends on grain sizes. This is due to the large surface area associated with the corner-shared lead octahedra in the black phase being available to interact with molecules. For different distributions of particle sizes, the estimated half-lives are given in Table 2.1, and their kinetic plots are shown in Figure 2.6. Subtleties in the half-lives  $\Delta t_{1/2} \sim 2$  h and rate constants  $\Delta k \sim 0.01 \text{ h}^{-1}$  are observed due to the partial overlap in the particle size distributions (Figure 2.5). To accurately calculate the half-lives of different particle sizes, kinetics studies of particles with uniform size and shape are required. One needs to take into account that the mere extrapolation of these kinetics plots to estimate the stability of FAPbI<sub>3</sub> thin films used in solar cells and other optoelectronic devices is less straightforward because the thin film stability depends on the surface and interfacial passivation

techniques and encapsulation strategies,<sup>58-67</sup> which requires further analysis at different humidity levels and different grain sizes with and without passivating agents. However, large grains benefit from enhanced stability.

### 2.2.2. The role of water vapor concentration on FAPbI<sub>3</sub> instability

The small particles (20-40  $\mu\text{m}$ ) of FAPbI<sub>3</sub> were used to study the role of humidity on  $\alpha \rightarrow \delta$  FAPbI<sub>3</sub> phase transformation. These particles were spread on a glass substrate and exposed to two different concentrations of water molecules in the air, i.e., 40% RH and 85% RH. The reaction kinetics of  $\alpha \rightarrow \delta$  FAPbI<sub>3</sub> transformation can be obtained by analyzing kinetic plots of FAPbI<sub>3</sub> obtained from <sup>1</sup>H MAS NMR spectroscopy. Although continuous exposure to water vapor at 85% RH leads to a  $\alpha \rightarrow \delta$  FAPbI<sub>3</sub> phase transformation in a few days with a rate constant of 0.042 h<sup>-1</sup> (Figure 2.7), the same material upon exposure to 40% RH leads to relatively slow transformation with a half-life decay time of 3327 h (~133 days), and the complete transformation is estimated to take up to a year by extrapolating the kinetics plots (Table 2.2). This is likely due to the much lower water vapor concentration as well as low ingress through the particle boundaries that are surface-covered by the yellow phase, thus leading to a sluggish phase transformation of black particles trapped in the sub-surfaces or reactive intra-grain interfaces in FAPbI<sub>3</sub> particles.

**Table 2.2** Half-life decay time associated with  $\alpha \rightarrow \delta$  phase FAPbI<sub>3</sub> transformation in the dark with varying relative humidity. The particle size distribution is 20-40  $\mu\text{m}$ .

Relative humidity (RH, %)	Half-life decay time ( $t_{1/2}$ , h)
85	16.5
40	3327

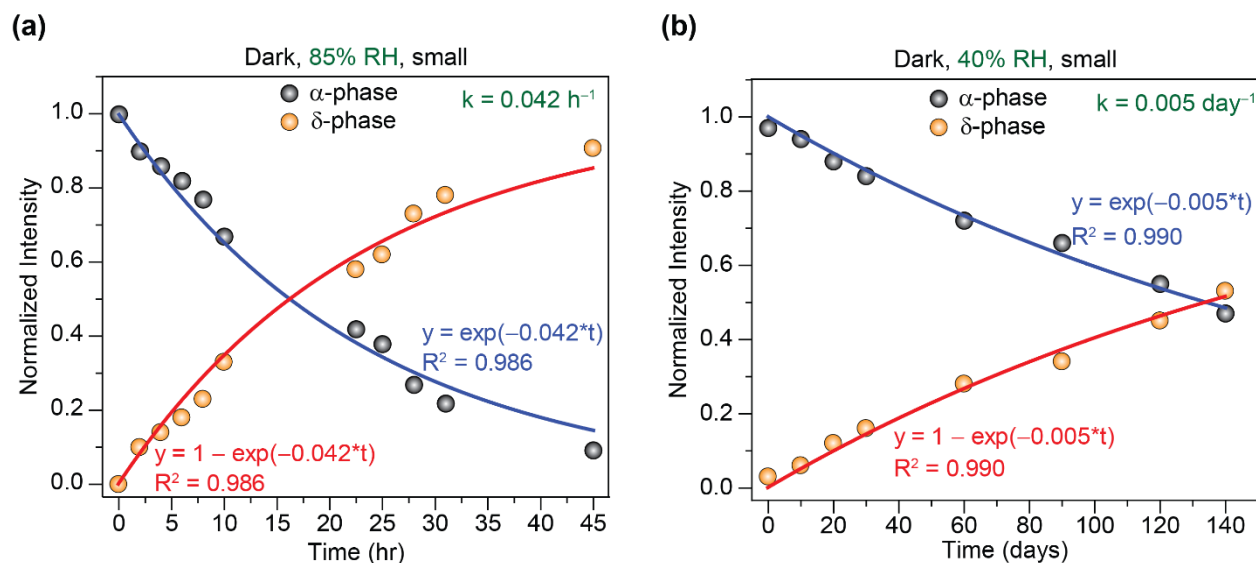


**Figure 2.7.** Kinetics plots of  $^1\text{H}$  signal intensity build-up of -CH sites of  $\text{FA}^+$  cations in  $\delta$ -FAPbI<sub>3</sub> and the simultaneous  $^1\text{H}$  signal intensity decay for the same sites in  $\alpha$ -FAPbI<sub>3</sub> as a function of exposure time to moisture in the dark at relative humidity levels of (a) 85% and (b) 40%.

### 2.2.3. Influence of light on $\alpha \rightarrow \delta$ FAPbI<sub>3</sub> phase transformation

Light illumination is another factor that could contribute to the  $\alpha \rightarrow \delta$  FAPbI<sub>3</sub> phase transformation. To test this, the moisture-induced (85% RH) degradation kinetics of small particles (20-40  $\mu\text{m}$ ) under dark and laboratory light illumination was studied. The presence of light illumination (500-750 Lux) accelerates  $\alpha \rightarrow \delta$  FAPbI<sub>3</sub> phase transformation, further reducing the half-lives from 16.5 h to 11.4 h (Figure 2.8). Interestingly, despite the excellent thermal stability of the FAPbI<sub>3</sub> black phase,<sup>68</sup> the large variation in the kinetics of  $\alpha \rightarrow \delta$  FAPbI<sub>3</sub> transformation is due to the deleterious effect of water molecules and light illumination combined.

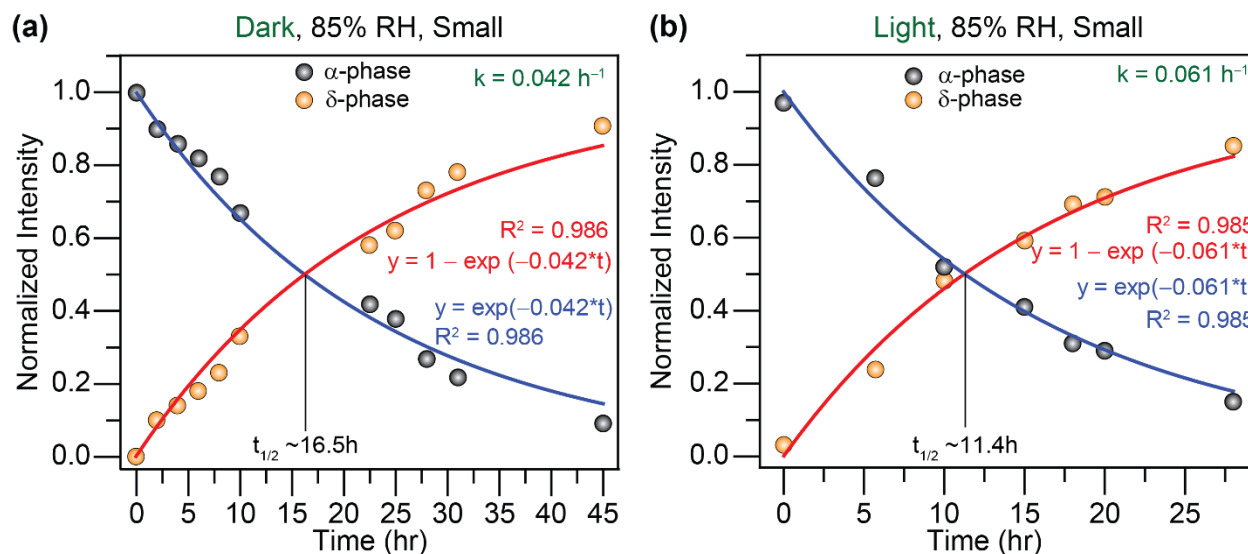


**Figure 2.8.** Kinetics plots of  $^1\text{H}$  signal intensity build-up of  $-\text{CH}$  sites associated with  $\delta\text{-FAPbI}_3$  and the simultaneous  $^1\text{H}$  signal intensity loss of the same sites in  $\alpha\text{-FAPbI}_3$  as a function of exposure time at 85% RH (a) in the absence and (b) presence of laboratory illumination. The phase transformation kinetics can be modeled to first-order rate kinetics, leading to the estimation of rate constants. For kinetic studies, smaller particles  $\alpha\text{-FAPbI}_3 \approx 32 \text{ nm}$  were used.

The most important takeaway from this study is that the impact of the concentration of water vapor and light illumination on the kinetics of transformative reactions can be disentangled and compared, among which relative humidity in the air seems to play a vital role in governing the environmental stability of optoelectronic devices. For example, it has been shown the  $\text{FAPbI}_3$ -based solar cell efficiency reduces to one-half of its initial value within a few hours upon exposure to moisture (40 °C, 70% RH, 5 h, AM 1.5G UV-light illumination), consistently with this study.<sup>69</sup> However, the stability of  $\text{FAPbI}_3$  and FA-rich thin films depends on various factors, such as deposition and annealing conditions, and the encapsulation and passivation strategies further exacerbate the situation. Therefore, an extrapolation of the kinetics plots of the crystals to the thin films in solar cells and other optoelectronic devices is less straightforward.

### 2.3. Insight into local interfacial structures of $\alpha\text{-}|\delta\text{-FAPbI}_3$

The fundamental pertinent question is how the phase transformation occurs at the particle boundaries, and how to resolve the interfacial structure of  $\alpha|\delta\text{-FAPbI}_3$  phase. It is important to investigate if there is significant mixing of cubic and hexagonal phases during the transformation

and any amorphous phases, as XRD shows only the reflections corresponding to  $\alpha$  and  $\delta$  phases. A schematic of  $\alpha \rightarrow \delta$  transformation with plausible intermediate products is shown in Figure 2.9. Much similar to the results presented in this Chapter, previous studies suggested that the temperature-induced transformations in lead halide perovskites occur through liquid-like interfaces.<sup>70</sup> The liquid-like behavior indeed facilitates surface reactions in order to modulate hybrid perovskite structures and properties.<sup>71</sup> Understanding the chemical nature of  $\alpha$ -|  $\delta$ -FAPbI<sub>3</sub> interface at short-length scales (< 1 nm) is expected to cast light on the surface/sub-surface reactions that cause perovskite degradation.

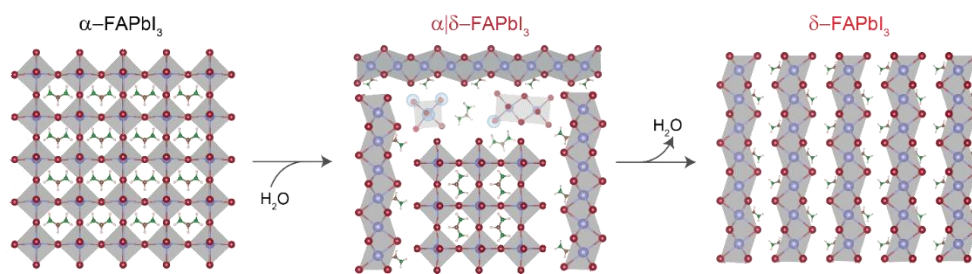
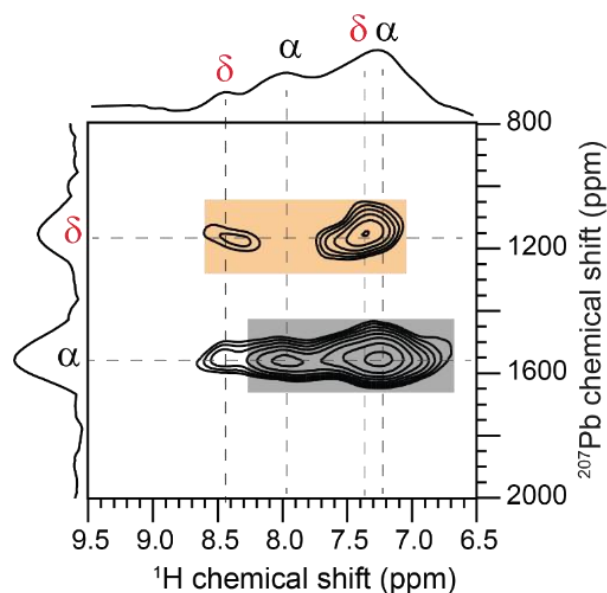


**Figure 2.9.** Schematic of  $\alpha \rightarrow \delta$  FAPbI<sub>3</sub> transformation upon exposure to moisture.

High-field NMR is suitable to resolve the local interfacial structures, for example, by analyzing the 2D <sup>207</sup>Pb-<sup>1</sup>H cross-polarization heteronuclear correlation (CP-HETCOR) spectrum of the  $\alpha$ | $\delta$ -FAPbI<sub>3</sub> phase (Figure 2.10) through-space sub-nanometer <sup>207</sup>Pb-<sup>1</sup>H proximities between FA<sup>+</sup> and PbI<sub>6</sub> octahedra at the organic-inorganic interface are distinguished and identified. Fast relaxation time associated with <sup>207</sup>Pb is advantageous as it is directly excited for <sup>207</sup>Pb  $\rightarrow$  <sup>1</sup>H CP transfer, followed by detection of the <sup>1</sup>H spins. 2D peaks at 1556 ppm (<sup>207</sup>Pb) and 7.4 and 8.1 ppm (<sup>1</sup>H) correspond to the organic-inorganic interface in  $\alpha$ -FAPbI<sub>3</sub>, and low-intensity signals between <sup>207</sup>Pb (1556 ppm) and <sup>1</sup>H (7.6 and 8.5 ppm) sites indicate that the through-space proximities between  $\alpha$ - and  $\delta$ -FAPbI<sub>3</sub> moieties. It can be hypothesized that the minuscule concentrations of [PbI<sub>6</sub>]<sup>4-</sup>, [Pb(H<sub>2</sub>O)<sub>6</sub>]<sup>2+</sup>, [PbI<sub>2</sub>.4H<sub>2</sub>O] [PbI<sub>3</sub>.3H<sub>2</sub>O]<sup>-</sup> [PbI<sub>4</sub>.2H<sub>2</sub>O]<sup>2-</sup> complexes may exist at the interface during the phase transformation, although undetected in both XRD and ssNMR experiments. In addition, these species are expected to have short lifetimes.

Insight into the organic-organic interface can be obtained by analyzing <sup>1</sup>H-<sup>1</sup>H correlation spectra. As mentioned in Chapter 1, the 2D <sup>1</sup>H-<sup>1</sup>H DQ-SQ correlation NMR experiment

provides information on through-space and dipolar coupled  $^1\text{H}$ - $^1\text{H}$  spin pairs within sub-nanometer ( $5 \text{ \AA}$ ) distances. In a 2D DQ-SQ correlation spectrum, the DQ frequencies are detected at the cumulative sum of the participating SQ frequencies of the dipolar coupled  $^1\text{H}$ - $^1\text{H}$  spin pairs. The enhanced resolution in the DQ dimension enables distinguishing and identifying the  $-\text{NH}_2$  and  $-\text{CH}$  sites in  $\alpha$ - and  $\delta$ -FAPbI<sub>3</sub> phases.



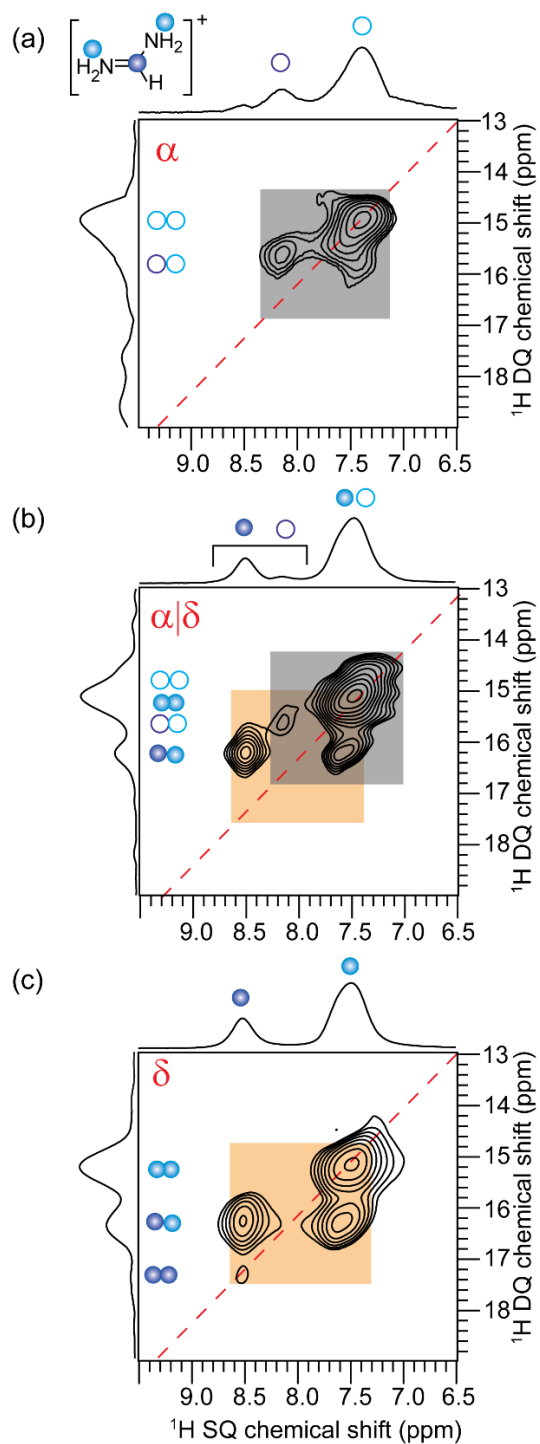
**Figure 2.10.** 2D  $^1\text{H}$ - $^{207}\text{Pb}$  CP-HETCOR spectra of  $\alpha|\delta$ -FAPbI<sub>3</sub> phase obtained after exposure to moisture (24 h, 85% RH), acquired with 6 ms of cross-polarization contact time, at room temperature, 18.8 T, 50 kHz MAS frequency.

Figure 2.11 shows the 2D  $^1\text{H}$ - $^1\text{H}$  DQ-SQ correlation NMR spectra of  $\alpha$ -FAPbI<sub>3</sub>,  $\alpha|\delta$ -FAPbI<sub>3</sub>, and  $\delta$ -FAPbI<sub>3</sub>. For the fresh FAPbI<sub>3</sub> (Figure 2.11a), the on-diagonal signal at  $7.4 + 7.4 = 14.8$  ppm corresponds to  $^1\text{H}$ - $^1\text{H}$  interactions in  $\text{NH}_2$  groups of  $\alpha$ -FAPbI<sub>3</sub>, and off-diagonal  $^1\text{H}$  DQ signal at  $8.2 + 7.4 = 15.6$  ppm is attributed to intramolecular  $\text{CH} \leftrightarrow \text{NH}_2$  dipole-dipole interactions in the same material. The intermolecular and intramolecular  $\text{CH} \leftrightarrow \text{NH}_2$  distances in the refined  $\alpha$ -FAPbI<sub>3</sub> crystal structure are  $\approx 4.54 \text{ \AA}$  and  $\approx 2.28 \text{ \AA}$ , such that both inter- and intramolecular  $^1\text{H}$ - $^1\text{H}$  dipole-dipole interactions are expected to contribute to the off-diagonal signal.<sup>41</sup> However, the on-diagonal DQ signal associated with  $-\text{CH}$  sites at  $8.2 + 8.2 = 16.4$  ppm is too weak to be detected due to the fast reorientational dynamics of  $\text{FA}^+$  cations in the cubic phase.



For an intermediate  $\alpha|\delta$ -FAPbI<sub>3</sub> phase (Figure 2.11b), two sets of DQ-SQ correlation peaks are detected. In addition to the above-discussed 2D correlation peaks associated with the cubic phase, a partially resolved <sup>1</sup>H DQ peak at  $7.6 + 7.6 = 15.2$  ppm and an additional DQ signal at  $7.6 + 8.6 = 16.2$  ppm corresponding to the intramolecular proximity between –NH<sub>2</sub> and –CH proton sites in the hexagonal FAPbI<sub>3</sub> phase are observed. It is noteworthy that there is no <sup>1</sup>H DQ peak corresponding to the through-space proximity between the <sup>1</sup>H sites in the cubic and hexagonal phases. These results suggest that the FA<sup>+</sup> cations in  $\alpha$  and  $\delta$ -FAPbI<sub>3</sub> materials are spatially phase segregated into different regions. In addition, the cations exhibit different dynamics and reorientational motions in the cubic and hexagonal phases that may partially or completely average out the dipole-dipole couplings between the FA<sup>+</sup> cations in these two phases, thus contributing to the loss of <sup>1</sup>H DQ signal intensity.

Upon further exposure to moisture (85% RH, 45 h), only the <sup>1</sup>H DQ signals corresponding to the yellow phase are observed (Figure 2.11c), whereby the on-diagonal signal at  $7.6 + 7.6 = 15.2$  ppm and  $8.6 + 8.6 = 17.2$  ppm arises due to proximate –NH<sub>2</sub> and –CH protons, respectively. In addition, an off-diagonal DQ signal at  $7.6 + 8.6 = 16.2$  ppm corresponding to the intramolecular CH $\leftrightarrow$ NH<sub>2</sub> dipolar interactions in  $\delta$ -FAPbI<sub>3</sub> is observed.



**Figure 2.11.** Solid-state 2D  $^1\text{H}$ - $^1\text{H}$  DQ-SQ correlation NMR spectra of (a) cubic  $\alpha$ -FAPbI<sub>3</sub>, (b) partially transformed  $\alpha|\delta$ -FAPbI<sub>3</sub>, and (c)  $\delta$ -FAPbI<sub>3</sub> materials acquired at 21 T ( $^1\text{H}$ , 900.2 MHz) and at 50 kHz MAS frequency. Signals corresponding to  $-\text{CH}$  and  $-\text{NH}_2$  are color-coded as depicted in the figure inset of (a).

Analysis of 2D  $^1\text{H}$ - $^1\text{H}$  spin-diffusion NMR provides further insight into the spatial distribution of  $\alpha$ - and  $\delta$ -FAPbI<sub>3</sub> phases. In a 2D  $^1\text{H}$  spin diffusion experiment, the  $^1\text{H}$  magnetization is allowed to exchange between dipole-dipole coupled  $^1\text{H}$ - $^1\text{H}$  sites. At a shorter mixing time, the magnetization exchange occurs between closely proximate protons, whereas longer mixing times enable the magnetization exchange to occur between the distant proton sites mediated through a network of dipolar coupled protons. It is noteworthy that these experiments extend the ssNMR length scales from sub-nanometer to up to a few hundreds of nanometers in rigid systems. Figure 2.12 shows the 2D  $^1\text{H}$ - $^1\text{H}$  spin-diffusion NMR spectra of  $\alpha$ -FAPbI<sub>3</sub>,  $\alpha|\delta$  FAPbI<sub>3</sub>, and  $\delta$ -FAPbI<sub>3</sub> with 1 ms and 200 ms. In a 2D  $^1\text{H}$ - $^1\text{H}$  spin-diffusion spectra acquired with  $\tau_{\text{mix}} = 1$  ms (Figure 2.12a-c), only diagonal peaks are observed that are identical to the signals in the 1D  $^1\text{H}$  NMR spectrum, meaning this mixing time is not sufficient to allow magnetization exchange between the different proton sites to occur in FAPbI<sub>3</sub>. In the 2D spectra acquired with  $\tau_{\text{mix}} = 200$  ms, off-diagonal peaks have emerged, which evidence the exchange of magnetization between different proton sites. The off-diagonal peaks in Figure 2.12d-f are attributable to spin magnetization exchange between  $-\text{CH}$  and  $-(\text{NH}_2)_2$  sites in  $\text{FA}^+$  cations within the  $\alpha$ -FAPbI<sub>3</sub> and within the  $\delta$ -FAPbI<sub>3</sub> phase. However, the off-diagonal peaks between  $-\text{CH}$  ( $\alpha$ -FAPbI<sub>3</sub>) and  $-\text{CH}$  ( $\delta$ -FAPbI<sub>3</sub>) are not detected even at longer mixing times (Figure 2.12e,  $\tau_{\text{mix}} = 200$  ms), indicating that there is no  $^1\text{H}$  spin magnetization exchange between  $\text{FA}^+$  cations in the black and yellow phases. These results corroborate the  $^1\text{H}$  DQ-SQ measurements that showed heterogeneous interfaces between the black and yellow regions of FAPbI<sub>3</sub> upon exposure to moisture. These results further suggest that the plausible flexible, heterogeneous, liquid-like interface between the black and yellow phase at the grain or sub-grain boundaries caused by surface wetting leads to a (pseudo)first-order reaction kinetics rather than a solid-to-solid transformation.<sup>72</sup> This calls for the need for investigation of the dynamic behavior of organic cations in the  $\alpha|\delta$ -FAPbI<sub>3</sub> phase.

Site-specific dynamics of organic cations have been previously studied by ssNMR and other complementary techniques.<sup>34,38,73-77</sup> This study employs  $^2\text{H}$  NMR spectroscopy lineshape analysis and quadrupolar splitting to gain insight into the dynamics aspects of the  $\text{FA}^+$  cations, such as fast and slow reorientational motions, which occur at much faster timescales (fs-ps) compared to the  $^1\text{H} \leftrightarrow ^2\text{H}$  isotopic exchange process that occurs at much slower time scales seconds to several hours.<sup>78,79</sup>

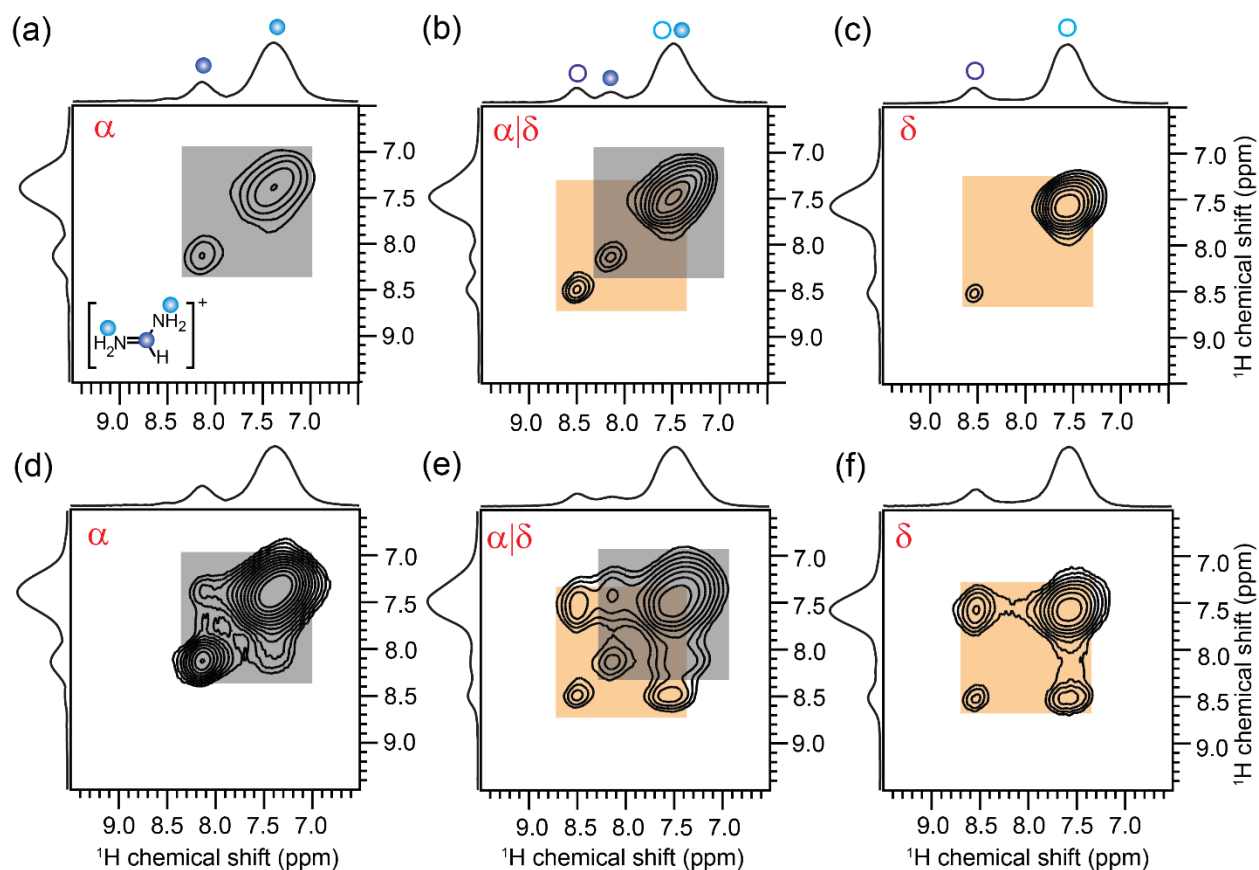


**Figure 2.12.** Solid-state 2D  $^1\text{H}$ - $^1\text{H}$  spin-diffusion NMR spectra of (a,d) fresh and aged (b,c,e,f) FAPbI<sub>3</sub> materials acquired at 21 T ( $^1\text{H}$  900.2 MHz) with 50 kHz MAS. Signals corresponding to  $-\text{CH}$  and  $-\text{NH}_2$  sites are color-coded as depicted in the figure inset of (a). (a-c) are acquired with 1 ms of mixing time, and (d-f) are acquired with 200 ms of spin diffusion time.

An *in situ* deuteration strategy was employed that enabled deuteration of FA<sup>+</sup> cations during the phase transformation. The deuteration of FA<sup>+</sup> cations in  $\alpha$ -FAPbI<sub>3</sub> was achieved by placing it in a dark humidity chamber at ambient temperature along with a saturated solution of KCl in D<sub>2</sub>O. Labile hydrogen atoms of NH<sub>2</sub> groups in FA cations exchange with deuterium sites in partially transformed  $\alpha$ -FAPbI<sub>3</sub>. Insight into the dynamics of FA<sup>+</sup> cations in perovskite and non-perovskite phases was then obtained by analyzing  $^2\text{H}$  NMR spectra of fresh and aged FAPbI<sub>3</sub> materials (Figure 2.13), whereby  $^2\text{H}$  lineshape is sensitive to the local mobility and dynamic nature of the local ND<sub>2</sub> groups in black and yellow phases, and surface adsorbed D<sub>2</sub>O molecules.<sup>80–82</sup>

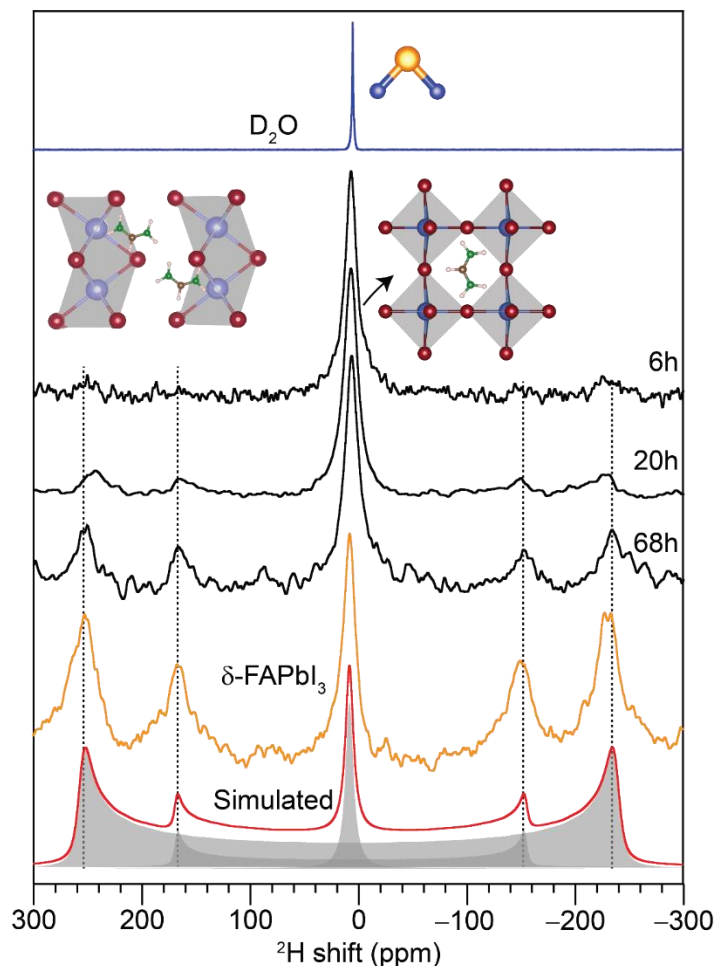
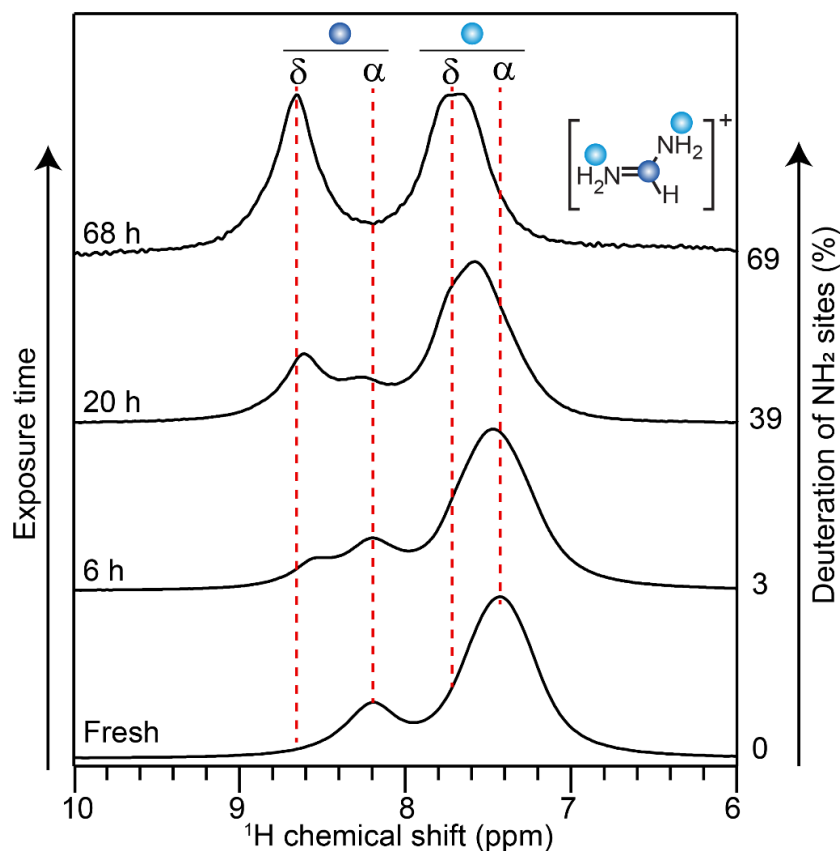


**Figure 2.13.** Solid-state static 1D  $^2\text{H}$  NMR spectra of  $\text{FAPbI}_3$  acquired at room temperature as a function of exposure time to  $\text{D}_2\text{O}$  vapor (85% RH) together with the 1D  $^2\text{H}$  NMR spectrum of liquid  $\text{D}_2\text{O}$  acquired under the same conditions. A static  $^2\text{H}$  NMR spectrum of control  $\delta\text{-FAPbI}_3$  material obtained after exposure to  $\text{D}_2\text{O}$  for 48h is acquired and compared. All spectra were acquired at 18.8 T ( $^2\text{H} = 122.8$  MHz) and at room temperature.

The 1D  $^2\text{H}$  spectrum of  $\text{FAPbI}_3$  treated with  $\text{D}_2\text{O}$  (6 h, 85% RH) shows a peak at  $\sim 7.4$  ppm corresponding to  $\text{ND}_2$  sites in the black phase of  $\text{FA}^+$  cations as well as a minuscule concentration of  $\text{D}_2\text{O}$  molecules ingress at the grain boundaries, both of these undergo fast reorientational motions at the NMR time scales leading to a narrow signal. To test this, a  $^2\text{H}$  spectrum of liquid  $\text{D}_2\text{O}$  was acquired and compared, which showed a narrow signal at  $\sim 4.8$  ppm due to the fast reorientational motion of  $\text{D}_2\text{O}$  molecules. A particularly interesting feature is that the same material after exposure to  $\text{D}_2\text{O}$  for 20 h displays different quadrupolar splittings

(detected at much higher intensities for the FAPbI<sub>3</sub> after 68h exposure to D<sub>2</sub>O), which are simulated to obtain the quadrupolar constants ( $C_Q$ ) of 53 and 81 kHz. This is in accord with the <sup>2</sup>H NMR spectra of the control sample: a neat  $\delta$ -FAPbI<sub>3</sub> material after exposure to D<sub>2</sub>O displays identical lineshape and quadrupolar splitting. It can be reasoned that these two different quadrupolar splittings correspond to relatively slow re-orientational motion of ND<sub>2</sub> sites of FA<sup>+</sup> cations in the yellow phase; one that corresponds to ND<sub>2</sub> sites facing toward the face-shared lead octahedra at the organic-inorganic interfaces, and the other corresponds to the ND<sub>2</sub> sites at the organic-organic (FA<sup>+</sup>/FA<sup>+</sup>) interface in between the chain-like lead octahedra. This suggests that the phase transformation occurs at the grain boundaries of the black phase triggered by the D<sub>2</sub>O ingress that transforms into the yellow phase, whereby the trapped water molecules (if any) and FA<sup>+</sup> cations in the black FAPbI<sub>3</sub> particles at sub-surface layers undergo relatively fast reorientational motion than the NMR timescales and are likely to exhibit a flexible “liquid-like” interface. This is also consistent with the first-order reaction kinetics.

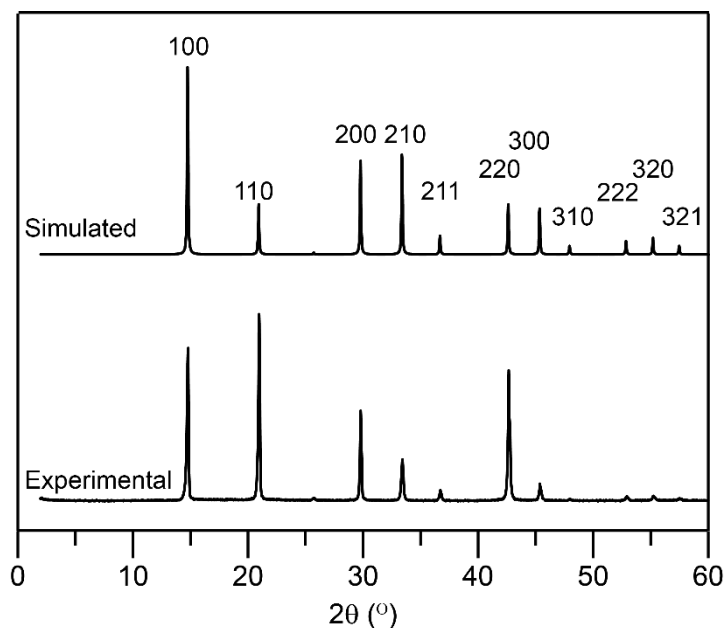
The degree of deuteration in the converted  $\delta$ -FAPbI<sub>3</sub> phase can be estimated based on the quantitative 1D <sup>1</sup>H NMR analysis. Upon exposure to D<sub>2</sub>O, the  $\alpha$ | $\delta$ -FAPbI<sub>3</sub> phase forms as shown in 1D <sup>1</sup>H NMR spectra (Figure 2.14). Starting from the fresh  $\alpha$ -FAPbI<sub>3</sub>, a 20 h of exposure to moisture (D<sub>2</sub>O) yields nearly 39 % of deuterated FA<sup>+</sup> cations, and prolonged exposure of about 68 h leads to 69 % of the FA<sup>+</sup> cations deuterated, and the signals corresponding to  $\delta$ -FAPbI<sub>3</sub> are well-resolved. Signal deconvolution of the 1D <sup>1</sup>H NMR spectrum can provide insights into the level of deuteration. Knowing the chemical shift from 1D <sup>1</sup>H and 2D <sup>1</sup>H-<sup>1</sup>H NMR experiments corresponding to distinct sites in  $\alpha$ - and  $\delta$ -FAPbI<sub>3</sub>, signal deconvolution is more reliable. Each of the spectra in Figure 2.14 was deconvoluted to estimate the extent of deuteration as a function of moisture exposure (D<sub>2</sub>O) time.



**Figure 2.14.** 1D  $^1\text{H}$  MAS NMR spectra indicate the  $\alpha$ - $\delta$  FAPbI<sub>3</sub> transformation upon exposure to D<sub>2</sub>O at 85% RH. Signal intensity loss associated with NH<sub>2</sub> sites (7-8 ppm) indicates the on-the-fly deuteration of NH<sub>2</sub> sites of FA<sup>+</sup> cations.

#### 2.4. The role of halide ions in the stability of FAPbX<sub>3</sub>

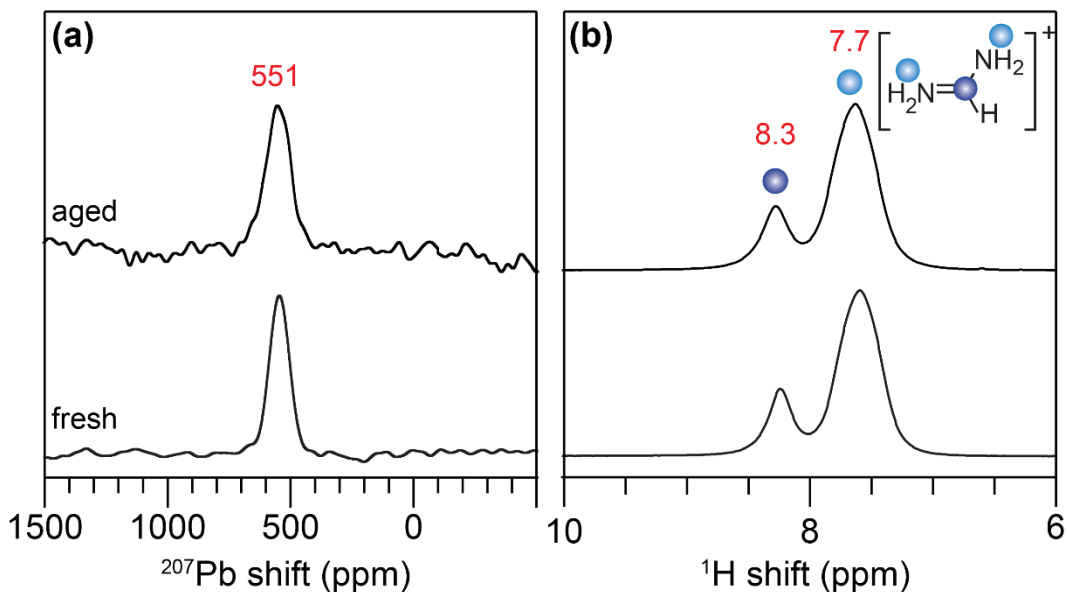
In contrast to FAPbI<sub>3</sub>, FAPbBr<sub>3</sub> exhibits enhanced moisture stability for several weeks, as revealed by combined XRD and ssNMR analysis. The experimental and simulated XRD powder patterns, shown in Figure 2.15, indicate the phase purity in bulk. The formability and stability of hybrid perovskites depend on the Goldschmidt tolerance factor ( $t$ ), with  $t$  values between 0.80 and 1.00 favoring the formation of cubic perovskite structures: FAPbI<sub>3</sub> and FAPbBr<sub>3</sub> exhibited  $t$  values of  $\sim 0.88$  and  $\sim 0.90$ , leading to different phase stabilities.<sup>83-85</sup> A theoretical study corroborates that the FAPbBr<sub>3</sub> shows a greater extent of hydrogen bonding interactions than FAPbI<sub>3</sub>.<sup>86</sup>



**Figure 2.15.** Powder X-ray diffraction patterns of experimental and simulated FAPbBr<sub>3</sub>.

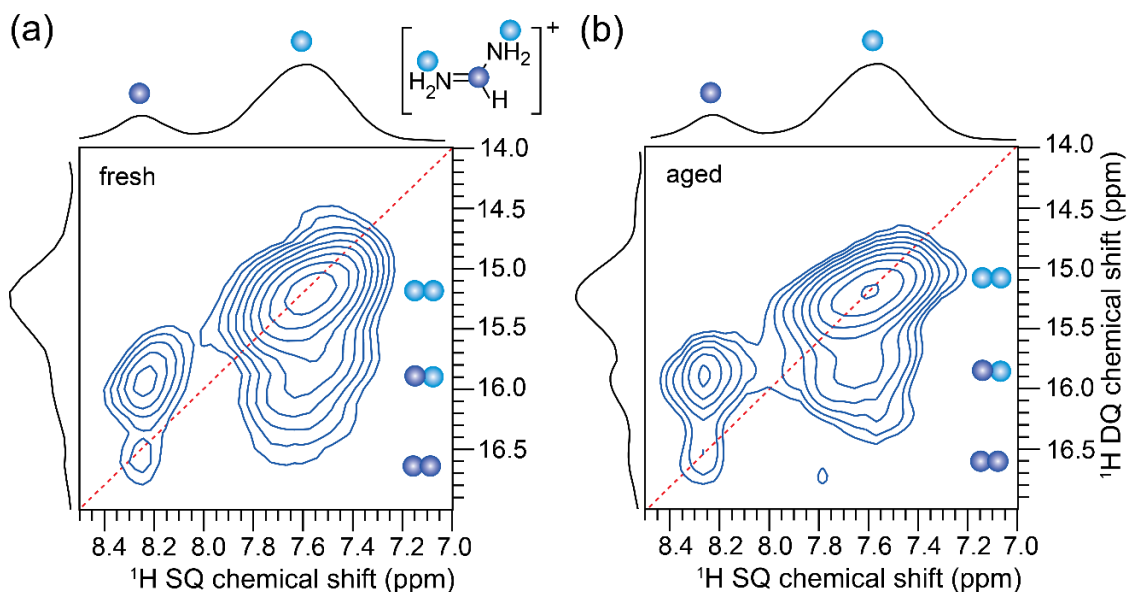
The high field <sup>1</sup>H MAS NMR data of FAPbI<sub>3</sub> and FAPbBr<sub>3</sub> confirms this trend: for FAPbBr<sub>3</sub>, the <sup>1</sup>H peaks are observed at higher frequencies (Figure 2.16 NH<sub>2</sub> and CH peaks at 7.7 and 8.3 ppm), indicating stronger hydrogen bonding interactions than the α-FAPbI<sub>3</sub> that displays peaks at lower frequencies (NH<sub>2</sub> and CH peaks at 7.4 and 8.1 ppm). 1D <sup>207</sup>Pb MAS spectrum (Figure 2.16a) of fresh FAPbBr<sub>3</sub> shows a <sup>207</sup>Pb signal centered at ~551 ppm, corresponding to Pb atoms in a cubic phase,<sup>87</sup> and this signal after exposure to moisture (85% RH, 7 days) retained its position, suggesting that the moisture has little impact on the local structures of lead octahedra.





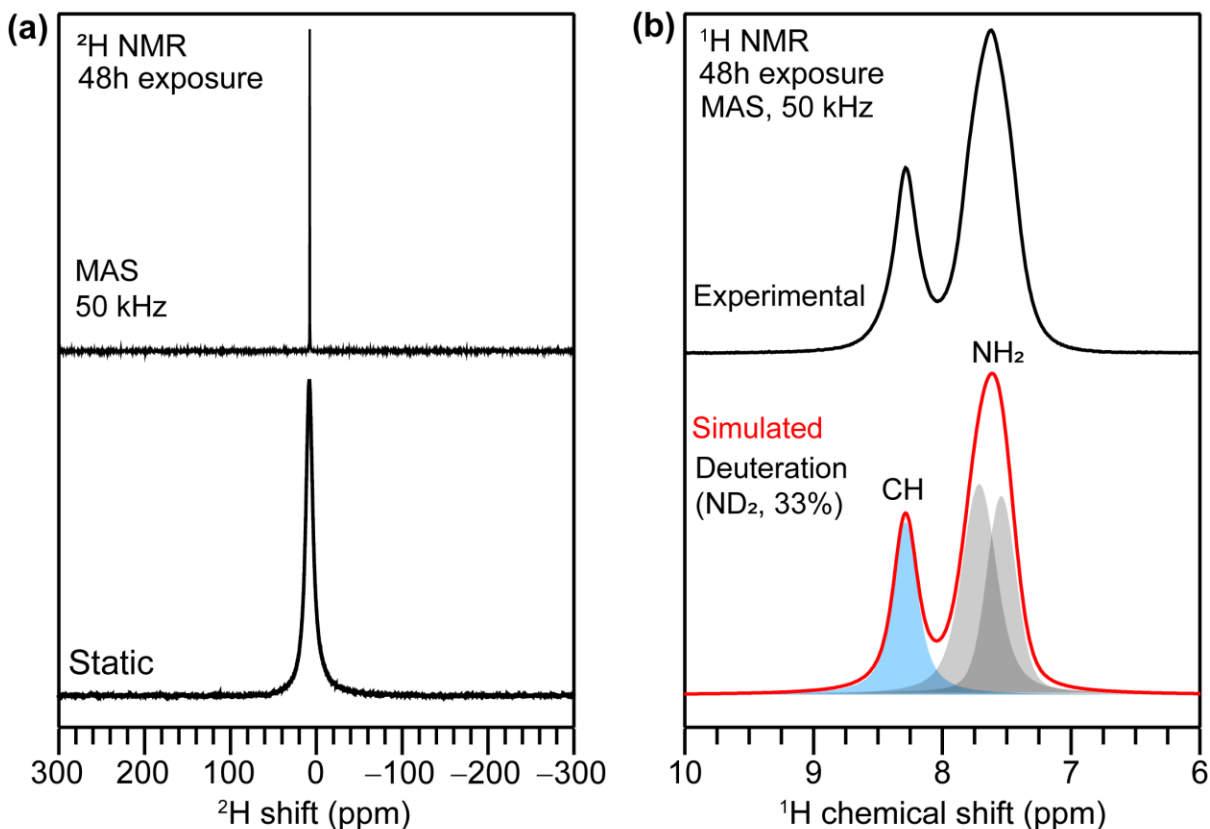
**Figure 2.16.** 1D (a)  $^{207}\text{Pb}$  and (b)  $^1\text{H}$  NMR spectra of fresh and aged (7 days, 85% RH) FAPbBr<sub>3</sub> acquired at 21.1 T, 50 kHz MAS

Figure 2.17 shows the 2D  $^1\text{H}$ - $^1\text{H}$  DQ-SQ correlation NMR spectra of fresh and aged FAPbBr<sub>3</sub>. For the fresh FAPbBr<sub>3</sub>, the on-diagonal signal at  $7.6 + 7.6 = 15.2$  ppm corresponds to  $^1\text{H}$ - $^1\text{H}$  interactions in NH<sub>2</sub> groups of FAPbBr<sub>3</sub>, and off-diagonal  $^1\text{H}$  DQ signal at  $8.3 + 7.6 = 15.9$  ppm is attributed to intramolecular CH $\leftrightarrow$ NH<sub>2</sub> dipole-dipole interactions in the same material. Moreover, the on-diagonal DQ signal associated with -CH sites at  $8.3 + 8.3 = 16.6$  ppm is observed, unlike in the case of FAPbI<sub>3</sub>, where the same signal was too weak to be detected due to fast reorientational dynamics of FA<sup>+</sup> cations in the cubic phase. Upon exposing this material to moisture (85% RH, 7 days), there are no significant changes observed in the 2D  $^1\text{H}$ - $^1\text{H}$  DQ-SQ correlation NMR spectrum of FAPbBr<sub>3</sub>, as shown in Figure 2.17b. Identical 2D  $^1\text{H}$ - $^1\text{H}$  DQ-SQ spectral patterns of fresh and aged (85% RH, 7 days) powders further confirmed the enhanced environmental stability of FAPbBr<sub>3</sub> material.



**Figure 2.17.** (a) Solid-state 2D  $^1\text{H}$ - $^1\text{H}$  DQ-SQ NMR correlation spectrum of fresh and aged ( $85 \pm 5\%$  RH, 7 days) FAPbBr<sub>3</sub> acquired at 21 T ( $^1\text{H}$  900 MHz) and at 50 kHz MAS frequency. The corresponding skyline projections are shown along the top  $^1\text{H}$  SQ horizontal and  $^1\text{H}$  DQ vertical axes, respectively. Correlated signal intensities originating from dipolar-coupled  $^1\text{H}$ - $^1\text{H}$  pairs are depicted by colored circles.

Figure 2.18a compares the static 1D  $^2\text{H}$  NMR, and  $^1\text{H}$  MAS NMR spectra of FAPbBr<sub>3</sub> acquired after exposing the material to D<sub>2</sub>O vapor for a period of 48 h. The 1D static  $^2\text{H}$  NMR spectrum (Figure 2.18a) shows a signal centered at 7.7 ppm attributed to the -ND<sub>2</sub> sites in FAPbBr<sub>3</sub>, while the  $^2\text{H}$  MAS NMR spectrum displays a narrow signal as the anisotropic contributions are averaged out, leading to an accurate measurement of the isotropic  $^2\text{H}$  NMR chemical shift. Deconvolution analysis of the 1D  $^1\text{H}$  MAS NMR spectrum (Figure 2.18b) has been used to determine the extent of deuteration. The extent of deuteration was examined by measuring and comparing the peak integral values for NH<sub>2</sub> and CH sites of FA<sup>+</sup> cations. Based on this analysis, it is estimated that 33% of -NH<sub>2</sub> sites of FAPbBr<sub>3</sub> are deuterated upon exposure to D<sub>2</sub>O for 48h.



**Figure 2.18.** Solid-state 1D (a)  $^2\text{H}$  NMR spectra recorded under static (bottom) and MAS (top) conditions, and (b)  $^1\text{H}$  MAS NMR spectra of  $\text{FAPbBr}_3$  acquired after exposure to  $\text{D}_2\text{O}$  for 48 h (top) and its line shape deconvolution analysis (bottom), suggesting 33% of deuteration of  $\text{NH}_2$  sites.

## 2.5. Instability in FA-rich formulations

Compositional engineering with regards to molecular /atomic size (hence, the tolerance factor) and their physical properties. It is of particular interest to understand the moisture stability of extensively explored FA-rich formulations such as  $\text{Cs}_{0.05}(\text{MA}_{0.17}\text{FA}_{0.83})_{0.95}\text{Pb}(\text{Br}_{0.17}\text{I}_{0.83})_3$  ( $\text{CsMAFA}$ ), which is among the most efficient formulation for high-performing single-junction PSCs<sup>88</sup> as well as tandem architecture with silicon with certified PCE of over 29%.<sup>89</sup> The introduction of  $\text{Cs}^+$  and  $\text{MA}^+$  cations is expected to bring the tolerance factor value to a favorable range to form a corner-sharing structure.

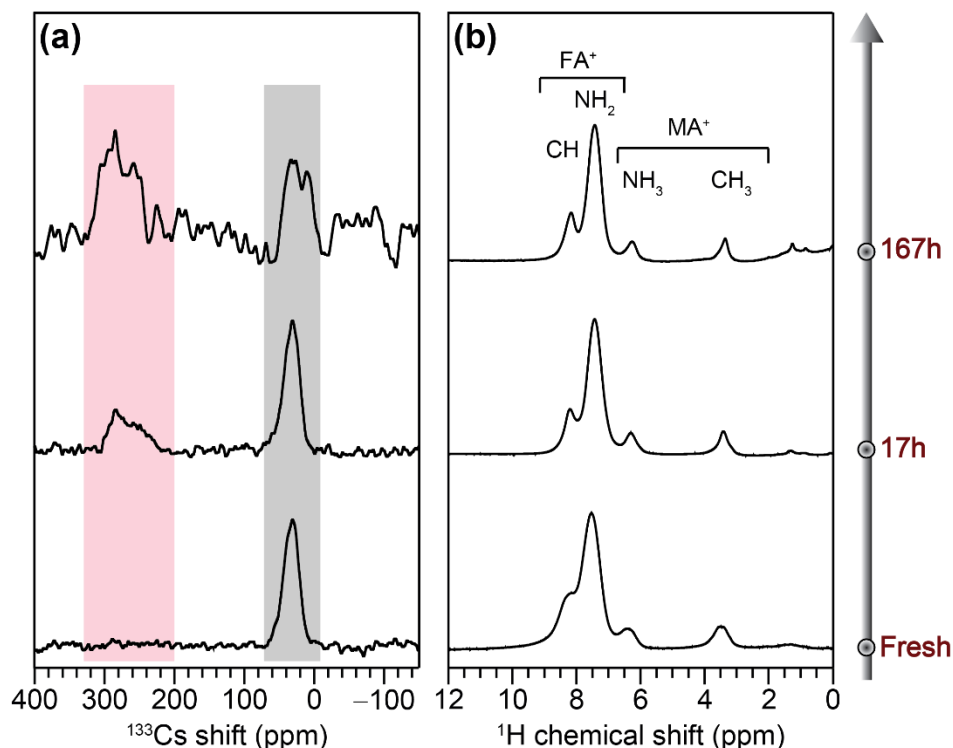


**Figure 2.19.** Solid-state 1D MAS NMR spectra of CsMAFA acquired at 18.8 T, room temperature: (a)  $^{133}\text{Cs}$  (b)  $^1\text{H}$  MAS NMR spectra before and after exposure to moisture at 85% RH. The black and magenta vertical bands indicate the Cs ions associated with perovskite and non-perovskite phases.

A handful of studies have investigated the A-site cation distribution in this formulation, in particular  $\text{Cs}^+$  ions. NMR spectroscopy is a suitable probe to investigate the moisture stability and the different distributions of  $\text{Cs}^+$  ions. Due to high sensitivity (100% natural abundance), spin  $I = 7/2$  that exhibits quadrupolar interactions and sufficiently large chemical shift dispersion,  $^{133}\text{Cs}$  is an excellent probe to understand local structures in the Cs-based perovskites. Here,  $^{133}\text{Cs}$  and  $^1\text{H}$  sites are examined to unravel the role of moisture on the morphology and stability of CsMAFA thin film before and after exposure to moisture. For the pristine CsMAFA, the  $^{133}\text{Cs}$  signal at  $\sim 30$  ppm is ascribed to the  $\text{Cs}^+$  in the CsMAFA perovskite framework, as shown in Figure 2.19a. The signal is displaced from the shifts reported in the literature due to variations in the local chemical environment in terms of neighboring halide and organic cation.<sup>90</sup> For moisture-exposed CsMAFA (85% RH for  $\sim 7$  days),  $^{133}\text{Cs}$  MAS NMR spectrum exhibits a distribution of peaks centered at 286 ppm, which can be attributed to the extra framework  $\text{Cs}^+$  cations due to the formation of Cs-based inorganic salts as plausible byproducts.<sup>91</sup>

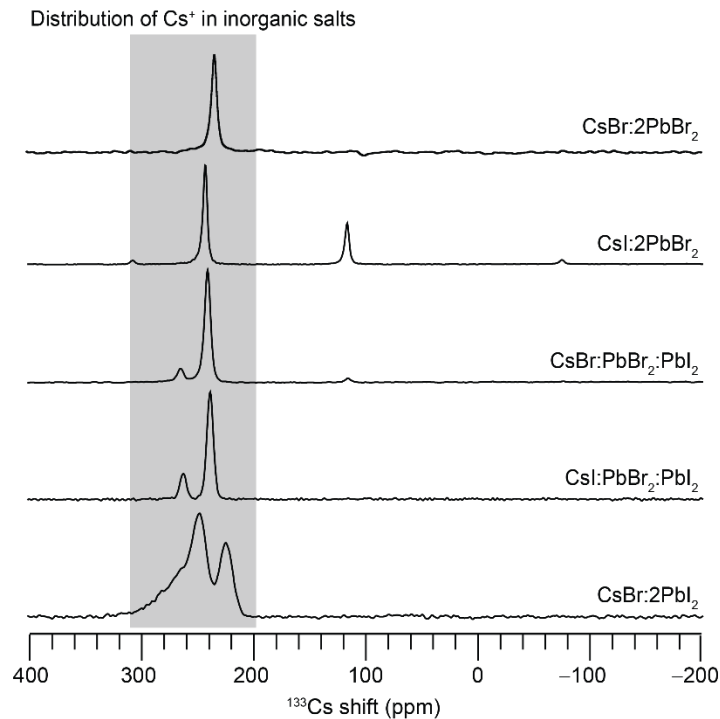


**Figure 2.20.**  $^{133}\text{Cs}$  NMR spectrum of  $\text{CsPb}_2\text{Br}_x\text{I}_{5-x}$  acquired at 18.8 T and room temperature.

To confirm this, the  $^{133}\text{Cs}$  spectra for  $\text{CsPb}_2\text{Br}_x\text{I}_{5-x}$  ( $x = 1-5$ ) were acquired and compared, which exhibit peaks in the range of 200-300 ppm (Figure 2.20). This suggests that the Cs cations migrate, at least in part, from the perovskite framework to form non-perovskite phases. The precise chemical nature of these byproducts is difficult to establish due to dilute concentration and the compositional and structural heterogeneity, as evidenced by the broad distribution of  $^{133}\text{Cs}$  chemical shifts. It is of particular interest to understand the chemical nature of  $\text{MA}^+$  and  $\text{FA}^+$  cations in CsMAFA before and after exposure to moisture. 1D  $^1\text{H}$  NMR was utilized to investigate the local environment of organic cations. For the pristine CsMAFA (Figure 2.19b), the methyl and ammonium proton of  $\text{MA}^+$  is observed at 3.4 and 6.3 ppm, respectively, while the ammonium and methylene protons of  $\text{FA}^+$  are observed at 7.4 and 8.2 ppm, respectively. Upon aging at 85% RH, 1D  $^1\text{H}$  NMR exhibited identical signals for  $\text{MA}^+$  and  $\text{FA}^+$  cations, but line narrowing is observed, which can be reasoned to the local ordering of organic cations as some of the  $\text{Cs}^+$  cations leave the perovskite framework.

Similar to the moisture-induced degradation of single cation/anion perovskite thin films, the water vapor concentration played a significant role in the stability of the CsMAFA thin film.

Upon exposing the CsMAFA material at 40% RH for one year, an additional  $^{133}\text{Cs}$  signal is observed at 278 ppm (Figure 2.21a), which is attributable to the formation of non-perovskite inorganic Cs salts – identical to those observed in the case of aged CsMAFA at 85% RH but at a much slower rate. Likewise, the 1D  $^1\text{H}$  NMR experiments of CsMAFA (aged at 40% RH for up to a year) showed identical results (Figure 2.21b). These results conclude that some of the  $\text{Cs}^+$  cations remain in the perovskite framework, and the other tends to migrate out to form the non-perovskite structure even in the presence of a low concentration of water molecules.

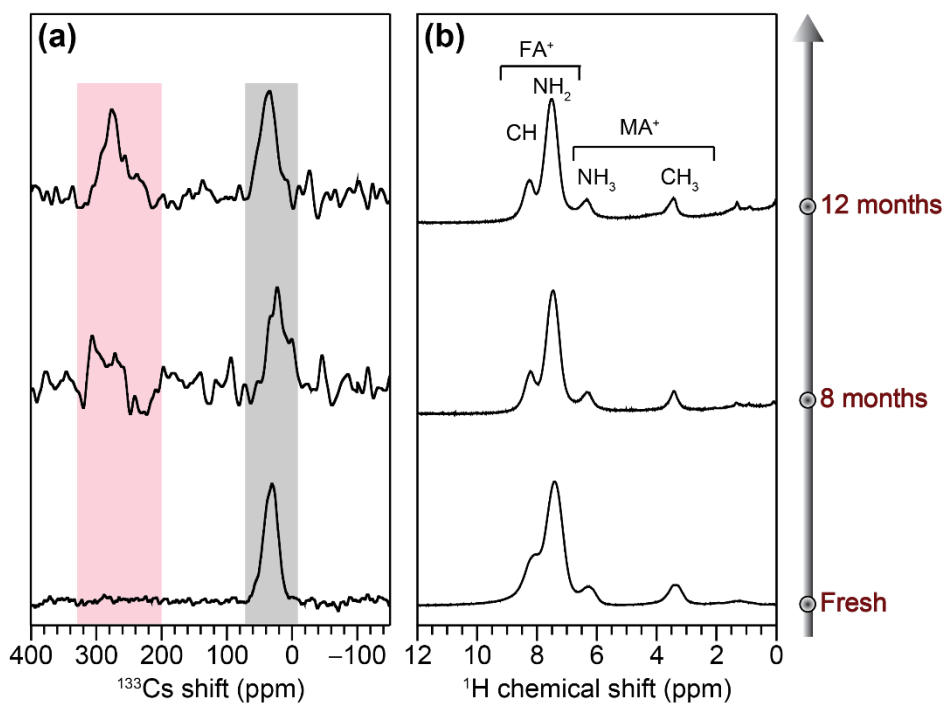


**Figure 2.21.** Solid-state 1D MAS NMR spectra of CsMAFA acquired at 18.8 T, room temperature: (a)  $^{133}\text{Cs}$  (b)  $^1\text{H}$  MAS NMR spectra before and after exposure to moisture at 40% RH. The black and magenta vertical bands indicate the Cs ions associated with perovskite and non-perovskite phases.

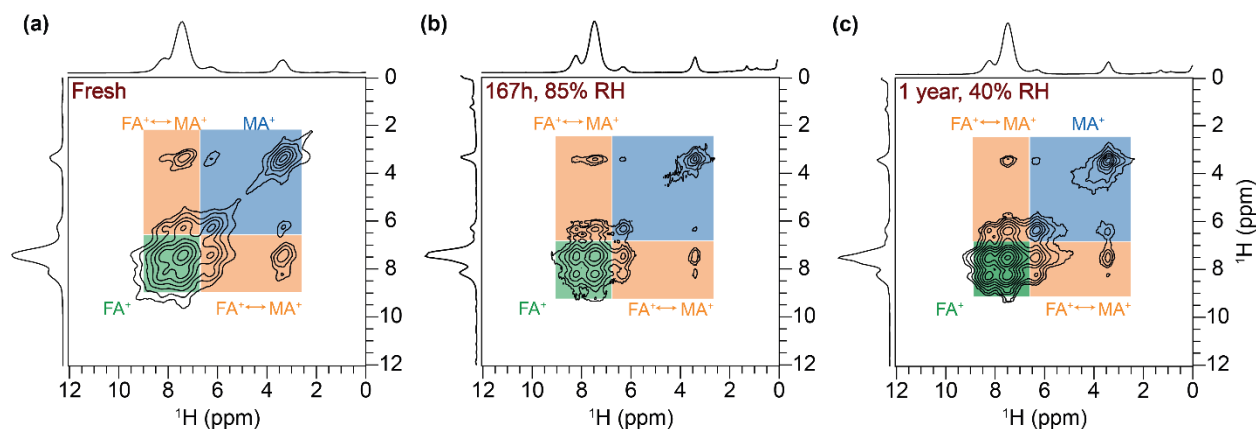


**Figure 2.22.** Solid-state 2D  $^1\text{H}$ - $^1\text{H}$  SD NMR spectrum of CsMAFA acquired with 500 ms mixing time for (a) pristine and after exposure to moisture for (b) 167 h at 85% RH and (c) 1 year at 40% RH. Peaks correspond to  $\text{MA}^+$ , and  $\text{FA}^+$  cations are color-coded as depicted in the boxes.

To probe the interactions between the A-site organic cations such as  $\text{MA}^+$  and  $\text{FA}^+$  in the fresh and moisture-exposed CsMAFA, 2D  $^1\text{H}$ - $^1\text{H}$  SD spectra acquired at 500 ms of mixing time (Figure 2.22) were analyzed. The 2D peaks depicted in the blue-shaded rectangle (3.4-6.6 ppm) correspond to  $\text{MA}^+$  cations, and the 2D peaks in the green-shaded rectangle (7.4-8.6 ppm) correspond to the  $\text{FA}^+$  moieties, respectively. Specifically, the 2D peaks highlighted in the orange-shaded rectangle indicate the intermolecular dipolar interactions between the  $\text{MA}^+$  and  $\text{FA}^+$  protons. For the aged CsMAFA, the 2D  $^1\text{H}$ - $^1\text{H}$  SD spectrum (Figure 2.22b) showed identical cross-peaks but with less intensity suggesting the subtle structure rearrangement and reorganization of  $\text{MA}^+$  and  $\text{FA}^+$  cations after exposure to moisture (for 167h (~7 days) at 85% RH). It has been shown that the driving force for such structural reorganization or local clustering of organic cations leads to its increased dynamical freedom lowering the free energy of the mixed-cation system.<sup>38</sup> However, the 2D SD spectrum acquired after exposure to moisture for 1 year aged at 40% RH leads to the relatively high-intensity cross-peaks (Figure 2.22c), further corroborating that the water molecules play important in the degradation kinetics of CsMAFA thin films. Interestingly, the moisture-aged CsMAFA thin film did not show the signatures corresponding to MAI or  $\delta$ -FAPbI<sub>3</sub>, irrespective of the aging conditions. This result is intriguing and calls for further investigation of organic cation stability in CsMAFA formulation.

## 2.6. Instability in formamidinium-based lead halide perovskite: Key learnings from ssNMR

Understanding transformative and reconstructive reactions of hybrid perovskites is a crucially important factor in developing environmentally stable perovskite-based optoelectronic devices. Multiscale characterization using ssNMR in conjunction with XRD and PL allows one to examine the perovskite degradation/transformation at different length scales. In particular, the kinetics of  $\alpha \rightarrow \delta$  FAPbI<sub>3</sub> reaction as functions of water vapor concentration, particle size, and light illumination is presented, along with the chemical nature of the  $\alpha/\delta$ -FAPbI<sub>3</sub> phase is studied using high-field NMR. These results indicate that the cubic phase of FAPbI<sub>3</sub> is kinetically stable, whilst the cubic phase of FAPbBr<sub>3</sub> is thermodynamically stable at ambient temperatures with a wide range of humidity levels and exposure times. The half-lives of  $\alpha$ -FAPbI<sub>3</sub>, intra-grain morphology, and chemical nature of intermediate species characterized at different length scales provide rich mechanistic insights. The key takeaway from this study is that the ambient stability of the black FAPbI<sub>3</sub> phase strongly depends on the external stimuli and kinetics of degradation reactions at the grain and sub-grain boundaries; a combination of these effects leads to a variation of the transformation time from days to several months or even a year. The reaction process that enables the transformation from the black phase to the yellow phase involves the surface-initiated local dissolution and precipitation mechanism, with water being the solvent. The synergy of multiscale characterization techniques that are complementary with respect to each other and on-the-fly deuteration of organic cations demonstrated in this study is likely to be an essential feature of the strategies to understand the transformative reactions in hybrid halide perovskites and develop interfacial engineering strategies in the future. The long-term moisture stability of FA-rich CsMAFA thin film was also examined to realize that exposure to moisture leads to partial elimination of Cs<sup>+</sup> cations, but organic cations tend to preserve the perovskite structure even after exposure to moisture for over a year. This study also suggests that the single crystal FAPbI<sub>3</sub> and FA-rich materials provide a path forward for stable and efficient optoelectronics.



## 2.7. References

- 1 C. C. Stoumpos, C. D. Malliakas and M. G. Kanatzidis, *Inorg. Chem.*, 2013, **52**, 9019–9038.
- 2 J. Jeong, M. Kim, J. Seo, H. Lu, P. Ahlawat, A. Mishra, Y. Yang, M. A. Hope, F. T. Eickemeyer, M. Kim, Y. J. Yoon, I. W. Choi, B. P. Darwich, S. J. Choi, Y. Jo, J. H. Lee, B. Walker, S. M. Zakeeruddin, L. Emsley, U. Rothlisberger, A. Hagfeldt, D. S. Kim, M. Grätzel and J. Y. Kim, *Nature*, 2021, **592**, 381–385.
- 3 Q. Jiang, Y. Zhao, X. Zhang, X. Yang, Y. Chen, Z. Chu, Q. Ye, X. Li, Z. Yin and J. You, *Nat. Photonics*, 2019, **13**, 460–466.
- 4 X. Zheng, Y. Hou, C. Bao, J. Yin, F. Yuan, Z. Huang, K. Song, J. Liu, J. Troughton, N. Gasparini, C. Zhou, Y. Lin, D.-J. Xue, B. Chen, A. K. Johnston, N. Wei, M. N. Hedhili, M. Wei, A. Y. Alsalloum, P. Maity, B. Turedi, C. Yang, D. Baran, T. D. Anthopoulos, Y. Han, Z.-H. Lu, O. F. Mohammed, F. Gao, E. H. Sargent and O. M. Bakr, *Nat. Energy*, 2020, **5**, 131–140.
- 5 E. H. Jung, N. J. Jeon, E. Y. Park, C. S. Moon, T. J. Shin, T.-Y. Yang, J. H. Noh and J. Seo, *Nature*, 2019, **567**, 511–515.
- 6 K. M. M. Salim, S. Masi, A. F. Gualdrón-Reyes, R. S. Sánchez, E. M. Barea, M. Krečmarová, J. F. Sánchez-Royo and I. Mora-Seró, *ACS Energy Lett.*, 2021, **10**, 3511–3521.
- 7 J. Chen, D. He and N. G. Park, *Sol. RRL*, 2022, **6**, 2100767.
- 8 S. H. Turren-Cruz, A. Hagfeldt and M. Saliba, *Science*, 2018, **362**, 449–453.
- 9 IEC 61215-1:2016 | IEC Webstore | rural electrification, solar power, solar panel, photovoltaic, PV, smart city, LVDC, <https://webstore.iec.ch/publication/24312>, (accessed 20 September 2021).
- 10 R. Cheacharoen, C. C. Boyd, G. F. Burkhard, T. Leijtens, J. A. Raiford, K. A. Bush, S. F. Bent and M. D. McGehee, *Sustain. Energy Fuels*, 2018, **2**, 2398–2406.
- 11 R. Cheacharoen, N. Rolston, D. Harwood, K. A. Bush, R. H. Dauskardt and M. D. McGehee, *Energy Environ. Sci.*, 2018, **11**, 144–150.

- 12 K. A. Bush, A. F. Palmstrom, Z. J. Yu, M. Boccard, R. Cheacharoen, J. P. Mailoa, D. P. McMeekin, R. L. Z. Hoye, C. D. Bailie, T. Leijtens, I. M. Peters, M. C. Minichetti, N. Rolston, R. Prasanna, S. Sofia, D. Harwood, W. Ma, F. Moghadam, H. J. Snaith, T. Buonassisi, Z. C. Holman, S. F. Bent and M. D. McGehee, *Nat. Energy*, 2017, **2**, 17009.
- 13 S. Nair and J. V. Gohel, *Opt. Mater.*, 2020, **109**, 110377.
- 14 S. Masi, A. F. Gualdrón-Reyes and I. Mora-Seró, *ACS Energy Lett.*, 2020, **5**, 1974–1985.
- 15 H. Min, D. Y. Lee, J. Kim, G. Kim, K. S. Lee, J. Kim, M. J. Paik, Y. K. Kim, K. S. Kim, M. G. Kim, T. J. Shin and S. Il Seok, *Nature*, 2021, **598**, 444–450.
- 16 W. Hui, L. Chao, H. Lu, F. Xia, Q. Wei, Z. Su, T. Niu, L. Tao, B. Du, D. Li, Y. Wang, S. Zuo, B. Li, W. Shi, X. Ran, P. Li, H. Zhang, Z. Wu, C. Ran, L. Song, G. Xing, X. Gao, J. Zhang, Y. Xia, Y. Chen and W. Huang, *Science*, 2021, **371**, 1359–1364.
- 17 B. wook Park, H. W. Kwon, Y. Lee, D. Y. Lee, M. G. Kim, G. Kim, K. jeong Kim, Y. K. Kim, J. Im, T. J. Shin and S. Il Seok, *Nat. Energy*, 2021, **6**, 419–428.
- 18 Y. Liu, S. Akin, A. Hinderhofer, F. T. Eickemeyer, H. Zhu, J. Seo, J. Zhang, F. Schreiber, H. Zhang, S. M. Zakeeruddin, A. Hagfeldt, M. I. Dar and M. Grätzel, *Angew. Chemie*, 2020, **132**, 15818–15824.
- 19 Y. Fan, H. Meng, L. Wang and S. Pang, *Sol. RRL*, 2019, **3**, 1900215.
- 20 Y. Li, F. Z. Liu, M. Waqas, T. L. Leung, H. W. Tam, X. Q. Lan, B. Tu, W. Chen, A. B. Djurišić and Z. B. He, *Small Methods*, 2018, **2**, 1700387.
- 21 T. A. S. Doherty, S. Nagane, D. J. Kubicki, Y.-K. Jung, D. N. Johnstone, A. N. Iqbal, D. Guo, K. Frohna, M. Danaie, E. M. Tennyson, S. Macpherson, A. Abfalterer, M. Anaya, Y.-H. Chiang, P. Crout, F. S. Ruggeri, S. M. Collins, C. P. Grey, A. Walsh, P. A. Midgley and S. D. Stranks, *Science*, 2021, **374**, 1598–1605.
- 22 A. Binek, F. C. Hanusch, P. Docampo and T. Bein, *J. Phys. Chem. Lett.*, 2015, **6**, 1249–1253.
- 23 S. Kim, T. Eom, Y.-S. Ha, K.-H. Hong and H. Kim, *Chem. Mater.*, 2020, **32**, 4265–4272.
- 24 W. Qiu, A. Ray, M. Jaysankar, T. Merckx, J. P. Bastos, D. Cheyons, R. Gehlhaar, J. Poortmans and P. Heremans, *Adv. Funct. Mater.*, 2017, **27**, 1700920.

- 25 T. Chen, B. J. Foley, C. Park, C. M. Brown, L. W. Harriger, J. Lee, J. Ruff, M. Yoon, J. J. Choi and S. H. Lee, *Sci. Adv.*, 2016, **2**, e1601650.
- 26 F. Cordero, F. Craciun, F. Trequattrini, A. Generosi, B. Paci, A. M. Paoletti and G. Zanotti, *J. Phys. Chem. C*, 2020, **124**, 22972–22980.
- 27 Q. Han, S.-H. Bae, P. Sun, Y.-T. Hsieh, Y. M. Yang, Y. S. Rim, H. Zhao, Q. Chen, W. Shi, G. Li and Y. Yang, *Adv. Mater.*, 2016, **28**, 2253–2258.
- 28 J. A. Steele, H. Yuan, C. Y. X. Tan, M. Keshavarz, C. Steuwe, M. B. J. Roeffaers and J. Hofkens, *ACS Nano*, 2017, **11**, 8072–8083.
- 29 H. Zheng, J. Duan and J. Dai, *Int. J. Mod. Phys. B*, 2017, **31**, 1744066.
- 30 J. Ali, Y. Li, P. Gao, T. Hao, J. Song, Q. Zhang, L. Zhu, J. Wang, W. Feng, H. Hu and F. Liu, *Nanoscale*, 2020, **12**, 5719–5745.
- 31 S. Kundu and T. L. Kelly, *EcoMat*, 2020, **2**, e12025.
- 32 F. Cordero, F. Craciun, F. Trequattrini, A. Generosi, B. Paci, A. M. Paoletti and G. Pennesi, *J. Phys. Chem. Lett.*, 2019, **10**, 2463–2469.
- 33 K. Ho, M. Wei, E. H. Sargent and G. C. Walker, *ACS Energy Lett.*, 2021, **6**, 934–940.
- 34 D. J. Kubicki, S. D. Stranks, C. P. Grey and L. Emsley, *Nat. Rev. Chem.*, 2021, **5**, 624–645.
- 35 C. J. Dahlman, D. J. Kubicki and G. N. M. Reddy, *J. Mater. Chem. A*, 2021, **9**, 19206–19244.
- 36 A. M. Askar, G. M. Bernard, B. Wiltshire, K. Shankar and V. K. Michaelis, *J. Phys. Chem. C*, 2017, **121**, 1013–1024.
- 37 W. M. J. Franssen and A. P. M. Kentgens, *Solid State Nucl. Magn. Reson.*, 2019, **100**, 36–44.
- 38 H. Grüniger, M. Bokdam, N. Leupold, P. Tinnemans, R. Moos, G. A. De Wijs, F. Panzer and A. P. M. Kentgens, *J. Phys. Chem. C*, 2021, **125**, 1742–1753.
- 39 M. A. A. Kazemi, P. Raval, K. Cherednichekno, J.-N. Chotard, A. Krishna, A. Demortiere, G. N. M. Reddy and F. Sauvage, *Small Methods*, 2021, **5**, 2000834.

- 40 B. A. Rosales, L. Men, S. D. Cady, M. P. Hanrahan, A. J. Rossini and J. Vela, *Chem. Mater.*, 2016, **28**, 6848–6859.
- 41 M. T. Weller, O. J. Weber, J. M. Frost and A. Walsh, *J. Phys. Chem. Lett.*, 2015, **6**, 3209–3212.
- 42 C. F. Macrae, I. Sovago, S. J. Cottrell, P. T. A. Galek, P. McCabe, E. Pidcock, M. Platings, G. P. Shields, J. S. Stevens, M. Towler and P. A. Wood, *J. Appl. Crystallogr.*, 2020, **53**, 226–235.
- 43 J. Lee, W. Lee, K. Kang, T. Lee and S. K. Lee, *Chem. Mater.*, 2021, **33**, 370–377.
- 44 M. P. Hanrahan, L. Men, B. A. Rosales, J. Vela and A. J. Rossini, *Chem. Mater.*, 2018, **30**, 7005–7015.
- 45 B. Febriansyah, T. M. Koh, P. J. S. Rana, T. J. N. Hooper, Z. Z. Ang, Y. Li, A. Bruno, M. Grätzel, J. England, S. G. Mhaisalkar and N. Mathews, *ACS Energy Lett.*, 2020, **5**, 2305–2312.
- 46 J. S. Yun, J. Kim, T. Young, R. J. Patterson, D. Kim, J. Seidel, S. Lim, M. A. Green, S. Huang and A. Ho-Baillie, *Adv. Funct. Mater.*, 2018, **28**, 1705363.
- 47 E. J. Mittemeijer, *J. Mater. Sci.*, 1992, **27**, 3977–3987.
- 48 A. Rollett, F. Humphreys, G. S. Rohrer and M. Hatherly, in *Recrystallization and Related Annealing Phenomena (Second Edition)*, Elsevier Ltd, 2004, pp. 215–267.
- 49 M. Avrami, *J. Chem. Phys.*, 2004, **9**, 177.
- 50 M. Avrami, *J. Chem. Phys.*, 2004, **8**, 212.
- 51 M. Avrami, *J. Chem. Phys.*, 2004, **7**, 1103.
- 52 A. K. Jena and M. C. Chaturvedi, *Phase transformation in materials*, Prentice Hall, 1992.
- 53 A. Khawam and D. R. Flanagan, *J. Phys. Chem. B*, 2006, **110**, 17315–17328.
- 54 L. A. Pérez-Maqueda, J. M. Criado and P. E. Sánchez-Jiménez, *J. Phys. Chem. A*, 2006, **110**, 12456–12462.
- 55 E. Segal, *Rev. Roum. Chim.*, 2012, **57**, 491–493.
- 56 W. Jander, *Zeitschrift für Anorg. und Allg. Chemie*, 1927, **163**, 1–30.

- 57 I. Spanopoulos, W. Ke, C. C. Stoumpos, E. C. Schueller, O. Y. Kontsevoi, R. Seshadri and M. G. Kanatzidis, *J. Am. Chem. Soc.*, 2018, **140**, 5728–5742.
- 58 A. F. Castro-Méndez, J. Hidalgo and J. P. Correa-Baena, *Adv. Energy Mater.*, 2019, **9**, 1901489.
- 59 H. Li, G. Wu, W. Li, Y. Zhang, Z. Liu, D. Wang, S. Liu, H. Li, G. Wu, W. Li, Z. Liu, D. Wang, S. Liu and Y. Zhang, *Adv. Sci.*, 2019, **6**, 1901241.
- 60 M. Hu, C. Bi, Y. Yuan, Y. Bai, J. Huang, M. Hu, C. Bi, Y. Yuan, Y. Bai and J. Huang, *Adv. Sci.*, 2016, **3**, 1500301.
- 61 M. Wang, Y. Yin, W. Cai, J. Liu, Y. Han, Y. Feng, Q. Dong, Y. Wang, J. Bian and Y. Shi, *Adv. Funct. Mater.*, 2022, **32**, 2108567.
- 62 Z. Wang, A. Pradhan, M. A. Kamarudin, M. Pandey, S. S. Pandey, P. Zhang, C. H. Ng, A. S. M. Tripathi, T. Ma and S. Hayase, *ACS Appl. Mater. Interfaces*, 2019, **11**, 10012–10020.
- 63 W. Kim, J. B. Park, H. Kim, K. Kim, J. Park, S. Cho, H. Lee, Y. Pak and G. Y. Jung, *J. Mater. Chem. A*, 2019, **7**, 20832–20839.
- 64 S. Ma, G. Yuan, Y. Zhang, N. Yang, Y. Li and Q. Chen, *Energy Environ. Sci.*, 2022, **15**, 13–55.
- 65 M. Mohammadi, S. Gholipour, M. Malekshahi Byranvand, Y. Abdi, N. Taghavinia and M. Saliba, *ACS Appl. Mater. Interfaces*, 2021, **13**, 45455–45464.
- 66 X. Zheng, B. Chen, J. Dai, Y. Fang, Y. Bai, Y. Lin, H. Wei, X. C. Zeng and J. Huang, *Nat. Energy*, 2017, **2**, 17102.
- 67 E. A. Alharbi, A. Y. Alyamani, D. J. Kubicki, A. R. Uhl, B. J. Walder, A. Q. Alanazi, J. Luo, A. Burgos-Caminal, A. Albadri, H. Albrithen, M. H. Alotaibi, J. E. Moser, S. M. Zakeeruddin, F. Giordano, L. Emsley and M. Grätzel, *Nat. Commun.*, 2019, **10**, 3008.
- 68 E. Smecca, Y. Numata, I. Deretzis, G. Pellegrino, S. Boninelli, T. Miyasaka, A. La Magna and A. Alberti, *Phys. Chem. Chem. Phys.*, 2016, **18**, 13413–13422.
- 69 T. Zhang, X. Meng, Y. Bai, S. Xiao, C. Hu, Y. Yang, H. Chen and S. Yang, *J. Mater. Chem. A*, 2017, **5**, 1103–1111.

- 70 C. G. Bischak, M. Lai, Z. Fan, D. Lu, P. David, D. Dong, H. Chen, A. S. Etman, T. Lei, J. Sun, M. Grünwald, D. T. Limmer, P. Yang and N. S. Ginsberg, *Matter*, 2020, **3**, 534–545.
- 71 J. Xue, R. Wang, K. L. Wang, Z. K. Wang, I. Yavuz, Y. Wang, Y. Yang, X. Gao, T. Huang, S. Nuryyeva, J. W. Lee, Y. Duan, L. S. Liao, R. Kaner and Y. Yang, *J. Am. Chem. Soc.*, 2019, **141**, 13948–13953.
- 72 J. S. Yun, J. Kim, T. Young, R. J. Patterson, D. Kim, J. Seidel, S. Lim, M. A. Green, S. Huang and A. Ho-Baillie, *Adv. Funct. Mater.*, 2018, **28**, 1705363.
- 73 L. Piveteau, V. Morad and M. V. Kovalenko, *J. Am. Chem. Soc.*, 2020, **142**, 19413–19437.
- 74 E. M. Mozur, M. A. Hope, J. C. Trowbridge, D. M. Halat, L. L. Daemen, A. E. Maughan, T. R. Prisk, C. P. Grey and J. R. Neilson, *Chem. Mater.*, 2020, **32**, 6266–6277.
- 75 K. Druzbicki, R. Lavén, J. Armstrong, L. Malavasi, F. Fernandez-Alonso and M. Karlsson, *J. Phys. Chem. Lett.*, 2021, **12**, 3503–3508.
- 76 D. H. Fabini, T. A. Siaw, C. C. Stoumpos, G. Laurita, D. Olds, K. Page, J. G. Hu, M. G. Kanatzidis, S. Han and R. Seshadri, *J. Am. Chem. Soc.*, 2017, **139**, 16875–16884.
- 77 C. J. Dahlman, R. M. Kennard, P. Paluch, N. R. Venkatesan, M. L. Chabynyc and G. N. M. Reddy, *Chem. Mater.*, 2021, **33**, 642–656.
- 78 A. Hvidt, *Biochim. Biophys. Acta*, 1955, **18**, 306–308.
- 79 G. R. Masson, J. E. Burke, N. G. Ahn, G. S. Anand, C. Borchers, S. Brier, G. M. Bou-Assaf, J. R. Engen, S. W. Englander, J. Faber, R. Garlish, P. R. Griffin, M. L. Gross, M. Guttman, Y. Hamuro, A. J. R. Heck, D. Houde, R. E. Iacob, T. J. D. Jørgensen, I. A. Kaltashov, J. P. Klinman, L. Konermann, P. Man, L. Mayne, B. D. Pascal, D. Reichmann, M. Skehel, J. Snijder, T. S. Strutzenberg, E. S. Underbakke, C. Wagner, T. E. Wales, B. T. Walters, D. D. Weis, D. J. Wilson, P. L. Wintrode, Z. Zhang, J. Zheng, D. C. Schriemer and K. D. Rand, *Nat. Methods*, 2019, **16**, 595–602.
- 80 O. Knop, R. E. Wasylishen, M. Anne White, T. Stanley Cameron and M. J. M Van Oort, *Can. J. Chem.*, 1990, **68**, 412.
- 81 D. J. Kubicki, D. Prochowicz, A. Hofstetter, P. Péchy, S. M. Zakeeruddin, M. Grätzel and

- L. Emsley, *J. Am. Chem. Soc.*, 2017, **139**, 10055–10061.
- 82 C. Roiland, G. Trippé-Allard, K. Jemli, B. Alonso, J. C. Ameline, R. Gautier, T. Bataille, L. Le Pollès, E. Deleporte, J. Even and C. Katan, *Phys. Chem. Chem. Phys.*, 2016, **18**, 27133–27142.
- 83 Z. Li, M. Yang, J. S. Park, S. H. Wei, J. J. Berry and K. Zhu, *Chem. Mater.*, 2016, **28**, 284–292.
- 84 Z. Fan, K. Sun and J. Wang, *J. Mater. Chem. A*, 2015, **3**, 18809–18828.
- 85 C. J. Bartel, C. Sutton, B. R. Goldsmith, R. Ouyang, C. B. Musgrave, L. M. Ghiringhelli and M. Scheffler, *Sci. Adv.*, 2019, **5**, eaav0693.
- 86 K. L. Svane, A. C. Forse, C. P. Grey, G. Kieslich, A. K. Cheetham, A. Walsh and K. T. Butler, *J. Phys. Chem. Lett.*, 2017, **8**, 6154–6159.
- 87 M. Aebli, L. Piveteau, O. Nazarenko, B. M. Benin, F. Krieg, R. Verel and M. V. Kovalenko, *Sci. Rep.*, 2020, **10**, 8229.
- 88 J. P. Correa-Baena, M. Saliba, T. Buonassisi, M. Grätzel, A. Abate, W. Tress and A. Hagfeldt, *Science*, 2017, **358**, 739–744.
- 89 A. Al-Ashouri, E. Köhnen, B. Li, A. Magomedov, H. Hempel, P. Caprioglio, J. A. Márquez, A. B. M. Vilches, E. Kasparavicius, J. A. Smith, N. Phung, D. Menzel, M. Grischek, L. Kegelman, D. Skroblin, C. Gollwitzer, T. Malinauskas, M. Jošt, G. Matič, B. Rech, R. Schlattmann, M. Topič, L. Korte, A. Abate, B. Stannowski, D. Neher, M. Stollerfoht, T. Unold, V. Getautis and S. Albrecht, *Science*, 2020, **370**, 1300–1309.
- 90 A. Karmakar, M. S. Dodd, X. Zhang, M. S. Oakley, M. Klobukowski and V. K. Michaelis, *Chem. Commun.*, 2019, **55**, 5079–5082.
- 91 M. A. A. Kazemi, N. Folastre, P. Raval, M. Sliwa, J. Marie, V. Nsanzimana, S. Golonu, A. Demortiere, J. Rousset, O. Lafon, L. Delevoye, G. N. M. Reddy and F. Sauvage, *Energy Environ. Mater.*, , DOI:10.1002/eem2.12335.

# Chapter 3- Probing moisture-induced degradation reactions in methylammonium-based perovskites

---

## 3.1. Methylammonium lead iodide (MAPbI<sub>3</sub>) for photovoltaic applications

As mentioned in Chapter 1, the application of MAPbI<sub>3</sub> perovskites for photovoltaic devices has begun in 2009 by Miyasaka *et al.*, who incorporated this material in the dye-sensitized solar cell (DSSC) as visible light sensitizer.<sup>1</sup> Having the tolerance factor,  $t = 0.91$  and an octahedral factor,  $\mu = 0.47$  (see equations 1.1 and 1.2), the cubic structure of MAPbI<sub>3</sub> is expected to be stable.<sup>2,3</sup> Favorable bandgap and high charge carrier mobility associated with this material make it suitable for the development of high-performing solar cells.<sup>4-6</sup> Today, MA is among the key components of the complex solid formulations used in high-performing perovskite solar cells.<sup>7-13</sup> The phase stability of MAPbI<sub>3</sub> has been investigated in greater detail.<sup>14,15</sup> The cubic MAPbI<sub>3</sub> phase is stable at high temperatures ( $T > 327$  K), and there exist two phases that are stable at lower temperatures, namely the orthorhombic phase ( $T < 165$  K) and the tetragonal phase ( $165$  K  $< T < 327$  K). Thermal phase transitions induce PbI<sub>6</sub> octahedral tilting (Figure 3.1), resulting in these tetragonal and orthorhombic phases.

The soft ionic lattice of MAPbI<sub>3</sub> is sensitive to external stimuli such as moisture, temperature, and light, leading to swift degradation of the perovskites.<sup>16-18</sup> Efforts to address the environmental stability of these materials are at the forefront today.<sup>19</sup> Among the other external factors that influence stability, exposure to moisture drastically reduces solar cell performance by catalyzing water vapor-assisted transformative reactions. In this regard, a few protocols have been proposed to examine the moisture-induced degradation of hybrid perovskites at (i) low relative humidity (< 40% RH) and (ii) high relative humidity (>70% RH) in the air, in order to assess the environmental stability of solar cell modules.<sup>20,21</sup>



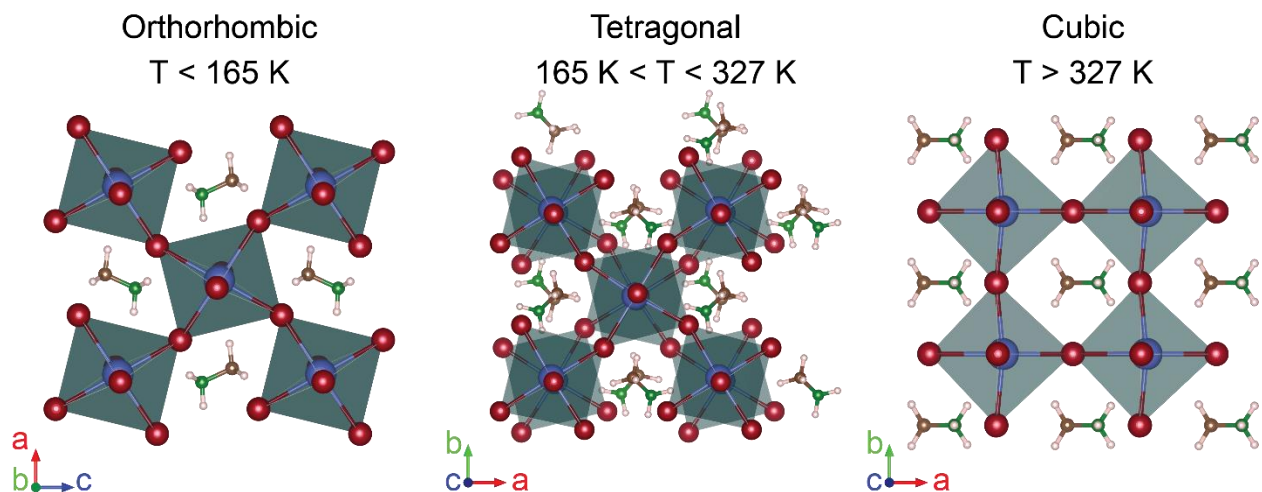


**Figure 3.1.** Orthorhombic, tetragonal, and cubic crystal structures of methylammonium lead iodide.

In attempting to address the stability issues, studies over the last decade have introduced several interfacial engineering and passivation techniques.<sup>7,22–37</sup> For example, defect passivation enabled by the introduction of dilute concentrations of small-molecule additives into the perovskite precursor solution during the film deposition leads to defect passivation (Section 1.4) of perovskite grains.<sup>29,38</sup> Passivation of point defects in MAPbI<sub>3</sub> and mixed-cation formulations has been used in conjunction with interfacial engineering of perovskite-contact layers to suppress non-radiative charge carrier recombination, enabling high stability and PCE of about 24%.<sup>7,28,39,40</sup> A wide variety of supramolecular chemistry approaches and molecular modulators have been proposed and employed to achieve defect passivation and environmental stability in perovskite solar cells.<sup>26,41</sup> For example, tetrapropylammonium cation (TPA<sup>+</sup>) passivated MAPbI<sub>3</sub> solar cells (non-encapsulated devices) exhibited a PCE of 18.7% with a  $T_{80}$  of 250 h (i.e., device operation time with 80% of original efficiency retained).<sup>25</sup> Methylammonium containing mixed-cation/anion composition passivated with thiophene-based ligands allows PCE values of over 24% with enhanced stability ( $T_{80} \sim 3570$  h).<sup>7</sup> The outdoor operational stability of perovskite solar cells has been widely studied by tracking the device physics and optoelectronic properties as functions of light, temperature, and moisture, however, a detailed analysis of the structural factors that contribute to the degradation/transformation reactions in different layers and interfaces between them is lacking. To this end, understanding of the thin-film morphology, microstructure, and intermolecular interactions between the passivating agents and perovskite

grains at the atomic-scale resolution is crucially important to develop interfacial engineering strategies and novel passivation ligands.

Various analytical techniques have been used to probe the instability of methylammonium and other organic-cation-based perovskites, including X-ray diffraction (XRD), thermogravimetry, mass spectrometry, optical or electron microscopy, ssNMR spectroscopy and the associated theoretical calculations.<sup>42–48</sup> Only a handful of studies have used atomic-scale characterization techniques to examine the different degradation products and their kinetic pathways, specifically for assessing the long-term stability of several months.<sup>19,45,48–52</sup> For the ordered regions of these device stacks, XRD studies can provide information on the crystallinity and morphology, which can be directly assessed by examining the thin film deposited on a glass substrate. However, the heterogeneous interfaces between crystalline perovskites and organic passivating agents are difficult probe by long-range techniques. In particular, examining the degradation pathways by means of organic A-site cations and passivating ligands is less straightforward by using XRD techniques.<sup>53</sup> Additional layer of complexity appears from the limitations associated with the spatial and temporal resolution of analytical techniques to probe the accurate chemical nature of intermediates, short-lived species at minuscule concentrations, and cascade degradation pathways. Nonetheless, the role of moisture on the thin film morphology, grain size, and long-range structural order can be obtained by electron microscopy and X-ray diffraction (XRD) techniques.<sup>54</sup> Owing to its complementary length scale and ability to probe atomic-level interactions, ssNMR spectroscopy has been increasingly used to characterize photo absorbers and contact layers and the interfaces between them.<sup>53,55–71</sup> Although ssNMR techniques can be used to study the short-range structures, relatively low sample masses present in thin films (of the order of milligram) further limit the application of this technique to characterize the interfaces in device stacks or surface passivated perovskite thin films.<sup>53,55</sup> To this end, this Chapter illustrate how ssNMR techniques facilitates the changes in local structures and intermolecular interactions in perovskite thin films (obtained by scratching thin films deposited on glass substrates) to be elucidated and distinguished.

Year-long moisture-induced degradation reactions in MAPbI<sub>3</sub> and defect-passivated MAPbI<sub>3</sub> thin films were examined at complementary length scales using XRD and ssNMR techniques. The reaction kinetics of cascade reactions and the associated degradation products are analyzed and compared. Specifically, the role of water vapor concentration in the air (40%

RH and 85% RH) on the instability of these materials are accessed. The evolution of metastable species, interconversions between them, and the formation of different inorganic/organic byproducts are systematically characterized by XRD and 1D/2D ssNMR spectroscopy techniques. In addition, an overview of the different degradation reactions in MA, FA, and Cs-based perovskites and their cation/anion alloys characterized in the study are compared with the degradation products reported in the literature studies.

### 3.2. Probing moisture-induced degradation reactions in methylammonium lead iodide

In order to probe the changes in crystallinity and short-range structures before and after exposure to moisture at 85% RH in the air, a combination of X-ray diffraction techniques and ssNMR spectroscopy techniques was applied.

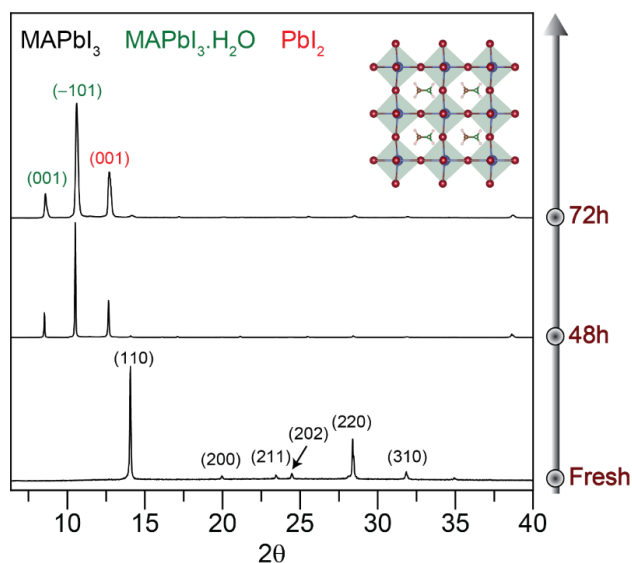


**Figure 3.2.** XRD patterns of MAPbI<sub>3</sub> before and after exposure to moisture (85% RH) for different durations as indicated. The peaks are labeled corresponding to Bragg planes of MAPbI<sub>3</sub> (black), MAPbI<sub>3</sub>·H<sub>2</sub>O (green), and PbI<sub>2</sub> (red), along with the schematic structure of MAPbI<sub>3</sub> in the inset.

First, the changes in the long-range crystallinity to identify the intermediate species and final byproducts by analyzing the XRD patterns are discussed (Figure 3.2). In the XRD patterns of the fresh material, peaks at 14.1°, 20.0°, 23.4°, 24.4°, 28.4°, and 31.8° correspond to (110), (200), (211), (202), (220), and (310) diffraction planes of the tetragonal structure of the MAPbI<sub>3</sub> perovskite (space group: I4/mcm). Upon exposure to moisture for 48 h, reflections at 8.1°, 10.5°,

and  $12.6^\circ$  corresponding to the (001) and (-101) planes of  $\text{MAPbI}_3 \cdot \text{H}_2\text{O}$  and (001) plane of  $\text{PbI}_2$ , respectively, are observed, consistently with the previous observations.<sup>48,72</sup> While these results confirm the formation of crystalline hydrate and inorganic  $\text{PbI}_2$ , the organic degradation products such as methyl ammonium iodide, are not detected in XRD, indicating the limitations of this technique.

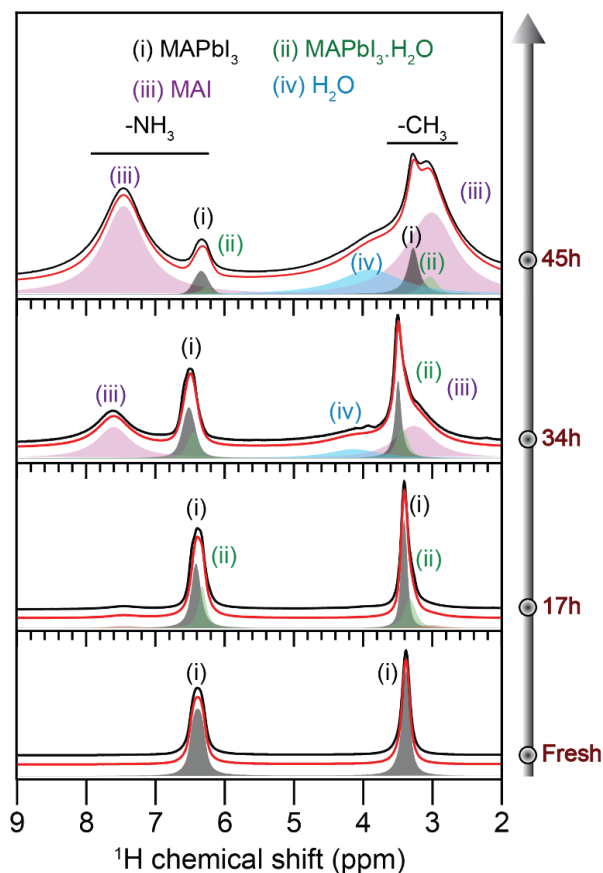


**Figure 3.3.** Experimental and simulated 1D  $^1\text{H}$  MAS NMR spectra of  $\text{MAPbI}_3$  before and after exposure to moisture (85% RH). The spectra were simulated as the sum of the signals of four species:  $\text{MAPbI}_3$  (black),  $\text{MAPbI}_3 \cdot \text{H}_2\text{O}$  (green), MAI (magenta) exhibiting signals of  $\text{NH}_3^+$  and  $\text{CH}_3$  groups, and  $\text{H}_2\text{O}$  (turquoise). The integrated intensities of the simulated spectra are indicated in Table 3.1. All spectra were acquired at 18.8 T and room temperature.

Solid-state 1D  $^1\text{H}$  NMR spectrum of the fresh  $\text{MAPbI}_3$  (Figure 3.3) exhibits two signals at 6.4 and 3.4 ppm attributed to  $\text{NH}_3^+$  and  $\text{CH}_3$  groups of methylammonium cation. In agreement with the degradation pathway determined from XRD, upon exposure to moisture for 17 h, subtle differences in the line shapes of  $\text{NH}_3^+$  and  $\text{CH}_3$  signals are observed, which could be attributable

to  $\text{MAPbI}_3 \cdot \text{H}_2\text{O}$  (Figure 3.4).<sup>48</sup> Intriguingly, the observation of low-intensity signals at 3.0 and 7.6 ppm indicate the formation of trace amounts of methyl ammonium iodide (MAI). To corroborate this analysis, a  $^1\text{H}$  NMR spectrum of pristine MAI is acquired and compared (Figure 3.5). The integrated intensities of simulated  $^1\text{H}$  spectra enable the relative molar fractions of pristine  $\text{MAPbI}_3$ ,  $\text{MAPbI}_3$  hydrate, and MAI to be estimated, which are 60%, 32%, and 8%, respectively after 17 h (Table 3.1). Further exposure to moisture at 85% RH increases MAI formation, as seen from the higher-intensity peaks at 3.0 and 7.6 ppm. MAI molar fraction has increased from 8% to 47% after 34 h and 65% after 45 h. Moreover, after 34 h, an additional broad peak at  $\sim 4.0$  ppm emerged, which could be hypothesized to originate from  $\text{MAPbI}_3$  hydrate and/or surface-adsorbed water molecules. These observations are strikingly important to understand the degradation pathways as well as reaction kinetics catalyzed by water molecules in the vapor. While the detailed understanding of the kinetic aspects of the cascade degradation of reactions requires more data to be acquired and analyzed, the XRD and NMR spectra acquired at different intervals of moisture exposure times enable the half-lives of  $\text{MAPbI}_3$  particles to be estimated. Approximately half of the  $\text{MAPbI}_3$  transformed into  $\text{MAPbI}_3$  hydrates or  $\text{PbI}_2/\text{MAI}$ , as revealed by the combined XRD and NMR study, leading to the half-life decay of the pristine  $\text{MAPbI}_3$  films estimated to be in the range of 10-20 h. However, the rest of the degradation reactions occur at relatively slower rates leading to the complete transformation of  $\text{MAPbI}_3$  to its degraded products in a few days. For example, approximately 6% of  $\text{MAPbI}_3$  still remained after exposure to moisture for two days. It is consistent with a previous study (Chapter 2), whereby the kinetics of transformative reactions occurs at different rates in hybrid perovskites with different half-lives of the photo absorbers. The rate at which the degradation occurs strongly depends on the concentration of water molecules in the vapor. To test this, the moisture-induced degradation reaction in the  $\text{MAPbI}_3$  after exposure to 40% RH was studied using  $^1\text{H}$  NMR spectroscopy.

**Table 3.1.** The integrated intensities associated with different phases obtained from the line shape deconvolution of the 1D  $^1\text{H}$  NMR spectrum in Figure 3.3.

Moisture exposure time	$^1\text{H}$ peak integrated intensities of different phases			
	MAPbI <sub>3</sub>	MAPbI <sub>3</sub> .H <sub>2</sub> O	MAI	H <sub>2</sub> O
0h	100%	-	-	-
17h	60%	32%	8%	-
34h	22%	12%	47%	19%
45h	6%	2%	65%	26%

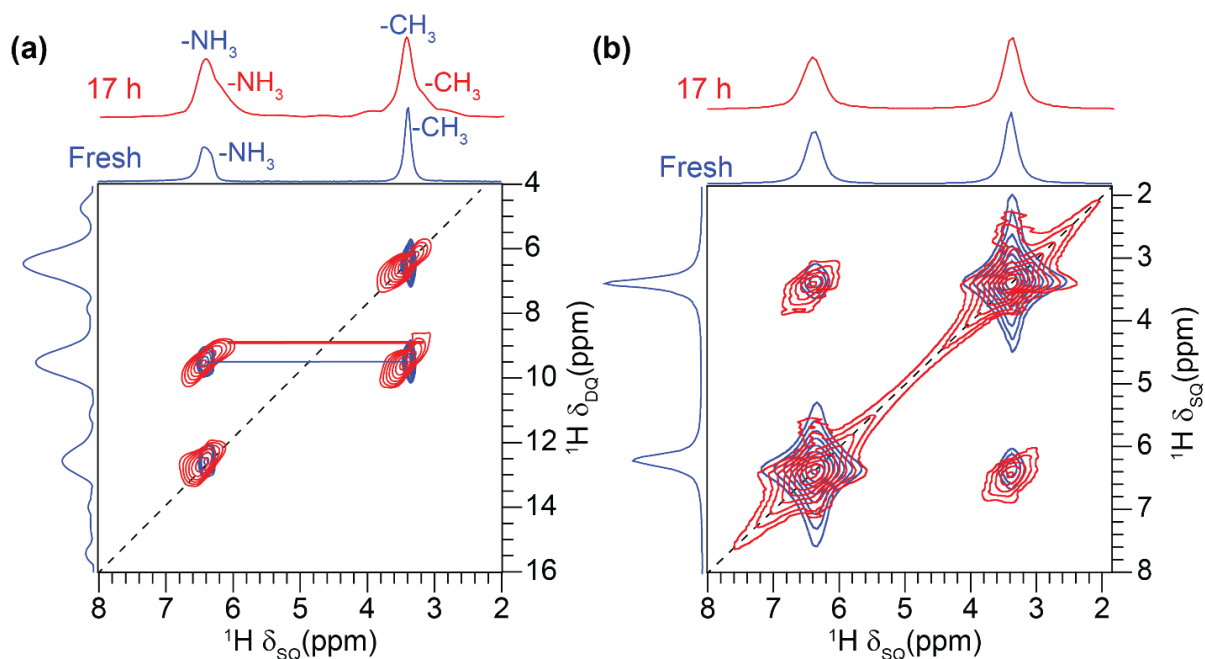


**Figure 3.4.** (a) 2D  $^1\text{H}$ - $^1\text{H}$  DQ-SQ and (b) 2D  $^1\text{H}$ - $^1\text{H}$  spin diffusion spectra of fresh MAPbI<sub>3</sub> (blue) and exposed to moisture (red) during 17 h at 85% RH acquired at 18.8 T.

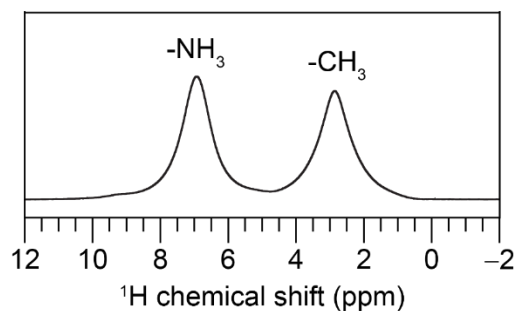


**Figure 3.5.** 1D <sup>1</sup>H MAS NMR spectrum of MAI acquired at 18.8 T, with peaks depicting CH<sub>3</sub> and NH<sub>3</sub> moieties.

Figure 3.6 presents 1D <sup>1</sup>H MAS NMR spectra of MAPbI<sub>3</sub> after exposure to moisture at 40% RH, which showed subtle changes in the resonant frequencies within the linewidth of the signal. Unlike 85% RH, for which MAI was detected after 34 h, there are no spectral features corresponding to MAI even after exposure to moisture at 40% RH for up to a year. However, subtle changes in the peak positions  $\Delta\delta$  (<sup>1</sup>H) = 157 Hz (within the <sup>1</sup>H linewidths) are observed, which is hypothesized to originate from the equilibrium between the MAPbI<sub>3</sub> and MAPbI<sub>3</sub>.H<sub>2</sub>O.<sup>48</sup> The formation of MAPbI<sub>3</sub> hydrate has previously been studied using XRD techniques.<sup>48,73</sup> In addition, the 2D <sup>1</sup>H-<sup>1</sup>H correlation spectroscopy resolves the different <sup>1</sup>H chemical shifts hidden in the line widths, as shown in Figure 3.4, indicating the formation of two different MAPbI<sub>3</sub> phases.<sup>48</sup> Based on these experimental results, the 1D <sup>1</sup>H NMR spectrum is deconvoluted into two separate signals corresponding to MAPbI<sub>3</sub>.H<sub>2</sub>O and MAPbI<sub>3</sub> species. It is noteworthy that accurate kinetics studies of the cascade degradation reactions require the acquisition of XRD and NMR spectra more frequently (i.e., improving temporal resolution) in order to construct kinetics plots from which the order of the reactions can be extracted.<sup>52</sup> In addition, the reaction kinetics and the half-lives of the reactants depend on the concentration of water molecules.

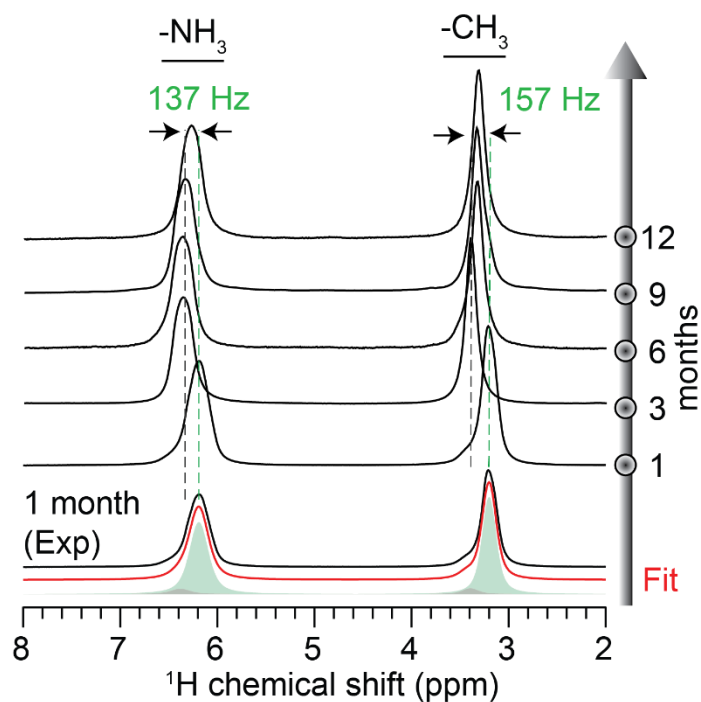


**Figure 3.6.** Solid-state 1D  $^1\text{H}$  NMR spectra of  $\text{MAPbI}_3$  after exposure to moisture at 40% RH during duration indicated on the right side of the spectra. All spectra were acquired at 18.8 T and room temperature.

To resolve the  $^1\text{H}$  peaks corresponding to the different degradation products, 2D  $^1\text{H}$ - $^1\text{H}$  correlation NMR experiments were carried out. Given the low sample mass (approximately ~5 milligrams of powder obtained by scratching the thin films) and longer spin-lattice relaxation delays of up to 20 seconds associated with these materials, the 2D correlation experiments require longer acquisition times of the order several hours, which limits the temporal resolution of 2D NMR to examine reaction kinetics. Nonetheless, 2D spectra of these materials before and after moisture exposure were acquired and compared to identify the peaks corresponding to the different degradation products and their local structures. First, 2D  $^1\text{H}$ - $^1\text{H}$  spin-diffusion (SD) spectra of fresh and aged  $\text{MAPbI}_3$  material is discussed. As explained in Chapters 1 and 2, in a 2D SD experiment, spin magnetization exchange occurs between the dipolar coupled protons in sub-nanometer to nanometer distances, yielding the off-diagonal peaks. In the 2D  $^1\text{H}$ - $^1\text{H}$  SD spectrum of fresh  $\text{MAPbI}_3$  (Figure 3.7), the off-diagonal peaks between 3.4 and 6.4 ppm indicate the magnetization exchange between the methyl and ammonium protons, as highlighted by the grey rectangle. Upon aging (17 h, 85% RH), the off-diagonal peaks corresponding to the



MAPbI<sub>3</sub> hydrate phase is observed, as indicated by the green-shaded rectangle. Upon further aging MAPbI<sub>3</sub> material (85% RH, 34 h, 45 h), the <sup>1</sup>H-<sup>1</sup>H spin-diffusion spectrum (Figure 3.7c,d) displays diagonal and cross peaks corresponding to the MAPbI<sub>3</sub> (grey box) and its hydrate(s) (green box), as well the peaks at 7.5 and 3.0 ppm associated with the ammonium and methyl groups of MAI (magenta), respectively. The absence of cross-peaks between the MAPbI<sub>3</sub> and MAI moieties (red circles) indicates that these moieties are not distributed in close proximities, indicating that the byproducts and MAPbI<sub>3</sub> exist as different domains, including the formation of MAPbI<sub>3</sub> hydrate. This is also reflected in the broadening of MA<sup>+</sup> peaks.

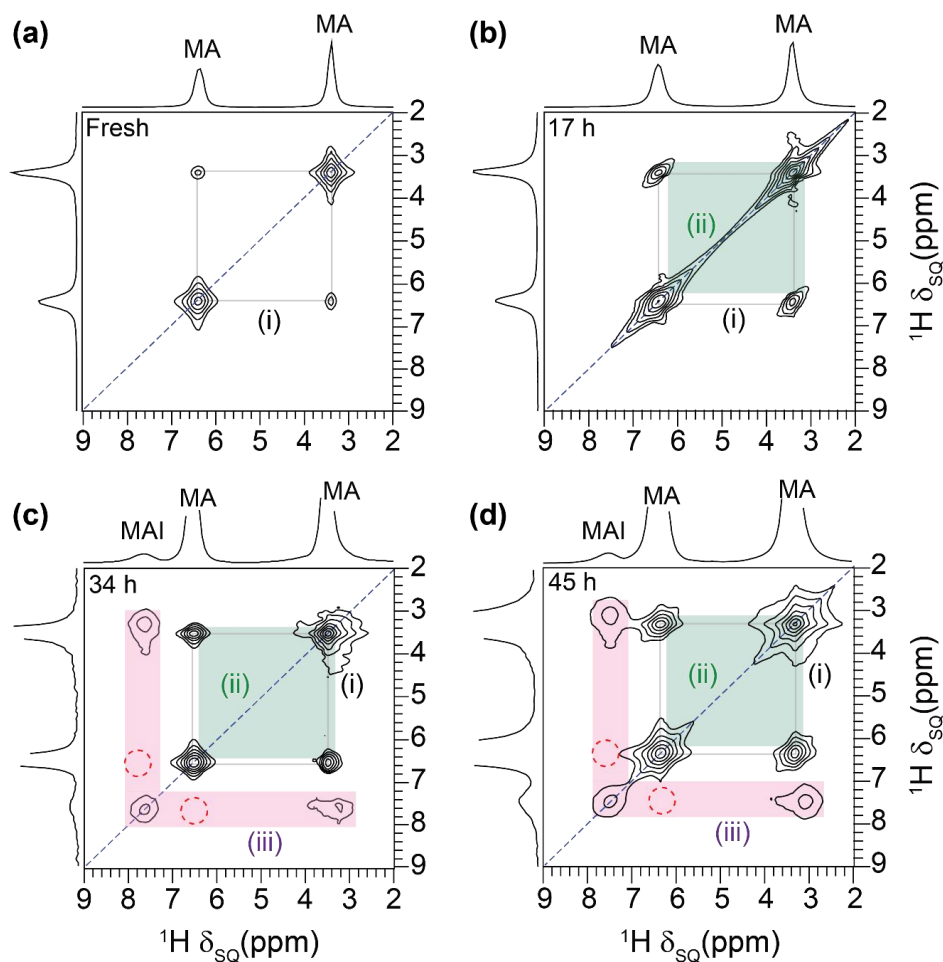


**Figure 3.7.** 2D <sup>1</sup>H-<sup>1</sup>H spin-diffusion spectra of MAPbI<sub>3</sub>: (a) fresh and (b-d) exposed to moisture (85% RH) during (b) 17 h, (c) 34 h and (d) 45 h, acquired at 18.8 T. The signals corresponding to different phases (i, ii, and iii) are color-coded, as depicted in Figure 3.2.

Next, 2D  $^1\text{H}$ - $^1\text{H}$  double-quantum–single-quantum (DQ-SQ) correlation experiments are described. As explained in Chapters 1 and 2, the DQ peaks can be excited for  $^1\text{H}$ - $^1\text{H}$  spin pairs ( $< 5 \text{ \AA}$ ) and are detected at the sum of SQ frequencies along the indirect (vertical) dimension of the 2D DQ-SQ correlation spectrum. In the 2D  $^1\text{H}$ - $^1\text{H}$  DQ-SQ spectrum of fresh MAPbI<sub>3</sub> (Figure 3.8), the on-diagonal DQ peak at  $3.4 + 3.4 = 6.8 \text{ ppm}$  and  $6.4 + 6.4 = 12.8 \text{ ppm}$  corresponds to  $^1\text{H}$  sites in the methyl and ammonium groups of MA<sup>+</sup> cations, respectively. The off-diagonal DQ peak at  $3.4 + 6.4 = 9.8 \text{ ppm}$  along the indirect dimension is due to intramolecular  $^1\text{H}$ - $^1\text{H}$  dipolar interactions between methyl protons and ammonium protons.

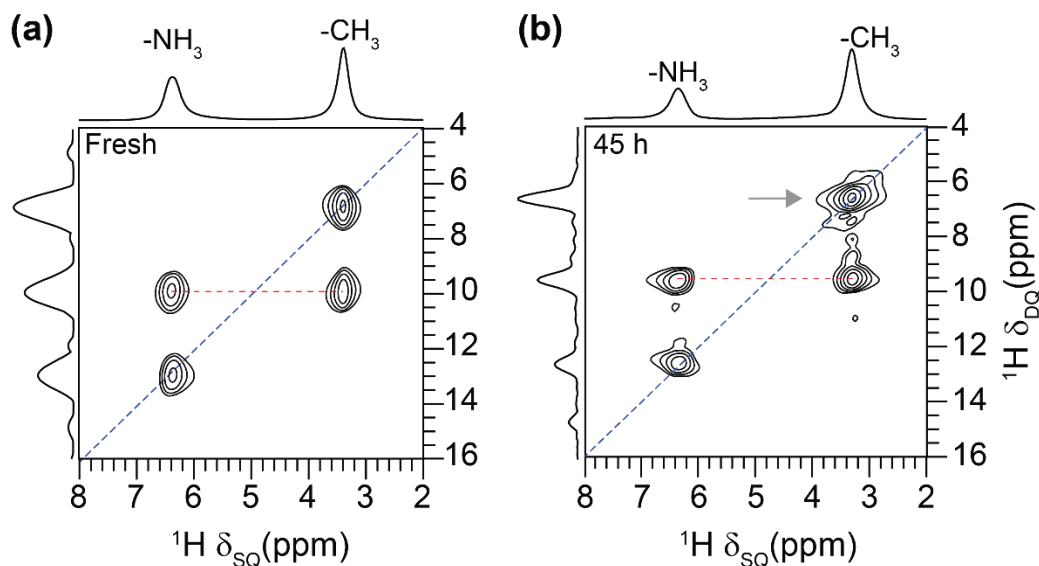


**Figure 3.8.** 2D  $^1\text{H}$ - $^1\text{H}$  DQ-SQ correlation NMR spectra of MAPbI<sub>3</sub> thin film acquired (a) before and (b) after exposure to 45 h moisture (85% RH). Gray arrow indicating distortions in the CH<sub>3</sub> peak corresponding to the formation of MAPbI<sub>3</sub> hydrate.

The DQ-SQ spectrum (Figure 3.8b) of the aged (45 h, 85% RH) MAPbI<sub>3</sub> material shows peaks that are akin to what is observed in MAPbI<sub>3</sub>, though subtle distortions in the CH<sub>3</sub> peak (gray arrow) indicate the formation of MAPbI<sub>3</sub> hydrate. Interestingly, 2D peaks for MAI are undetected, which could be reasoned to the microscopically distant distribution of MAI. This analysis further indicates that the water vapor concentration has a detrimental role on the degradation kinetics as well the types and concentrations of the different byproducts. To confirm this, similar experiments and analyses were carried out after exposure to MAPbI<sub>3</sub> for over a year at a relatively low water vapor concentration (40% RH).

The 2D  $^1\text{H}$ - $^1\text{H}$  SD and DQ-SQ spectra of aged (40% RH, 1 year)  $\text{MAPbI}_3$  (Figure 3.9) do not display the peaks corresponding to MAI, consistently with the analysis of 1D  $^1\text{H}$  NMR spectra presented above (Figure 3.6). However, a broadening of the diagonal and cross peaks is observed, which can be reasoned to the formation of  $\text{MAPbI}_3$  hydrate phase.<sup>72</sup> Key learning from this study is that the combination of XRD and ssNMR study allows the moisture-induced degradation of organic cations and inorganic species to be identified and distinguished. Based on these findings, it can be reasoned that at relatively high concentrations of water vapor (85% RH), the equilibrium shifts towards the formation of byproducts, but at the low concentration of water molecules, the equilibrium is retained between  $\text{MAPbI}_3$  and  $\text{MAPbI}_3\cdot\text{H}_2\text{O}$ , inhibiting the formation of MAI, enabling the materials to be stable for several months. The observed long-term stability of  $\text{MAPbI}_3$  at a low concentration of water vapor ( $\text{RH} \leq 40\%$ ) is consistent with the study by Wang et al., which showed the performance of the PSC device (with  $\text{Ag}/\text{spiro-OMeTAD}/\text{MAPbI}_3/\text{TiO}_2/\text{FTO}/\text{glass}$  architecture) is not significantly affected even after storing the material at 40% RH for 100 days.<sup>74</sup>

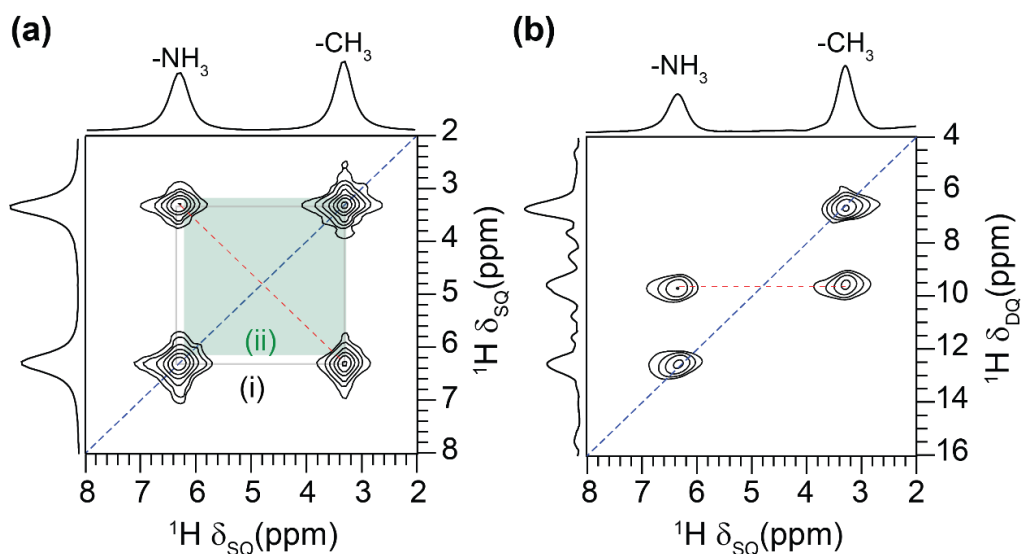


**Figure 3.9.** Solid-state 2D  $^1\text{H}$ - $^1\text{H}$  (a) spin-diffusion and (b) DQ-SQ MAS NMR spectra of aged (1 year, 40% RH)  $\text{MAPbI}_3$  acquired at 18.8 T, room temperature. The signals corresponding to different phases (i and ii) are color-coded, as depicted in Figure 3.2.

### 3.3. Defect-passivated methylammonium lead iodide and its moisture stability

The longevity of MAPbI<sub>3</sub> thin films can be enhanced, at least in part, by passivating grain boundaries using organic cations. For example, the addition of a Lewis base tetrapropylammonium iodide (TPAI) (<sup>1</sup>H spectrum in Figure 3.10) at a minuscule concentration (2-4 mol%) in conjunction with an excess of PbI<sub>2</sub> (9 mol%) enhances the stability of MAPbI<sub>3</sub>-based solar cells as well as reduces non-radiative energy losses by passivation of the surface defects through TPA<sup>+</sup> and the formation of low-dimensional TPAPb<sub>4</sub>I<sub>9</sub> within the grain boundaries.<sup>25</sup> It is of particular interest to understand how the passivating agents impact the kinetics of degradation reactions in MAPbI<sub>3</sub> thin films. To examine the role of surface passivation on MAPbI<sub>3</sub> degradation, the X-ray diffractograms and 1D/2D <sup>1</sup>H NMR spectra of MAPbI<sub>3</sub> treated with 4 mol.% of TPA passivating agent before and after the exposure to moisture at 85% RH were acquired and compared. In the XRD plot (Figure 3.11), the fresh material exhibits peaks at 14.1°, 20.0°, 23.4°, 24.4°, 28.4°, and 31.8° which can be attributed to the (110), (200), (211), (202), (220), and (310) diffraction planes of the modified MAPbI<sub>3</sub> perovskite. The lattice cell parameters are similar to MAPbI<sub>3</sub>: a = 9.002(2) Å, c = 12.937(2) Å, and a cell volume V = 1048.4(2) Å<sup>3</sup>, suggesting that the addition of TPA<sup>+</sup> does not lead to MAPbI<sub>3</sub> lattice expansion/contraction.<sup>25</sup>

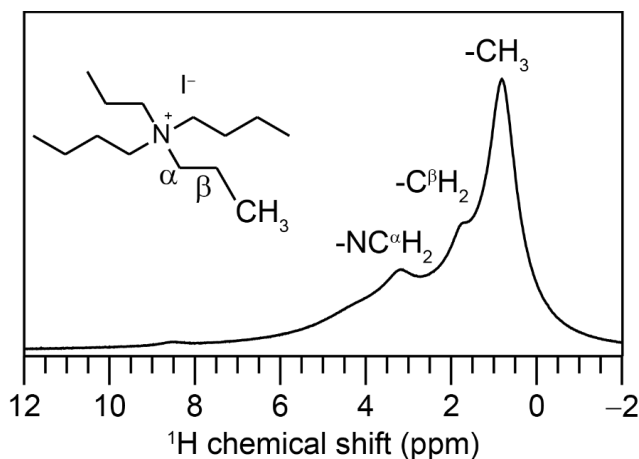


**Figure 3.10.** 1D <sup>1</sup>H NMR spectrum of TPAI acquired at 18.8 T, with MAS frequency of 58 kHz along with its structure.

To examine the influence of defect passivation on the moisture stability of MAPbI<sub>3</sub> perovskite, TPA<sup>+</sup>-passivated MAPbI<sub>3</sub> thin films were exposed to 85% RH. Upon exposure to

moisture at 85% RH for over 2 days, new diffraction peaks at  $10.5^\circ$  and  $12.6^\circ$  corresponding to  $(-101)$  and  $(001)$  planes of  $\text{MAPbI}_3 \cdot \text{H}_2\text{O}$  and  $\text{PbI}_2$  have emerged, respectively. In addition, traces of the  $\text{TPAPb}_4\text{I}_9$  phase may exist, which are formed only when excess of  $\text{PbI}_2$  is added during the synthesis of  $\text{MAPbI}_3 \cdot \text{TPA}$ .<sup>25</sup> This peak intensity increases as a function of moisture-exposure time. Interestingly, the intensity corresponds to the  $(-101)$  plane of  $\text{MAPbI}_3 \cdot \text{H}_2\text{O}$  in aged (72h, 85% RH)  $\text{MAPbI}_3 \cdot \text{TPA}$  (4 mol.% TPA) is less-intense compared to the same reflection in aged (72h, 85% RH)  $\text{MAPbI}_3$ , as depicted in Figures 3.2 and 3.11.

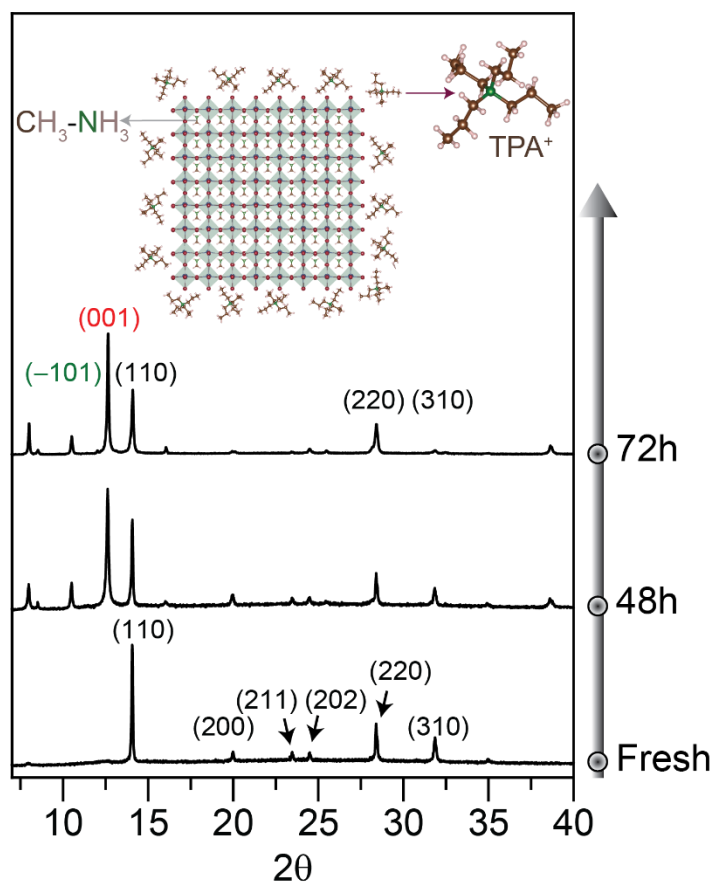


**Figure 3.11.** XRD patterns of  $\text{MAPbI}_3 \cdot \text{TPA}$  (4 mol%) before and after exposure to moisture (85% RH) with Bragg reflections labeled for  $\text{MAPbI}_3$  (black),  $\text{MAPbI}_3 \cdot \text{H}_2\text{O}$  (green), and  $\text{PbI}_2$  (red) along with the schematic of  $\text{MAPbI}_3 \cdot \text{TPA}$  (4 mol.%) in the inset.

The moisture-induced degradation reactions in  $\text{MAPbI}_3 \cdot \text{TPA}$  (4 mol%) probed by 1D  $^1\text{H}$  MAS NMR provides complementary information on the reaction kinetics. In the 1D  $^1\text{H}$  NMR spectrum (Figure 3.12) of fresh  $\text{MAPbI}_3 \cdot \text{TPA}$  (4%), the strong intensity  $^1\text{H}$  peaks at 3.5 and 6.5

ppm are due to  $\text{MA}^+$  cation in  $\text{MAPbI}_3$ , and the weak intensity signals at 4.9, 1.3, and 0.9 ppm due to the  $\text{NC}^\alpha\text{H}_2$ ,  $\text{C}^\beta\text{H}_2$  and  $\text{CH}_3$  protons of  $\text{TPA}^+$ , respectively. After exposure to moisture (85% RH, 15h), the intensity of the  $^1\text{H}$  signals associated with  $\text{TPA}^+$  cation decreases, and a new peak at 4.0 ppm emerges upon prolonged exposure. More importantly, a very weak intensity peak centered at 7.3 ppm appeared in the  $^1\text{H}$  spectrum (Figure 3.12, magnified inset) acquired after exposure to moisture for 48 h, which can be ascribed to the  $-\text{NH}_3^+$  peak of MAI, akin to what is observed in the pristine  $\text{MAPbI}_3$ . Even after 72 h exposure to 85% RH, these TPA signals are visible, and the key degradation product (MAI) is only present in a minuscule concentration (estimated  $\sim 5\%$  based on the weak intensity peaks). It suggests that only a small amount of  $\text{MAPbI}_3$  is converted into MAI, conforming that the introduction of  $\text{TPA}^+$  cation enhances moisture stability and decelerates the kinetics of moisture-induced degradation reactions.

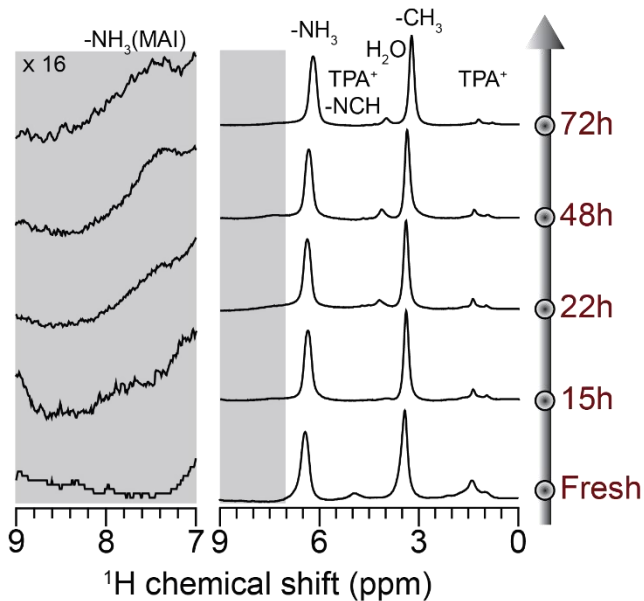


**Figure 3.12.** Solid-state 1D  $^1\text{H}$  MAS NMR spectra of  $\text{MAPbI}_3\text{.TPA}$  (4 mol%) before and after exposure to moisture at 85% RH acquired at 18.8 T. Grey band indicates the region (7-9 ppm, inset) corresponding to the  $\text{NH}_3$  signal of MAI.

Much similar to pristine  $\text{MAPbI}_3$ , the extent of water vapor concentration plays a crucial role in driving the degradation pathway forward for the same  $\text{MAPbI}_3\text{.TPA}$  (4mol.%) material. To access this, we exposed the defected passivated  $\text{MAPbI}_3\text{.TPA}$  (4mol.%) material to 40% RH and  $^1\text{H}$  NMR spectra were acquired at different time periods (Figure 3.13). While these spectra

show no particular signatures of the peaks corresponding to the degradation products, however, a broadening of the proton peaks for the  $\text{-NCH}_2$  site of  $\text{TPA}^+$  cation is observed after 9 months of exposure to 40% RH. More importantly, the peaks corresponding to MAI are undetected (magnified inset) even after 1 year of exposure to 40% RH, indicating that the defect passivation significantly improves the longevity of  $\text{MAPbI}_3$  thin films.

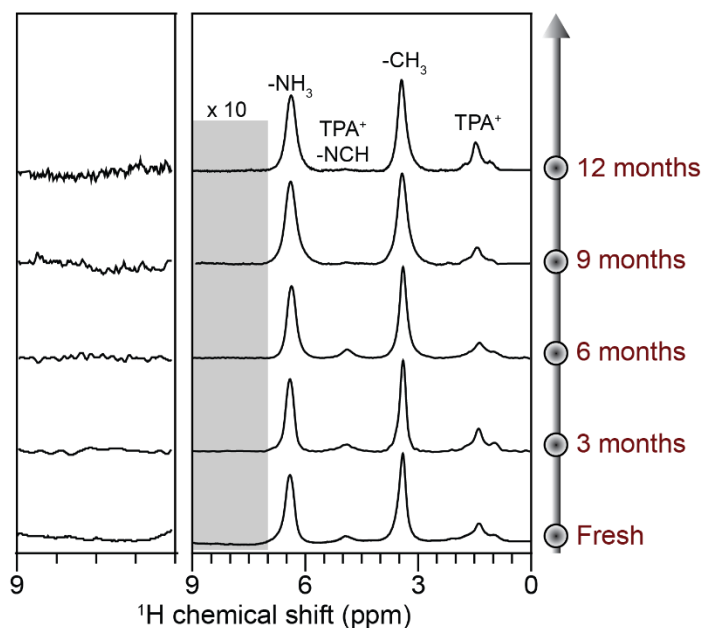


**Figure 3.13.** Solid-state 1D  $^1\text{H}$  MAS NMR spectra of  $\text{MAPbI}_3\cdot\text{TPA}$  (4 mol%) before and after exposure to moisture at 40% RH during duration indicated on the right side of the spectra acquired at 18.8 T. The inset on the left shows the expanded region (7-9 ppm) of the  $\text{NH}_3$  signal of MAI.

Insight into the through-space proximities and intermolecular interactions between  $\text{TPA}^+$  cations and  $\text{MAPbI}_3$  in fresh and aged thin films can be obtained by analyzing 2D NMR spectra. For fresh  $\text{MAPbI}_3\cdot\text{TPA}$  (4 mol.%), the 2D  $^1\text{H}$ - $^1\text{H}$  SD spectrum acquired with 500 ms mixing time (Figure 3.14a) displays off-diagonal peaks due to intramolecular  $^1\text{H}$ - $^1\text{H}$  dipolar interactions between methyl and ammonium proton of  $\text{MA}^+$  cations (black shaded rectangle) as well as intermolecular  $^1\text{H}$ - $^1\text{H}$  dipolar interactions between  $\text{MA}^+$  protons and  $\text{TPA}^+$  protons (blue shaded rectangle), corroborating the molecular-level mixing of the  $\text{TPA}^+$  and  $\text{MAPbI}_3$ . The cross-peaks between  $\text{C}^\beta\text{H}_2$  and  $\text{NC}^\alpha\text{H}_2$  groups of  $\text{TPA}^+$  are not detected owing to the low concentration of these cations and the distribution of  $\text{TPA}^+$  cations on the  $\text{MAPbI}_3$  particles. In 2D  $^1\text{H}$ - $^1\text{H}$  DQ-SQ

NMR spectrum of fresh MAPbI<sub>3</sub>.TPA (4 mol.%) presented in Figure 3.14b, the autocorrelation peaks at 0.9 + 0.9 = 1.8 ppm, 1.3 + 1.3 = 2.6 ppm and 4.9 + 4.9 = 9.8 ppm, stems from the short-range proximities between protons within methyl, C<sup>β</sup>H<sub>2</sub> and -NC<sup>α</sup>H<sub>2</sub> groups of TPA<sup>+</sup>, respectively. No cross-peak between C<sup>β</sup>H<sub>2</sub> and -NC<sup>α</sup>H<sub>2</sub> groups is detected owing to the low concentration of TPA<sup>+</sup> as well as the weaker dipolar interactions between vicinal protons compared to those between geminal ones. Furthermore, the BaBa recoupling is affected by dipolar truncation (the recoupling of a small dipolar coupling is severely diminished in the presence of a third spin that is strongly coupled to one of the first two spins), and the intensity of cross-peaks between remote protons is attenuated by the dipolar coupling with the nearest protons.<sup>75</sup> The autocorrelation peaks at 3.5 + 3.5 = 7.0 ppm and 6.5 + 6.5 = 13.0 ppm stem from proximities within the methyl and ammonium groups of MA<sup>+</sup> cations. Cross-peaks between protons of these groups are also observed.

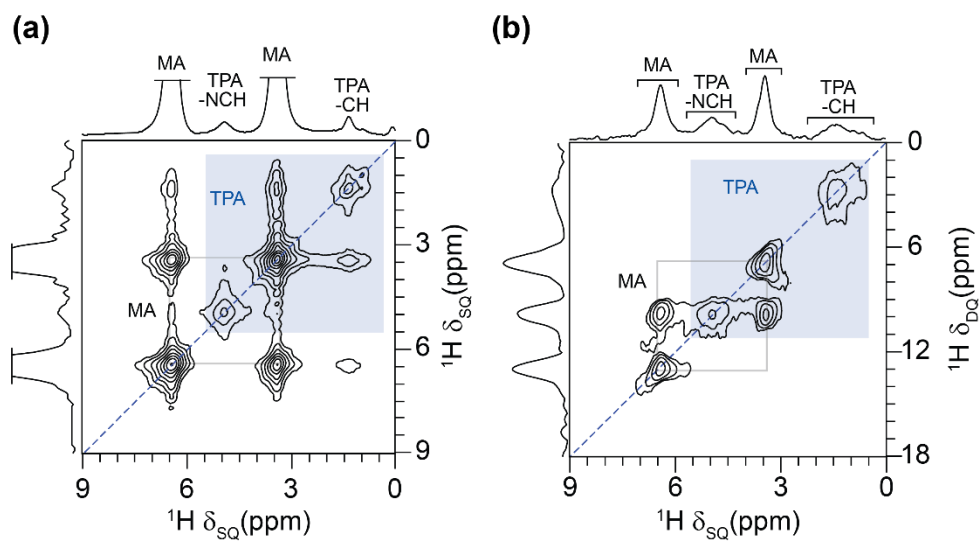


**Figure 3.14.** Solid-state 2D (a)  $^1\text{H}$ - $^1\text{H}$  SD and (b)  $^1\text{H}$ - $^1\text{H}$  DQ-SQ correlation NMR spectra of pristine MAPbI<sub>3</sub>.TPA (4mol.%).

After exposure to MAPbI<sub>3</sub>.TPA (4 mol.%) to moisture for 72 h at 85% RH, the 2D  $^1\text{H}$ - $^1\text{H}$  SD spectrum (Figure 3.15a) corroborates the decreased intensity of TPA<sup>+</sup> cations since the diagonal peaks of NC<sup>α</sup>H<sub>2</sub> groups as well as the cross-peaks between the TPA<sup>+</sup>, and MA<sup>+</sup> signals are also not detected. The magenta rectangle in Figure 3.15a highlights the emergence of MAI as it marks the cross-peaks between the methyl and ammonium protons of MAI. However, the 2D



$^1\text{H}$ - $^1\text{H}$  DQ-SQ NMR spectrum (Figure 3.15b) shows the 2D peaks identical to those observed in the fresh sample, except the on-diagonal peak of the  $\text{NC}^\alpha\text{H}_2$  group (as shown in the red arrow). The absence of this signal is consistent with the reduced intensity of  $\text{TPA}^+$  cations in the 1D spectra owing to subtle cationic rearrangement in the presence of moisture.

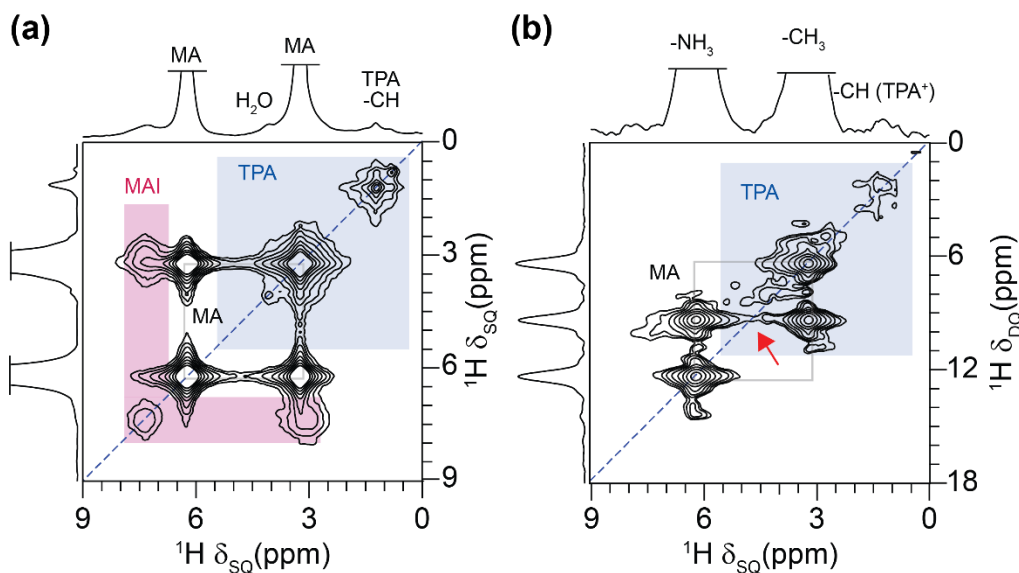


**Figure 3.15.** Solid-state 2D  $^1\text{H}$ - $^1\text{H}$  (a) spin-diffusion and (b) DQ-SQ MAS NMR spectra of aged (72 h, 85% RH)  $\text{MAPbI}_3\cdot\text{TPA}$  (4mol.%).

After a year of exposure of  $\text{MAPbI}_3\cdot\text{TPA}$  (4 mol.%) to low water vapor concentration (40% RH), 2D  $^1\text{H}$ - $^1\text{H}$  SD and DQ-SQ correlation NMR spectra were acquired and compared. In the 2D  $^1\text{H}$ - $^1\text{H}$  SD NMR spectrum of this material (Figure 3.16a), the diagonal peaks of the  $\text{NC}^\alpha\text{H}_2$  group of the  $\text{TPA}^+$  group are also not detected but a diagonal peak at 4.0 ppm is detected and is hypothesized to be originating from the adsorbed water. In addition, cross-peak between  $\text{C}^\beta\text{H}_2$  protons of  $\text{TPA}^+$  and methyl protons of  $\text{MA}^+$  cations is detected. This observation indicates that some  $\text{TPA}^+$  cations remain in close proximity to  $\text{MA}^+$ , however, the intensity of these cross-peaks is reduced when compared to the fresh sample. In addition, the signals corresponding to the MAI phase are undetected. The 2D DQ-SQ correlation spectrum of the same sample (Figure 3.16b) exhibits on-diagonal peaks that are similar to the fresh material, but the intensities of the peaks associated with  $\text{NC}^\alpha\text{H}_2$  groups of  $\text{TPA}^+$  are decreased, and a peak broadening is observed, indicating the disorder in the local chemical environments of  $\text{TPA}^+$  cations.

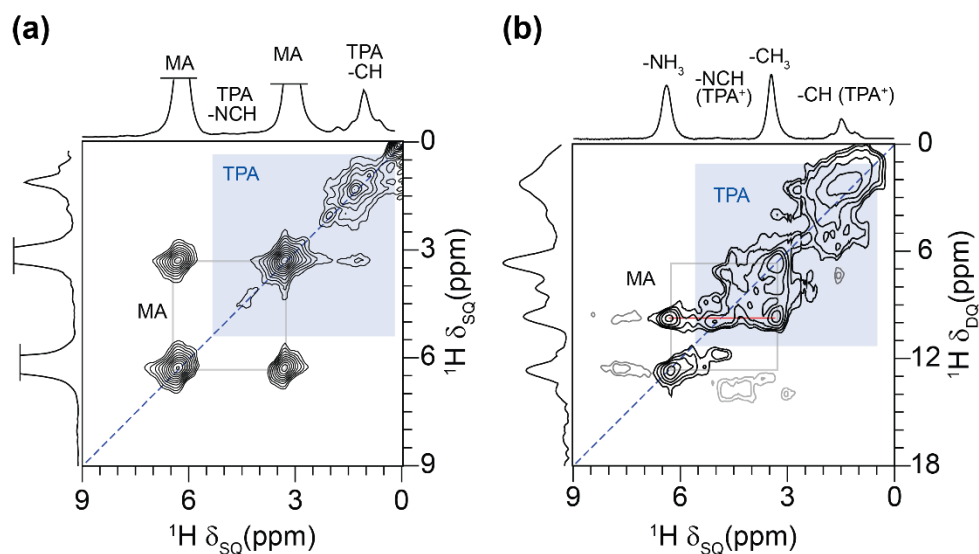


**Figure 3.16.** Solid-state 2D  $^1\text{H}$ - $^1\text{H}$  (a) spin-diffusion and (b) DQ-SQ MAS NMR spectra of aged (1 year, 40% RH)  $\text{MAPbI}_3\cdot\text{TPA}$  (4mol.%).

Together, a systematic XRD and ssNMR study confirms that the concentration of water molecules plays an important role in governing the instability of defect-passivated hybrid perovskite thin films. Take home message from this study is that the defect passivation reduces the degree penetration of water molecules into the perovskite slabs in the presence of low concentration of water molecules (40% RH or lower), however, exposure to high water concentration (85% RH) may lead to surface wettability of  $\text{TPA}^+$  species and allows the water molecules to enter into the  $\text{MAPbI}_3$  lattice and leads to the formation of  $\text{MAPbI}_3$  hydrate, as detected from XRD, and correspondingly MAI that can be detected by 1D/2D  $^1\text{H}$  ssNMR techniques. The identification of degradation products by examining organic cations is a key outcome, as the detection is less straightforward from long-range techniques such as XRD and electron microscopy.

### 3.4. Moisture-catalyzed transformative reactions and degradation products: Summary

Figure 3.17 summarizes the different reaction pathways and the intermediate species produced by the exposure of perovskite thin films/crystals to moisture at different vapor concentrations, as characterized by XRD and ssNMR techniques, in Chapters 2 and 3. These results indicate that the  $\text{MAPbI}_3$  transforms into  $\text{MAPbI}_3$  hydrate,  $\text{PbI}_2$ , and MAI in the presence of a relatively high concentration of water vapor (85% RH), but the same material in the

presence of low water vapor content (40% RH) leads to interconversion between  $\text{MAPbI}_3$  and its hydrate  $\text{MAPbI}_3 \cdot \text{H}_2\text{O}$ , which are in an equilibrium, inhibiting the degradation reactions to complete. In contrast to this, the defect passivated  $\text{MAPbI}_3 \cdot \text{TPA}$  (4 mol.%) tends to undergo transformative reactions at a much slower rate than pristine  $\text{MAPbI}_3$  even at high concentration of water vapor (Figure 3.17b), leading to enhanced moisture stability, although a minuscule concentration of MAI (~5%) is formed after exposure to moisture for over 3 days. The longevity of this material is further enhanced in the presence of low water vapor concentration in the air (40% RH). As discussed in Chapter 2, the FA-rich CsMAFA appears to be the most stable against moisture among the hybrid perovskite thin films studied here. However, some of the  $\text{Cs}^+$  ions appear to migrate from the perovskite framework to form non-perovskite inorganic salts, whereby the concentration of water molecules in the vapor determines the rate of the degradation reaction. The organic cations ( $\text{MA}^+$ ,  $\text{FA}^+$ ) tend to be part of the perovskite structure even after exposure to moisture for a prolonged duration of up to one year. This is particularly intriguing because the pristine  $\alpha\text{-FAPbI}_3$ ,  $\alpha\text{-CsPbI}_3$  as well as  $\text{MAPbI}_3$  are unstable with respect to moisture,<sup>19,48,52,76</sup> but their mixed cation alloy CsMAFA is stable. A detailed understanding of cation mapping in this formulation using XRD and ssNMR techniques is less straightforward and necessitates further investigation.<sup>77</sup> It is noteworthy that the degradation caused by the other stimuli, such as light and temperature, were not subjected to the  $\text{MAPbI}_3$ -based and CsMAFA-based perovskites, thus disentangling the impact of these factors on material degradation. However, an accurate understanding of perovskite degradation in the presence of moisture, light, and temperature is much more complex and strongly depends on the compositions and structures as well as exposure conditions. The role played by each of these factors needs to be studied and compared in an independent manner.

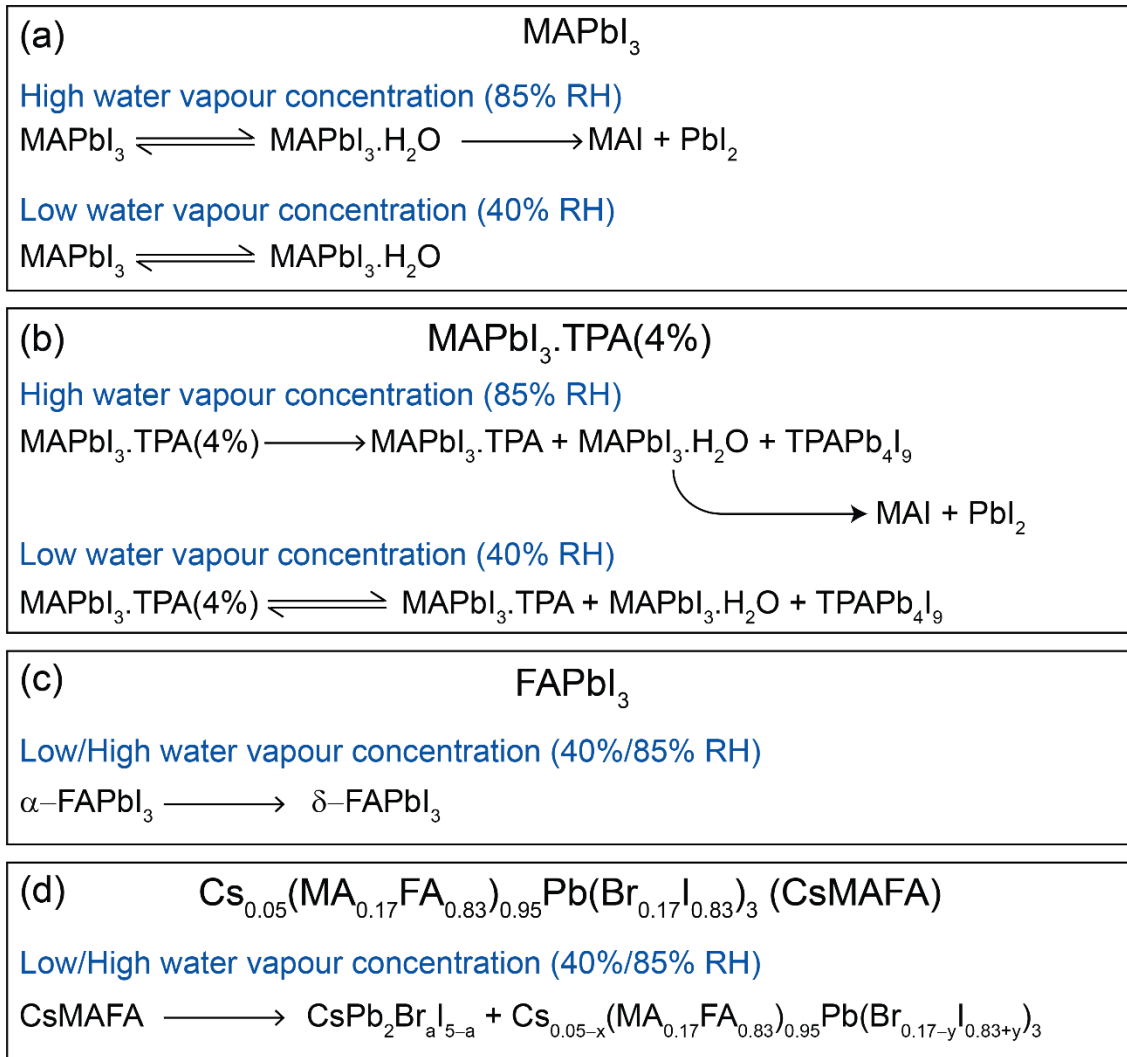


**Figure 3.17.** Proposed reaction degradation pathways of (a) MAPbI<sub>3</sub>, (b) MAPbI<sub>3</sub>·TPA (4 mol.%), (c) FAPbI<sub>3</sub>, and (d) CsMAFA materials after exposure to different water vapor concentration (85%/ 40% RH).

**Table 3.2.** Moisture-induced degradation products in hybrid perovskites as analyzed by different characterization techniques.

Material	Exposure to moisture	Byproducts	Characterization technique	Ref.
MAPbI <sub>3</sub> (thin film)	40% RH	MAPbI <sub>3</sub> .H <sub>2</sub> O	ssNMR	This Chapter
MAPbI <sub>3</sub> (thin film)	85% RH	MAPbI <sub>3</sub> .H <sub>2</sub> O, MAI	XRD, ssNMR	This Chapter
MAPbI <sub>3</sub> .TPA (thin film)	40% RH	-	ssNMR	This Chapter
MAPbI <sub>3</sub> .TPA (thin film)	85% RH	TPAPb <sub>4</sub> I <sub>9</sub> , MAI	XRD, ssNMR	This Chapter
CsMAFA (thin film)	40% RH	CsPb <sub>2</sub> Br <sub>x</sub> I <sub>5-x</sub>	ssNMR	Chapter 2
CsMAFA (thin film)	85% RH	CsPb <sub>2</sub> Br <sub>x</sub> I <sub>5-x</sub>	ssNMR	Chapter 2
MAPbI <sub>3</sub> (crystal)	80% RH	MAPbI <sub>3</sub> .H <sub>2</sub> O	ssNMR	45
MAPbI <sub>3</sub> (crystal)	Aqueous solution	MAPbI <sub>3</sub> .H <sub>2</sub> O, PbI <sub>2</sub>	ssNMR	45
MAPbI <sub>3</sub> (crystal)	Aqueous solution	MAPbI <sub>3</sub> .H <sub>2</sub> O	XRD	73
MAPbI <sub>3</sub> (crystal)	Aqueous solution	MA <sub>4</sub> PbI <sub>6</sub> .2H <sub>2</sub> O	XRD	78
MAPbI <sub>3</sub> (thin film)	90% RH	MA <sub>4</sub> PbI <sub>6</sub> .2H <sub>2</sub> O	XRD	79
MAPbI <sub>3</sub> (thin film)	Water vapor	MA <sub>4</sub> PbI <sub>6</sub> .2H <sub>2</sub> O	Grazing incidence X-ray diffraction	80
MAPbI <sub>3</sub> (thin film)	60% RH	PbI <sub>2</sub>	XRD	81
CsMAFA (thin film)	85% RH	CsPb <sub>2</sub> Br <sub>5</sub> , Cs <sub>0.05-x</sub> (MA <sub>0.17</sub> FA <sub>0.83</sub> ) <sub>0.95</sub> Pb(Br <sub>0.17-2y</sub> I <sub>0.83+2y</sub> ) <sub>3</sub>	TEM, XRD, ssNMR	51
α- FAPbI <sub>3</sub> (thin film)	85% RH	δ-FAPbI <sub>3</sub>	FT-IR, AFM, XRD	82
α- FAPbI <sub>3</sub> (crystal)	40% RH	δ-FAPbI <sub>3</sub>	ssNMR	<sup>52</sup> , Chapter-2
α- FAPbI <sub>3</sub> (crystal)	85% RH	δ-FAPbI <sub>3</sub>	XRD, ssNMR	<sup>52</sup> , Chapter-2

Different degradation products of MA and FA-based perovskites studied by different analytical techniques are summarized in Table 3.2. A broad spectrum of analytical techniques, including XRD and electron microscopy, are suitable for tracking the morphological changes in the perovskite thin films. Short-range probes, such as ssNMR spectroscopy, are particularly important to correlate and complement the results obtained by long-range probes. In addition, *in situ* techniques with adequate spatial and temporal resolution need to be applied to gain insight into the structural changes in order to comprehensively understand the macroscopic physical performance of the PSCs devices. In addition, extending these understandings to the photoactive layer degradation in encapsulated PV devices is less straightforward and calls for further investigation. Nonetheless, these results and analysis are particularly relevant in the context of unraveling interfacial interactions between passivating agents and perovskite layer, and structural transformations within the perovskite layers. Therefore, the molecular level analysis has much wider relevance in the context of developing novel molecular passivators and perovskite formulations.

### 3.5. Conclusion

Molecular level understanding of transformative and cascading degradation reactions of hybrid perovskites is a crucially important factor in developing environmentally stable perovskite-based optoelectronic devices. This Chapter describes a detailed assessment of long-term moisture stability and the associated degradation kinetics for up to a year for MAPbI<sub>3</sub> and MAPbI<sub>3</sub>.TPA (4 mol%) thin films. For MAPbI<sub>3</sub>, exposure to moisture leads to the formation of aMAPbI<sub>3</sub> hydrate, PbI<sub>2</sub>, as identified by XRD, and MAI byproduct detected by ssNMR techniques. ssNMR spectroscopy aids in determining dilute organic degradation products that are challenging to detect using other structure-determining techniques. In all cases, the kinetics of the degradation reaction depends on the concentration of water molecules in the vapor. The higher water concentration (85% RH) shifts the equilibrium towards the formation of byproducts, and the relatively low water vapor concentration (40% RH) leads to an equilibrium between MAPbI<sub>3</sub> and MAPbI<sub>3</sub>.H<sub>2</sub>O. Consequently, the moisture stability of MAPbI<sub>3</sub> can be adjusted from a few hours to several months, depending on the concentration of water vapor. Surface defect passivation by TPA<sup>+</sup> cations impedes the moisture-induced degradation processes, however, prolonged exposure to moisture triggers the degradation process leading to the

formation of organic and inorganic byproducts as identified by XRD and 1D/2D NMR techniques. One key feature of this study is that the degradation of the MAPbI<sub>3</sub>-based material is solely triggered by moisture, thus disentangling the impact of light and temperature. This approach can be extended to investigate the structural stability of organic/ hybrid materials towards different stress factors.

### 3.6. References

- 1 A. Kojima, K. Teshima, Y. Shirai and T. Miyasaka, *J. Am. Chem. Soc.*, 2009, **131**, 6050–6051.
- 2 G. Kieslich, S. Sun and A. K. Cheetham, *Chem. Sci.*, 2014, **5**, 4712–4715.
- 3 W. Travis, E. N. K. Glover, H. Bronstein, D. O. Scanlon and R. G. Palgrave, *Chem. Sci.*, 2016, **7**, 4548–4556.
- 4 M. M. Lee, J. Teuscher, T. Miyasaka, T. N. Murakami and H. J. Snaith, *Science*, 2012, **338**, 643–647.
- 5 G. Xing, N. Mathews, S. Sun, S. S. Lim, Y. M. Lam, M. Grätzel, S. Mhaisalkar and T. C. Sum, *Science*, 2013, **342**, 344–347.
- 6 S. D. Stranks, G. E. Eperon, G. Grancini, C. Menelaou, M. J. P. Alcocer, T. Leijtens, L. M. Herz, A. Petrozza and H. J. Snaith, *Science*, 2013, **342**, 341–344.
- 7 A. Krishna, H. Zhang, Z. Zhou, T. Gallet, M. Dankl, O. Ouellette, F. T. Eickemeyer, F. Fu, S. Sanchez, M. Mensi, S. M. Zakeeruddin, U. Rothlisberger, G. N. M. Reddy, A. Redinger, M. Grätzel and A. Hagfeldt, *Energy Environ. Sci.*, 2021, **14**, 5552–5562.
- 8 G. E. Eperon, S. D. Stranks, C. Menelaou, M. B. Johnston, L. M. Herz and H. J. Snaith, *Energy Environ. Sci.*, 2014, **7**, 982–988.
- 9 A. Binek, F. C. Hanusch, P. Docampo and T. Bein, *J. Phys. Chem. Lett.*, 2015, **6**, 1249–1253.
- 10 N. Pellet, P. Gao, G. Gregori, T. Y. Yang, M. K. Nazeeruddin, J. Maier and M. Grätzel, *Angew. Chemie Int. Ed.*, 2014, **53**, 3151–3157.
- 11 T. M. Koh, K. Fu, Y. Fang, S. Chen, T. C. Sum, N. Mathews, S. G. Mhaisalkar, P. P. Boix

- and T. Baikie, *J. Phys. Chem. C*, 2014, **118**, 16458–16462.
- 12 O. J. Weber, B. Charles and M. T. Weller, *J. Mater. Chem. A*, 2016, **4**, 15375–15382.
- 13 M. Saliba, T. Matsui, J. Y. Seo, K. Domanski, J. P. Correa-Baena, M. K. Nazeeruddin, S. M. Zakeeruddin, W. Tress, A. Abate, A. Hagfeldt and M. Grätzel, *Energy Environ. Sci.*, 2016, **9**, 1989–1997.
- 14 F. Brivio, J. M. Frost, J. M. Skelton, A. J. Jackson, O. J. Weber, M. T. Weller, A. R. Goñi, A. M. A. Leguy, P. R. F. Barnes and A. Walsh, *Phys. Rev. B - Condens. Matter Mater. Phys.*, 2015, **92**, 144308.
- 15 P. S. Whitfield, N. Herron, W. E. Guise, K. Page, Y. Q. Cheng, I. Milas and M. K. Crawford, *Sci. Rep.*, 2016, **6**, 35685.
- 16 D. Bryant, N. Aristidou, S. Pont, I. Sanchez-Molina, T. Chotchunangatchaval, S. Wheeler, J. R. Durrant and S. A. Haque, *Energy Environ. Sci.*, 2016, **9**, 1655–1660.
- 17 L. Ma, D. Guo, M. Li, C. Wang, Z. Zhou, X. Zhao, F. Zhang, Z. Ao and Z. Nie, *Chem. Mater.*, 2019, **31**, 8515–8522.
- 18 G. Niu, X. Guo and L. Wang, *J. Mater. Chem. A*, 2015, **3**, 8970–8980.
- 19 S. Kundu and T. L. Kelly, *EcoMat*, 2020, **2**, e12025.
- 20 M. V. Khenkin, E. A. Katz, A. Abate, G. Bardizza, J. J. Berry, C. Brabec, F. Brunetti, V. Bulović, Q. Burlingame, A. Di Carlo, R. Checharoen, Y. B. Cheng, A. Colmann, S. Cros, K. Domanski, M. Dusza, C. J. Fell, S. R. Forrest, Y. Galagan, D. Di Girolamo, M. Grätzel, A. Hagfeldt, E. von Hauff, H. Hoppe, J. Kettle, H. Köbler, M. S. Leite, S. (Frank) Liu, Y. L. Loo, J. M. Luther, C. Q. Ma, M. Madsen, M. Manceau, M. Matheron, M. McGehee, R. Meitzner, M. K. Nazeeruddin, A. F. Nogueira, Ç. Odabaşı, A. Osherov, N. G. Park, M. O. Reese, F. De Rossi, M. Saliba, U. S. Schubert, H. J. Snaith, S. D. Stranks, W. Tress, P. A. Troshin, V. Turkovic, S. Veenstra, I. Visoly-Fisher, A. Walsh, T. Watson, H. Xie, R. Yıldırım, S. M. Zakeeruddin, K. Zhu and M. Lira-Cantu, *Nat. Energy*, 2020, **5**, 35–49.
- 21 D. Zhang, D. Li, Y. Hu, A. Mei and H. Han, *Commun. Mater.*, 2022, **3**, 58.
- 22 D. Y. Son, J. W. Lee, Y. J. Choi, I. H. Jang, S. Lee, P. J. Yoo, H. Shin, N. Ahn, M. Choi,



- D. Kim and N. G. Park, *Nat. Energy*, , DOI:10.1038/nenergy.2016.81.
- 23 M. Wang, F. Cao, K. Deng and L. Li, *Nano Energy*, 2019, **63**, 103867.
- 24 F. Zhang, D. Bi, N. Pellet, C. Xiao, Z. Li, J. J. Berry, S. M. Zakeeruddin, K. Zhu and M. Grätzel, *Energy Environ. Sci.*, 2018, **11**, 3480–3490.
- 25 A. Krishna, M. A. Akhavan Kazemi, M. Sliwa, G. N. M. Reddy, L. Delevoye, O. Lafon, A. Felten, M. T. Do, S. Gottis and F. Sauvage, *Adv. Funct. Mater.*, 2020, **30**, 1909737.
- 26 D. Bi, X. Li, J. V. Milić, D. J. Kubicki, N. Pellet, J. Luo, T. LaGrange, P. Mettraux, L. Emsley, S. M. Zakeeruddin and M. Grätzel, *Nat. Commun.*, 2018, **9**, 4482.
- 27 C. Qin, T. Matsushima, T. Fujihara, C. Adachi, C. Qin, T. Matsushima, C. Adachi and T. Fujihara, *Adv. Mater.*, 2017, **29**, 1603808.
- 28 R. Wang, J. Xue, K. L. Wang, Z. K. Wang, Y. Luo, D. Fenning, G. Xu, S. Nuryyeva, T. Huang, Y. Zhao, J. L. Yang, J. Zhu, M. Wang, S. Tan, I. Yavuz, K. N. Houk and Y. Yang, *Science*, 2019, **366**, 1509–1513.
- 29 S. Wang, A. Wang, X. Deng, L. Xie, A. Xiao, C. Li, Y. Xiang, T. Li, L. Ding and F. Hao, *J. Mater. Chem. A*, 2020, **8**, 12201–12225.
- 30 J. Cao, X. Jing, J. Yan, C. Hu, R. Chen, J. Yin, J. Li and N. Zheng, *J. Am. Chem. Soc.*, 2016, **138**, 9919–9926.
- 31 C. Li, A. Wang, L. Xie, X. Deng, K. Liao, J. A. Yang, T. Li and F. Hao, *J. Mater. Chem. A*, 2019, **7**, 24150–24163.
- 32 W. Zhao, Z. Yao, F. Yu, D. Yang, S. Liu, W. Zhao, Z. Yao, F. Yu, D. Yang and S. Liu, *Adv. Sci.*, 2018, **5**, 1700131.
- 33 J. Zhang, R. Chen, Y. Wu, M. Shang, Z. Zeng, Y. Zhang, Y. Zhu, L. Han, J. Zhang, R. Chen, Z. Zeng, Y. Zhang, Y. Zhu, Y. Wu, L. Han and M. Shang, *Adv. Energy Mater.*, 2018, **8**, 1701981.
- 34 M. Abdi-Jalebi, Z. Andaji-Garmaroudi, S. Cacovich, C. Stavrakas, B. Philippe, J. M. Richter, M. Alsari, E. P. Booker, E. M. Hutter, A. J. Pearson, S. Lilliu, T. J. Savenije, H. Rensmo, G. Divitini, C. Ducati, R. H. Friend and S. D. Stranks, *Nature*, 2018, **555**, 497–501.

- 35 J. Li, F. Cai, L. Yang, F. Ye, J. Zhang, R. S. Gurney, D. Liu and T. Wang, *Appl. Phys. Lett.*, 2017, **111**, 053301.
- 36 S. Li, Z. Shi, F. Zhang, L. Wang, Z. Ma, D. Yang, Z. Yao, D. Wu, T. T. Xu, Y. Tian, Y. Zhang, C. Shan and X. J. Li, *Chem. Mater.*, 2019, **31**, 3917–3928.
- 37 N. K. Noel, A. Abate, S. D. Stranks, E. S. Parrott, V. M. Burlakov, A. Goriely and H. J. Snaith, *ACS Nano*, 2014, **8**, 9815–9821.
- 38 J. Kim, A. Ho-Baillie and S. Huang, *Sol. RRL*, 2019, **3**, 1800302.
- 39 Y. Zhao, P. Zhu, S. Huang, S. Tan, M. Wang, R. Wang, J. Xue, T. H. Han, S. J. Lee, A. Zhang, T. Huang, P. Cheng, D. Meng, J. W. Lee, J. Marian, J. Zhu and Y. Yang, *J. Am. Chem. Soc.*, 2020, **142**, 20071–20079.
- 40 L. Fu, H. Li, L. Wang, R. Yin, B. Li and L. Yin, *Energy Environ. Sci.*, 2020, **13**, 4017–4056.
- 41 Q. Peng, X. Zheng, X. Zhang, S. You, L. Li, Y. Zhao, S. Zhang, L. Luo, H. Zeng and X. Li, *Front. Chem.*, 2020, **8**, 825.
- 42 I. Deretzis, A. Alberti, G. Pellegrino, E. Smecca, F. Giannazzo, N. Sakai, T. Miyasaka and A. La Magna, *Appl. Phys. Lett.*, 2015, **106**, 131904.
- 43 J. Zhao, B. Cai, Z. Luo, Y. Dong, Y. Zhang, H. Xu, B. Hong, Y. Yang, L. Li, W. Zhang and C. Gao, *Sci. Rep.*, 2016, **6**, 21976.
- 44 J. Huang, S. Tan, P. D. Lund and H. Zhou, *Energy Environ. Sci.*, 2017, **10**, 2284–2311.
- 45 A. M. Askar, G. M. Bernard, B. Wiltshire, K. Shankar and V. K. Michaelis, *J. Phys. Chem. C*, 2017, **121**, 1013–1024.
- 46 E. J. Juarez-Perez, L. K. Ono and Y. Qi, *J. Mater. Chem. A*, 2019, **7**, 16912–16919.
- 47 X. Zheng, C. Wu, S. K. Jha, Z. Li, K. Zhu and S. Priya, *ACS Energy Lett.*, 2016, **1**, 1014–1020.
- 48 M. A. A. Kazemi, P. Raval, K. Cherednichekno, J.-N. Chotard, A. Krishna, A. Demortiere, G. N. M. Reddy and F. Sauvage, *Small Methods*, 2021, **5**, 2000834.
- 49 X. Meng, X. Tian, S. Zhang, J. Zhou, Y. Zhang, Z. Liu and W. Chen, *Sol. RRL*, 2022, **6**,

2200280.

- 50 J. I. J. Choi, M. E. Khan, Z. Hawash, K. J. Kim, H. Lee, L. K. Ono, Y. Qi, Y. H. Kim and J. Y. Park, *J. Mater. Chem. A*, 2019, **7**, 20760–20766.
- 51 M. A. A. Kazemi, N. Folastre, P. Raval, M. Sliwa, J. Marie, V. Nsanzimana, S. Golonu, A. Demortiere, J. Rousset, O. Lafon, L. Delevoye, G. N. M. Reddy and F. Sauvage, *Energy Environ. Mater.*, , DOI:10.1002/eem2.12335.
- 52 P. Raval, R. M. Kennard, E. S. Vasileiadou, C. J. Dahlman, I. Spanopoulos, M. L. Chabinyk, M. Kanatzidis and G. N. M. Reddy, *ACS Energy Lett.*, 2022, **7**, 1534–1543.
- 53 C. J. Dahlman, D. J. Kubicki and G. N. M. Reddy, *J. Mater. Chem. A*, 2021, **9**, 19206–19244.
- 54 M. A. A. Kazemi, A. Jamali and F. Sauvage, *Front. Energy Res.*, 2021, **9**, 1–10.
- 55 D. J. Kubicki, S. D. Stranks, C. P. Grey and L. Emsley, *Nat. Rev. Chem.*, 2021, **5**, 624–645.
- 56 D. J. Kubicki, D. Prochowicz, E. Salager, A. Rakhmatullin, C. P. Grey, L. Emsley and S. D. Stranks, *J. Am. Chem. Soc.*, 2020, **142**, 7813–7826.
- 57 C. Roiland, G. Trippé-Allard, K. Jemli, B. Alonso, J. C. Ameline, R. Gautier, T. Bataille, L. Le Pollès, E. Deleporte, J. Even and C. Katan, *Phys. Chem. Chem. Phys.*, 2016, **18**, 27133–27142.
- 58 S. Samanta, P. Raval, G. N. M. Reddy and D. Chaudhuri, *ACS Cent. Sci.*, 2021, **7**, 1391–1399.
- 59 A. Dučinskas, G. Y. Kim, D. Moia, A. Senocrate, Y.-R. Wang, M. A. Hope, A. Mishra, D. J. Kubicki, M. Siczek, W. Bury, T. Schneeberger, L. Emsley, J. V. Milić, J. Maier and M. Grätzel, *ACS Energy Lett.*, 2021, **6**, 337–344.
- 60 P. Raval, M. Dhennin, H. Vezin, T. Pawlak, P. Roussel, T.-Q. Nguyen and G. N. M. Reddy, *Electrochim. Acta*, 2022, **424**, 140602.
- 61 B. R. Luginbuhl, P. Raval, T. Pawlak, Z. Du, T. Wang, N. Schopp, S. Chae, S. Yoon, A. Yi, H. J. Kim, V. Coropceanu, J.-L. Brédas, T.-Q. Nguyen and G. N. M. Reddy, *Adv. Mater.*, 2022, **34**, 2105943.

- 62 D. Sarkar, R. W. Hooper, A. Karmakar, A. Bhattacharya, A. Pominov, V. V. Terskikh and V. K. Michaelis, *ACS Mater. Lett.*, 2022, **4**, 1255–1263.
- 63 R. W. Hooper, D. Sarkar and V. K. Michaelis, *Curr. Opin. Colloid Interface Sci.*, 2022, 101631.
- 64 A. Mishra, M. A. Hope, M. Almalki, L. Pfeifer, S. M. Zakeeruddin, M. Grätzel and L. Emsley, *J. Am. Chem. Soc.*, 2022, **144**, 15175–15184.
- 65 D. J. Kubicki, D. Prochowicz, A. Pinon, G. Stevanato, A. Hofstetter, S. M. Zakeeruddin, M. Grätzel and L. Emsley, *J. Mater. Chem. A*, 2019, **7**, 2326–2333.
- 66 L. Piveteau, V. Morad and M. V. Kovalenko, *J. Am. Chem. Soc.*, 2020, **142**, 19413–19437.
- 67 C. J. Dahlman, R. M. Kennard, P. Paluch, N. R. Venkatesan, M. L. Chabinyk and G. N. M. Reddy, *Chem. Mater.*, 2021, **33**, 642–656.
- 68 B. A. Rosales, L. Men, S. D. Cady, M. P. Hanrahan, A. J. Rossini and J. Vela, *Chem. Mater.*, 2016, **28**, 6848–6859.
- 69 J. Lee, W. Lee, K. Kang, T. Lee and S. K. Lee, *Chem. Mater.*, 2021, **33**, 370–377.
- 70 W. C. Qiao, J. Wu, R. Zhang, W. Ou-Yang, X. Chen, G. Yang, Q. Chen, X. L. Wang, H. F. Wang and Y. F. Yao, *Matter*, 2020, **3**, 2042–2054.
- 71 A. R. Lim, S. H. Kim and Y. L. Joo, *Sci. Rep.*, 2020, **10**, 13140.
- 72 A. M. A. Leguy, Y. Hu, M. Campoy-Quiles, M. I. Alonso, O. J. Weber, P. Azarhoosh, M. Van Schilfgaarde, M. T. Weller, T. Bein, J. Nelson, P. Docampo and P. R. F. Barnes, *Chem. Mater.*, 2015, **27**, 3397–3407.
- 73 A. Poglitsch and D. Weber, *J. Chem. Phys.*, 1987, **87**, 6373–6378.
- 74 B. Wang and T. Chen, *Adv. Sci.*, 2015, **3**, 1500262.
- 75 M. J. Bayro, M. Huber, R. Ramachandran, T. C. Davenport, B. H. Meier, M. Ernst and R. G. Griffin, *J. Chem. Phys.*, 2009, **130**, 114506.
- 76 Y. Zhou and Y. Zhao, *Energy Environ. Sci.*, 2019, **12**, 1495–1511.
- 77 H. Grüninger, M. Bokdam, N. Leupold, P. Tinnemans, R. Moos, G. A. De Wijs, F. Panzer

- and A. P. M. Kentgens, *J. Phys. Chem. C*, 2021, **125**, 1742–1753.
- 78 B. R. Vincent, K. N. Robertson, T. S. Cameron and O. Knop, *Can. J. Chem.*, 1987, **65**, 1042–1046.
- 79 J. A. Christians, P. A. Miranda Herrera and P. V. Kamat, *J. Am. Chem. Soc.*, 2015, **137**, 1530–1538.
- 80 J. Yang, B. D. Siempelkamp, D. Liu and T. L. Kelly, *ACS Nano*, 2015, **9**, 1955–1963.
- 81 G. Niu, W. Li, F. Meng, L. Wang, H. Dong and Y. Qiu, *J. Mater. Chem. A*, 2014, **2**, 705–710.
- 82 K. Ho, M. Wei, E. H. Sargent and G. C. Walker, *ACS Energy Lett.*, 2021, **6**, 934–940.

# Chapter 4 - Structural insights into the p-doped hole transporting materials

## 4.1 Organic semiconductors as hole-transporting materials in perovskite solar cells

In a perovskite-based photovoltaic cell, the photoactive layer is sandwiched between the hole and electron transport layers. The role of these layers is that they extract the positive and negative charges towards the top (cathode) and bottom (anode) electrodes. Organic, inorganic, and hybrid semiconductors have been used as charge transporters in perovskite solar cells (PSCs). Specifically, organic semiconductors (OSCs) have been used as hole-transporting layers (HTLs).

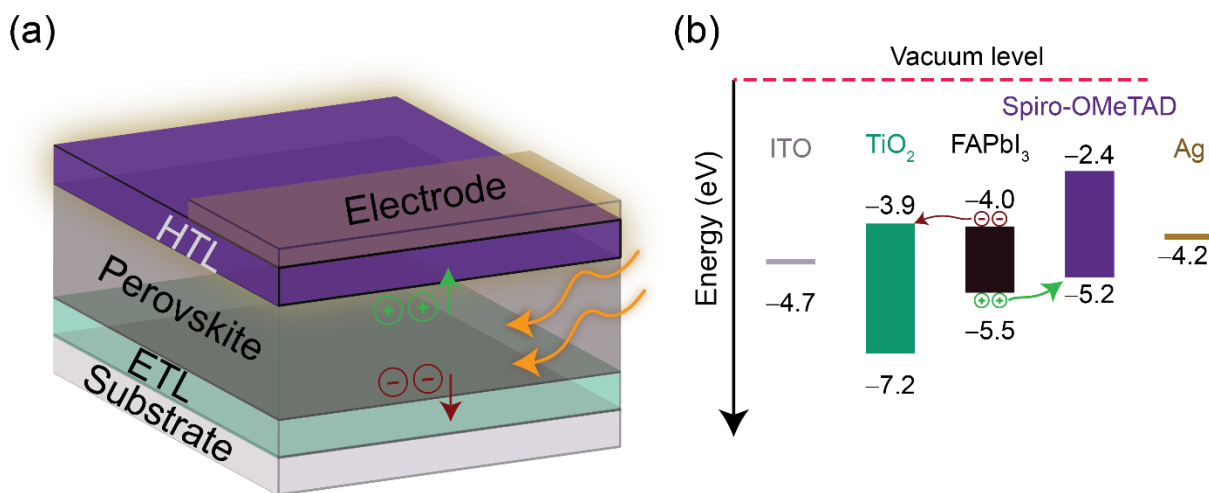


**Figure 4.1.** (a) Schematic of n-i-p perovskite solar cell device with different layers stacked on top of each other as indicated. (b) Energy level diagram adapted from reference <sup>1</sup>

The main function of the hole-transporting materials (HTMs) in solar cell devices (Figure 4.1a) is to extract and transport holes from the photoactive absorber while blocking the passage of electrons. This facilitates an effective separation of electrons and holes, which is an essential part of solar cells. For a high-performing perovskite solar cell (PSC), the HTM must have a suitable highest occupied molecular orbital (HOMO) energy level close to that of the valence band of perovskite material while the lowest unoccupied molecular orbital (LUMO) higher than the conduction band of the perovskite material (Figure 4.1b). In addition, it should possess

adequately high hole mobility (hence high conductivity) and have great photochemical, thermal, and moisture stability with suitable light absorption in the visible and near-IR regions of the solar spectrum.<sup>2-7</sup> Ideally, the thin film deposition conditions of HTLs should be compatible with the manufacturing and processing conditions of solution-processed photovoltaic cells in a cost-effective manner.

Numerous organic hole-transporting materials have been used as HTLs in perovskite solar cells. For example, 2,2',7,7'-tetrakis(N, N-di-p-methoxyphenyl-amine) 9,9'-spirobifluorene (also referred to as spiro-OMeTAD) is the most commonly used HTL in PSCs. Poly[bis(4-phenyl)(2,4,6-trimethylphenyl)amine] (PTAA), poly(3,4-ethylene dioxythiophene)-poly(styrene-sulfonate) (PEDOT:PSS) and poly(3-hexylthiophene-2,5-diyl) (P3HT) are amongst other organic hole transporting material developed (Table 4.1).<sup>8,9</sup> Structures of these molecules are presented in Figure 4.2. In particular, spiro-OMeTAD and its derivatives are suitable HTLs due to high glass transition temperature ( $T_g$ , 125 °C) and melting point ( $T_m$ , 248 °C), which leads to morphological stability during the thin film processing while maintaining good electronic properties. Therefore, spiro-linked molecules have been widely used in PSCs as well as in solid-state dye-sensitized solar cells (ssDSSC), and organic light-emitting diodes (OLED).<sup>10,11</sup>

**Table 4.1.** Hole mobility ( $\text{cm}^2 \cdot \text{V}^{-1} \cdot \text{s}^{-1}$ ) of a few common organic hole transporting materials.

HTM	Dopant	Hole mobility ( $\text{cm}^2 \cdot \text{V}^{-1} \cdot \text{s}^{-1}$ )	Reference
Spiro-OMeTAD	-	$1.6 \times 10^{-4}$	12
	Li-TFSI	$1.6 \times 10^{-3}$	
PTAA	-	$7.5 \times 10^{-5}$	13
	Li-TFSI/t-BP	$4.3 \times 10^{-4}$	
PEDOT:PSS	-	$5.6 \times 10^{-5}$	14
	GO	$1.6 \times 10^{-4}$	
P3HT	-	$\sim 1.0 \times 10^{-5}$	15

The popularity of spiro-OMeTAD as HTM in PSCs can be principally attributed to its ease of processing and favorable HOMO-valence band match with conventional perovskites light absorbers. However, pristine spiro-OMeTAD exhibits mediocre hole mobility, and hence, the mobility of holes must be enhanced using chemical doping of HTMs by additives such as 2,3,5,6-tetrafluoro-7,7,8,8-tetracyanoquinodimethane (F4TCNQ), bis(trifluoromethane) sulfonamide lithium salt (LiTFSI), benzoyl peroxide, and 4-tert-butyl pyridine (tBP).<sup>16–19</sup> These additive engineering strategies facilitate better charge transport, suppresses recombination, and impede the formation of trap states.<sup>18,19</sup> Addition of LiTFSI and tBP also improves the thin-film morphology.<sup>20</sup> In addition, doping with a considerable amount of additives can have substantial effects on the overall stability of the PSC.<sup>21</sup> These doping strategies lead to undesired chemical transformation. For example, Li-TFSI dopant oxidizes spiro-OMeTAD in the presence of moisture, oxygen, light, or thermal excitation,<sup>12,22,23</sup> leading to degradation reactions that impart hysteresis in device reproducibility, stability, and performance.<sup>22–27</sup> Due to its small size and high diffusion tendency,  $\text{Li}^+$  ions in the Li-TFSI doped spiro-OMeTAD layer have been shown to migrate through the device.<sup>28</sup>

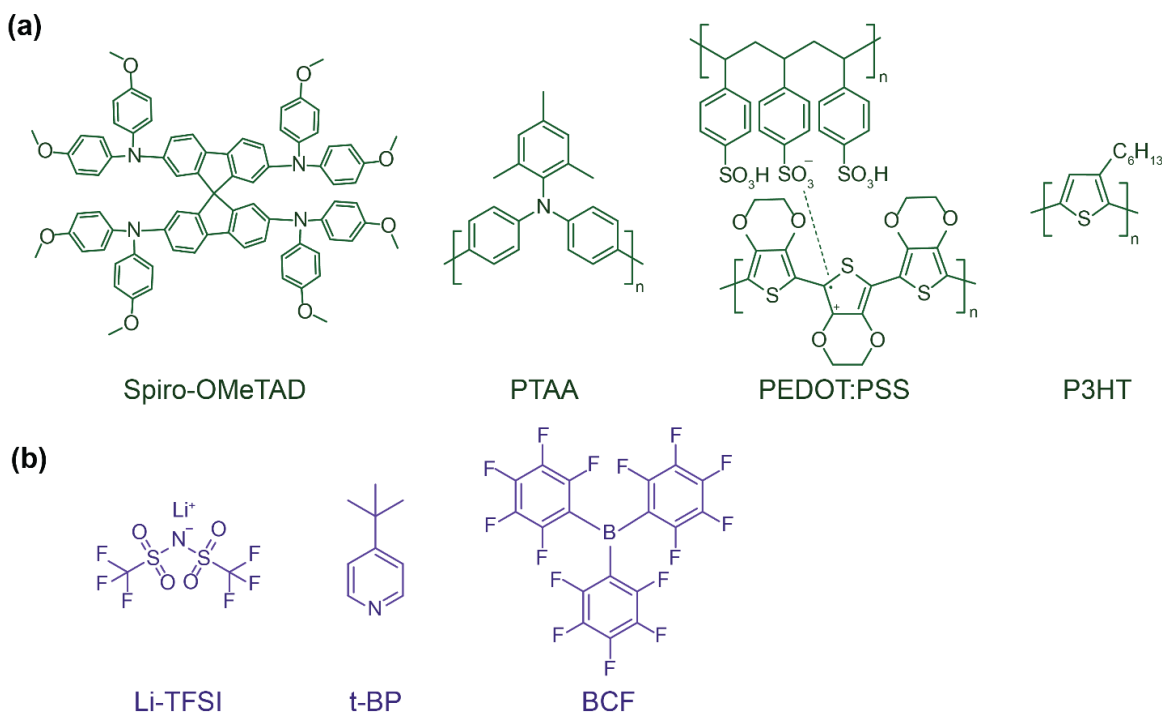


**Figure 4.2.** Chemical structures of (a) common organic hole transporting material and (b) their dopants



Molecular doping strategies based on small molecules such as tris(pentafluorophenyl)borane (BCF), dimethylsulphoxide (DMSO)/HBr adducts, ionic modulators, acid additives, and organic metal salts have been used to improve the conductivity, stability, and performance of spiro-OMeTAD based HTMs.<sup>29–33</sup> Lewis acid BCF is a promising dopant for organic semiconductors (OSCs) because of its strong electron-accepting ability, high solubility in common organic solvents, and low cost. It has been shown that the BCF molecules interact with water molecules to generate Brønsted acid BCF-water complexes. A combination of Lewis-acid BCF and Brønsted acid BCF-water complexes has been demonstrated to p-dope a diverse variety of Lewis basic conjugated molecules. The photophysical properties of OSCs can be effectively tuned by adding BCF molecules to OSCs.<sup>34–38</sup> In addition, BCF-doped OSCs are generally used in organic light-emitting diodes (OLEDs), photodetectors, field effect transistors, and more recently as HTM and molecular passivator in perovskite-based photovoltaic devices.<sup>29,34,35,39,40</sup> BCF-doping mechanisms of OSCs have been extensively addressed in the literature, as backed by experimental and theoretical results.<sup>41–45</sup> These mechanisms either involve the formation of a charge-transfer supramolecular complex between BCF and OSC or a partial charge-transfer system where Lewis basic OSC shares its lone pair with the B atom of BCF to form an acid-base complex.<sup>42,43,46</sup> A molecular-level understanding of these different doping mechanisms demands a precise characterization of intermolecular interactions between dopant and OSC.

Compositional and structural heterogeneity associated with such doped organic materials makes it challenging to obtain molecular-level insight into intermolecular interactions between OSC and dopant. The addition of a dopant induces changes in the self-assembly and morphology of these molecules that are difficult to resolve by X-ray scattering and microscopy techniques due to the lack of long-range structural order. Although macroscopic changes in the optoelectronic properties, such as a change in absorption, bandgap, and upon chemical doping, can be investigated by electroanalytical and optical spectroscopy (e.g., UV-visible) techniques, insights related to dopant/OSC miscibility, mechanistic details of the doping process, and relevant intermolecular interactions are difficult to obtain and compare. As illustrated in a recent study by Dixon et al., a combination of solid-state EPR and NMR techniques is expected to provide insight into the local structures and hyperfine interactions between the dopants and

OSCs.<sup>47</sup> This chapter extends this approach to provide local structural understandings of doped spiro-OMeTAD.

In this chapter, optical and morphological changes associated with BCF doping of spiro-OMeTAD are presented. To identify the morphological and local structural changes in BCF-doped spiro-OMeTAD, it is important to interpret various packing interactions in pristine spiro-OMeTAD. First, packing interactions in neat spiro-OMeTAD thin films are discussed using an NMR crystallography approach. In a broader context, the term “NMR crystallography” implies the combined use of experiment (NMR, X-ray/neutron diffraction) and calculations (DFT, first principles approach, structure prediction methods, NMR shielding calculations using gauge including projector augmented wave (GIPAW) method) in order gain insight into packing interactions, polymorphism and 3D structures of molecular entities. Over the last decade, this approach has been implemented to address complex structural chemistry problems.<sup>48–58</sup> This approach has also been used to refine XRD-derived structures by correcting atom positions and rationalizing the packing interactions. While the whole procedure involves an intricate structure determination process and requires enormous computational input, a large number of literature examples use XRD and ssNMR characterization with input from DFT-based modeling studies to elucidate structures and predict the properties.<sup>48,55,59,60</sup> For instance, crystal structure prediction without a priori knowledge of XRD data and building structural models, or using ssNMR structural constraints and XRD patterns to identify energy minimized geometry and validate structural models.

## 4.2 NMR crystallography of spiro-OMeTAD

Here, the main objective of using the NMR crystallography study is to compare the structural changes in spiro-OMeTAD thin film and crystals. To prepare a film of pristine spiro-OMeTAD, a 10 mg/mL solution of spiro-OMeTAD in chlorobenzene was drop-casted on indium-doped tin oxide (ITO) -coated glass substrate, followed by annealing at 70 °C for 20 min. The film formed was scratched from the glass substrate and packed in the 1.3 mm NMR rotor. Figure 4.3a shows the <sup>1</sup>H NMR spectrum of pristine spiro-OMeTAD. Methoxy groups are responsible for the partially resolved signals at 2–5 ppm, while phenyl and fluorene protons are responsible for the peaks at 5–8 ppm.

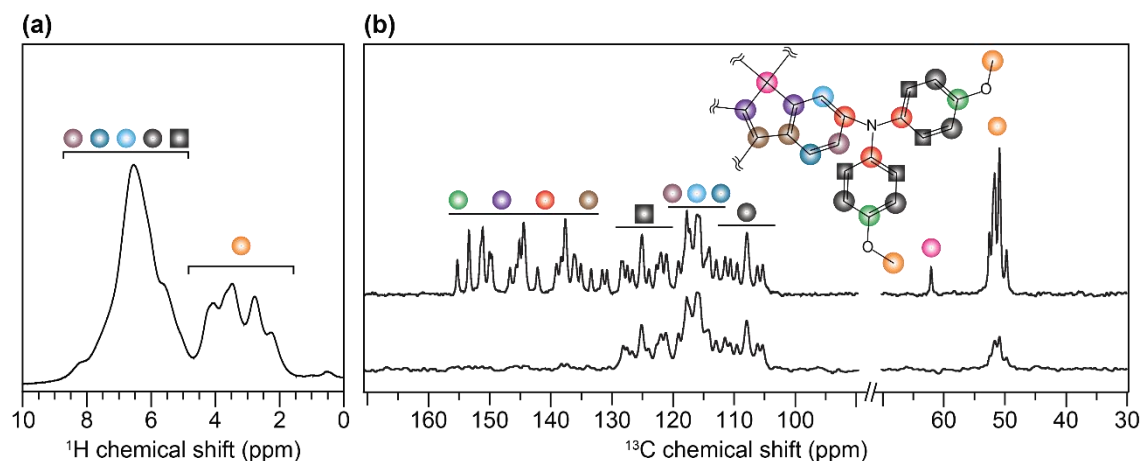


**Figure 4.3.** Solid-state 1D (a)  $^1\text{H}$  MAS and (b)  $^1\text{H}\rightarrow^{13}\text{C}$  CP-MAS NMR spectra of neat spiro-OMeTAD (CP contact time of 2 ms – top and 60  $\mu\text{s}$  – bottom). The peaks are color-coded, as depicted in the schematic structure in (b). All the spectra were acquired at 18.8 T, room temperature, and 50 kHz MAS frequency.

The directly bonded C-H moieties and longer-range  $^1\text{H}$ - $^{13}\text{C}$  proximities can be distinguished by examining  $^1\text{H}\rightarrow^{13}\text{C}$  cross-polarization (CP)-MAS NMR spectra of spiro-OMeTAD obtained with different CP contact times (Figure 4.3b). A high level of structural order in the pristine spiro-OMeTAD material can be deduced from well-resolved  $^{13}\text{C}$  signals. The signal at 53-56 ppm is assigned to the methoxy  $^{13}\text{C}$  sites (orange dots), and the signal at 66 ppm is attributed to the quaternary carbon atom at the bridging position (pink dot) of central bifluorene moiety. The  $^{13}\text{C}$  signals in the range of 107-133 ppm are assigned to the directly bonded C-H groups in the phenyl and bifluorene moiety as indicated by blue, teal, black, and raisin-colored dots and black squares in Figure 4.3b. The signals at 135–160 ppm are assigned to the quaternary carbon atoms (green, purple, red, and brown dots), which are further supported by periodic DFT calculated NMR chemical shifts of spiro-OMeTAD using the GIPAW approach. In order to examine inter- and intramolecular packing interactions, 2D  $^1\text{H}$ - $^{13}\text{C}$  heteronuclear correlation NMR spectroscopy experiments were employed. The through-space and dipolar coupled  $^1\text{H}$ - $^{13}\text{C}$  pairs within sub-nanometer distances manifest 2D peaks in these experiments. Notably, calculated  $^1\text{H}$  and  $^{13}\text{C}$  chemical shifts using the GIPAW DFT-D (Dispersion corrected DFT) approach facilitate the analysis of 2D NMR spectra of pristine spiro-OMeTAD molecules.<sup>61</sup> This further helps in deducing the information on molecular self-assembly and packing interactions between spiro-OMeTAD molecules in a crystal versus a thin film.

Figure 4.4 shows the 2D  $^1\text{H}$ - $^{13}\text{C}$  Cross Polarization (CP) HETCOR spectra of pristine spiro-OMeTAD acquired with different CP contact times. Figure 4.4a highlights a few packing interactions that lead to the observation of the 2D peaks. The experimental spectra are superimposed with the GIPAW DFT-D predicted  $^1\text{H}$  and  $^{13}\text{C}$  chemical shifts for dipolar coupled  $^1\text{H}$ - $^{13}\text{C}$  pairs (C-H cut-off distance 1.3 Å for Figure 4.4a and 2.6 Å for Figure 4.4b). The 2D correlation peaks associated with the directly bonded  $^{13}\text{C}$ - $^1\text{H}$  spin pairs are observed in the spectrum acquired with a short CP contact time (100  $\mu\text{s}$ , Figure 4.4b). Although there are slight variations in the experimental  $^1\text{H}$  chemical shifts (9-10 ppm), there is good agreement between experimental and DFT-calculated 2D peaks for directly bonded  $^1\text{H}$ - $^{13}\text{C}$  pairs. These subtle discrepancies can be attributed to changes in the local packing interactions due to a high degree of conformational flexibility associated with phenyl rings and methoxy groups. The C-H pairs of the methoxy group (orange dots) of spiro-OMeTAD are observed at 2.8-4.1 ppm ( $^1\text{H}$ ) and 53-56 ppm ( $^{13}\text{C}$ ). The directly bonded phenyl C-H moieties (black dots and squares) arise the 2D peak at  $^1\text{H}$  (5.6-6.4 ppm) and  $^{13}\text{C}$  (113-119 ppm) signals and at  $^1\text{H}$  (6.6 ppm) and  $^{13}\text{C}$  (133-135 ppm). On the other hand, the 2D peaks associated with the fluorene group (blue, teal, and raisin dots) at the core of spiro-OMeTAD appeared at  $^1\text{H}$  (5.4-7.5 ppm) and  $^{13}\text{C}$  (122-130 ppm).

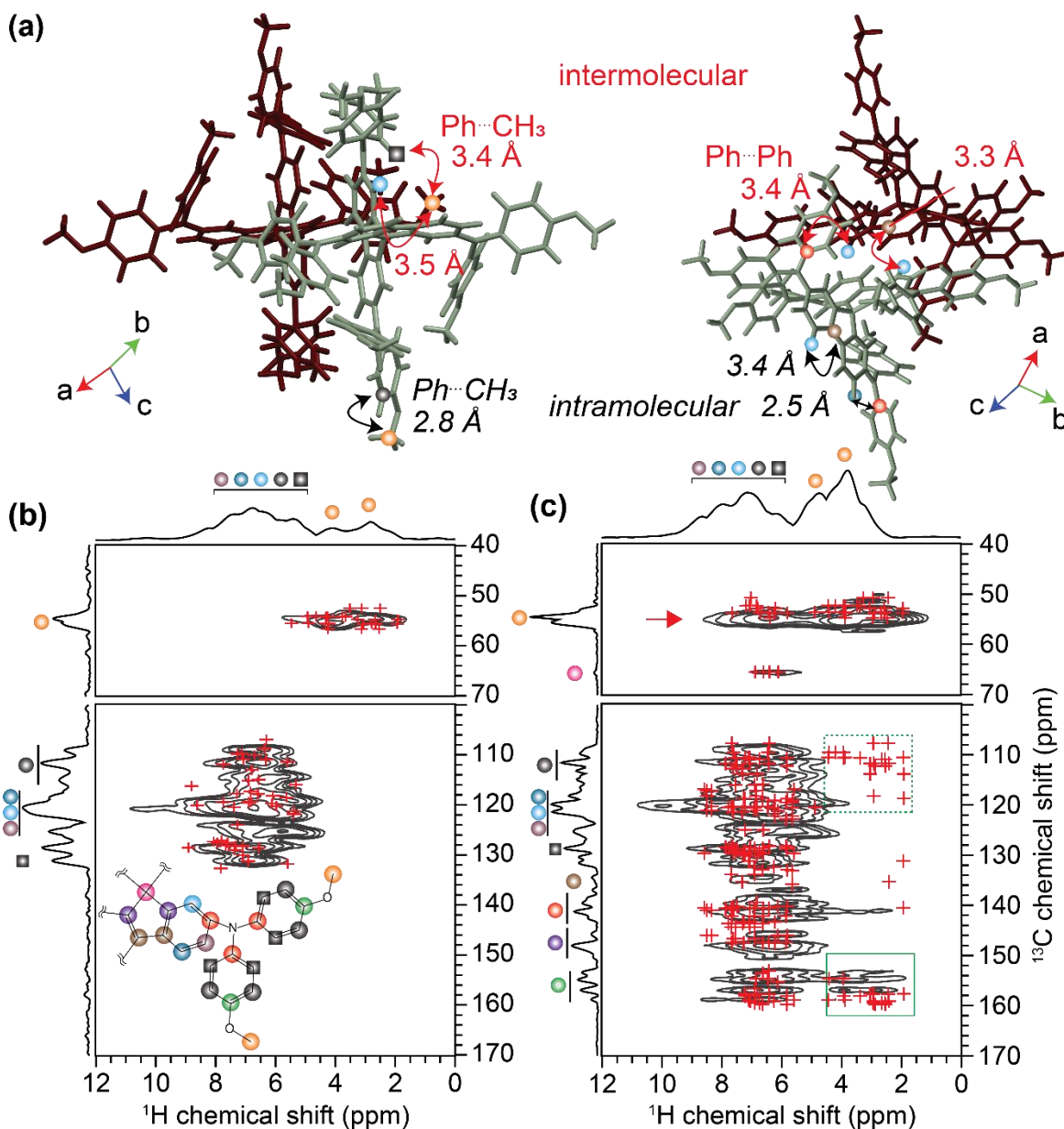


**Figure 4.4.** (a) GIPAW DFT-D geometry optimized crystal structure of spiro-OMeTAD with specific inter- and intramolecular packing interactions that contribute to 2D peaks in the  $^1\text{H}$ - $^{13}\text{C}$  HETCOR NMR spectra. Solid-state 2D  $^1\text{H}$ - $^{13}\text{C}$  HETCOR NMR spectra of spiro-OMeTAD with CP contact time of (b) 100  $\mu\text{s}$  (c) 3 ms along with the skyline projections of  $^1\text{H}$  and  $^{13}\text{C}$  spectra in the top and left, respectively. DFT calculated NMR chemical shifts of spiro-OMeTAD are overlaid on their spectra. All 2D spectra were acquired at 18.8 T, room temperature, and 50 kHz MAS frequency. For the crystal structures of spiro-OMeTAD, the DFT calculated  $^1\text{H}$  and  $^{13}\text{C}$

chemical shifts for all  $^1\text{H}$ - $^{13}\text{C}$  pairs within (a) 1.3 Å and (b) 2.6 Å is depicted by the overlaid crosses.

On the other hand, the correlation peaks in the 2D HETCOR spectrum of pristine spiro-OMeTAD acquired with longer CP contact time (3 ms) arise from a combination of intra- and inter-molecular  $^1\text{H}$ - $^{13}\text{C}$  dipolar coupled spin pairs. The calculated  $^1\text{H}$  and  $^{13}\text{C}$  chemical shifts using the GIPAW DFT-D method for all the  $^{13}\text{C}$ - $^1\text{H}$  spin pairs within 2.8 Å are overlaid on the experimental spectrum. The inter- and intramolecularly dipolar coupled methoxy  $^{13}\text{C}$  (yellow dots) and phenyl  $^1\text{H}$  sites (grey dot and square) lead to a 2D peak at  $^1\text{H}$  (6.2-6.6 ppm) and  $^{13}\text{C}$  (53-56 ppm) chemical shifts as indicated by the red arrow. The 2D peak at  $^{13}\text{C}$  (~55 ppm, pink dot) and the  $^1\text{H}$  (6-7 ppm, blue dots) is due to the intramolecular through-space interactions between quaternary carbon atom at the bridged position of bifluorene moieties and bifluorene protons. Furthermore, a 2D peak between  $^{13}\text{C}$  (135-139 ppm) and  $^1\text{H}$  (6.5-6.9 ppm) originates from the inter-, and intramolecularly proximate bifluorene quaternary carbon atoms (brown dots) and bifluorene protons, with the closest inter- and intramolecular distances, are 3.3 Å and 2.2 Å in the GIPAW DFT-D optimized crystal structure of spiro-OMeTAD. Subsequently, the 2D correlation corresponding to the closest inter- and intramolecular C-H distances of 3.4 and 2.2 Å for the quaternary phenyl  $\text{C}_\alpha$  (141-144 ppm, red dots) and fluorene protons (5.1–7.4 ppm) is observed. The 2D peaks in the range of 146-150 ppm ( $^{13}\text{C}$ ) and 5.4-7.6 ppm ( $^1\text{H}$ ) occur from the fluorene and phenyl protons being in close proximity to the same quaternary fluorene C (red dot). The fluorene carbon sites (purple dots) and the fluorene protons are intra- and intermolecularly dipolar coupled, leading to the 2D peaks at  $^{13}\text{C}$  (153-155 ppm) and  $^1\text{H}$  (5.6-7.2 ppm) signals. The quaternary phenyl carbon atoms (denoted by green dots that are adjacent to methoxy groups) are inter- and intramolecularly dipolar coupled to phenyl protons within 3.4 Å distance, leading to the 2D peaks between  $^{13}\text{C}$  (158-163 ppm) and  $^1\text{H}$  (5.5- 7.1 ppm) signals. The 2D peaks between  $^{13}\text{C}$  (150-160 ppm) and  $^1\text{H}$  (2-4 ppm) depicted in the box suggest the close proximity between quaternary phenyl carbons and the methoxy protons; however, a substantial deviation between the experimental and calculated 2D  $^1\text{H}$ - $^{13}\text{C}$  peaks are observed. Furthermore, only calculated 2D  $^1\text{H}$ - $^{13}\text{C}$  peaks for the  $^{13}\text{C}$  chemical shifts (100-140 ppm) and the methoxy  $^1\text{H}$  chemical shifts (2-4 ppm) are observed denoted in dashed rectangles suggesting the changes in local structures and packing interactions occur as a result of varied conformational degrees of

freedom associated with the methoxy groups. A detailed NMR crystallography analysis of spiro-OMeTAD crystals and the thin film is expected to help to analyze the local structures and intermolecular interactions in the spiro-OMeTAD:BCF blends, as demonstrated in the following section.

### 4.3 Chemically doped spiro-OMeTAD by BCF

To understand the impact of the addition of BCF on the optical properties of the host spiro-OMeTAD, UV-Vis absorption spectroscopy measurements were performed. Dilute solutions (0.01mmol/L) of spiro-OMeTAD:BCF blends in chlorobenzene with different doping concentrations were prepared. Figure 4.5 compares the absorption spectra of undoped and doped spiro-OMeTAD as a function of the BCF concentration.

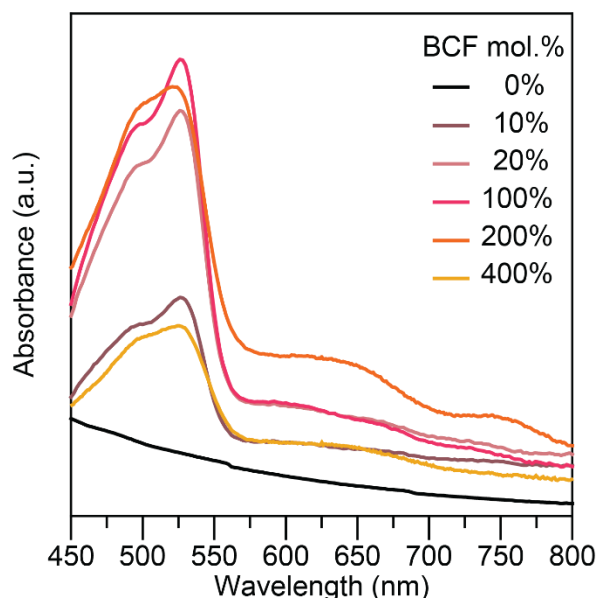


**Figure 4.5.** UV-Vis spectra of undoped and BCF-doped spiro-OMeTAD as a function of dopant concentration in chlorobenzene.

When BCF solution is added to a pristine spiro-OMeTAD solution, absorption peaks in the range of 490-530 nm are observed, the intensity of which rises upon the increase in BCF concentration from 0.1 to 1 molar equivalent. These optical absorption features are characteristic of the oxidized spiro-OMeTAD<sup>+</sup> molecules. This is in line with earlier research that demonstrated how the p-dopant addition altered the optical absorbance of HTMs.<sup>29,62</sup> Furthermore, for the spiro-OMeTAD:BCF (1:4 molar ratio) blend, broad and weak intensity

peaks appeared at 650 and 750 nm. These features can be attributed to BCF anion and spiro-OMeTAD<sup>+</sup> cation species. Formation of Lewis acid-base adduct would normally lead to the red-shift in the optical absorption peak.<sup>43</sup> This was not observed in the case of spiro-OMeTAD:BCF blends, indicating that the BCF molecules are closely associated with spiro-OMeTAD backbone moieties rather than forming the adduct. As mentioned in Section 4.1, the hygroscopic nature of BCF material leads to the formation of BCF-water complex is expected to accept an electron from the ground state of spiro-OMeTAD, as suggested by the increased intensity of the peak at ~530 nm.<sup>46</sup> Although the optical properties of pristine spiro-OMeTAD are altered upon the addition of BCF, it is challenging to determine solely from UV-Vis spectroscopy the molecular level origins that contribute to the changes in absorption characteristics, requiring structural characterization.

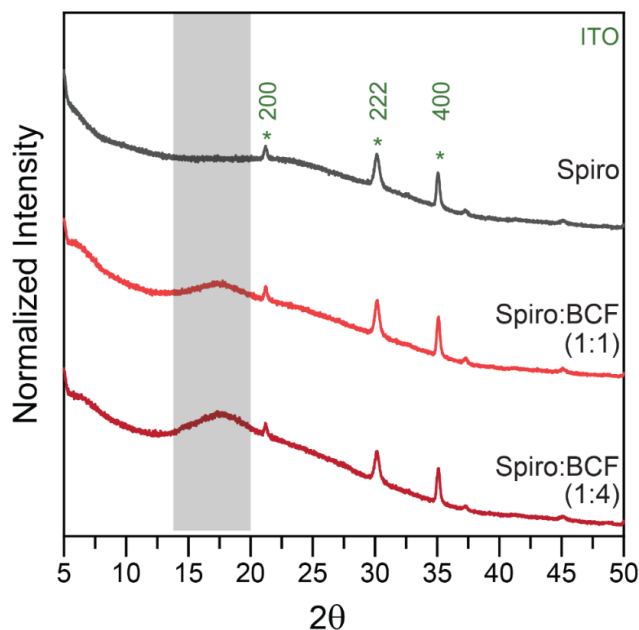


**Figure 4.6.** Powder XRD patterns of pristine undoped and doped spiro-OMeTAD thin films drop cast on ITO-coated glass substrates.

Understanding the morphological aspects at various length scales is anticipated to provide insights into the dopant and OSC interactions. However, these materials pose a characterization challenge due to the presence of minuscule concentrations of dopant molecules and the naturally heterogeneous nature of OSCs-dopant blends, and difficulties associated with locating dopant molecules in the OSCs network. Although some dopant molecules are involved in the doping process, the majority of them are expected to distribute into the OSC network as local



aggregates. Structural characterization studies of blends by varying the dopant concentrations were carried out. Figure 4.6 presents the powder XRD patterns of the neat spiro-OMeTAD and spiro-OMeTAD:BCF blends (1:1 and 1:4 molar ratios) drop cast on the ITO-coated glass substrate. A strong background signal is observed in the powder XRD pattern of the drop-cast spiro-OMeTAD film, indicating its amorphous nature. This background signal has appeared in conjunction with reflections that correspond to the (200), (222), and (400) plane of the ITO glass substrate. A subtle change in the long-range order detected by XRD suggests that the presence of BCF molecules alters the morphology of the spiro-OMeTAD thin film. The spiro-OMeTAD:BCF (1:1 and 1:4 molar ratios) blends exhibited a broad distribution of scattered intensities centered at  $\sim 18^\circ$ . This  $2\theta$  value corresponds to the  $d$ -spacing value of 0.45 nm, which is anticipated to result from very weak  $\pi$ - $\pi$  stacking interactions between BCF and spiro-OMeTAD molecules. It is difficult to gain a deeper knowledge of these doped spiro-OMeTAD blends at the molecular level due to their amorphous nature using long-range probes like X-ray diffraction. This demands the need for atomic-level probes, which offer details on the changes in local structures upon the addition of BCF molecules to the spiro-OMeTAD.

The influence of p-doping on spiro-OMeTAD molecules was further investigated by employing Fourier transform infrared (FTIR) spectroscopy. FTIR helps in identifying the changes in the nature of chemical bonds. Figure 4.7 presents solid-state FTIR spectra of drop-cast films of pristine and doped spiro-OMeTAD. The presence of BCF molecules in the spiro-OMeTAD:BCF blend films can be inferred from the observation of the vibrational bands corresponding to B-C stretching in the range of  $900\text{-}1000\text{ cm}^{-1}$ .<sup>63</sup> Stretching frequencies in the range of  $1000\text{-}1400\text{ cm}^{-1}$  are attributable to C-O and C-N bonds in spiro-OMeTAD and C-F bonds in BCF molecules.<sup>64-66</sup> The stretching frequencies of aromatic C=C bonds, phenyl and bifluorene moieties of spiro-OMeTAD, and fluorinated phenyl rings in BCF molecules are observed in the range of  $1400\text{-}1600\text{ cm}^{-1}$ .<sup>67</sup> The vibrational band at  $1562\text{ cm}^{-1}$  is associated with B-O stretching, that is arising from the BCF-OH<sup>-</sup> anions. This is further corroborated by the strong and broad vibrational band centered at  $\sim 3200\text{ cm}^{-1}$ , corresponding to O-H stretching.<sup>68</sup> In addition, the vibrational band at  $\sim 3200\text{ cm}^{-1}$  can also be ascribed to N-H stretching frequency, which corroborates the presence of spiro-OMeTAD-H<sup>+</sup> cations. The alterations in the local C-H bonding environments of spiro-OMeTAD upon the addition of BCF molecules are observed via

subtle changes in the vibrational bands in the range of 2800-3100  $\text{cm}^{-1}$ . Analysis of FT-IR spectra indicates the presence of different dopant species, which corroborates the optical spectroscopy measurements and analysis.

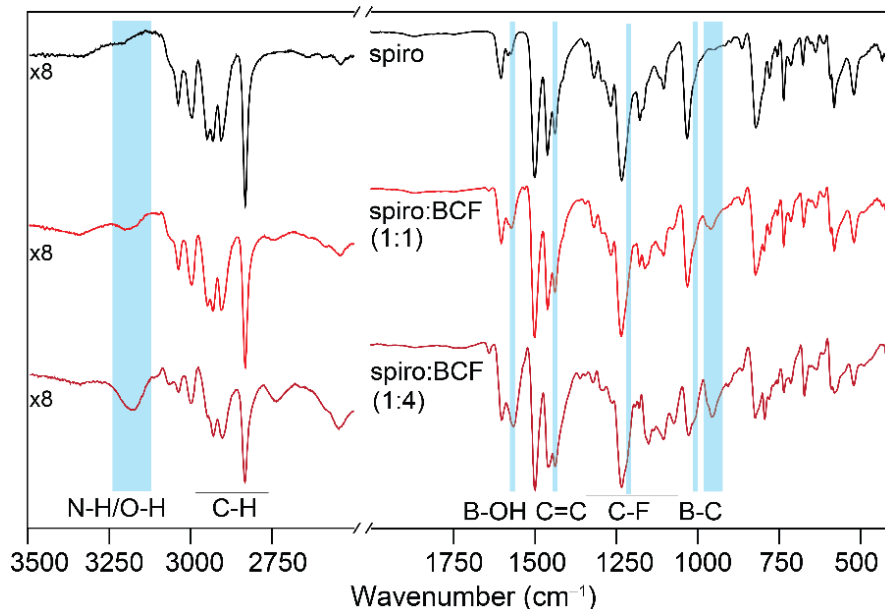


**Figure 4.7.** Solid-state attenuated total reflection FT-IR spectra of undoped and doped spiro-OMeTAD thin films acquired at room temperature.

To understand the local compositions, structures, and intermolecular interactions in BCF-doped spiro-OMeTAD films, multinuclear ( $^1\text{H}$ ,  $^{13}\text{C}$ ,  $^{11}\text{B}$ , and  $^{19}\text{F}$ ) solid-state (ss)NMR spectra of blends were acquired and compared. Multinuclear ssNMR spectroscopy has been extensively employed to understand the local structures in organic semiconductors and their blends.<sup>55,69–71</sup> As described in Section 4.2, 2D NMR correlation spectra acquired at high fields with fast magic-angle spinning (MAS) techniques provide enhanced resolution to probe inter- and intramolecular interactions, as reported for a wide range of organic materials consisting of ordered/disordered regions.<sup>55,72–77</sup>

Tri-coordinated boron atoms in pristine BCF and tetra-coordinated boron atoms in BCF-water complexes produce two distinct peaks in the 1D  $^{11}\text{B}$  spectrum. Tetrahedral boron atoms in the BCF anions contribute to the narrow  $^{11}\text{B}$  NMR signal centered at  $-5$  ppm for the spiro-OMeTAD:BCF blend (1:1 molar ratio). The weak intensity signals centered at 17 and 23 ppm are attributable to distinct BCF-water complexes. These signals in the range of 17-23 ppm

appeared at a much higher intensity in the  $^{11}\text{B}$  MAS NMR spectrum of the spiro-OMeTAD:BCF blend (1:4 molar ratio), suggesting that the BCF-water complexes (BCF- $\text{H}_2\text{O}$  and BCF- $\text{H}_2\text{O}\cdot 2\text{H}_2\text{O}$ ) are formed when a higher concentration of BCF ( $> 1$  molar equivalents) is added to spiro-OMeTAD.<sup>78,79</sup>

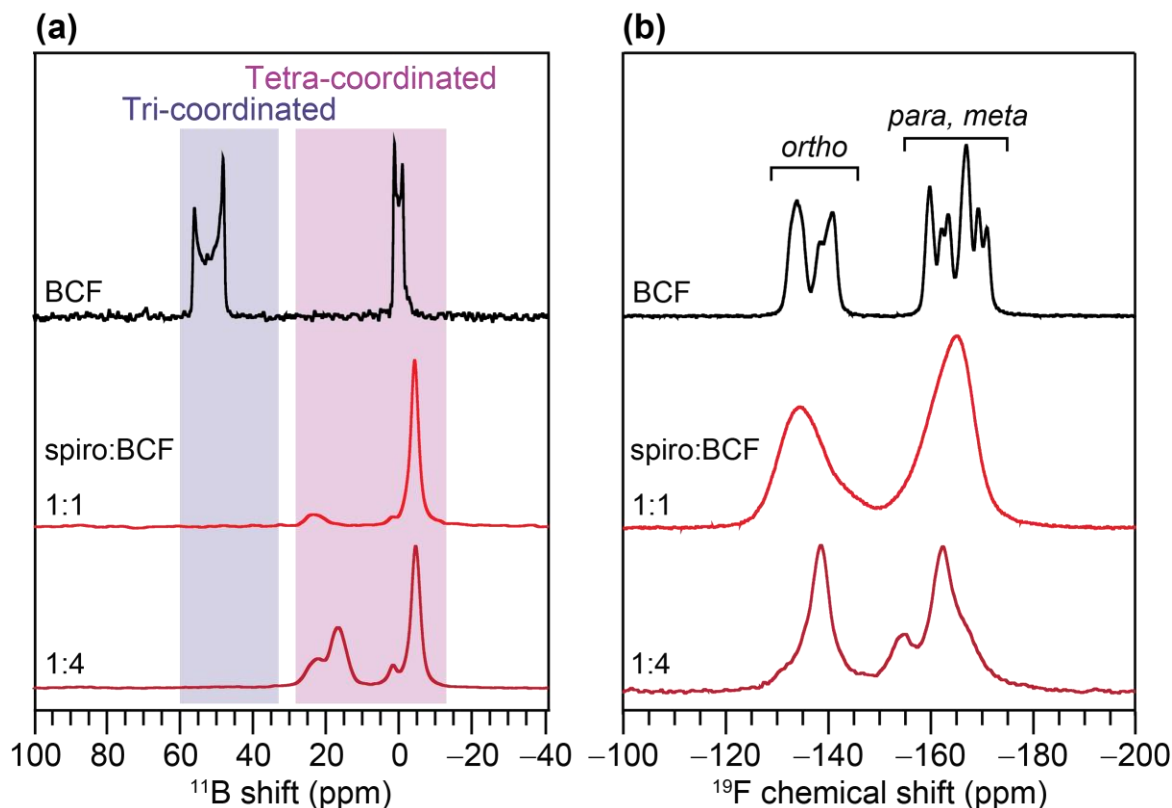


**Figure 4.8.** Solid-state (a)  $^{11}\text{B}$  and (b)  $^{19}\text{F}$  MAS NMR spectra of neat BCF and spiro-OMeTAD:BCF blends of the relative molar concentration of 1:1 and 1:4.

1D  $^{19}\text{F}$  MAS NMR experiments allow one to examine and compare the structural changes in the pentafluorophenyl groups in pristine BCF and spiro-OMeTAD:BCF blends (Figures 4.8b). For pristine BCF, *ortho*-fluorine sites are observed in the range of  $-134$  and  $-141$  ppm, and the peaks between  $-160$  and  $-171$  ppm are due to *meta* and *para* fluorine sites of pentafluorophenyl rings.<sup>43</sup> Most importantly, the narrow  $^{19}\text{F}$  signals indicate the well-ordered pentafluorophenyl rings in BCF molecules. By comparison, the spiro-OMeTAD:BCF blends with a 1:1 molar ratio exhibit broad signals that indicate the different local chemical environments of fluorinated phenyl groups. This could be due to the heterogeneity in local chemical environments of spiro-OMeTAD and BCF molecules. Upon further increasing the BCF concentration, the  $^{19}\text{F}$  signals

corresponding to ortho-para- and meta-fluorine sites are observed at  $-138$ ,  $-155$ , and  $-162$  ppm in the spiro-OMeTAD:BCF blend (1:4 molar ratio) material. These signals, in comparison to the 1:1 molar ratio blend, are narrower, indicating a more locally ordered environment, which can be attributed to the clusters of BCF-water complexes.

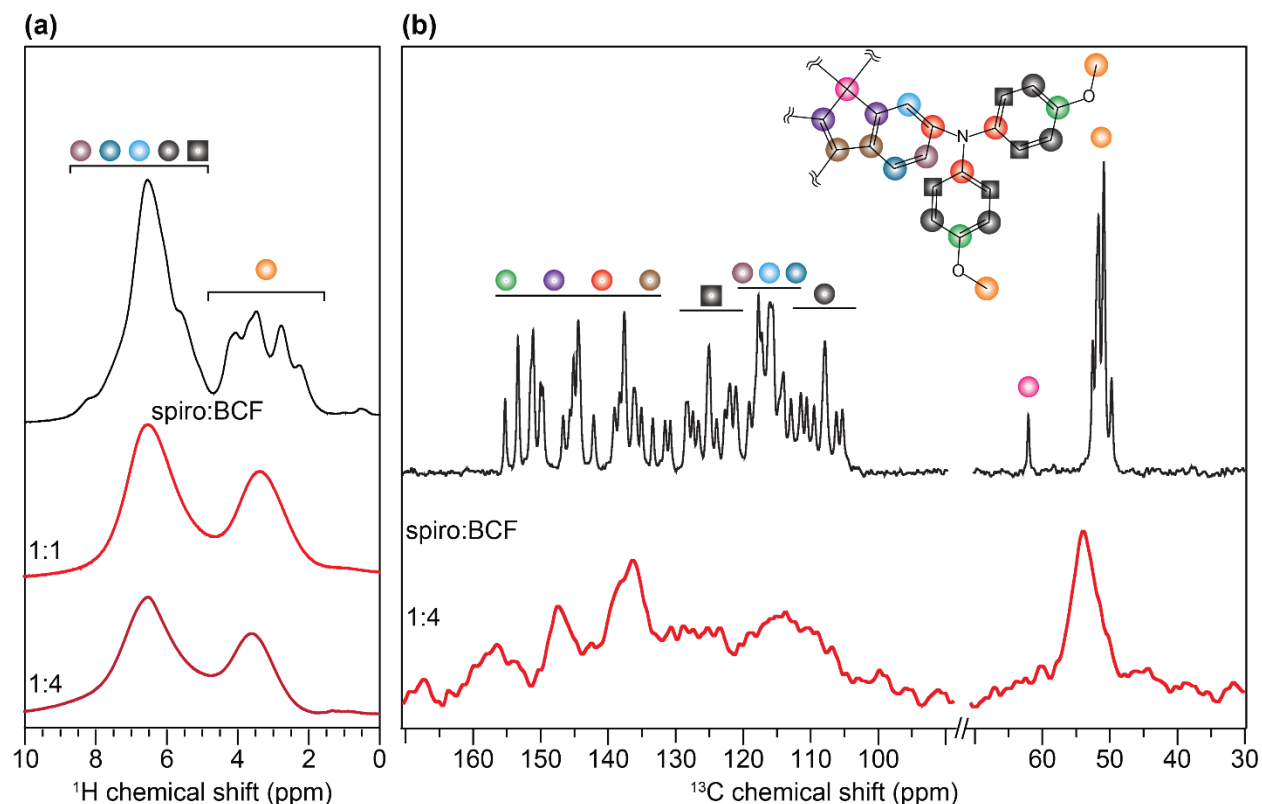


**Figure 4.9.** Solid-state 1D (a)  $^1\text{H}$  and (b)  $^1\text{H}\rightarrow^{13}\text{C}$  CPMAS NMR spectra of spiro-OMeTAD:BCF blends of relative molar concentration indicated in the inset. 1D  $^1\text{H}$  and  $^{13}\text{C}$  MAS NMR spectra of pristine spiro-OMeTAD are presented as well for comparison.

1D  $^1\text{H}$  MAS NMR experiments were implemented to observe the structural changes in the spiro-OMeTAD upon doping with BCF. Compared to the 1D  $^1\text{H}$  MAS NMR spectrum of pristine spiro-OMeTAD, the addition of BCF to spiro-OMeTAD causes signal broadening and intensity losses. For example, the peak integrals associated with aromatic protons reduce to 52% (spiro-OMeTAD:BCF, 1:1) and 31% (spiro-OMeTAD:BCF, 1:4). On the other hand, the methoxy  $^1\text{H}$  signals exhibited 37% and 70% intensity losses for spiro-OMeTAD: BCF blends (1:1 and 1:4 molar ratios). The loss in the signal intensity and the signal broadening indicates the presence of paramagnetic species in the form of radical cations in the doped material, as will be

confirmed by the EPR analysis described later. It is worth recalling that similar signal broadening was also observed in 1D  $^{19}\text{F}$  MAS spectra of doped spiro-OMeTAD, and hence in conjunction with the local structural heterogeneity, the presence of paramagnetic species would cause the signal broadening as well.

Moving to 1D  $^1\text{H}\rightarrow^{13}\text{C}$  CP-MAS NMR analyses, the  $^{13}\text{C}$  spectrum of the spiro-OMeTAD:BCF (1:4) blend exhibited relatively broad signals for both methoxy and aromatic regions, consistently with the  $^1\text{H}$  and  $^{19}\text{F}$  NMR peak broadening due to the interpenetration of BCF molecules that disrupt the self-assembly and packing interactions in spiro-OMeTAD molecules as well as the formation active radical species. Although a systematic analysis of 2D  $^1\text{H}\text{-}^{13}\text{C}$  HETCOR NMR spectra (as presented for neat spiro-OMeTAD in Section 4.2) can also be extended to spiro-OMeTAD:BCF blends in order to identify key interactions in distinct species formed upon doping, the extensive peak broadening and signal intensity losses make it difficult to acquire 2D  $^1\text{H}\text{-}^{13}\text{C}$  HETCOR spectra for these blends. Instead, 2D  $^1\text{H}\text{-}^1\text{H}$  correlation experiments were applied to examine the morphological changes in the BCF-doped spiro-OMeTAD material, as these experiments benefit from inherently high sensitivity associated with protons.

Figure 4.10 presents 2D  $^1\text{H}\text{-}^1\text{H}$  DQ-SQ correlation spectra of undoped and BCF-doped spiro-OMeTAD blends. The GIPAW DFT-D calculated chemical shifts for all  $^1\text{H}\text{-}^1\text{H}$  pairs within 2.5 Å are superimposed on the 2D  $^1\text{H}\text{-}^1\text{H}$  DQ-SQ spectrum of pristine spiro-OMeTAD. A broad distribution of  $^1\text{H}$  DQ peaks centered at ~3 ppm at the diagonal corresponds to dipolar coupled  $^1\text{H}\text{-}^1\text{H}$  pairs in methoxy groups, and the distribution of DQ signals at 10-16 ppm is due to the close  $^1\text{H}\text{-}^1\text{H}$  proximities in aromatic groups. Specifically, the off-diagonal DQ signals at 7.5 and 10.5 ppm (blue arrows) are attributed to the inter- and intramolecular dipolar interactions between methoxy and aromatic groups with the closest  $^1\text{H}\text{-}^1\text{H}$  distances of 2.5 Å and 2.3 Å, respectively. Broader DQ-SQ features are observed in BCF-doped spiro-OMeTAD compared to pristine spiro-OMeTAD, suggesting that the addition of BCF molecules induces variation in the local order and intermolecular interactions between spiro-OMeTAD molecules. Furthermore, these variations in the local structures and proximities due to BCF doping cause the deshielding of the off-diagonal DQ peaks at 9.0-11.0 ppm (compared to 7.5 -10.5 ppm) along the indirect F1 dimension. In addition, the 2D peaks between methoxy and aromatic protons (blue arrows) were

not detected in the DQ-SQ spectrum of the spiro-OMeTAD:BCF blend due to the changes in the packing interactions of spiro-OMeTAD molecules. Intriguingly, upon examining and comparing the horizontal line-cut spectra of 2D  $^1\text{H}$  DQ spectra of pristine and doped spiro-OMeTAD, one can clearly observe that the degree of signal intensity loss in the aromatic regions is higher than the methoxy groups. This suggests, to a certain extent, that the paramagnetic species are closer to the aromatic rings than the methoxy groups. Overall, this analysis suggests that the addition of dopant molecules perturbs the local structures and packing interactions due to the OSC-dopant miscibility and intermolecular interactions.

The key learnings from multinuclear ( $^1\text{H}$ ,  $^{11}\text{B}$ ,  $^{13}\text{C}$ , and  $^{19}\text{F}$ ) ssNMR analyses of undoped and doped spiro-OMeTAD can be summarized in the following points: (i) distinct BCF and BCF-water complexes are identified using 1D  $^{11}\text{B}$  NMR analyses; (ii) molecular self-assembly and packing interactions in spiro-OMeTAD are perturbed upon the addition of BCF molecules as observed by the changes in  $^1\text{H}$ ,  $^{19}\text{F}$  and  $^{13}\text{C}$  NMR chemical shifts and  $^1\text{H}$ - $^1\text{H}$  dipolar interactions, and (iii) significant reduction of signal intensity is observed upon addition of BCF dopant (predominantly for aromatic spiro-OMeTAD moieties) suggesting the formation of paramagnetic species in doped material.

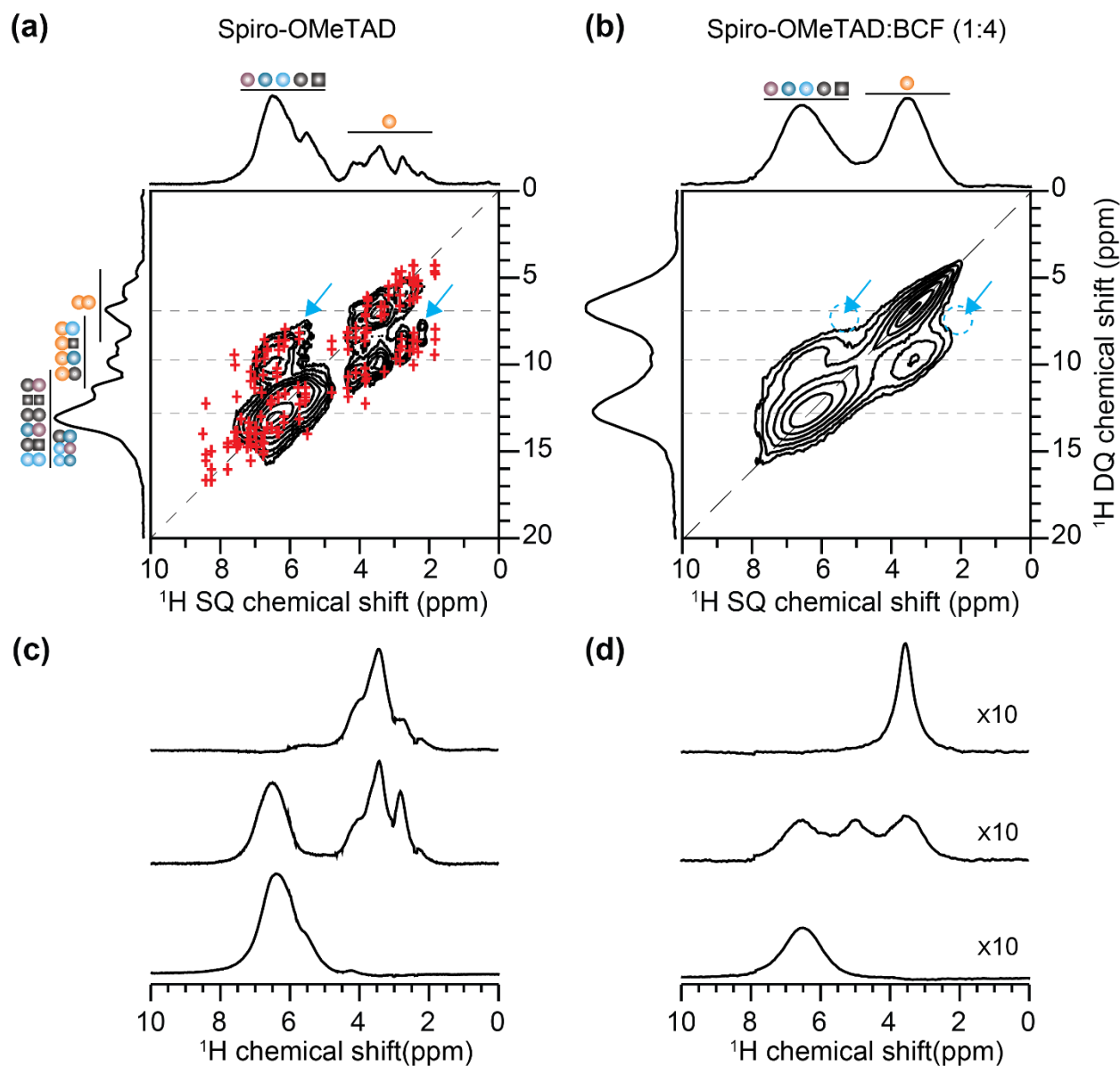


**Figure 4.10.** Solid-state  $^1\text{H}$ - $^1\text{H}$  DQ-SQ correlation MAS NMR spectra of (a) undoped and (b) spiro-OMeTAD:BCF (1:4) blend acquired at 18.8 T ( $^1\text{H}$  800 MHz), 50 kHz MAS and at room temperature. For the undoped spiro-OMeTAD shown in (a), the GIPAW DFT-D calculated chemical shifts for all  $^1\text{H}$ - $^1\text{H}$  pairs within 2.5 Å are overlaid on top of the experimental spectrum (blue crosses). The horizontal line-cut spectra of (c) undoped spiro-OMeTAD and (d) spiro-OMeTAD:BCF blend are extracted and compared for specific  $^1\text{H}$  DQ peaks (~7.0, 9.7, and 12.9 ppm) as indicated by the horizontal dashed lines in (a) and (b).

To further confirm the presence of paramagnetic species and hyperfine interactions in doped OSCs, 1D, and 2D solid-state EPR spectroscopy has been employed.<sup>47,80-82</sup> Figure 4.11 compares the X-band continuous-wave length (CW) EPR spectra of pristine and doped spiro-OMeTAD material. The undoped spiro-OMeTAD exhibits a weak intensity signal with a  $g$ -factor of 2.0042, corresponding to a free-electron  $g$ -factor, at a magnetic field centered at 3494 Gauss (G). This signal is attributed to the presence of a small concentration of spiro-OMeTAD<sup>+</sup> cation species produced upon exposure to oxygen.<sup>10,25,83</sup> A linewidth of 4.5 G and broad distribution of signals near 3493 G for the spiro-OMeTAD:BCF (1:1 molar ratio) indicate the presence of different paramagnetic species, most notably spiro-OMeTAD<sup>+</sup> and spiro-OMeTAD-NH•. For example, it has been reported that an electron transfer process can occur from the adjacent neutral OSC molecules to the protonated OSC molecules to lead to radical species.<sup>44,78,80,83-85</sup> The optical absorption spectra suggest the formation of spiro-OMeTAD-NH• (peak at ~620 nm). However, such species are expected to react with each other to release hydrogen gas and regenerate neutral spiro-OMeTAD.<sup>86</sup> For spiro-OMeTAD:BCF molar ratio 1:4, we observed a further increase in the EPR signal intensity at ~3495 G with a decrease of EPR linewidth to 1.6 G and a  $g$  factor of 2.0024 close to the free-electron value. Additionally, longitudinal ( $T_{1e}$ ) and transverse ( $T_{2e}$ ) relaxation times of electron spins were measured and compared for the doped materials with 1 and 4 BCF molar equivalents. For the spiro-OMeTAD:BCF (1:1), inhomogeneous  $T_{1e}$  and  $T_{2e}$  values of electrons were found to be 1.2  $\mu$ s and 60 ns, respectively, as measured by the inversion recovery and Hahn-echo experiments. For the same sample, heterogeneity in the EPR lineshape (broader) is in accord with the presence of different radical species along with spiro-OMeTAD<sup>+</sup>. For the spiro-OMeTAD:BCF (1:4 molar ratio), the 1D EPR lineshape is homogenous, and a free induction decay (25 ns) has been acquired with  $T_{1e}$  of 500 ns. The different electron spin relaxation times ( $T_{1e}$  and  $T_{2e}$ ) corroborate that the different paramagnetic (or active radical) species co-exist in p-type doped spiro-OMeTAD:BCF blends, indicating that the different doping mechanisms, depending on the concentrations of the dopant molecules, consistently with the different doping mechanism suggested in the previous studies.<sup>29,83</sup>



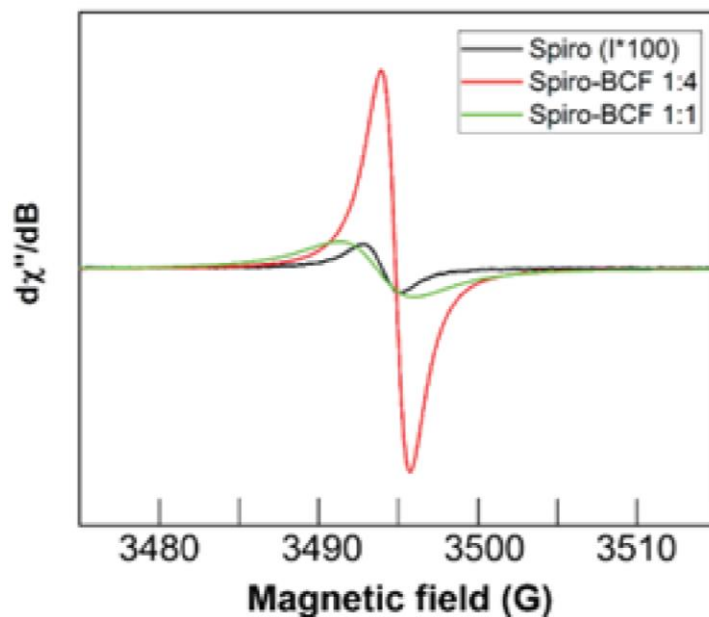


**Figure 4.11.** Solid-state CW EPR spectrum for the neat spiro-OMeTAD and spiro-OMeTAD:BCF blends at 1:1 and 1:4 molar ratios.

The hyperfine sub-level correlation spectroscopy (HYSCORE) technique is particularly suitable to characterize the hyperfine interactions between electron and nuclear spins in doped OSCs. The HYSCORE spectrum exhibits 2D peaks due to the hyperfine couplings that originate from (i) anisotropic dipole-dipole interaction, which depends on the relative orientation of spin magnetic moments, and (ii) isotropic fermi-contact interaction that arises when there is a finite spin density of the electron spin at the nucleus. While insight into the local hyperfine interactions in the doped systems can be obtained from pulse 2D EPR techniques, the very fast relaxation times, even at 10 K, makes it difficult to carry out such experiments. Nevertheless, it has been feasible to acquire the 2D HYSCORE spectrum of spiro-OMeTAD:BCF (1:1) blend (Figure 4.11), whereby the hyperfine coupling associated with  $^1\text{H}$  ( $\sim 15$  MHz) is detected in the (+,+) quadrant of the HYSCORE spectrum.<sup>87,88</sup> A well-resolved  $^{19}\text{F}$  peak at  $\nu=12.5$  MHz indicates that the fluorine atoms are spin-polarized by the electrons. The  $^1\text{H}$  signal at  $\nu=15$  MHz indicates a strong electron-proton hyperfine coupling dominated by the dipolar interaction, with a vertical shift of 1.8 MHz indicating an electron- $^1\text{H}$  distance of  $\sim 0.35$  nm, suggesting that the bulky aromatic BCF molecules are located in the vicinity of spiro-OMeTAD, as estimated based on the dipole single-point approximation. The same HYSCORE spectrum exhibits weak hyperfine

couplings with the two isotopes of boron  $^{10}\text{B}$  ( $\nu = 1.6$  MHz) and  $^{11}\text{B}$  ( $\nu = 4.8$  MHz) on the diagonal (red arrows) but does not show an anti-diagonal signal, indicating that these hyperfine interactions arise purely from the dipolar interaction. The broad distributions of signals in the  $(-,+)$  quadrant of the same spectrum are expected to originate from the single-quantum and double-quantum signals associated with  $^{14}\text{N}$  sites and weak hyperfine couplings associated with  $^{13}\text{C}$  and with  $^{14}\text{N}$  sites, which are difficult to resolve and distinguish.

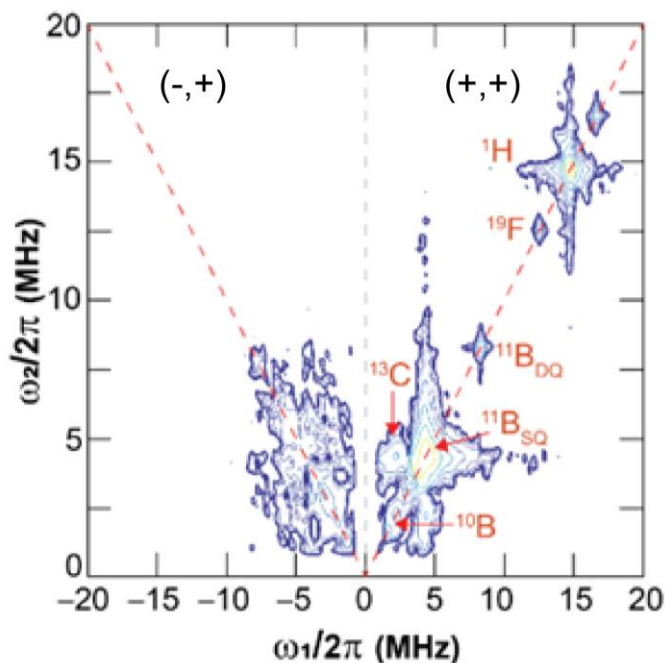


**Figure 4.12.** Solid-state 2D HYSORE spectrum of spiro-OMeTAD: BCF (1:1 molar ratio) acquired at 10 K.

Overall, detailed 2D ssNMR and EPR spectroscopy analyses corroborate that the BCF molecules exhibit different intermolecular interactions with spiro-OMeTAD due to the different ionic species and radicals that are formed during the p-type doping process. The addition of a dilute concentration of BCF molecules leads to p-doping of spiro-OMeTAD, which is hypothesized to occur via a doping process induced by Lewis acid BCF molecules.<sup>29</sup> (See Equation 4.2) The doping process is expected to occur by transferring the electron from spiro-OMeTAD to BCF molecules, leading to a spiro-OMeTAD radical cation species. The positively charged spiro-OMeTAD is hypothesized to be stabilized by the electron transfer from a neighboring neutral spiro-OMeTAD molecule leading to a cation and radical species. In addition, BCF-water

complexes serve as Brønsted acid sites to transfer a proton to spiro-OMeTAD molecules, which are hypothesized to trigger p-type doping particularly at higher concentrations of BCF (greater than 1 molar equivalent),<sup>86</sup> leading to the formation of small amounts of spiro-OMeTAD-H<sup>+</sup> species as indicated by changes in the optical absorption (UV-vis spectroscopy) and vibrational spectra (FT-IR spectroscopy).<sup>83</sup> (See Equation 4.2) Doped spiro-OMeTAD, or organic semiconductors in general, are challenging to characterize due to the presence of dia- and paramagnetic regions, which lead to homogenous and inhomogeneous signal broadening in ssNMR spectra as a consequence of anisotropic bulk magnetic susceptibility (ABMS) induced shifts. However, the presented NMR crystallography approach offers key advantages of identifying various packing interactions that play a crucial role in determining the properties of the material and can be extended to other types of organic materials.



#### 4.4 Moisture stability of chemically doped spiro-OMeTAD:BCF blends

As described in the previous two chapters, moisture has been a notorious factor causing the structural transformation of the perovskite phase to deteriorate the performance of the material. The instability issues also persist in HTLs, though its characterization at the molecular level is seldomly carried out. The different degradation reactions associated HTLs can be studied by ssNMR spectroscopy techniques. The hygroscopicity of Li-TFSI is a well-known stability concern for PSCs with doped spiro-OMeTAD. Hence it is important to evaluate the moisture stability of BCF-doped spiro-OMeTAD material. Akin to what is presented in previous chapters, the spiro-OMeTAD:BCF (1:1 molar ratio) blend were systematically exposed to low water vapour concentration condition (40% RH) and high water vapour concentration (85% RH) in accordance with the protocol proposed to evaluate the stability of PSCs.<sup>89</sup>

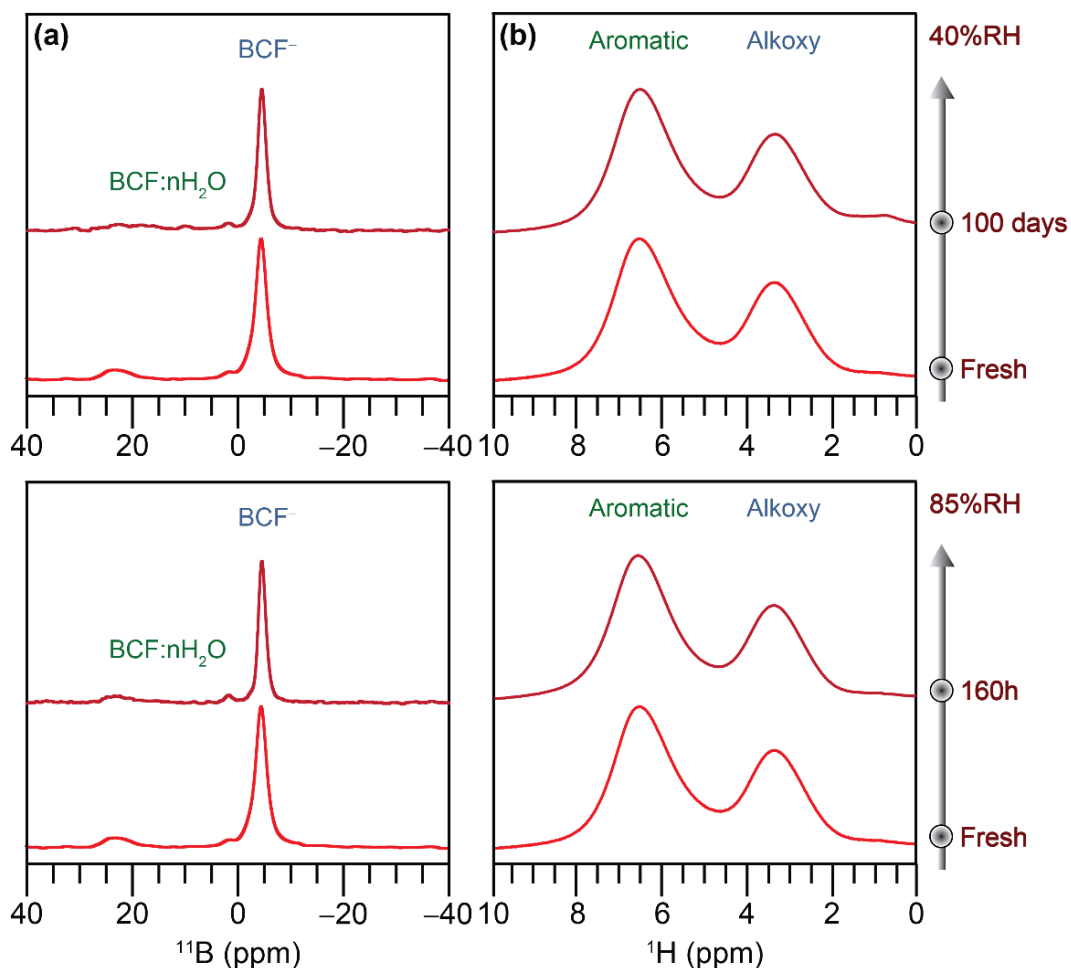


**Figure 4.13.** 1D (a)  $^{11}\text{B}$  and (b)  $^1\text{H}$  MAS NMR spectra of spiro-OMeTAD:BCF (1:1 molar ratio) blend as a function of moisture exposure at 40% RH (top) and 85% RH (bottom) for the time indicated on the right side of the spectra. All the spectra were acquired at 18.8 T, room temperature, and 50 kHz MAS frequency.

Figure 4.13 shows 1D  $^{11}\text{B}$  and  $^1\text{H}$  MAS NMR spectra of spiro-OMeTAD:BCF blends before and after exposure to moisture. Upon aging the material at 40% RH for 100 days (> 3 months), there is no significant change for the narrow signal at  $-5$  ppm, corresponding to BCF anion species. There is a subtle decrease in the intensity of signal corresponding to BCF-water complexes. Similar results were observed upon exposing the material at 85% RH for 160 hours (~ 7 days). Much like 1D  $^{11}\text{B}$  NMR spectra, 1D  $^1\text{H}$  MAS spectra for the aged spiro-OMeTAD:BCF blends did not show dramatic changes in the alkoxy and aromatic sites. The  $^1\text{H}$  signal broadening and intensity were invariant regardless of the extent of water vapour concentration and time of exposure, suggesting the subtle (or no) change in the spatial

arrangement of paramagnetic species. The spatial proximity of spiro-OMeTAD and BCF in spiro-OMeTAD:BCF (1:1 molar ratio) was further confirmed by the 2D  $^1\text{H}$ - $^{11}\text{B}$  CP-HETCOR experiment.

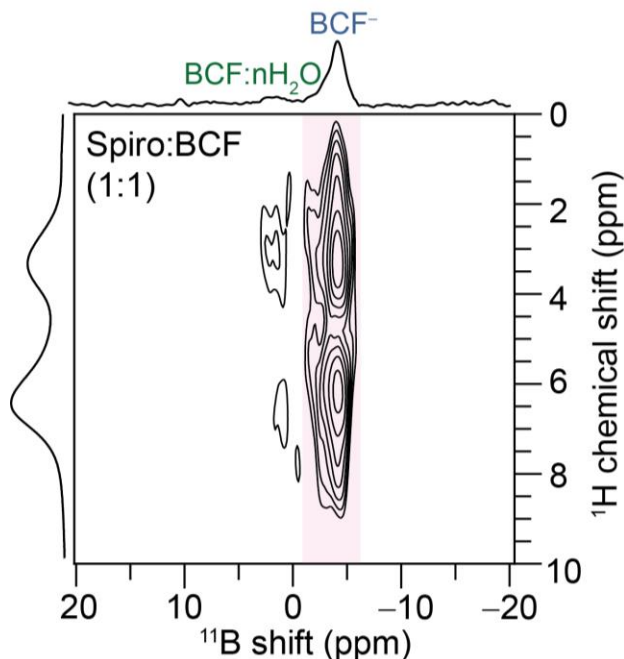


**Figure 4.14.** Solid-state 2D  $^1\text{H}$ - $^{11}\text{B}$  CP-HETCOR NMR spectrum of aged (160h, 85% RH) spiro-OMeTAD:BCF (1:1 molar ratio) blend with CP contact time of 2 ms along with the skyline projections of  $^{11}\text{B}$  and  $^1\text{H}$  spectra in the top and left, respectively. The spectrum was acquired at 18.8 T, room temperature, and 50 kHz MAS frequency.

Figure 4.14 exhibits the 2D  $^1\text{H}$ - $^{11}\text{B}$  CP-HETCOR NMR spectrum of spiro-OMeTAD:BCF (1:1 molar ratio) blend exposed to 85% RH for 160h (~7 days), acquired with CP contact time of 2 ms. The BCF anions ( $^{11}\text{B}$ , -5 ppm) are proximate to methoxy and aromatic protons of spiro-OMeTAD (3.2 ppm, and 6.2 ppm, respectively). In addition, the BCF-water complexes ( $^{11}\text{B}$ , ~1.6 ppm) are also proximate to these different proton sites of spiro-OMeTAD. These suggest that the nanoscale proximity between the dopant (BCF) and the host OSC (spiro-OMeTAD) is not affected upon prolonged exposure to moisture, highlighting the robustness of this blend.

## 4.5 Conclusion

To summarize, a suite of characterization methods have been used to explore the local compositions and structures in BCF-doped spiro-OMeTAD thin films. The formation of oxidized spiro-OMeTAD species is observed employing optical absorption spectroscopy upon doping with BCF. Intermolecular interactions between spiro-OMeTAD and BCF are characterized by FTIR and 1D/2D ssNMR spectroscopy. Specifically,  $^{11}\text{B}$  NMR signals corresponding to pristine BCF, which is tri-coordinated in nature, and tetracoordinate BCF anions and BCF-water complexes are observed. The changes associated with 1D  $^1\text{H}$ ,  $^{13}\text{C}$ , and  $^{19}\text{F}$  MAS NMR spectra of doped versus the pristine spiro-OMeTAD indicate that the local structures and packing interactions of spiro-OMeTAD are different before and after chemical doping with BCF molecules. This was further confirmed by 2D  $^1\text{H}$ - $^1\text{H}$  DQ-SQ spectroscopy. The signal broadening associated with 1D  $^1\text{H}$ ,  $^{13}\text{C}$ , and  $^{19}\text{F}$  MAS NMR spectra of doped spiro-OMeTAD species collectively indicate the presence of various paramagnetic species. Formation of spiro-OMeTAD radical cation (during electron transfer process) or spiro-OMeTAD- $\text{H}^+$  species (BCF-water complex transferring proton to spiro-OMeTAD) can be hypothesized, which indicates that the molecular doping occurs by interactions with both Lewis acid and Brønsted acid sites of BCF. This is further corroborated by the 1D/2D EPR spectroscopy, which indicated the presence of paramagnetic species. The blend of spiro-OMeTAD and BCF also exhibited remarkable moisture stability, as no significant structural changes in aged material were observed. Despite the structural heterogeneity associated with such organic molecules, molecular-level magnetic resonance techniques supported by a few macroscopic-level techniques assisted in understanding the doping mechanism. This approach has some drawbacks as the doped OSCs consist of diamagnetic and paramagnetic species, leading to homogenous and inhomogeneous signal broadening in ssNMR spectra. The signal broadening originates from anisotropic bulk magnetic susceptibility (ABMS)- induced shifts and dipolar contributions from locally disordered regions, which makes it more challenging to accurately analyze the NMR spectra.

## 4.6 References

- 1 M. Zhang, F. Zhang, Y. Wang, L. Zhu, Y. Hu, Z. Lou, Y. Hou and F. Teng, *Sci. Rep.*, 2018, **8**, 11157.
- 2 Z. Yu, L. Sun, Z. Yu and L. Sun, *Adv. Energy Mater.*, 2015, **5**, 1500213.
- 3 S. Ameen, M. A. Rub, S. A. Kosa, K. A. Alamry, M. S. Akhtar, H. S. Shin, H. K. Seo, A. M. Asiri and M. K. Nazeeruddin, *ChemSusChem*, 2016, **9**, 10–27.
- 4 J. Urieta-Mora, I. García-Benito, A. Molina-Ontoria and N. Martín, *Chem. Soc. Rev.*, 2018, **47**, 8541–8571.
- 5 J. Chen and N. G. Park, *Adv. Mater.*, 2019, **31**, 1803019.
- 6 G. W. Kim, H. Choi, M. Kim, J. Lee, S. Y. Son and T. Park, *Adv. Energy Mater.*, 2020, **10**, 1903403.
- 7 A. Krishna and A. C. Grimsdale, *J. Mater. Chem. A*, 2017, **5**, 16446–16466.
- 8 E. H. Jung, N. J. Jeon, E. Y. Park, C. S. Moon, T. J. Shin, T.-Y. Yang, J. H. Noh and J. Seo, *Nature*, 2019, **567**, 511–515.
- 9 J. H. Heo, H. J. Han, D. Kim, T. K. Ahn and S. H. Im, *Energy Environ. Sci.*, 2015, **8**, 1602–1608.
- 10 S. Fantacci, F. De Angelis, M. K. Nazeeruddin and M. Grätzel, *J. Phys. Chem. C*, 2011, **115**, 23126–23133.
- 11 S. Shahnawaz, S. Sudheendran Swayamprabha, M. R. Nagar, R. A. K. Yadav, S. Gull, D. K. Dubey and J. H. Jou, *J. Mater. Chem. C*, 2019, **7**, 7144–7158.
- 12 H. J. Snaith and M. Grätzel, *Appl. Phys. Lett.*, 2006, **89**, 262114.
- 13 J. Luo, J. Xia, H. Yang, L. Chen, Z. Wan, F. Han, H. A. Malik, X. Zhu and C. Jia, *Energy Environ. Sci.*, 2018, **11**, 2035–2045.
- 14 J. Niu, D. Yang, X. Ren, Z. Yang, Y. Liu, X. Zhu, W. Zhao and S. (Frank) Liu, *Org. Electron.*, 2017, **48**, 165–171.
- 15 Y. Kim, S. Cook, S. M. Tuladhar, S. A. Choulis, J. Nelson, J. R. Durrant, D. D. C. Bradley, M. Giles, I. McCulloch, C. S. Ha and M. Ree, *Nat. Mater.*, 2006, **5**, 197–203.

- 16 Y. Yang Michael, Q. Chen, Y. T. Hsieh, T. Bin Song, N. De Marco, H. Zhou and Y. Yang, *ACS Nano*, 2015, **9**, 7714–7721.
- 17 J. Jeong, M. Kim, J. Seo, H. Lu, P. Ahlawat, A. Mishra, Y. Yang, M. A. Hope, F. T. Eickemeyer, M. Kim, Y. J. Yoon, I. W. Choi, B. P. Darwich, S. J. Choi, Y. Jo, J. H. Lee, B. Walker, S. M. Zakeeruddin, L. Emsley, U. Rothlisberger, A. Hagfeldt, D. S. Kim, M. Grätzel and J. Y. Kim, *Nature*, 2021, **592**, 381–385.
- 18 P. Murugan, H. Ting, H. Xiaotian and Y. Chen, *J. Mater. Chem. A*, 2022, **10**, 5044–5081.
- 19 G. Ren, W. Han, Y. Deng, W. Wu, Z. Li, J. Guo, H. Bao, C. Liu and W. Guo, *J. Mater. Chem. A*, 2021, **9**, 4589–4625.
- 20 Z. Hawash, L. K. Ono and Y. Qi, *Adv. Mater. Interfaces*, 2018, **5**, 1700623.
- 21 F. M. Rombach, S. A. Haque and T. J. Macdonald, *Energy Environ. Sci.*, 2021, **14**, 5161–5190.
- 22 Z. Hawash, L. K. Ono and Y. Qi, *Adv. Mater. Interfaces*, 2016, **3**, 1600117.
- 23 R. Schölin, M. H. Karlsson, S. K. Eriksson, H. Siegbahn, E. M. J. Johansson and H. Rensmo, *J. Phys. Chem. C*, 2012, **116**, 26300–26305.
- 24 E. Kasparavicius, M. Franckevičius, V. Malinauskiene, K. Genevičius, V. Getautis and T. Malinauskas, *ACS Appl. Energy Mater.*, 2021, **4**, 13696–13705.
- 25 A. Abate, T. Leijtens, S. Pathak, J. Teuscher, R. Avolio, M. E. Errico, J. Kirkpatrick, J. M. Ball, P. Docampo, I. McPherson and H. J. Snaith, *Phys. Chem. Chem. Phys.*, 2013, **15**, 2572–2579.
- 26 G. Tumen-Ulzii, T. Matsushima and C. Adachi, *Energy & Fuels*, 2021, **35**, 18915–18927.
- 27 G. Tumen-Ulzii, C. Qin, T. Matsushima, M. R. Leyden, U. Balijipalli, D. Klotz and C. Adachi, *Sol. RRL*, 2020, **4**, 2000305.
- 28 Z. Li, C. Xiao, Y. Yang, S. P. Harvey, D. H. Kim, J. A. Christians, M. Yang, P. Schulz, S. U. Nanayakkara, C. S. Jiang, J. M. Luther, J. J. Berry, M. C. Beard, M. M. Al-Jassim and K. Zhu, *Energy Environ. Sci.*, 2017, **10**, 1234–1242.
- 29 T. Ye, J. Wang, W. Chen, Y. Yang and D. He, *ACS Appl. Mater. Interfaces*, 2017, **9**,



- 17923–17931.
- 30 N. Sakai, R. Warren, F. Zhang, S. Nayak, J. Liu, S. V. Kesava, Y.-H. Lin, H. S. Biswal, X. Lin, C. Grovenor, T. Malinauskas, A. Basu, T. D. Anthopoulos, V. Getautis, A. Kahn, M. Riede, P. K. Nayak and H. J. Snaith, *Nat. Mater.*, 2021, **20**, 1248–1254.
- 31 J. Y. Seo, S. Akin, M. Zalibera, M. A. R. Preciado, H. S. Kim, S. M. Zakeeruddin, J. V. Milić and M. Grätzel, *Adv. Funct. Mater.*, 2021, **31**, 2102124.
- 32 Z. Li, J. Tinkham, P. Schulz, M. Yang, D. H. Kim, J. Berry, A. Sellinger, K. Zhu, Z. Li, P. Schulz, M. Yang, D. H. Kim, J. Berry, A. Sellinger, K. Zhu and J. Tinkham, *Adv. Energy Mater.*, 2017, **7**, 1601451.
- 33 T. Zhang, F. Wang, H. B. Kim, I. W. Choi, C. Wang, E. Cho, R. Konefal, Y. Puttison, K. Terado, L. Kobera, M. Chen, M. Yang, S. Bai, B. Yang, J. Suo, S. C. Yang, X. Liu, F. Fu, H. Yoshida, W. M. Chen, J. Brus, V. Coropceanu, A. Hagfeldt, J. L. Brédas, M. Fahlman, D. S. Kim, Z. Hu and F. Gao, *Science*, 2022, **377**, 495–501.
- 34 Y. Han, G. Barnes, Y. H. Lin, J. Martin, M. Al-Hashimi, S. Y. Alqaradawi, T. D. Anthopoulos and M. Heaney, *Chem. Mater.*, 2016, **28**, 8016–8024.
- 35 P. Zalar, Z. B. Henson, G. C. Welch, G. C. Bazan and T. Q. Nguyen, *Angew. Chemie Int. Ed.*, 2012, **51**, 7495–7498.
- 36 P. Pingel, M. Arvind, L. Kölln, R. Steyrleuthner, F. Kraffert, J. Behrends, S. Janietz, D. P. Neher Pingel, L. Kölln, S. Janietz, M. Arvind, D. Neher, R. Steyrleuthner, F. Kraffert and J. Behrends, *Adv. Electron. Mater.*, 2016, **2**, 1600204.
- 37 G. C. Welch, R. Coffin, J. Peet and G. C. Bazan, *J. Am. Chem. Soc.*, 2009, **131**, 10802–10803.
- 38 G. C. Welch and G. C. Bazan, *J. Am. Chem. Soc.*, 2011, **133**, 4632–4644.
- 39 J. Jia, J. Dong, B. Shi, J. Wu, Y. Wu and B. Cao, *ACS Appl. Mater. Interfaces*, 2021, **13**, 2472–2482.
- 40 T. Ye, W. Chen, S. Jin, S. Hao, X. Zhang, H. Liu and D. He, *ACS Appl. Mater. Interfaces*, 2019, **11**, 14004–14010.
- 41 A. D. Scaccabarozzi, A. Basu, F. Aniés, J. Liu, O. Zapata-Arteaga, R. Warren, Y. Firdaus,

- M. I. Nugraha, Y. Lin, M. Campoy-Quiles, N. Koch, C. Müller, L. Tsetseris, M. Heeney and T. D. Anthopoulos, *Chem. Rev.*, 2022, **122**, 4420–4492.
- 42 P. Zalar, M. Kuik, Z. B. Henson, C. Woellner, Y. Zhang, A. Sharenko, G. C. Bazan, T.-Q. Nguyen, P. Zalar, M. Kuik, Z. B. Henson, C. Woellner, Y. Zhang, A. Sharenko, G. C. Bazan and T. Nguyen, *Adv. Mater.*, 2014, **26**, 724–727.
- 43 B. Yurash, D. Leifert, G. N. M. Reddy, D. X. Cao, S. Biberger, V. V. Brus, M. Seifrid, P. J. Santiago, A. Köhler, B. F. Chmelka, G. C. Bazan and T. Q. Nguyen, *Chem. Mater.*, 2019, **31**, 6715–6725.
- 44 B. Yurash, D. X. Cao, V. V. Brus, D. Leifert, M. Wang, A. Dixon, M. Seifrid, A. E. Mansour, D. Lungwitz, T. Liu, P. J. Santiago, K. R. Graham, N. Koch, G. C. Bazan and T. Q. Nguyen, *Nat. Mater.*, 2019, **18**, 1327–1334.
- 45 M. Arvind, C. E. Tait, M. Guerrini, J. Krumland, A. M. Valencia, C. Cocchi, A. E. Mansour, N. Koch, S. Barlow, S. R. Marder, J. Behrends and D. Neher, *J. Phys. Chem. B*, 2020, **124**, 7694–7708.
- 46 L. Huang, Z. Hu, J. Xu, K. Zhang, J. Zhang, J. Zhang and Y. Zhu, *Electrochim. Acta*, 2016, **196**, 328–336.
- 47 A. L. Dixon, H. Vezin, T.-Q. Nguyen and G. N. M. Reddy, *Mater. Horizons*, 2022, **9**, 981–990.
- 48 P. Hodgkinson, *Prog. Nucl. Magn. Reson. Spectrosc.*, 2020, **118–119**, 10–53.
- 49 T. Charpentier, *Solid State Nucl. Magn. Reson.*, 2011, **40**, 1–20.
- 50 N. T. Duong, Y. Aoyama, K. Kawamoto, T. Yamazaki and Y. Nishiyama, *Molecules*, 2021, **26**, 4652.
- 51 C. Guzmán-Afonso, Y. L. Hong, H. Colaux, H. Iijima, A. Saitow, T. Fukumura, Y. Aoyama, S. Motoki, T. Oikawa, T. Yamazaki, K. Yonekura and Y. Nishiyama, *Nat. Commun.*, 2019, **10**, 3537.
- 52 D. H. Brouwer, S. Cadars, J. Eckert, Z. Liu, O. Terasaki and B. F. Chmelka, *J. Am. Chem. Soc.*, 2013, **135**, 5641–5655.
- 53 A. L. Webber, L. Emsley, R. M. Claramunt and S. P. Brown, *J. Phys. Chem. A*, 2010, **114**,

- 10435–10442.
- 54 C. J. Pickard, E. Salager, G. Pintacuda, B. Elena and L. Emsley, *J. Am. Chem. Soc.*, 2007, **129**, 8932–8933.
- 55 B. R. Luginbuhl, P. Raval, T. Pawlak, Z. Du, T. Wang, N. Schopp, S. Chae, S. Yoon, A. Yi, H. J. Kim, V. Coropceanu, J.-L. Brédas, T.-Q. Nguyen and G. N. M. Reddy, *Adv. Mater.*, 2022, **34**, 2105943.
- 56 C. E. Hughes, G. N. M. Reddy, S. Masiero, S. P. Brown, P. A. Williams and K. D. M. Harris, *Chem. Sci.*, 2017, **8**, 3971–3979.
- 57 M. Cordova, M. Balodis, A. Hofstetter, F. Paruzzo, S. O. Nilsson Lill, E. S. E. Eriksson, P. Berruyer, B. Simões de Almeida, M. J. Quayle, S. T. Norberg, A. Svensk Ankarberg, S. Schantz and L. Emsley, *Nat. Commun.*, 2021, **12**, 2964.
- 58 T. Pawlak, I. Sudgen, G. Bujacz, D. Iuga, S. P. Brown and M. J. Potrzebowski, *Cryst. Growth Des.*, 2021, **21**, 3328–3343.
- 59 C. Bonhomme, C. Gervais, F. Babonneau, C. Coelho, F. Pourpoint, T. Azaïs, S. E. Ashbrook, J. M. Griffin, J. R. Yates, F. Mauri and C. J. Pickard, *Chem. Rev.*, 2012, **112**, 5733–5779.
- 60 A. R. Oganov, C. J. Pickard, Q. Zhu and R. J. Needs, *Nat. Rev. Mater.*, 2019, **4**, 331–348.
- 61 S. Sturniolo, T. F. G. Green, R. M. Hanson, M. Zilka, K. Refson, P. Hodgkinson, S. P. Brown and J. R. Yates, *Solid State Nucl. Magn. Reson.*, 2016, **78**, 64–70.
- 62 J. Liu, W. Liu, E. Aydin, G. T. Harrison, F. H. Isikgor, X. Yang, A. S. Subbiah and S. De Wolf, *ACS Appl. Mater. Interfaces*, 2020, **12**, 23874–23884.
- 63 J. Romanos, M. Beckner, D. Stalla, A. Tekeei, G. Suppes, S. Jalisatgi, M. Lee, F. Hawthorne, J. D. Robertson, L. Firlej, B. Kuchta, C. Wexler, P. Yu and P. Pfeifer, *Carbon N. Y.*, 2012, **54**, 208–214.
- 64 E. Karakaş Sarıkaya and Ö. Dereli, *J. Mol. Struct.*, 2013, **1052**, 214–220.
- 65 R. Ramasamy, *Int. J. Phys. Appl.*, 2014, **6**, 1–6.
- 66 S. Gunasekaran, S. Seshadri and S. Muthu, *Indian J. Pure Appl. Phys.*, 2006, **44**, 581–

586.

- 67 J. Wang, J. Li, X. Xu, Z. Bi, G. Xu and H. Shen, *RSC Adv.*, 2016, **6**, 42413–42420.
- 68 C. Kallol, C. Wei-Chih, A. B. Paul, M. V. Vineeth, C. C. Chen and A. C. Shane, *Materials*, 2020, **13**, 3622.
- 69 M. Seifrid, G. N. M. Reddy, B. F. Chmelka and G. C. Bazan, *Nat. Rev. Mater.*, 2020, **5**, 910–930.
- 70 M. R. Hansen, R. Graf and H. W. Spiess, *Chem. Rev.*, 2016, **116**, 1272–1308.
- 71 N. C. Miller, E. Cho, M. J. N. Junk, R. Gysel, C. Risko, D. Kim, S. Sweetnam, C. E. Miller, L. J. Richter, R. J. Kline, M. Heeney, I. McCulloch, A. Amassian, D. Acevedo-Feliz, C. Knox, M. R. Hansen, D. Dudenko, B. F. Chmelka, M. F. Toney, J. L. Brédas and M. D. McGehee, *Adv. Mater.*, 2012, **24**, 6071–6079.
- 72 M. T. Seifrid, G. N. M. Reddy, C. Zhou, B. F. Chmelka and G. C. Bazan, *J. Am. Chem. Soc.*, 2019, **141**, 5078–5082.
- 73 S. R. Chaudhari, J. M. Griffin, K. Broch, A. Lesage, V. Lemaur, D. Dudenko, Y. Olivier, H. Sirringhaus, L. Emsley and C. P. Grey, *Chem. Sci.*, 2017, **8**, 3126–3136.
- 74 D. Dudenko, A. Kiersnowski, J. Shu, W. Pisula, D. Sebastiani, H. W. Spiess and M. R. Hansen, *Angew. Chemie Int. Ed.*, 2012, **51**, 11068–11072.
- 75 H. N. Tsao, D. M. Cho, I. Park, M. R. Hansen, A. Mavrinskiy, D. Y. Yoon, R. Graf, W. Pisula, H. W. Spiess and K. Müllen, *J. Am. Chem. Soc.*, 2011, **133**, 2605–2612.
- 76 A. Karki, G.-J. A. H. Wetzelaer, G. N. M. Reddy, V. Nádaždy, M. Seifrid, F. Schauer, G. C. Bazan, B. F. Chmelka, P. W. M. Blom and T.-Q. Nguyen, *Adv. Funct. Mater.*, 2019, **29**, 1901109.
- 77 S. Samanta, P. Raval, G. N. M. Reddy and D. Chaudhuri, *ACS Cent. Sci.*, 2021, **7**, 1391–1399.
- 78 P. S. Marqués, G. Londi, B. Yurash, T. Q. Nguyen, S. Barlow, S. R. Marder and D. Beljonne, *Chem. Sci.*, 2021, **12**, 7012–7022.
- 79 M. Becker, A. Schulz, A. Villinger and K. Voss, *RSC Adv.*, 2011, **1**, 128–134.

- 80 C. E. Tait, A. Reckwitz, M. Arvind, D. Neher, R. Bittl and J. Behrends, *Phys. Chem. Chem. Phys.*, 2021, **23**, 13827–13841.
- 81 T. Biskup, *Front. Chem.*, 2019, **7**, 10.
- 82 A. Privitera, R. Warren, G. Londi, P. Kaienburg, J. Liu, A. Sperlich, A. E. Lauritzen, O. Thimm, A. Ardavan, D. Beljonne and M. Riede, *J. Mater. Chem. C*, 2021, **9**, 2944–2954.
- 83 A. Abate, D. J. Hollman, J. Teuscher, S. Pathak, R. Avolio, G. D’Errico, G. Vitiello, S. Fantacci and H. J. Snaith, *J. Am. Chem. Soc.*, 2013, **135**, 13538–13548.
- 84 F. J. D. Alvarez, C. Orelle and A. L. Davidson, *J. Am. Chem. Soc.*, 2010, **132**, 9513–9515.
- 85 M. Goetz, I. Frisch and I. Sartorius, *Beilstein J. Org. Chem.*, 2013, **9**, 437–446.
- 86 L. H. Doerrler and M. L. H. Green, *J. Chem. Soc. Dalton Trans.*, 1999, 4325–4329.
- 87 A. Pöpl and L. Kevan, *J. Phys. Chem.*, 1996, **100**, 3387–3394.
- 88 J. McCracken, T. M. Casey and R. P. Hausinger, *Appl. Magn. Reson.*, 2021, **52**, 971–994.
- 89 M. V. Khenkin, E. A. Katz, A. Abate, G. Bardizza, J. J. Berry, C. Brabec, F. Brunetti, V. Bulović, Q. Burlingame, A. Di Carlo, R. Cheacharoen, Y. B. Cheng, A. Colsmann, S. Cros, K. Domanski, M. Dusza, C. J. Fell, S. R. Forrest, Y. Galagan, D. Di Girolamo, M. Grätzel, A. Hagfeldt, E. von Hauff, H. Hoppe, J. Kettle, H. Köbler, M. S. Leite, S. (Frank) Liu, Y. L. Loo, J. M. Luther, C. Q. Ma, M. Madsen, M. Manceau, M. Matheron, M. McGehee, R. Meitzner, M. K. Nazeeruddin, A. F. Nogueira, Ç. Odabaşı, A. Osherov, N. G. Park, M. O. Reese, F. De Rossi, M. Saliba, U. S. Schubert, H. J. Snaith, S. D. Stranks, W. Tress, P. A. Troshin, V. Turkovic, S. Veenstra, I. Visoly-Fisher, A. Walsh, T. Watson, H. Xie, R. Yıldırım, S. M. Zakeeruddin, K. Zhu and M. Lira-Cantu, *Nat. Energy*, 2020, **5**, 35–49.

# Chapter 5 - Conclusions and perspectives

---

## 5.1 Conclusions

In a broad context, the objectives and results presented in the thesis cover various aspects of structure-stability-property relationships in perovskite-based photovoltaic materials. A significant part of the thesis discusses the different degradation reactions and kinetics aspects of these reactions in hybrid perovskite layers and charge transport layers that are frequently used in emerging perovskite solar cells (PSCs). The performance of PSCs is reduced due to several factors that are intrinsic (thermodynamic phase stability) and extrinsic (moisture, thermochemical, photostability, electrical bias, oxidation, and electrode degradation) in nature, *vide supra* (Chapter 1). The power conversion efficiency of encapsulated PSCs dramatically decreases in about 6 weeks (1000 hours as set by the damp heat test) under stringent operating conditions. The origins of degradation reactions could be manifold. Figure 5.1 illustrates these aspects. While the performance decay can be examined by electronic properties, such as changes in current density and voltage, the molecular-level origins of various organic/inorganic and hybrid species remain elusive and represents a characterization challenge.

Various analytical techniques have been implemented to understand the underlying degradation/transformation mechanism. X-ray diffraction has been extensively utilized to identify crystalline phases formed as a function of aging time. Investigating thin film using this technique is straightforward to have a direct comparison with the devices.<sup>1</sup> However, identifying low- concentrations of organic byproducts can be challenging with this technique. *In operando* electron microscopy technique has been employed to provide a live visualization of morphological changes in the films happening upon aging with cautious use of low electron dosage.<sup>1</sup> Probing interface and depth profiling is feasible to explore the compositional changes using X-ray photoemission spectroscopy (XPS).<sup>2</sup> Photoluminescence spectroscopy has also been widely implemented to examine the bulk emission response of the material.<sup>1</sup> Fluorescence lifetime imaging microscopy facilitates determining the distribution of emission intensity and lifetime on the thin films.<sup>3</sup> However, these techniques do not directly provide structural insights into the thin film/crystalline material.

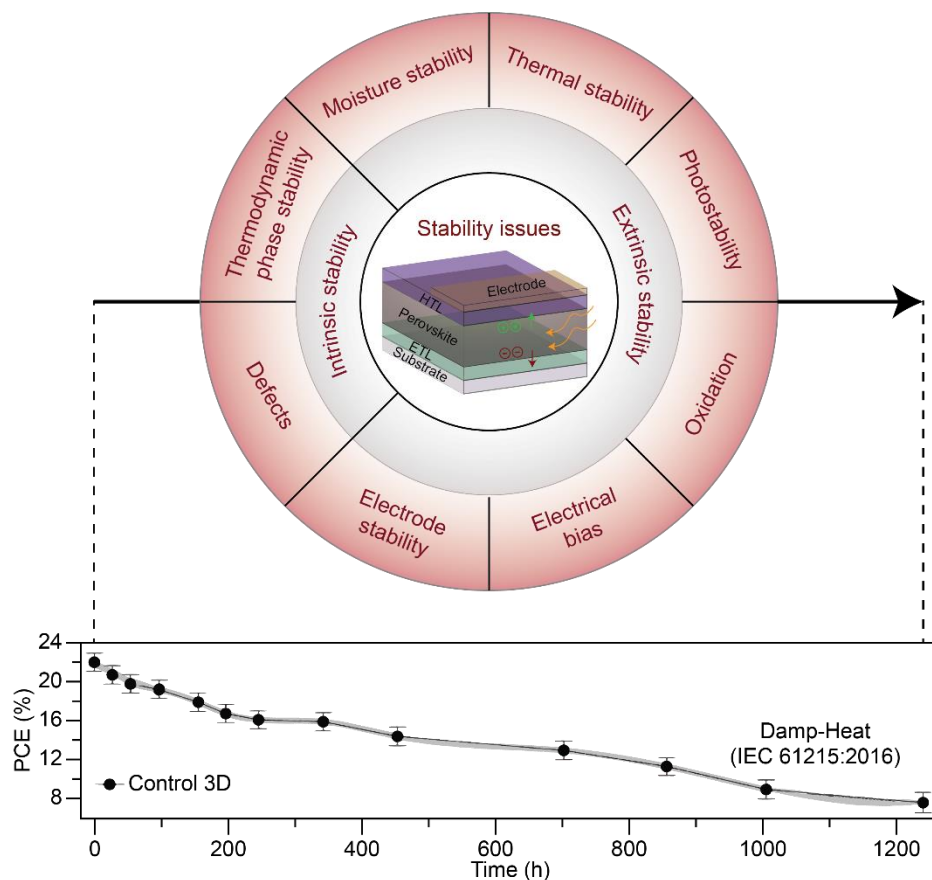


**Figure 5.1.** Stability issues in perovskite material and perovskite solar cells that cause variation in PCEs during the damp-heat test (85% RH and 85 °C) of encapsulated 3D perovskite devices. These figures have been adapted from Ref. <sup>4,5</sup>.

In this regard, ssNMR spectroscopy is a local technique and does not require long-range order in the material, allowing the interfacial chemistry and different organic byproducts formed during degradation to be probed.<sup>6,7</sup> However, intrinsically low sensitivity associated with the technique makes it less straightforward to study thin films, which are mass-limited samples. Since early-state studies of MAS NMR spectroscopy for probing local structures and dynamics in layered perovskites,<sup>8,9</sup> significant progress has been made in understanding the impact of cation doping, surface passivation, light, temperature, solvent, and moisture on structurally complex perovskite formulations and their interfaces.<sup>6,7,10–12</sup> In addition, characterizing nuclei such as bromine and chlorine is challenging due to their high quadrupolar interaction; however, detecting the NQR spectrum for such nuclei as well as iodine is feasible.<sup>11,13</sup> Given these constraints, a multi-technique characterization approach has been employed to probe the

degradation reactions in methylammonium (MA) and formamidinium (FA)-based perovskite formulation, including MAPbI<sub>3</sub>, FAPbI<sub>3</sub>, and CsMAFAPbI<sub>x</sub>Br<sub>3-x</sub>. Beyond the perovskite photoactive layer, insights into the structure-stability-property relationship in tris(pentafluorophenyl) borane (BCF) doped a hole-transporting material, spiro-OMeTAD, is provided.

As illustrated in Chapter 2, high-field multinuclear ssNMR reveals that the  $\alpha \rightarrow \delta$  FAPbI<sub>3</sub> transformation involves surface-initiated local dissolution and precipitation process with water being the solvent. Fast MAS and high-field <sup>1</sup>H NMR results enable one to distinguish and measure -CH sites in  $\alpha$ - and  $\delta$ - FAPbI<sub>3</sub> phases, which can be utilized to construct the kinetic plots. The  $\alpha \rightarrow \delta$  FAPbI<sub>3</sub> phase transformation follows first-order kinetics, facilitating estimation of the half-life decay time for the  $\alpha$ -FAPbI<sub>3</sub> phase. The sluggish  $\alpha \rightarrow \delta$  FAPbI<sub>3</sub> transformation after prolonged exposure to moisture can be reasoned to sparse contact of water molecules with  $\alpha$ -FAPbI<sub>3</sub> phase as they are believed to be encapsulated by  $\delta$ -FAPbI<sub>3</sub> phase. The kinetics of  $\alpha \rightarrow \delta$  FAPbI<sub>3</sub> reaction as functions of water vapor concentration, particle size, and light illumination reveal that exposure of larger particle size to lower water vapor concentration in the absence of light has a much longer half-life decay time. This suggests that the single crystal FAPbI<sub>3</sub> and FA-rich formulations provide a path forward for stable and efficient optoelectronics. In addition, FAPbBr<sub>3</sub> being thermodynamically stable, does not exhibit any phase transformation for a wide range of humidity levels and exposure time. As mentioned earlier, thin films of perovskite material are more comparable to perovskite-based photovoltaic devices, and hence, stability studies on thin films are expected to provide a more accurate understanding of the robustness of the devices. Moisture stability of compositionally tailored FA-rich CsMAFA formulation is examined using ssNMR spectroscopy. Exposure to moisture leads to partial removal of Cs<sup>+</sup> cations from the inorganic perovskite framework leading to different CsPb<sub>2</sub>I<sub>x</sub>Br<sub>5-x</sub> salts, but organic cations tend to preserve the perovskite structure even after exposure to moisture for over a year.



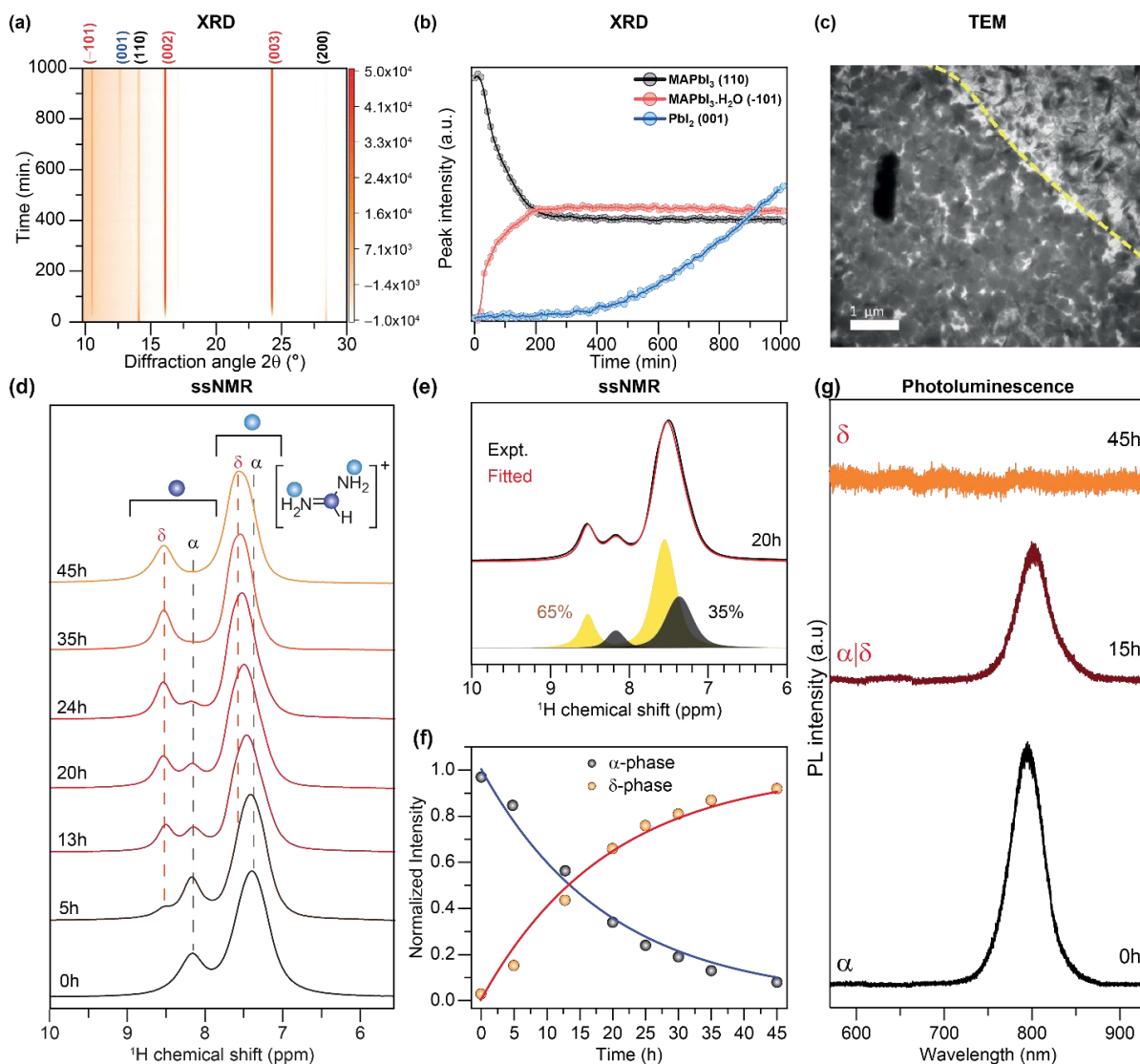


**Figure 5.2.** (a) *In situ* X-ray diffraction patterns of MAPbI<sub>3</sub> as a function of aging time until 1000 min under 85% RH. (b) corresponding evolution of the peak intensity as a function of time for the (110) plane of MAPbI<sub>3</sub> (black), (-101) plane of MAPbI<sub>3</sub>.H<sub>2</sub>O (red), and (001) plane of PbI<sub>2</sub> (blue). (c) *In situ* Transmission Electron Microscopy (TEM) showing the morphology of MAPbI<sub>3</sub>, MAPbI<sub>3</sub>.H<sub>2</sub>O, and PbI<sub>2</sub>. (d) <sup>1</sup>H MAS NMR spectra of fresh ( $\alpha$ -FAPbI<sub>3</sub>) and aged ( $\alpha$ -| $\delta$ -FAPbI<sub>3</sub>,  $\delta$ -FAPbI<sub>3</sub>) materials upon exposure to moisture (85% RH) (Same as Figure 2.3b). (e) Line shape deconvolution analyses for <sup>1</sup>H MAS NMR spectrum of 20 h aged (85% RH) FAPbI<sub>3</sub> to estimate the quantity of  $\alpha$ - and  $\delta$ -FAPbI<sub>3</sub>. (f) Kinetics plots of <sup>1</sup>H signal intensity buildup of -CH sites (FA<sup>+</sup> cations) in  $\delta$ -FAPbI<sub>3</sub> and the simultaneous <sup>1</sup>H signal intensity decay for the same sites in  $\alpha$ -FAPbI<sub>3</sub> as a function of exposure time to moisture (85% RH). (g) Photoluminescence spectra of FAPbI<sub>3</sub> as a function of moisture (85% RH) exposure time (Same as Figure 2.1). These figures have been adapted from Ref.<sup>1,14</sup>.

Extending on this multiscale characterization approach, a detailed assessment of the long-term moisture stability of MA-based perovskite thin films is provided in Chapter 3. A particularly interesting aspect of this study is that the thin films (milligram masses obtained by scratching the materials from glass substrates) can be used to study the degradation reactions. Cascade reactions and associated degradation kinetics are presented for MAPbI<sub>3</sub> thin films. The moisture-induced structural changes are examined via XRD to probe inorganic species (such as MAPbI<sub>3</sub>·H<sub>2</sub>O and PbI<sub>2</sub>) in the cascade reaction. ssNMR spectroscopy helps in determining dilute organic degradation products, such as MAI, that are challenging to detect using other structure-determining techniques. The kinetics of the degradation reaction is dramatically influenced due to the concentration of water molecules in the vapor. The higher water concentration (85% RH) shifts the equilibrium towards the formation of byproducts, and the relatively low water vapor concentration (40% RH) leads to a long-lasting (one year) equilibrium between MAPbI<sub>3</sub> and MAPbI<sub>3</sub> hydrate. Surface defect passivation by TPA<sup>+</sup> cations impedes the moisture-induced degradation processes. However, prolonged exposure to moisture triggers the degradation process leading to the formation of organic and inorganic byproducts as identified by XRD and 1D/2D ssNMR techniques.

Beyond the photoactive layer, charge-transporting layers also influence the performance and stability of the perovskite solar cells, which brings additional challenges for atomic-scale characterization. For example, structural characterization of the inherently heterogeneous organic semiconductor hole-transporting materials (HTMs, spiro-OMeTAD) is challenging. BCF-doped spiro-OMeTAD is extensively examined with interest in understanding underlying doping mechanisms. Despite the structural heterogeneity associated with such organic molecules, magnetic resonance techniques supported by a few macroscopic-level techniques assists in obtaining crucial insights into the doping mechanism. Specifically, multinuclear NMR (<sup>11</sup>B, <sup>19</sup>F, <sup>1</sup>H, and <sup>13</sup>C) results provide key information on changes in the coordination, chemical environment, and heterogeneity in the magnetic properties in the blends of spiro-OMeTAD and BCF. These outcomes also supported BCF/BCF-water complexes acting as Lewis acid/ Brønsted acid. 1D/2D EPR techniques confirm the presence of paramagnetic species and further corroborate the miscibility of the host and dopant. The BCF-doped spiro-OMeTAD blend demonstrated exceptional moisture stability, with no major structural changes seen in aged material.

## 5.2 Perspectives

The multi-technique approach described in this thesis can be extended to understand structure-stability-property relationships in emerging photovoltaic materials. In pursuit of more efficient and durable perovskite-based devices, interfacial, dimensional, compositional, and additive engineering will be sought. In such a scenario, ssNMR spectroscopy will continue to provide unique atomic-level solutions to issues pertaining to processing, performance, and stability evaluations. The main challenge of intrinsically low sensitivity associated with ssNMR spectroscopy must be dodged to characterize layer-by-layer or a complete perovskite-based device. DNP-NMR experiments can be further utilized to enhance the sensitivity of thin films, perovskite materials with self-assembled molecules (SAM), and 3D/2D perovskite materials for superior stability.<sup>15</sup> *In operando* characterization of the material will be highly beneficial for thorough stability studies. Development of NMR probes that allow accurate tuning of the light intensity, temperature, and humidity in conjunction with fast MAS is required for the *in-operando* characterization. Characterizing the interfaces using NMR can be more straightforward if ssNMR experiments' limitation with sub-nm length scale can be resolved.

In the context of hole-transporting materials, numerous chemically tuned organic conjugated structures need to be explored for a cost-effective alternative to spiro-OMeTAD. In addition, a wide range of organic dopants utilized in the context of organic solar cells can be blended with spiro-OMeTAD for enhanced charge mobility and stability. Naturally available dyes and pigments with energy levels aligned with an ideal HTM for perovskites can also be screened for their application as HTMs. These materials might not be as desired as spiro-OMeTAD/PTAA, but they can be economically and environmentally viable.

### 5.3 References

- 1 M. A. A. Kazemi, P. Raval, K. Cherednichekno, J.-N. Chotard, A. Krishna, A. Demortiere, G. N. M. Reddy and F. Sauvage, *Small Methods*, 2021, **5**, 2000834.
- 2 S. Béchu, M. Ralaiarisoa, A. Etcheberry, P. Schulz, S. Béchu, A. Etcheberry, M. Ralaiarisoa and P. Schulz, *Adv. Energy Mater.*, 2020, **10**, 1904007.
- 3 M. A. A. Kazemi, N. Folastre, P. Raval, M. Sliwa, J. Marie, V. Nsanzimana, S. Golonu, A. Demortiere, J. Rousset, O. Lafon, L. Delevoye, G. N. M. Reddy and F. Sauvage, *Energy Environ. Mater.*, , DOI:10.1002/eem2.12335.
- 4 S. Mazumdar, Y. Zhao and X. Zhang, *Front. Electron.*, 2021, **2**, 712785.
- 5 R. Azmi, E. Ugur, A. Seitkhan, F. Aljamaan, A. S. Subbiah, J. Liu, G. T. Harrison, M. I. Nugraha, M. K. Eswaran, M. Babics, Y. Chen, F. Xu, T. G. Allen, A. ur Rehman, C. L. Wang, T. D. Anthopoulos, U. Schwingenschlögl, M. De Bastiani, E. Aydin and S. De Wolf, *Science*, 2022, **376**, 73–77.
- 6 D. J. Kubicki, S. D. Stranks, C. P. Grey and L. Emsley, *Nat. Rev. Chem.*, 2021, **5**, 624–645.
- 7 C. J. Dahlman, D. J. Kubicki and G. N. M. Reddy, *J. Mater. Chem. A*, 2021, **9**, 19206–19244.
- 8 T. Ueda, K. Shimizu, H. Ohki and T. Okuda, *Zeitschrift fur Naturforsch.*, 1996, **51**, 910–914.
- 9 T. Ueda, M. Omo, K. Shimizu, H. Ohki and T. Okuda, *Zeitschrift fur Naturforsch.*, 1997, **52**, 502–508.
- 10 W. M. J. Franssen and A. P. M. Kentgens, *Solid State Nucl. Magn. Reson.*, 2019, **100**, 36–44.
- 11 L. Piveteau, V. Morad and M. V. Kovalenko, *J. Am. Chem. Soc.*, 2020, **142**, 19413–19437.
- 12 R. W. Hooper, D. Sarkar and V. K. Michaelis, *Curr. Opin. Colloid Interface Sci.*, 2022, 101631.

- 13 D. Sarkar, R. W. Hooper, A. Karmakar, A. Bhattacharya, A. Pominov, V. V. Terskikh and V. K. Michaelis, *ACS Mater. Lett.*, 2022, **4**, 1255–1263.
- 14 P. Raval, R. M. Kennard, E. S. Vasileiadou, C. J. Dahlman, I. Spanopoulos, M. L. Chabiny, M. Kanatzidis and G. N. M. Reddy, *ACS Energy Lett.*, 2022, **7**, 1534–1543.
- 15 A. Mishra, M. A. Hope, M. Almalki, L. Pfeifer, S. M. Zakeeruddin, M. Grätzel and L. Emsley, *J. Am. Chem. Soc.*, 2022, **144**, 15175–15184.

# Experimental Section

---

## Chapter 2

**Material synthesis.** Large crystals (40-100 micrometers) of  $\alpha$ -FAPbI<sub>3</sub> were synthesized following the synthetic protocol of the previous report by first preparing a solution of 8 mL of 57% w/w aqueous HI and 1.2 mL of 50% w/w aqueous H<sub>3</sub>PO<sub>2</sub> and heating it to boiling during constant magnetic stirring in a fume hood.<sup>1</sup> 1137 mg (3 mmol) of lead acetate (Pb[CH<sub>3</sub>CO<sub>2</sub>]<sub>2</sub>·3H<sub>2</sub>O) were dissolved in the solution until it became a clear yellow color. Then, 312 mg (3 mmol) of formamidine acetate (FACH<sub>3</sub>CO<sub>2</sub>) were added to the solution, forming yellow crystals. The reaction mixture was heated for an additional 30 minutes until all of the yellow crystals turned black. Before allowing the solution to cool, the hot yellow solution was carefully pipetted out of the container. The remaining black crystals in the mixture were quickly vacuum-filtered and dried in a vacuum oven at 110 °C for 12h. It is noteworthy that the exposure of the black crystals to the solution at lower temperatures (e.g., allowing the mixture to cool before drying the crystals) caused the black crystals to partially convert back to the yellow crystal phase. Small crystals of  $\alpha$ -FAPbI<sub>3</sub> were synthesized by adjusting the final annealing step. In this case, 1137 mg (3 mmol) of Pb(CH<sub>3</sub>CO<sub>2</sub>)<sub>2</sub>·3H<sub>2</sub>O were dissolved in a solution consisting of 8 mL of 57% w/w aqueous HI and 1.2 mL of 50% aqueous H<sub>3</sub>PO<sub>2</sub>, by heating to boiling whilst undergoing constant magnetic stirring. Then 312 mg (3 mmol) of formamidine acetate were added to the hot yellow solution, leading to the formation of yellow crystals ( $\delta$ -phase) and black crystals ( $\alpha$ -phase). They were collected by suction filtration and dried under vacuum at 180°C for 14h. This treatment gave rise to a stabilized black  $\alpha$ -phase with a narrow distribution of particle sizes in the range of 20-40 micrometers. Yield: 1044 mg, (55% based on Pb).

**Materials synthesis and processing for CsMAFA thin films and CsPb<sub>2</sub>Br<sub>x</sub>I<sub>5-x</sub>.** Unless specified, all chemicals were purchased from Sigma-Aldrich. Mesoporous TiO<sub>2</sub> paste and FK209 were purchased from GreatCell Solar. PbI<sub>2</sub>, PbBr<sub>2</sub>, and CsI were purchased from TCI. CsBr was purchased from Alfa Aesar. FAI and MABr were purchased from Dyenamo. Glass substrate were systematically cleaned with 2 vol.% of hellmanex solution in DI water, isopropanol

(Sigma-Aldrich), acetone (Sigma-Aldrich) and treated with UV-O<sub>3</sub> cleaner for 15 minutes prior usage. The CsMAFA precursor solution was prepared by dissolving 1.1 mol/L PbI<sub>2</sub> (508mg), 0.22 mol/L PbBr<sub>2</sub> (80.7mg), 1 mol/L FAI (172 mg), 0.20 mol/L MABr (22.4 mg) and 0.06 mol/L CsI (17.5 mg) in anhydrous N,N-dimethylformamide (Sigma-Aldrich) and anhydrous dimethylsulfoxide (Sigma-Aldrich) with 4:1 ratio (v/v), respectively. The solution was kept at 70 °C for two hours under stirring and then cooled down to ambient temperature and filtrated through a 0.45 μm syringe filter, yielding a nominal composition of Cs<sub>0.05</sub>(FA<sub>0.83</sub>MA<sub>0.17</sub>)<sub>0.95</sub>Pb(I<sub>0.83</sub>Br<sub>0.17</sub>)<sub>3</sub>. The solution was spin-coated according to a two-step procedure inside an Ar-filled glovebox (MBraun Unilab Pro SP), first at 2000 rpm for 10 s and then 4000 rpm for 20 s. During the second step, 100 μL of chlorobenzene as an anti-solvent was dropped 10 s before the program's end. These films were annealed at 110 °C for 45 minutes inside the glovebox to crystallize the perovskite structure leading to a mirror-like dark film.

The CsPb<sub>2</sub>Br<sub>5</sub> powder was synthesized by crystallization reaction of lead bromide (1.4 mmol) and cesium bromide (0.7 mmol). They were dissolved in 6 mL of HBr (HBr, 48%, Fisher chemicals). The mixture was heated at 118 °C and stirred overnight. After that, the reaction vessel was led to cool down at room temperature, and the precipitates were collected by vacuum filtration and washed by diethyl ether. The precipitates were dried under vacuum at 60 °C to obtain the powder. Different cesium lead Br/I stoichiometry powders were prepared by crystallization method (detailed for the synthesis of CsPb<sub>2</sub>Br<sub>5</sub>) of various precursor salts (PbI<sub>2</sub>:PbBr<sub>2</sub>:CsBr:CsI) in HBr.

**X-ray diffraction.** X-ray diffraction patterns were acquired using an Empyrean Powder Diffractometer with a step size of 0.01313°, and a Cu-Kα source, operating with an accelerating voltage of 45 kV and the beam current of 40 mA, with samples rotated at 4 revolutions/min to improve signal-to-noise ratios. For high humidity *ex-situ* XRD experiments, powders of α-FAPbI<sub>3</sub> were placed in a small (4 mL) vial. This vial was placed in a larger (20 mL) vial containing water, such that the liquid water was not in direct contact with the powder. Then, the larger vial was capped with a Teflon-lined seal so that the relative humidity in this experiment was approximately 100%. To keep light out, a large vial made of dark brown glass was selected. For humidity tests (85% RH) with *ex-situ* powder XRD experiments, powder composition of fresh α-FAPbI<sub>3</sub> was suspended on glue placed on a zero-diffraction silicon substrate. This

substrate was placed in a hydration chamber maintained at  $85\pm 2\%$  RH (relative humidity in the air) in the presence of laboratory illumination. The substrate was taken out at regular intervals to acquire powder XRD patterns at a Rigaku MiniFlex powder diffractometer. All XRD measurements were carried out at room temperature.

**Scanning electron microscopy (SEM)** experiments were performed using an FEI Nova Nano 650 FEG SEM with beam currents of 0.40-0.80 nA, and at 7-10 keV accelerating voltage. Prior to SEM measurements, the samples were sputter-coated with gold to prevent charging.

**Optical microscopy.** All microscopy images were acquired with Leica S9i Digital Stereo Microscope, with a zoom range of 0.61x - 5.5x for a total magnification of 6.1x - 55x with 10x eyepieces. The microscope was integrated with a 10 M.P. camera to provide 1080P high-definition photographs of the perovskite particles. The perovskite particles with varying sizes of a few 10's to 100's micrometers were dispersed on a glass slide, which was then placed in a hydration chamber with 85% relative humidity in the air at room temperature ( $\sim 300$  K). The glass slide was taken out from the hydration chamber at regular intervals to acquire micrographs, whereby the materials were exposed to moisture (45-60% RH) during the image collection. Photographs were acquired for the fresh black phase, intermediate black/yellow, and yellow phase at different magnifications for the small and large particles to be identified and distinguished.

**Photoluminescence.** For photoluminescence (PL) studies, fresh FAPbI<sub>3</sub> black phase and intermediate black/yellow and yellow FAPbI<sub>3</sub> materials (after exposure to moisture at 85% RH) were considered. All samples were measured using a Horiba LabRam Evolution high-resolution confocal Raman microscope spectrometer (600 g/mm diffraction grating) equipped with a diode continuous-wave laser (473 nm, 25 mW) and a Synapse charge-coupled device camera. The utilized power output of the laser source was filtered to 1% of the maximum power output.

**Solid-state NMR spectroscopy for FAPbX<sub>3</sub> crystals.** Fresh and moisture-aged FAPbI<sub>3</sub> and FAPbBr<sub>3</sub> materials were separately packed into air-tight and opaque 1.3 mm (outer diameter) zirconia rotors fitted with VESPEL caps to ensure the material stability during NMR data acquisition. All solid-state MAS NMR experiments were conducted *ex-situ* either on a 21.1 T (<sup>1</sup>H, 900 MHz) Bruker AVANCE-NEO or 18.8 T (<sup>1</sup>H, 800 MHz) Bruker AVANCE NEO NMR



spectrometer using a 1.3 mm H-X probehead. Unless specified, the MAS frequency was 50 kHz in all ssNMR experiments. 1D  $^1\text{H}$  MAS NMR spectra were acquired by co-addition of 16 transients. The relaxation delays were set to 45 s, as determined from saturation recovery measurements and analyses, leading to the total experimental time of  $\sim 12$  minutes each. For  $\text{FAPbI}_3$ , 1D  $^{207}\text{Pb}$  experiments were carried out using a spin-echo sequence with 4096 co-added transients using a relaxation delay of 800 ms, leading to an overall experimental time of  $\sim 1\text{h}$  each, and for  $\text{FAPbBr}_3$  2048 co-added transients were acquired under the same experimental conditions required  $\sim 30$  minutes to complete. 2D  $^1\text{H}$ - $^1\text{H}$  double-quantum(DQ)-single-quantum(SQ) NMR spectra were acquired using Back-to-Back (BaBa) sequence under fast MAS.<sup>2-4</sup> A rotor-synchronized  $t_1$  increment of 20  $\mu\text{s}$  was applied with a recoupling time of 40  $\mu\text{s}$ , which corresponds to two rotor periods ( $2\tau_r$ ). The indirect  $^1\text{H}$  DQ dimension was acquired using 128  $t_1$  increments, each with 16 co-added transients, leading to an experimental time of  $\sim 25\text{h}$ . 2D  $^1\text{H}$ - $^1\text{H}$  spin diffusion NMR experiments were acquired using three-pulse noesy-like sequence with 1, 50, and 200 ms of mixing times.<sup>5,6</sup> A rotor-synchronized increment of 20  $\mu\text{s}$  was applied to detect 400  $t_1$  increments, each with 2 scans, leading to an experimental time of  $\sim 9\text{h}$  each. The  $^1\text{H}$ -detected 2D  $^1\text{H}$ - $^{207}\text{Pb}$  cross-polarization (CP) heteronuclear correlation (HETCOR) spectra were acquired with 28  $t_1$  increments, each with 800 co-added transients, using a recycle delay of 300 milliseconds, leading to a total experimental time of  $\sim 2\text{h}$ .<sup>7,8</sup> CP contact time was 5 ms. The  $^1\text{H}$  experimental shift was calibrated with respect to neat TMS using adamantane as an external reference ( $^1\text{H}$  resonance, 1.82 ppm). The experimental  $^{207}\text{Pb}$  shifts were calibrated using  $\text{Pb}(\text{NO}_3)_2$  as an external standard according to IUPAC recommendation.<sup>9</sup>

To understand the impact of particle size on moisture-induced degradation, large and small  $\text{FAPbI}_3$  particles are placed in a closely packed desiccator at a controlled humidity (85% RH), and the water vapor content is examined using a hygrometer placed in a desiccator. To carry out 1D and 2D experiments, these particles are taken out from the desiccator at regular intervals and packed into air-tight 1.3 mm NMR rotors. For the controlled humidity (40% RH) exposure, the  $\text{FAPbI}_3$  samples were placed in a desiccator along with silica beads which maintained the relative humidity of  $40\pm 5\%$ . In all cases, the sample packing time was 3-5 mins at ambient humidity of  $\sim 45\pm 5\%$  RH, so that any material degradation during the packing process is negligible compared to several hours of exposure to moisture in desiccators.

For light illumination experiments, small FAPbI<sub>3</sub> particles (20-40 micrometer) are considered. The samples were placed in separate air-tight glass desiccators, one of which is exposed to laboratory illumination while the other is stored under dark conditions. These materials were separately packed into the 1.3 mm NMR rotors, and *ex-situ* <sup>1</sup>H MAS NMR experiments were carried out.

For <sup>2</sup>H ssNMR studies, the deuteration of FA<sup>+</sup> cations in  $\alpha$ -FAPbI<sub>3</sub> was achieved by placing it in a dark humidity chamber at ambient temperature along with a saturated solution of KCl in D<sub>2</sub>O. The sample was then packed into a 1.3 mm zirconia rotor for <sup>1</sup>H and <sup>2</sup>H NMR experiments. The static 1D <sup>2</sup>H NMR spectrum was acquired by co-adding 4096 transients. In FA<sup>+</sup> cations, only NH<sub>2</sub> sites are expected to be deuterated during the exposure to D<sub>2</sub>O vapor. The percentage of isotopic <sup>2</sup>H labeling of -NH<sub>2</sub> sites was measured by integrating the <sup>1</sup>H signals of NH<sub>2</sub> sites and comparing it with the -CH signal of the FA cation. This procedure allows up to 70% of NH<sub>2</sub> sites in FA<sup>+</sup> cations to be deuterated. To understand the effect of <sup>1</sup>H $\leftrightarrow$ <sup>2</sup>H isotopic exchange and <sup>2</sup>H NMR lineshapes of cubic perovskite ( $\alpha$ ) and non-perovskites ( $\delta$ ) phases, two different control experiments were carried out: First, an  $\alpha$ -FAPbBr<sub>3</sub> phase was used as a control material for cubic phase because it does not undergo a phase transformation in the presence of moisture. FAPbBr<sub>3</sub> was stored in a dark humidity chamber with D<sub>2</sub>O vapor for 48h at ambient temperature. The D<sub>2</sub>O exposed FAPbBr<sub>3</sub> material was then packed into a 1.3 mm air-tight zirconia rotor. The static 1D <sup>2</sup>H NMR experiment was acquired by co-adding 8192 transients. The extent of deuteration was examined by carrying out a 1D <sup>1</sup>H MAS NMR spectrum for the same material, acquired by co-adding 4 transients. A deconvolution analysis leads to an estimation of the degree of deuteration, which was found to be 33% (i.e., ~33% of -NH<sub>2</sub> sites were deuterated). Second, a non-perovskite  $\delta$ -FAPbI<sub>3</sub> material (obtained after exposure of  $\alpha$ -FAPbI<sub>3</sub> material to 85% RH for over a week) was used as a control sample.

The  $\delta$ -FAPbI<sub>3</sub> material was then placed in the dark humidity chamber with D<sub>2</sub>O vapor for 48h. A static 1D <sup>2</sup>H NMR spectrum of this material was acquired by co-adding 73728 transients. Deconvolution of 1D <sup>1</sup>H MAS NMR spectrum, acquired by co-adding 4 transients, suggests ~30% of deuteration. These two different control experiments aid the analysis of <sup>2</sup>H NMR line shapes of fresh and moisture aged target  $\alpha$ -FAPbI<sub>3</sub> materials.

**Solid-state NMR spectroscopy for CsMAFA thin films and CsPb<sub>2</sub>Br<sub>x</sub>I<sub>5-x</sub>.** For solid-state NMR spectroscopy experiments, Cs<sub>0.05</sub>(MA<sub>0.17</sub>FA<sub>0.83</sub>)<sub>0.95</sub>Pb(Br<sub>0.17</sub>I<sub>0.83</sub>)<sub>3</sub>(CsMAFA) films spin-coated on glass substrates were scratched to obtain approximately 12 mg of the powder. For aging the CsMAFA material in moisture, it was stored in the dark in a desiccator where the humidity (water vapour concentration) was controlled at 40±5% RH in the air. For the exposure at 85±5% RH in the air, the material was stored for different exposure times in a humidity-controlled hydration chamber. The sample was packed into a 1.3 mm rotor closed with Vespel® caps. All 1D <sup>1</sup>H and <sup>133</sup>Cs NMR experiments of fresh and aged CsMAFA materials were carried out on a Bruker Avance Neo (18.8 T, <sup>1</sup>H Larmor frequency = 800.1 MHz) spectrometer using a double-resonance HX 1.3 mm MAS probe. The MAS frequency was 50 kHz. The nutation frequency of <sup>1</sup>H was 192 kHz, corresponding to a 90° pulse duration of 1.3 μs. The <sup>1</sup>H spin–lattice relaxation times (*T*<sub>1</sub>) were determined to be 24 s for CH<sub>3</sub> and NH<sub>3</sub> protons in methylammonium cation and 26 s for formamidinium cation in CsMAFA using inversion-recovery measurements and analyses. 1D <sup>1</sup>H MAS NMR spectrum was acquired using 16 co-added transients and a recovery delay τ<sub>RD</sub> = 32 s. 2D <sup>1</sup>H-<sup>1</sup>H spin-diffusion (SD) NMR spectrum of aged CsMAFA (168 h, 85% RH) was acquired with rotor-synchronized 160 *t*<sub>1</sub> increments. The nutation frequency of <sup>133</sup>Cs was 69 kHz, which corresponds to a 90° pulse duration of 3.6 μs. 1D <sup>133</sup>Cs MAS NMR spectrum of fresh CsMAFA material was acquired using 192 co-added transients, and a <sup>133</sup>Cs MAS NMR spectra of the same material after exposure to moisture (168 h) was acquired with 3072 co-added transients. To understand the different distributions of <sup>133</sup>Cs signals in the aged CsMAFA material and identify different by-products, solid-state <sup>133</sup>Cs NMR experiments of solid solution of CsBr: 2PbBr<sub>2</sub> and CsI:2PbI<sub>2</sub> materials were separately carried out. These materials were packed into a 3.2 mm rotor, and <sup>133</sup>Cs spectra were acquired using a double-resonance HX 3.2 mm MAS probe at MAS frequency of 20 kHz. <sup>133</sup>Cs nutation frequency was 125 kHz corresponding to a 90° pulse duration of 2.0 μs. 1D <sup>133</sup>Cs spectra were acquired using 32 co-added transients, corresponding to *T*<sub>exp</sub> = 34 min. The <sup>1</sup>H chemical shifts were calibrated with respect to neat TMS using adamantane as an external reference (<sup>1</sup>H resonance, 1.8 ppm). The <sup>133</sup>Cs shifts were calibrated with respect to 0.1 M CsCl solution.

### Chapter 3

**Sample preparation.** For MAPbI<sub>3</sub> thin films, the precursor solution was prepared by dissolving 1 mol/L methylammonium iodide (MAI) (159 mg), 1 mol/L PbI<sub>2</sub> (461 mg) in anhydrous N, N-dimethylformamide (Sigma-Aldrich), and anhydrous dimethylsulfoxide (Sigma-Aldrich) with a 4:1 v/v ratio, respectively. The solution was kept at 70 °C overnight under stirring and then cooled down to ambient temperature. The solution was spin-coated (MBraun SC210) on a glass substrate according to a two-step procedure inside an Ar-filled glovebox (MBraun Unilab Pro SP), first at 1000 rpm for 10 s and 4000 rpm for 20 seconds. During the second step, 1 mL of toluene as an anti-solvent was dropped 10 s before the end of the program. These films were annealed at 110 °C for 30 min inside the glovebox to crystallize the perovskite structure leading to a mirror-like dark film. For TPA<sup>+</sup> passivated MAPbI<sub>3</sub>, stoichiometric 4 mol.% of tetrapropylammonium iodide (TPAI) was utilized to substitute MAI.

**X-ray Diffraction.** X-ray diffraction patterns of thin films were acquired *in situ* by Bruker D8 diffractometer with a Cu-K $\alpha$  source ( $\lambda_{\text{CuK}\alpha 1} = 1.54056 \text{ \AA}$  and  $\lambda_{\text{CuK}\alpha 2} = 1.54439 \text{ \AA}$ ), equipped with a LynxEye detector. Each diffraction pattern was acquired from  $2\theta = 7^\circ - 40^\circ$  with a step size of  $0.01^\circ$ .

**Solid-state NMR spectroscopy.** Pristine and passivated perovskite material was obtained by scratching off the spin-coated thin films. The samples were then packed into a 1.3, 1.6, or 2.5 mm rotor. All 1D <sup>1</sup>H MAS and 2D <sup>1</sup>H-<sup>1</sup>H correlation NMR experiments on pristine and moisture-exposed perovskites were carried out on a Bruker Avance Neo (18.8 T, <sup>1</sup>H Larmor frequency = 800.1 MHz) spectrometer using a 1.3 mm Bruker double-resonance HX probe, 1.6 mm Phoenix triple-resonance HXY probe or 2.5 mm Bruker triple-resonance HXY probe. All the 1D <sup>1</sup>H MAS NMR spectra were acquired using a single pulse experiment. All the 2D <sup>1</sup>H-<sup>1</sup>H double-quantum (DQ)-single-quantum (SQ) NMR spectrum was acquired using a Back-to-Back (BaBa) sequence.<sup>2,10,11</sup> The 2D <sup>1</sup>H-<sup>1</sup>H spin-diffusion NMR spectrum was acquired using a three-pulse noesy-like sequence.<sup>12</sup> Detailed NMR acquisition parameters are given in Tables (A.1.-A.4.). The <sup>1</sup>H chemical shifts were calibrated with respect to neat TMS using the <sup>1</sup>H signal of adamantane at 1.8 ppm as a secondary external reference.

**Table ES.1.** Experimental parameters used for the acquisition of NMR spectra of MAPbI<sub>3</sub> exposed to 85% RH.

Exposure time	NMR experiment	Probe diameter (mm)	$NS^a$	$N_1^b$	$\tau_{\text{mix}} / \tau_{\text{rec}}^c$
0 h	1D <sup>1</sup> H	1.3	8	-	-
	2D <sup>1</sup> H- <sup>1</sup> H	1.3	16	128	40 $\mu$ s
	DQ-SQ	1.3	4	300	200 ms
	2D <sup>1</sup> H- <sup>1</sup> H SD	1.3	4	300	200 ms
17 h	1D <sup>1</sup> H	1.3	8	-	-
	2D <sup>1</sup> H- <sup>1</sup> H	1.3	16	128	40 $\mu$ s
	DQ-SQ	1.3	1	500	200 ms
	2D <sup>1</sup> H- <sup>1</sup> H SD	1.3	1	500	200 ms
34 h	1D <sup>1</sup> H	1.3	8	-	-
	2D <sup>1</sup> H- <sup>1</sup> H SD	1.3	4	400	500 ms
45 h	1D <sup>1</sup> H	1.3	8	-	-
	2D <sup>1</sup> H- <sup>1</sup> H	1.3	32	128	57 $\mu$ s
	DQ-SQ	1.3	4	400	500 ms
	2D <sup>1</sup> H- <sup>1</sup> H SD	1.3	4	400	500 ms

<sup>a</sup> Number of scans,  $NS$ . <sup>b</sup> Number of  $t_1$ -increments,  $N_1$ . <sup>c</sup> Length of mixing time,  $\tau_{\text{mix}}$ , for <sup>1</sup>H-<sup>1</sup>H SD and recoupling time,  $\tau_{\text{rec}}$ , for <sup>1</sup>H-<sup>1</sup>H DQ-SQ.

**Table ES.2.** Experimental parameters used for the acquisition of NMR spectra of MAPbI<sub>3</sub> exposed to 40% RH.

Exposure time	NMR experiment	Probe diameter (mm)	$NS^a$	$N_1^b$	$\tau_{\text{mix}}/\tau_{\text{rec}}^c$
1 month	1D <sup>1</sup> H	1.3	16	-	-
3 months	1D <sup>1</sup> H	1.6	32	-	-
6 months	1D <sup>1</sup> H	1.3	48	-	-
9 months	1D <sup>1</sup> H	1.3	60	-	-
12 months	1D <sup>1</sup> H	1.6	16	-	-
	2D <sup>1</sup> H- <sup>1</sup> H DQ-SQ	1.3	16	80	67 $\mu$ s
	2D <sup>1</sup> H- <sup>1</sup> H SD	1.6	1	256	500 ms

<sup>a</sup> Number of scans,  $NS$ . <sup>b</sup> Number of  $t_1$ -increments,  $N_1$ . <sup>c</sup> Length of mixing time,  $\tau_{\text{mix}}$ , for <sup>1</sup>H-<sup>1</sup>H SD and recoupling time,  $\tau_{\text{rec}}$ , for <sup>1</sup>H-<sup>1</sup>H DQ-SQ.

**Table ES.3.** Experimental parameters used for the acquisition of NMR spectra of MAPbI<sub>3</sub>.TPA(4%) exposed to 85% RH.

Exposure time	NMR experiment	Probe diameter (mm)	$NS^a$	$N_1^b$	$\tau_{\text{mix}}/\tau_{\text{rec}}^c$
0 h	1D <sup>1</sup> H	2.5	8	-	-
	2D <sup>1</sup> H- <sup>1</sup> H DQ-SQ	2.5	16	160	40 $\mu$ s
	2D <sup>1</sup> H- <sup>1</sup> H SD	2.5	2	400	500 ms
	1D <sup>1</sup> H	2.5	32	-	-
15 h	1D <sup>1</sup> H	2.5	32	-	-
22 h	1D <sup>1</sup> H	2.5	32	-	-
48 h	1D <sup>1</sup> H	2.5	32	-	-
72 h	1D <sup>1</sup> H	2.5	16	-	-
	2D <sup>1</sup> H- <sup>1</sup> H DQ-SQ	2.5	32	102	40 $\mu$ s
	2D <sup>1</sup> H- <sup>1</sup> H SD	2.5	8	256	500 ms

<sup>a</sup> Number of scans,  $NS$ . <sup>b</sup> Number of  $t_1$ -increments,  $N_1$ . <sup>c</sup> Length of mixing time,  $\tau_{\text{mix}}$ , for <sup>1</sup>H-<sup>1</sup>H SD and recoupling time,  $\tau_{\text{rec}}$ , for <sup>1</sup>H-<sup>1</sup>H DQ-SQ.

**Table ES.4.** Experimental parameters used for the acquisition of NMR spectra of MAPbI<sub>3</sub>.TPA(4%) exposed to 40% RH.

<b>Exposure time</b>	<b>NMR experiment</b>	<b>Probe diameter (mm)</b>	$NS^a$	$N_1^b$	$\tau_{\text{mix}} / \tau_{\text{rec}}^c$
3 months	1D <sup>1</sup> H	1.3	8	-	-
6 months	1D <sup>1</sup> H	1.3	4	-	-
9 months	1D <sup>1</sup> H	1.3	64	-	-
12 months	1D <sup>1</sup> H	1.6	32	-	-
	2D <sup>1</sup> H- <sup>1</sup> H DQ-SQ	1.3	32	128	50 $\mu$ s
	2D <sup>1</sup> H- <sup>1</sup> H SD	1.6	4	55	500 ms

<sup>a</sup> Number of scans,  $NS$ . <sup>b</sup> Number of  $t_1$ -increments,  $N_1$ . <sup>c</sup> Length of mixing time,  $\tau_{\text{mix}}$ , for <sup>1</sup>H-<sup>1</sup>H SD and recoupling time,  $\tau_{\text{rec}}$ , for <sup>1</sup>H-<sup>1</sup>H DQ-SQ.

## Chapter 4

**Materials and methods.** The solvents, spiro-OMeTAD, and BCF were purchased from Sigma Aldrich in a purity greater than 98% and used as received. All solvents were purchased dry, and molecular sieves were added to the solvents. The BCF was stored and handled in a nitrogen atmosphere glovebox to prevent water contamination. However, BCF is hygroscopic and interacts with traces of water molecules (present in solvents during the film deposition, and upon exposure to ambient moisture during the sample preparation to ssNMR experiments, i.e., scratching of thin films from the glass substrates and packing NMR rotors), which leads to the formation of BCF-water complexes. For solution-state optical spectroscopy measurements, separate solutions of spiro-OMeTAD and BCF were prepared (0.01 mmol/L) using chlorobenzene as the solvent. These solutions were placed on a vortex mixer for 10 minutes at room temperature to ensure the complete dissolution of OSC and dopant molecules. Stoichiometric amounts of BCF solution were added to the spiro-OMeTAD solution to prepare spiro-OMeTAD:BCF blends with 1:0.1, 1:0.2, 1:0.5, 1:1, 1:2, and 1:4 molar ratios, and the resultant solutions were homogenized with a vortex agitator for 10 minutes at room temperature.

**UV-visible absorption spectroscopy.** UV-visible absorption spectra were measured using Perkin Elmer Lambda 650 spectrophotometer. All experiments were carried out at room temperature. The spectra were acquired for the liquid samples (0.01 mmol.L<sup>-1</sup>) prepared as mentioned in the above section with a resolution of 1 nm.

**X-ray diffraction.** A Rigaku Smartlab diffractometer equipped with a copper rotated anode operated at 45kV and 200mA was used to record patterns of pristine, undoped, and doped spiro-OMeTAD thin films drop cast on ITO-coated glass substrates. Diffractograms were acquired in parallel beam configuration between 5 and 50° with a 0.01° step on a Rigaku HyPix3000 detector.

**Attenuated total reflectance Fourier transform infrared (ATR-FTIR) spectroscopy.** Perkin Elmer FTIR Spectrum two UATR spectrometer was used to acquire IR spectra of thin films of neat and doped spiro-OMeTAD, which were obtained by scratching the drop-casted film. The spectra were acquired with 20 scans and spectral resolutions of 4 cm<sup>-1</sup>.



**Solid-state NMR spectroscopy.** Samples for the ssNMR experiments were obtained by drop-casting the solutions (10 mg/mL) containing pristine spiro-OMeTAD, BCF, spiro-OMeTAD:BCF (1:0.25, 1:0.5, 1:1, 1:4 molar ratios) on ITO-coated glass substrates, and annealed at 70 °C for 20 minutes. These thin films were scratched from the glass substrates to collect enough material (~10 mg) into a glass vial. The samples were separately packed into either 1.3 mm or 2.5 mm (outer diameter) cylindrical zirconia rotors and fitted with Vespel® caps. All 1D  $^1\text{H}$ ,  $^{13}\text{C}$ ,  $^{11}\text{B}$ , and 2D  $^1\text{H}$ - $^1\text{H}$  MAS NMR experiments of pristine spiro-OMeTAD, BCF, and spiro-OMeTAD:BCF blends (1:1 and 1:4 molar ratio) were carried out on a Bruker AVANCE NEO (18.8 T, Larmor frequencies of  $^1\text{H}$ ,  $^{13}\text{C}$ , and  $^{11}\text{B}$  were 800.1 MHz, 201.2 MHz, and 256.7 MHz, respectively) spectrometer with 1.3 mm H-X probe head operating at room temperature. Unless otherwise mentioned, the magic-angle spinning (MAS) frequency was 50 kHz for all experiments. The  $^1\text{H}$  and  $^{13}\text{C}$  chemical shifts were calibrated with respect to neat TMS using adamantane as an external reference (higher ppm  $^{13}\text{C}$  resonance, 38.5 ppm, and the  $^1\text{H}$  resonance, 1.85 ppm), and the  $^{11}\text{B}$  NMR shifts were referenced using an external standard  $\text{NaBH}_4$  ( $^{11}\text{B}$  peak at -42.06 ppm), which is calibrated to  $\text{BF}_3\cdot\text{OEt}_2$  ( $^{11}\text{B}$ , 0 ppm) in  $\text{CDCl}_3$ . The  $^{19}\text{F}$  NMR spectra were calibrated with respect to  $^{19}\text{F}$  chemical shifts of neat  $\text{CFCl}_3$  ( $^{19}\text{F}$ , 0 ppm) as an external reference.<sup>9</sup>

All 1D  $^1\text{H}$  MAS NMR experiments were carried out by co-adding 32 transients using a relaxation delay of 4 seconds. The 1D  $^{11}\text{B}$  MAS NMR spectrum of neat BCF material was acquired by co-adding 256 transients, and the spectra of spiro-OMeTAD:BCF blends were acquired with 2048 co-added transients using a repetition delay of 2 seconds. All the 1D  $^{19}\text{F}$  MAS NMR experiments were carried out at 9.4 T ( $^{19}\text{F}$  Larmor frequency = 376.5 MHz) with 30 kHz MAS using a 2.5 mm H-X probehead, and each spectrum was acquired by co-adding 32 transients with a relaxation delay of 3 seconds. For undoped and doped Spiro-OMeTAD materials, the 1D  $^1\text{H}\rightarrow^{13}\text{C}$  CP-MAS spectra were acquired with 2048 and 5120 co-added transients and CP contact times of 2 ms and 4 ms, respectively. The 2D  $^1\text{H}$ - $^1\text{H}$  DQ-SQ spectra of pristine and doped spiro-OMeTAD were acquired with 96  $t_1$  increments, each with 16 co-added transients, using a Back-to-Back (BaBa) sequence at fast MAS.<sup>3,11</sup> The  $^1\text{H}$  detected 2D  $^1\text{H}$ - $^{13}\text{C}$  HETCOR spectra of pure spiro-OMeTAD were acquired with 256  $t_1$  increments, each with co-addition of 24 transients, with short (100  $\mu\text{s}$ ) and long (3 ms) CP contact times.

**Quantum mechanical calculations.** Input files for periodic DFT calculations were prepared by taking molecular coordinates from previously published crystal structures of spiro-OMeTAD (The Cambridge Crystallography Data Centre (CCDC) code: 1475944),<sup>13</sup> and BCF-water complexes (CCDC codes: 10429, and 1861707).<sup>14,15</sup> The pristine spiro-OMeTAD molecule is a 1292-electron system, and the BCF-water complex is a 556-electron system. For spiro-OMeTAD, we first performed a convergence test. In this test, we carried out a series of calculations by varying cut-off energy and monitored the convergence of the total energy of the molecular system in its irreducible representation (i.e., an asymmetric unit cell). The geometry optimization was performed using periodic DFT calculations, and the gauge including the projected augmented wave (GIPAW) method as described by Pickard and Mauri was used for the computation of NMR nuclear shieldings.<sup>16</sup> All DFT calculations were performed using the CASTEP 19.11 code.<sup>17</sup> Each SCF loop was performed until the energy was converged within  $3.67 \times 10^{-8}$  Hartrees. For all calculations, the generalized density approximation DFT functional PBE with the Tkatchenko-Scheffler (TS) dispersion correction scheme (DFT-D method) was applied, and the maximum plane wave cut-off energy was 29.4 Hartrees using an ultrasoft pseudopotential.<sup>18–20</sup> In all cases, the optimization algorithm was BFGS and the Monkhorst–Pack grid of minimum sample spacing  $0.07 \times 2\pi \text{ \AA}^{-1}$  was used to sample the Brillouin zone.<sup>21,22</sup> During the calculations, the positions of the atoms were varied within the unit cell until the average forces, energies, and displacements were converged to below  $3.6749 \times 10^{-7}$  Hartree/Å, 0.0011025 Hartrees, and 0.001 Å, respectively. The crystallographic information (CIF) and magnetic resonance shielding (magres) files are visualized using Mercury4.0 and Magresview tools.<sup>23</sup> The 2D spectra of calculated chemical shifts were generated using the Magresview package (available at [www.ccpnc.ac.uk](http://www.ccpnc.ac.uk)).

**Solid-state EPR spectroscopy.** All 1D X-band continuous-wave length (CW) EPR spectra were acquired with a Bruker ELEXYS E500 operating at cryogenic temperatures. For EPR pulses, the amplitude modulation and microwave power were 0.5 G and 1 mW, respectively. Relaxation times were measured on a Bruker ELEXYS E580 at 10 K using a 1D Hahn-echo sequence for  $T_2$  (transverse relaxation) and inversion recovery for  $T_1$  (longitudinal relaxation) measurements. For the homogenous EPR spectral lineshape,  $T_2$  was measured from FID decay as  $T_1$  was measured using FID inversion recovery sequence. The  $\pi/2$  and  $\pi$  pulses were 24 and 50 ns, respectively.

For pulsed 2D hyperfine sublevel correlation spectroscopy (HYSCORE) experiments, a four-pulse sequence  $(\pi/2)-\tau-(\pi/2)-t_1-(\pi)-t_2-(\pi/2)$ -detection(echo) sequence was used. The pulse lengths of  $\pi/2$  and  $\pi$  pulses of 28 ns and 52 ns, and the delay  $\tau = 300$  ns were chosen to remove the strong FID signal due to the homogenous part of the EPR signal in order to prevent blind spot effects. The 2D spectra were acquired with  $256 \times 256$  time-domain (t) data points to build  $t_1$  and  $t_2$  dimensions. The unmodulated part of the echo was removed by second-order polynomial subtraction. Finally, 2D Fourier transformation and a Hamming apodization window function were applied to obtain the HYSCORE spectra.

## References

- 1 I. Spanopoulos, W. Ke, C. C. Stoumpos, E. C. Schueller, O. Y. Kontsevoi, R. Seshadri and M. G. Kanatzidis, *J. Am. Chem. Soc.*, 2018, **140**, 5728–5742.
- 2 I. Schnell, A. Lupulescu, S. Hafner, D. E. Demco and H. W. Spiess, *J. Magn. Reson.*, 1998, **133**, 61–69.
- 3 G. N. M. Reddy, M. Malon, A. Marsh, Y. Nishiyama and S. P. Brown, *Anal. Chem.*, 2016, **88**, 11412–11419.
- 4 W. Sommer, J. Gottwald, D. E. Demco and H. W. Spiess, *J. Magn. Reson. Ser. A*, 1995, **113**, 131–134.
- 5 B. Elena and L. Emsley, *J. Am. Chem. Soc.*, 2005, **127**, 9140–9146.
- 6 B. Elena, G. Pintacuda, N. Mifsud and L. Emsley, *J. Am. Chem. Soc.*, 2006, **128**, 9555–9560.
- 7 M. P. Hanrahan, L. Men, B. A. Rosales, J. Vela and A. J. Rossini, *Chem. Mater.*, 2018, **30**, 7005–7015.
- 8 J. Lee, W. Lee, K. Kang, T. Lee and S. K. Lee, *Chem. Mater.*, 2021, **33**, 370–377.
- 9 R. K. Harris, E. D. Becker, S. M. Cabral De Menezes, R. Goodfellow and P. Granger, *Pure Appl. Chem.*, 2001, **73**, 1795–1818.
- 10 M. Feike, D. E. Demco, R. Graf, J. Gottwald, S. Hafner and H. W. Spiess, *J. Magn.*

- Reson. - Ser. A*, 1996, **122**, 214–221.
- 11 K. Saalwächter, F. Lange, K. Matyjaszewski, C. F. Huang and R. Graf, *J. Magn. Reson.*, 2011, **212**, 204–215.
  - 12 A. F. de Jong, A. P. M. Kentgens and W. S. Veeman, *Chem. Phys. Lett.*, 1984, **109**, 337–342.
  - 13 D. Shi, X. Qin, Y. Li, Y. He, C. Zhong, J. Pan, H. Dong, W. Xu, T. Li, W. Hu, J. L. Brédas and O. M. Bakr, *Sci. Adv.*, 2016, **2**, e1501491.
  - 14 A. A. Danopoulos, J. R. Galsworthy, M. L. H. Green, S. Cafferkey, L. H. Doerrer and M. B. Hursthouse, *Chem. Commun.*, 1998, 2529–2560.
  - 15 L. H. Doerrer and M. L. H. Green, *J. Chem. Soc. Dalt. Trans.*, 1999, 4325–4329.
  - 16 C. J. Pickard and F. Mauri, *Phys. Rev. B*, 2001, **63**, 245101.
  - 17 S. J. Clark, M. D. Segall, C. J. Pickard, P. J. Hasnip, M. I. J. Probert, K. Refson and M. C. Payne, *Zeitschrift für Krist.*, 2005, **220**, 567–570.
  - 18 J. P. Perdew, K. Burke and M. Ernzerhof, *Phys. Rev. Lett.*, 1996, **77**, 3865.
  - 19 A. Tkatchenko and M. Scheffler, *Phys. Rev. Lett.*, 2009, **102**, 073005.
  - 20 D. Vanderbilt, *Phys. Rev. B*, 1990, **41**, 7892.
  - 21 J. Nocedal and S.J. Wright, *Numerical Optimization*, Springer New York, 2006.
  - 22 H. J. Monkhorst and J. D. Pack, *Phys. Rev. B*, 1976, **13**, 5188.
  - 23 S. Sturniolo, T. F. G. Green, R. M. Hanson, M. Zilka, K. Refson, P. Hodgkinson, S. P. Brown and J. R. Yates, *Solid State Nucl. Magn. Reson.*, 2016, **78**, 64–70.



# Curriculum Vitae

---

## Parth Raval

Email: parthanraval@gmail.com

LinkedIn: parthraval14

---

### Education

#### **PhD (Chemistry)**

**2019-Present**

*University of Lille (France)*

Dissertation: Insights into structure-stability-property relationships in hybrid perovskites using solid-state NMR spectroscopy

Advisors: Prof. Olivier Lafon, Dr. Laurent Delevoye, and Dr. G N Manjunatha Reddy

#### **Integrated BS-MS (Chemistry)**

**2014-2019**

*Indian Institute of Science Education and Research, Mohali (India)*

Dissertation: Synthesis of Pb-based and Pb-free Perovskite Systems

Advisor: Dr. Debrina Jana

### Research Experiences

#### **University of Lille, France (PhD)**

**2019-Present**

Understanding the structure-stability-function correlations in metal halide perovskites and organic semiconductors for optoelectronic applications. In particular,

- Understanding morphology, microstructures, and stability of photovoltaic thin films using X-ray diffraction, microscopy, and solid-state NMR spectroscopy.
- Probing kinetics of transformative reactions in formamidinium-based perovskites.
- Outdoor stability of metal halide perovskites.
- Magnetic resonance spectroscopy (NMR and EPR) to understand the chemical doping of organic semiconductors.
- Employing the NMR crystallography approach to resolve molecular self-assembly and packing interactions in organic semiconductors and pharmaceutical solids.

#### **Indian Institute of Science Education and Research, Mohali, India (MS)**

**2018-2019**

Stable all-inorganic perovskite nanocrystals were synthesized, and their optical properties were tuned. A protocol was conceptualized to obtain a stable white light-emitting material. Photophysical and structural characterizations were carried out to understand the white-light emission process.

#### **Bhabha Atomic Research Centre, Dept. of Atomic Energy, India**

**2017**

Tungstate, molybdate, vanadate, and zirconate of zinc nanoparticles were synthesized using the sonochemical and sol-gel methods. The influence of doping these host materials with various transition metal ions and rare earth ions was investigated using XRD, SEM, and PL spectroscopy.

## **Publications**

1. **Raval, P.**; Kennard, R. M.; Vasileiadou, E. S.; Dahlman, C. J.; Spanopoulos, I.; Chabynyc, M. L.; Kanatzidis, M.; Reddy, G. N. M. Understanding Instability in Formamidinium Lead Halide Perovskites: Kinetics of Transformative Reactions at Grain and Subgrain Boundaries. *ACS Energy Lett.* 2022, 7, 1534–1543. <https://doi.org/10.1021/acseenergylett.2c00140>.
2. **Raval, P.**; Dhennin, M.; Vezin, H.; Pawlak, T.; Roussel, P.; Nguyen, T.-Q.; Reddy, G. N. M. Understanding the p-doping of spiroOMeTAD by tris(pentafluorophenyl)borane. *Electrochim. Acta* 2022, 424, 140602. <https://doi.org/10.1016/j.electacta.2022.140602>.
3. Kazemi, M. A. A.; **Raval, P.**; Cherednichekno, K.; Chotard, J.-N.; Krishna, A.; Demortiere, A.; Reddy, G. N. M.; Sauvage, F. Molecular-Level Insight into Correlation between Surface Defects and Stability of Methylammonium Lead Halide Perovskite Under Controlled Humidity. *Small Methods* 2021, 5, 2000834. <https://doi.org/10.1002/smt.202000834>.
4. Kazemi, M.A.A.; Folastre, N.; **Raval, P.**; Sliwa, M.; Marie, J.; Nsanzimana, V.; Golonu, S.; Demortiere, A.; Rousset, J.; Lafon, O.; Delevoye, L.; Reddy, G. N. M.; Ed, F.; Sauvage, E. Moisture-Induced Non-Equilibrium Phase Segregation in Triple Cation Mixed Halide Perovskite Monitored by In Situ Characterization Techniques and Solid-State NMR. *Energy Environ. Mater.* 2021. <https://doi.org/10.1002/EEM2.12335>.
5. Luginbuhl, B. R.<sup>#</sup>; **Raval, P.**<sup>#</sup>; Pawlak, T.; Du, Z.; Wang, T.; Schopp, N.; Chae, S.; Yoon, S.; Yi, A.; Kim, H. J.; Coropceanu, V.; Brédas, J.-L.; Nguyen, T.-Q.; Reddy, G. N. M. Resolving Atomic-Scale Interactions in Nonfullerene Acceptor Organic Solar Cells with Solid-State NMR Spectroscopy, Crystallographic Modelling, and Molecular Dynamics Simulations. *Adv. Mater.* 2022, 34, 2105943. <https://doi.org/10.1002/adma.202105943>. (# Equal Contribution)
6. Samanta, S.; **Raval, P.**; Reddy, G. N. M.; Chaudhuri, D. Cooperative Self-Assembly Driven by Multiple Noncovalent Interactions: Investigating Molecular Origin and Reassessing Characterization. *ACS Cent. Sci.* 2021, 7, 1391–1399. <https://doi.org/10.1021/acscentsci.1c00604>.
7. **Raval, P.**; Trébosc, J.; Pawlak, T.; Nishiyama, Y.; Brown, S. P.; Reddy, G.N.M. Combining heteronuclear correlation NMR with spin-diffusion to detect relayed Cl–H–H and N–H–H proximities in molecular solids. *Solid State Nucl. Magn. Reson.* 2022, 101808. <https://doi.org/10.1016/j.ssnmr.2022.101808>.
8. Welton, C. <sup>#</sup>; **Raval, P.** <sup>#</sup>; Trébosc, J.; Reddy, G. N. M. Chemical exchange of labile protons by deuterium enables selective detection of pharmaceuticals in solid formulations. *Chem. Commun.* 2022. <https://doi.org/10.1039/D2CC04585K>. (# Equal Contribution)
9. Azmy, A., Li, S., Angeli, G.K., Welton, C., **Raval, P.**, Li, M., Zibouche, N., Wojtas, L., Reddy, G.N.M., Guo, P., Trikalitis, P.N. and Spanopoulos, I. (2023), Porous and Water Stable 2D Hybrid Metal Halide with Broad Light Emission and Selective H<sub>2</sub>O Vapor Sorption. *Angew. Chem.* Accepted Author Manuscript. <https://doi.org/10.1002/anie.202218429>
10. Dutta, D. P.; **Raval, P.** Effect of transition metal ion (Cr<sup>3+</sup>, Mn<sup>2+</sup> and Cu<sup>2+</sup>) doping on the photocatalytic properties of ZnWO<sub>4</sub> nanoparticles. *J. Photochem. Photobiol. A Chem.* 2018, 357, 193–200. <https://doi.org/10.1016/j.jphotochem.2018.02.026>

11. **Raval, P.;** Kazemi, M. A. A.; Ruellou, J.; Trébosc, J.; Lafon, O.; Delevoye, L.; Sauvage, F.; Reddy, G. N. M. Examining year-long chemical degradation process and reaction kinetics in pristine and defect-passivated lead halide perovskites. *Chem Mater*. In revision.
12. **Raval, P.;** Hamdouna, L.; Thomas, N.; Delevoye, L.; Lafon, O.; Reddy, G. N. M. Boron adsorption kinetics of microcrystalline cellulose and polymer resin. *Submitted*.
13. **Raval, P.;** Sao, S.; Pal, T.; Pawlak, T.; Bhowal, R.; Chhetri S.; Khan, S.; Vijayaraghavan, R.K.; Chopra, D.; Chaudhuri, D.; and Reddy G.N.M. Synergy between molecular packing interactions and bulk optoelectronic properties in naphthalene diimides revealed by NMR crystallography. *In preparation*.

## **Conference Presentations**

1. **15<sup>th</sup> International conference on hybrid and organic photovoltaics** (May 2022)  
**Oral presentation:** Understanding morphology, microstructure, and stability of photovoltaic materials using solid-state NMR spectroscopy  
Contributors: **P.Raval**, R. Kennard, E. Vasileiadou, C. Dahlman, M. Dhennin, T. Pawlak, MAA. Kazemi, O. Lafon, L. Delevoye, F. Sauvage, I. Spanopoulos, P. Roussel, H. Vezin, M. Chabinye, T-Q. Nguyen, M.Kanatzidis, G. N. M. Reddy
2. **2<sup>nd</sup> Atomic-level characterization of hybrid perovskites conference** (Feb 2022)  
**Oral Presentation:** Probing moisture-induced structural and compositional changes in triple cation mixed halide hybrid perovskites  
Contributors: Kazemi, M.A.A.; Folastre, N.; **Raval, P.**; Sliwa, M.; Marie, J.; Nsanzimana, V.; Golonu, S.; Demortiere, A.; Rousset, J.; Lafon, O.; Delevoye, L.; Reddy, G. N. M.; Sauvage, F.
3. **13<sup>th</sup> International conference on hybrid and organic photovoltaics** (May 2021)  
**Poster presentation:** Probing structural and compositional changes in methylammonium-based and triple cation-based hybrid perovskites  
Contributors: **P.Raval**, M.A.A. Kazemi, J.Ruellou, J.Trébosc, O.Lafon, L.Delevoye, F.Sauvage, and G. N. M. Reddy
4. **6<sup>ème</sup> Journées Pérovskites Halogénées (Best Presentation Award)** (Apr 2021)  
**Oral presentation:** Solid-state NMR characterization of perovskites  
Contributors: **P.Raval**, M.A.A. Kazemi, J.Trébosc, O.Lafon, L.Delevoye, F.Sauvage, and G. N. M. Reddy
5. **Atomic-level characterization of hybrid perovskites conference (Best Poster Award) (Jan 2021)**  
**Poster Presentation:** Understanding long-term moisture stability of crystalline and defect-passivated methylammonium lead halide perovskites  
Contributors: **P.Raval**, M.A.A. Kazemi, J.Trébosc, O.Lafon, L.Delevoye, F.Sauvage, and G. N. M. Reddy